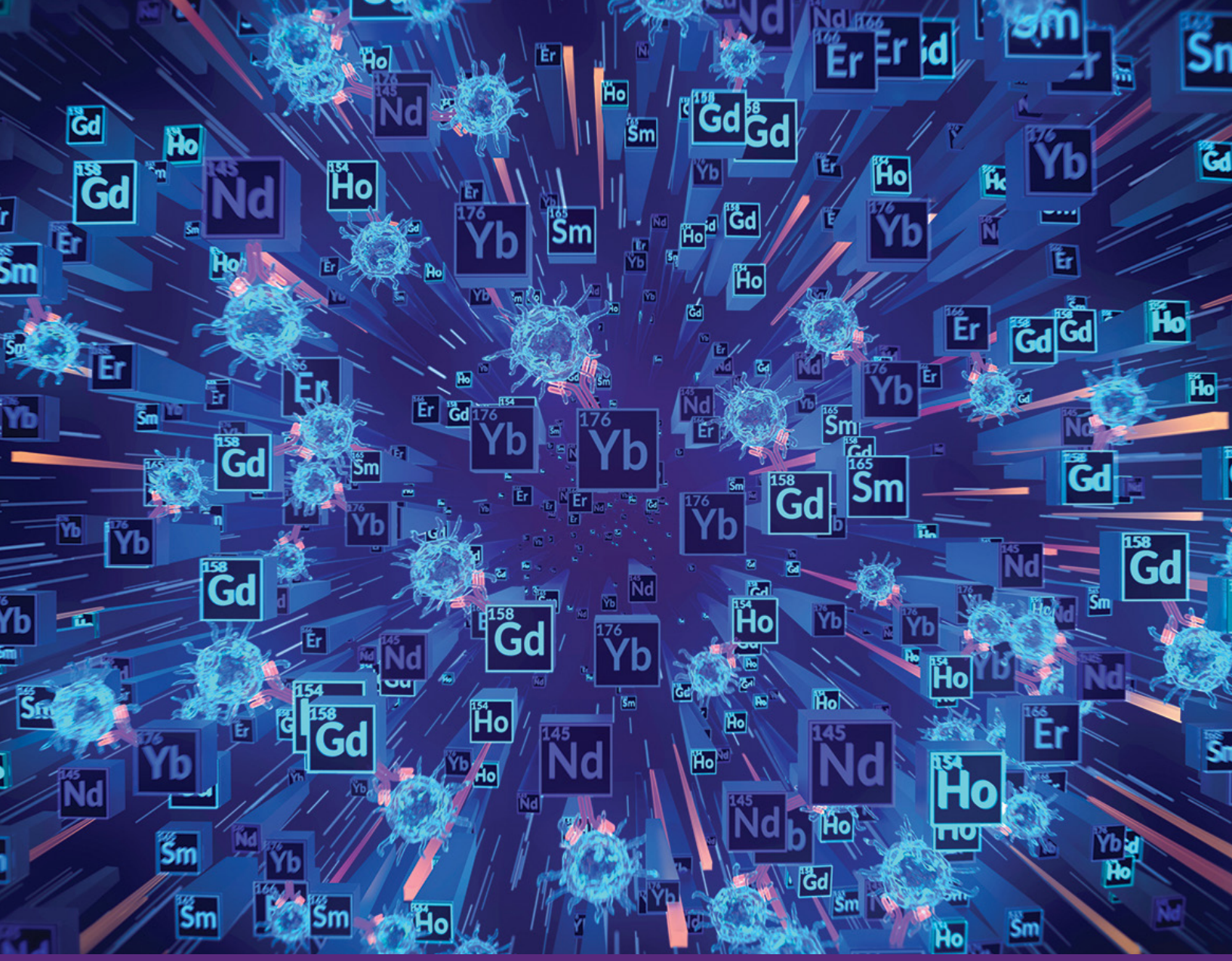

Surveying the Immune Landscape of Cancer with Mass Cytometry

ARTICLE COLLECTION

Cytometry PART A
ISAC
Journal of Quantitative Cell Science

FLUIDIGM®

FLUIDIGM®

It's not just about what you get with CyTOF XT. It's about what you save.

Save time. Save sample. Save effort. Save money.

Get all the advantages of mass cytometry for clinical research packaged in an easy-to-use and highly economical format with the new CyTOF XT.™

Mass cytometry provides

- Maxpar® Direct™ Assays: easy, efficient, high-content immune-profiling kits with a software solution
- the most data for every cell: 50-plus unique markers per panel
- flexible workflows: stain, freeze, store and ship samples

CyTOF XT is

- fully automated: hands-free instrument calibration, sample resuspension and acquisition
- easy to use: simplified cleaning and maintenance workflows
- highly economical: automation frees lab personnel, lower price point frees budget

See how much you can save with CyTOF XT >

CyTOF® XT

For Research Use Only. Not for use in diagnostic procedures.

Contents

Introduction

The immune system has emerged as a key player in the direction of cancer progression, displaying both pro- and antitumor capabilities as well as the capacity to be leveraged for treatment. To fully tease apart the interaction of immune cells within tumor microenvironments, researchers need to be able to clearly identify the presence and state of immune subpopulations. Conventional flow cytometry has been a mainstay of immunophenotyping for decades. Spectral flow cytometry, a relatively new approach to fluorescence cytometry, is also being used for immunophenotyping studies. However, both approaches suffer in the number of cell markers that can be incorporated into a single panel due to issues of emission spectra overlap. Mass cytometry or cytometry by time-of-flight mass spectroscopy (used in CyTOF® instruments) has emerged as a critical tool in the identification and monitoring of immune cells in the research and clinical spaces due to the precision of signal detection and lack of anything analogous to spectral overlap.

In contrast to fluorescence cytometry, cells for CyTOF analysis are stained with antibodies labeled with heavy metal isotopes not endogenous to biological systems. Labeled cells are injected as single-cell droplets and passed through a hot inductively-coupled plasma to ionize the isotope labels of bound antibodies. The ionized cloud enters the time-of-flight chamber and, based on the label's atomic mass, the time to reach the detector identifies the metal isotopes and associated antibody label with high precision. By virtue of this labeling and identification technology, CyTOF can incorporate 50 or more cellular markers in a single panel with negligible overlap in detection. Therefore, CyTOF is ideal for immunological studies and monitoring of therapeutic efficacy in clinical research. Key benefits are sensitive immunophenotyping assays where fluorescence spillover and autofluorescence are eliminated as sources of background signal and less precious sample is required for analysis.

In this article collection, we provide examples of how CyTOF technology allows for a highly precise and informative interrogation of immune cells in response to clinically relevant treatment approaches. To begin, we present four articles illustrating examples of using mass cytometry to monitor immune responses to cancer and effectiveness of therapeutic interventions in research studies.

First, Pisano et al. (2021) utilized a preclinical model of ovarian cancer to examine the immune landscape of the ascitic fluid surrounding the tumor and tumor nodules. Mass cytometry was able to identify both pro- and antitumor activity of immune cells in the ascitic fluid and cell populations in the tumor nodules that could serve as targets for therapeutic intervention.

Eiva et al. (2022) further expanded on the use of CyTOF for examining ovarian cancer by analyzing biomarkers for tumor infiltrating lymphocytes (TILs) and their origin in tumor tissue and *ex vivo* cells. Three identifiable populations of TILs were found to differentiate from a subset of CD137 expressing TILs, thereby indicating that CD137 may be of use as a selective biomarker identifying tumor-specific TILs.

Wang et al. (2020) used CyTOF to gain a better understanding of the immune checkpoint signals associated with multiple myeloma (MM). They discovered a distinct signature pattern of increased activated CD4 and CD8 T cells, and CD8+ natural killer T-like and NK cells in bone marrow of MM patients, providing new targets for immune checkpoint blockade therapy.

Last, Saxena et al. (2021) presented a clinical trial on the safety and efficacy of combining an anti-PD-L1 checkpoint inhibitor (avelumab) with a hypomethylating agent (azacytidine) in the treatment of relapsed/refractory acute myeloid leukemia (AML). This method of treatment, which primarily targets the PD-L1 ligand, has displayed limited ability to treat AML. Mass cytometric analysis of bone marrow samples from study participants treated with this combination uncovered a previously unknown activity of another PD-1 receptor ligand (PD-L2) that could potentiate immune evasion or tolerance. This suggests that blockade of PD-1 receptor itself instead of the ligand may be a more effective treatment.

While all of the above articles provide examples of the use of mass cytometry for immune monitoring and characterization, recent advances in the technology stand to give researchers and clinicians an even deeper and more reproducible ability to understand immune system activity. The CyTOF XT™ system is the next generation of mass cytometry technology, automating many aspects of the CyTOF workflow to increase throughput and reproducibility. Further, when combined with the Maxpar® Direct™ Immune

Profiling Assay™, the use of high-parameter cytometry for immune studies that are highly reproducible is facilitated. The full advantages of the system and supporting data can be found in the provided application note titled CyTOF XT: The Next Generation of Mass Cytometry.

Importantly, mass cytometry has demonstrated multi-site reproducibility. To support this, we provide two additional publications utilizing CyTOF with the Maxpar Direct Immune Profiling Assay. Bagwell et al. (2019) reported the findings of a multi-site study for validating the use of the assay in identifying immune cell populations from whole blood and peripheral blood mononuclear cell samples. Each site utilized the same instrumentation and assay on the provided samples. The study concluded that the Maxpar Direct Immune Profiling Assay can robustly and reproducibly detect 37 distinct immune cell populations using a 30-marker dry-format panel. Finally, Corneau et al. (2021) detailed the customization and validation of a Maxpar Direct Immune Profiling Assay based panel for CAR T cells and non-CAR cells in peripheral blood to monitor the outcomes of CAR T cell therapies in development.

With the ever-increasing complexity of the immune system becoming apparent during the development of therapeutic interventions, methods to clearly identify and track the activity of immune cell types are crucial to determining their effectiveness. Mass cytometry stands to revolutionize the ability of researchers and clinicians to monitor immune responses to therapies in a precise manner not afforded by conventional flow cytometry. By providing examples of applied mass cytometry for immune monitoring, we hope to educate readers on this powerful tool and how it may be leveraged for their specific translational and clinical research goals. For more information and resources for CyTOF, we encourage you to visit the Fluidigm Maxpar Direct Immune Profiling System and CyTOF XT webpages.

By Jeremy Petravicz, Ph.D., Editor,
Current Protocols

References

Pisano, S. et al. (2021). Assessment of the immune landscapes of advanced ovarian cancer in an optimized in vivo model. *Clin Transl Med;* 11: e551. https://doi.org/10.1002/ctm2.551

Eiva, M.A. et al. (2022). Systematic analysis of CD39, CD103, CD137, and PD-1 as biomarkers for naturally occurring tumor antigen-specific TILs. *Eur J Immunol;* 52: 96–108. https://doi.org/10.1002/eji.202149329

Wang, J. et al. (2020). Identification of the immune checkpoint signature of multiple myeloma using mass cytometry-based single-cell analysis. *Clin Transl Immunol;* 9: e1132. https://doi.org/10.1002/cti2.1132

Saxena, K. et al. (2021). A phase 1b/2 study of azacitidine with PD-L1 antibody avelumab in relapsed/refractory acute myeloid leukemia. *Cancer;* 127: 3761–71. https://doi.org/10.1002/cncr.33690

CyTOF XT: the next generation of mass cytometry. Fluidigm Application Note

Bagwell, C.B. et al. (2020). Multi-site reproducibility of a human immunophenotyping assay in whole blood and peripheral blood mononuclear cells preparations using CyTOF technology coupled with Maxpar Pathsetter, an automated data analysis system. *Cytometry;* 98: 146–60. https://doi.org/10.1002/cyto.b.21858

Corneau, A. et al. (2021). Mass cytometry: a robust platform for the comprehensive immunomonitoring of CAR-T-cell therapies. *Br J Haematol;* 194: 788–92. https://doi.org/10.1111/bjh.17551

For research use only.
Not for use in diagnostic procedures.

Received: 14 January 2021 | Revised: 6 August 2021 | Accepted: 9 August 2021

DOI: 10.1002/ctm2.551

CLINICAL AND TRANSLATIONAL MEDICINE

WILEY

RESEARCH ARTICLE

Assessment of the immune landscapes of advanced ovarian cancer in an optimized in vivo model

Simone Pisano[1,2] | **Stefania Lenna**[1] | **Gareth D. Healey**[2] | **Fereshteh Izardi**[2] | **Lucille Meeks**[1] | **Yajaira S. Jimenez**[1,3] | **Oscar S Velazquez**[1] | **Deyarina Gonzalez**[2] | **Robert Steven Conlan**[1,2] | **Bruna Corradetti**[1,2,3]

[1] Department of Nanomedicine, Houston Methodist Research Institute, Houston, Texas

[2] Center for NanoHealth, Swansea University Medical School, Swansea, UK

[3] Texas A&M Health Science Center, College of Medicine, Bryan, Texas

Correspondence
Bruna Corradetti, Department of Nanomedicine, Houston Methodist Research Institute, 6670 Bertner Ave., Houston, TX 77030.
Email: bcorradetti2@houstonmethodist.org

Funding information
European Union's Horizon 2020 Research and Innovation Program, Grant/Award Number: 663830

Abstract

Background: Ovarian cancer (OC) is typically diagnosed late, associated with high rates of metastasis and the onset of ascites during late stage disease. Understanding the tumor microenvironment and how it impacts the efficacy of current treatments, including immunotherapies, needs effective in vivo models that are fully characterized. In particular, understanding the role of immune cells within the tumor and ascitic fluid could provide important insights into why OC fails to respond to immunotherapies. In this work, we comprehensively described the immune cell infiltrates in tumor nodules and the ascitic fluid within an optimized preclinical model of advanced ovarian cancer.

Methods: Green Fluorescent Protein (GFP)-ID8 OC cells were injected intraperitoneally into C57BL/6 mice and the development of advanced stage OC monitored. Nine weeks after tumor injection, mice were sacrificed and tumor nodules analyzed to identify specific immune infiltrates by immunohistochemistry. Ascites, developed in tumor bearing mice over a 10-week period, was characterized by mass cytometry (CyTOF) to qualitatively and quantitatively assess the distribution of the immune cell subsets, and their relationship to ascites from ovarian cancer patients.

Results: Tumor nodules in the peritoneal cavity proved to be enriched in T cells, antigen presenting cells and macrophages, demonstrating an active immune environment and cell-mediated immunity. Assessment of the immune landscape in the ascites showed the predominance of $CD8^+$, $CD4^+$, B^-, and memory T cells, among others, and the coexistance of different immune cell types within the same tumor microenvironment.

Conclusions: We performed, for the first time, a multiparametric analysis of the ascitic fluid and specifically identify immune cell populations in the peritoneal cavity of mice with advanced OC. Data obtained highlights the impact of CytOF

as a diagnostic tool for this malignancy, with the opportunity to concomitantly identify novel targets, and define personalized therapeutic options.

KEYWORDS
ascites, CyTOF, immunotherapy, mass cytometry, model, ovarian cancer, peritoneal cancers

1 | INTRODUCTION

Ovarian cancer (OC) is the 7th most common cause of death in women worldwide, with over 21 000 new cases expected in the United States in 2020.[1] Survival rates vary according to the stage of disease, with a 5-year survival rate of around 30% for advanced cancers,[2,3] the most common of which is high-grade serous ovarian carcinoma (HGSOC) accounting for more than 50% of cases. Unfortunately, only 33% of OC cases are identified early, the majority being diagnosed at a later, more advanced stage, and associated with a significantly worse prognosis.[4]

According to the National Comprehensive Cancer Network (NCCN) guidelines, the standard of care therapy for HGSOC involves debulking surgery followed by platinum- or taxol-based chemotherapies. Among other recommended treatments, liposomal doxorubicin is a viable option for both early and advanced-stage disease.[5] Targeted therapeutic approaches, recently added to standard clinical practice, provide improved survival rates and include: vascular endothelial growth factor (VEGF)-A inhibitors,[6] and poly (ADP-ribose) polymerase (PARP) inhibitors, which are indicated for patients with a BReast CAncer gene (BRCA1/2) mutation.[5] OC remains a complex disease to treat, owing to the high chemotherapy-resistance emergence rate,[7] and in recent years great emphasis has been placed on the employment of immunotherapies to combat this issue, although currently no clinically approved immunotherapy for HGSOC exists. Modest activity within recurrent OC patients (which included epithelial, fallopian, or primary peritoneal OC) has been reported in the Phase II KEYNOTE-100 study for the checkpoint inhibitor (CPI) Pembrolizumab.[8] Additionaly, several Phase III trials are exploring the combination of CPI with PARP or VEGF inhibitors to determine any therapeutic synergies.[9]

Limited immunotherapy efficacy observed to date, however, could be explained by the typically "cold" immune status of OC. Indeed, the advanced OC tumor microenvironment (TME) is characterized by a lack tumor infiltrating lymphocytes (TILs) and failed T-cell priming due to a combination of poor antigen presentation and an intrinsic insensitivity to T-cell killing.[10,11] More specifically, tumor growth is associated with a scarcity (if not total absence) of CD8+ T cells within the TME,[12] or the inability of dendritic cells (DCs) to effectively present antigen and stimulate a cytotoxic response.[13] One of the possible mechanisms behind DC inactivation has been provided by Cubillos-Ruiz et al.[14] The authors demonstrated that the reduced capability of DC to support an anticancer immune response is associated to the transient, yet abnormal lipid accumulation in the endoplasmic reticulum, which obstructs their normal antigen-presenting capacity.[14] Another factor proposed to play a role in ovarian cancer progression at advanced stages and resistance to immunotherapy is the presence of transforming growth factor-β (TGF-β). Specifically, TGF-β is a potent immunosuppressor within the tumor environment being involved in several tumor-associated processes, including the increase of the epithelial to mesenchymal transition, the promotion of angiogenesis and immune suppression. The enhanced secretion of TGF-β within the tumor microenvironment is associated to the recruitment of regulatory T cells via expression of FoxP3, which ultimately results in diminished cytotoxic T-lymphocytes and in a reduced presence of DCs.[15,16] There is, however, a paucity of evidence on the specific roles of immune cell populations within the OC TME. Hence, a more comprehensive understanding of the immune cell landscape would provide an important platform for the development of more efficacious immunotherapeutic strategies.

The accumulation of fluid within the peritoneal cavity (ascites), which contains a variety of soluble and cellular components, is characteristic of advanced stage OC. Indeed, more than one third of OC patients present with ascites at diagnosis, which has been correlated with its spread within the peritoneal cavity and poor patient prognosis.[17] The accumulation of ascites occurs as a consequence of unbalanced drainage of the peritoneal cavity, due to obstruction of the lymphatic system by cancer cells,[17] or by increased leakage of fluid from the microvessels lining the peritoneum.[18] Ascites build-up also contributes to malignant progression by facilitating multifocal cancer cell dissemination on the peritoneal surface.[19] The presence of an intraperitoneal ascitic current, which acts as a means of transport of OC spheroids, further facilitates peritoneal, lymphatic, and hematogenous metastasis,[20] a phenomenon that falls within the multistep process of

metastatic dissemination. Soluble and cellular components within the ascitic fluid have also been shown to influence metastatic behavior.[17] Soluble components, including growth factors, cytokines, chemokines, and extracellular matrix pieces, inhibit T helper cell proliferation[21] and DC maturation[22] mediated by IL-10. Cellular components, such as resident tumor cells or tumor-associated fibroblasts, or nonresident immune cells, on the other hand, have a wide ranging impact on the TME. The presence, functionality, and effect of specific, singularly taken immune cell populations within the ascitic fluid has been widely described, unraveling the association between the presence of tumor-infiltrating CD8+ T cells and the prolonged disease-free survival,[23] or unmasking the role of T regulatory cells in creating an immunosuppressive environment.[24] As such, ascites represents a potentially very informative source of information regarding the effect of immune cells on metastatic disease progression. Moreover, its presence in over 30% of patients at diagnosis renders it an important issue to tackle and explore. Hence, a complete profiling of the ascites immune content would prove useful if done on patients in a tailored fashion. However, fundamental research on the biological interactions of the components of advanced OC ascites requires reliable in vivo models.

In this study, we optimize the development of an advanced OC model in immunocompetent mice to fill the gap in the understanding of the immune landscape within the peritoneal cavity. For the first time, we apply mass cytometry to comprehensively describe the immunological TME within the ascites and to provide insights about the effectiveness of the selected preclinical model in reproducing the human tumor immunomicroenvironment. Finally, we propose mass cytometry as an accurate strategy for the development of personalized strategies against advanced OC and all cancers metastasizing within the peritoneal cavity.

2 | METHODS

2.1 | Cell line

The ID8 cell line, originated from mouse ovarian surface epithelial cells (MOSEC), was purchased from Merck-Millipore. Cells were cultured in High Glucose Dulbecco's Modified Eagle medium (HG-DMEM) (Sigma) supplemented with 10% fetal bovine serum (FBS, ThermoFisher), 5 μg/mL insulin, 5 μg/mL transferrin and 5 ng/mL sodium selenite (1× ITS, Sigma) and 1× Penicillin-Streptomycin Solution (Sigma). Culture conditions were 37°C in a humidified 5% CO_2 atmosphere.

2.2 | Lentivirus transduction, lentiviral infection of ID8 cells with the luciferase vector and cell line selection

The ID8-Luc/GFP cell line was generated by transduction with Lentivirus particles containing the CMV promoter for the expression of humanized firefly luciferase (hLUC) and the SV40 promoter for the expression of GFP protein according to manufacturer's protocol (GeneCopoeia). Briefly, ID8 cells were plated at 2×10^4 cells per well (12-well plate, Corning) and incubated overnight at 37°C in a humidified 5% CO_2 atmosphere. Cells were then infected with 10 MOI of Lenti-PAC™ plasmid mix (GeneCopoeia Inc.) in the presence of 8 μg/mL polybrene (Sigma). After overnight incubation at 37°C/5% CO_2, the viral supernatant was discarded, and cells were washed with 1× PBS (ThermoFisher) prior to the addition of warmed HG-DMEM media. Three days after infection, cells with high levels of GFP expression were selected by Cell Sorter NIR Aria II (BD Bioscience) and expanded for a week in HG-DMEM media in presence of 1 μg/mL puromycin (Invitrogen) to further select transfected cells and generate a stable cell line.

2.3 | In vivo propagation of ID8-GFP tumors

Female C57BL/6 (5-6 weeks old) were purchased from the Charles Rivers laboratories. All animal studies were carried out in accordance with guidelines determined by the Animal Welfare Act and the Guide for the Care and Use of Laboratory Animals and complied with protocols approved by the Institutional Animal Care and Use Committee at the Houston Methodist Research Institute (AUP-0219-0013). Briefly, C57BL/6 female mice were divided into 3 groups ($n = 5$ mice per group) and injected intraperitoneally with 5×10^6, 1×10^7, or 1.5×10^7 ID8-Luc/GFP cells in 200 μL of PBS. Cells were injected into the lower right quadrant of the abdomen. Mice weights (g) were recorded daily following ID8-Luc/GFP cell injection and plotted as fold change. Representative macroscopic images of tumors and ascites development were taken with a smartphone camera.

2.4 | Bioluminescence, imaging, and tumor localization within the abdominal cavity

To track tumor growth, luciferase luminescence was detected using a Xenogen IVIS Spectrum imaging system

(PerkinElmer) as previously described.[25] Briefly, 200 μL of 15 mg/mL D-luciferin was injected into the mice abdomen and the bioluminescent signal evaluated after 10 min to obtain the peak photon emission per second. The signal was quantified using the Living Image software (PerkinElmer) and the total photon flux emission (photons/second) in the regions of interest (ROI) recorded, starting at day 8 after tumor cell injection. Images were normalized using the Living Image software (PerkinElmer) with a minimum and maximum radiance of 1.7×10^4 and 9.7×10^4 photons/s, respectively.

2.5 | Hematoxylin and eosin (H&E) staining and immunohistochemistry (IHC)

Sixty-three days after ID8-Luc/GFP cell injection, mice had a strong tumor signal intensity by IVIS. Hence, mice were sacrificed and the peritoneal membrane, abdominal tumors, and liver were sampled, fixed in 4% paraformaldehyde solution overnight, and embedded in paraffin. Paraffin embedded tissues were subsequently sectioned at a thickness of 5 μm and hematoxylin and eosin (H&E) staining performed to enable general inspection of the tissues. The 5 μm thick sections were also used for immunohistochemical staining. Sections were incubated with primary anti-CD3 (rabbit, Dako), anti-MHC-II (rat, eBioscience), or anti-F4/80 (rat, BioRad) for 1 h at room temperature (RT) in a moist chamber. Sections were imaged with a EVOS® FL Auto Imaging System (Life Technologies).

2.6 | Ascites extraction and mass cytometry by time of flight (CyTOF) analysis

Seventy days after tumor cell injection with 1×10^7 ID8-Luc/GFP cells, mice started developing ascitic fluid. Ascites onset was detected by abdomen palpation, by eye and by weight increase. After reaching a weight of 30 g, three mice were sacrificed, and the ascetic fluid collected by syringe suction following abdominal incision. Ascitic fluid was centrifuged, and red blood cells lysed by incubation in Ammonium-Chloride-Potassium (ACK) lysing buffer (ThermoFisher) for 10 min at RT. Immune cell enrichment was achieved using Percoll gradient centrifugation. Briefly, the cell pellet was resuspended in 85% Percoll (GE Healthcare), then carefully layered onto 50% Percoll and centrifuged at 620 × g without the brake for 30 min at 4°C. After centrifugation, three layers of cells were present. The middle layer, consisting of the immune cells of interest, was recovered and used for mass cytometry staining. Cell viability was determined by incubation with 25 μM cisplatin for 5 min. At these conditions, cisplatin preferentially reacts with proteins in dead cells and it widely established as a viability reagent for mass cytometry.[26] After washing in Maxpar® Cell Staining Buffer (Fluidigm), cells were resuspended in 40 μL surface-staining antibody (Ab) mix and incubated at RT for 30 min. Antibodies were purchased from Biolegend (except for Arginase-1 and NOS2, which were purchased from eBioscience) and conjugated to the metals using the Maxpar® X8 Multimetal Labeling Kit (Fluidigm). Selected Ab are shown in Table 1. Cells were then washed 2× and fixed with 100 μL of Fix/Perm buffer (eBioScience)

TABLE 1 Panel of the antibodies selected for mass cytometry, CyTOF. List of the 33 antibodies used, and their metal conjugation

Target	Metal tag
CD45	Pr141
MHC II	Nd142
CD11b	Nd143
Ly6C	Nd144
Ly6G	Nd145
F4/80	Nd146
CD11c	Sm147
CD38	Nd148
Arg-1	Sm149
SiglecF	Nd150
CD206	Eu151
CD62L	Sm152
CD103	Eu153
iNOS	Sm154
PD-L1	Gd155
TNFa	Gd156
CD64	Gd158
TCRgd	Tb159
Foxp3	Gd160
RORgt	Dy161
CD8α	Dy162
Tbet	Dy163
CD25	Dy164
IFN-γ	Ho165
CD44	Er166
CD86	Er167
CD80	Er168
PD-1	Tm169
B220	Er170
NK1.1	Yb171
CD19	Yb173
CD4	Yb174
TCR β	Lu175

for 10 min, followed by the addition of 200 μL Perm buffer (eBioScience) for 10 min. The intracellular staining was performed by diluting cells in 50 μL Ab mix and incubating them at RT for 60 min. After the washing steps, the cell ID DNA intercalator (500 μM, Fluidigm) was added to cells in a 1:1000 dilution for 30 min at RT. Cells were then washed, counted, and filtered through blue-capped tubes (35 μm) before resuspension in 50 μl deionized water and the addition of 50 μl of EQ-beads (eBioScience). Samples were acquired by Helios CyTOF machine. A total of 100 000 events were recorded for each sample, and subsequently analyzed on Cytobank. Immune cell populations were identified by manual gating. The intensity of the signal in the viSNE plots obtained was divided into three main groups. The following thresholds were used for categorization of the immune cell subtypes and applied to each specific viSNE plot: if the majority of the region was in the high range of expression (the red colored area, with numerical values varying according to the analyzed marker), the marker was considered highly expressed (++); if the region was in the middle range of expression (color-coded azure to orange) then the marker was considered to be moderately lowly expressed (+). Finally, if the area exhibited mostly lower expression (indicated by blue and dark blue colors), markers were considered not expressed (−).

2.7 | Statistical analysis

Statistical analysis was performed by ANOVA for all experiments that required it. More specifically, a two-way ANOVA with post hoc Dunnett comparisons to week 1 or Day 0 was employed for tumor signal and tumor weight analyses, respectively. Data with a $P < 0.05$ were considered significant ($*P < 0.05$, $**P < 0.01$, $***P < 0.001$). All results were obtained from independent experiments and expressed as the mean ± standard deviation (SD).

3 | RESULTS

3.1 | Tumor model optimization

After ID8-Luc/GFP cells (5×10^6, 1×10^7 or 1.5×10^7) were intraperitoneally injected, tumor growth was assessed over a 9-week period. After 9 weeks, animals injected with 1×10^7 cells showed a 13.6 ± 9 fold increase in tumor growth, based on fluorescence signal, compared to week 1 ($P < 0.001$), as quantified by IVIS (Figure 1A). Mice injected with 5×10^6 or 1.5×10^7 cells showed a 8.2 ± 4 fold and 5.6 ± 43.9 fold increase in tumor growth, respectively, again based on fluorescence signal, compared to week 1 ($P < 0.001$). No differences in tumor growth were noted between the three treatment groups, although all three groups showed increased tumor size over time. Representative pictures of the signal produced by the tumor within the abdomen are shown in Figure 1B. Figure 1C shows the fold variation of mice weights over the 9-week period, indicating a correlation between tumor growth and mouse weight, which was particularly evident following injection of 1×10^7 or 1.5×10^7 cells. Statistical difference was seen within groups at different time points when compared to the day of injection ($P < 0.001$). This difference became more marked after day 23 days in 5×10^6 group and after 37 days in 1×10^7 group. No statistically significant intragroup differences were recorded in 1.5×10^7 group. Sixty-three days after tumor cell injection, mice were sacrificed and organs extracted to better localize the tumors within the abdomen. ID8-Luc/GFP cells were identified in several abdominal organs including liver, kidneys, and spleen, and multiple tumor nodules/formations were randomly distributed around the abdominal cavity within the peritoneum (Figure 1D).

3.2 | Histological analysis of liver and tumor nodules

Tumors, extracted at day 63 after intraperitoneal injection, were processed and stained with H&E. Tumor growth occurred in two main areas; firstly the inner surface of the peritoneal membrane, as can be inferred from nodules visible in mice from the 1×10^7 group (Figure 2A), and second, the abdomen, where multiple tumor masses were found in multiple organs of the lower abdomen (Figure 2B). H&E staining of the liver, peritoneal membrane, and tumor masses within the abdominal cavity shows the presence of tumor growth within all three treatment groups and illustrates the extent of tumor infiltration throughout the peritoneal cavity (Figure 2C).

3.3 | Immunohistochemistry of immune infiltrates within tumors

Tissue sections were also analyzed by immunohistochemistry (IHC) to identify immune cell infiltration within tumors found on the peritoneal membrane. The presence of cell surface markers for T cells, antigen presenting cells (APC), and macrophages (CD3, MHC-II, and F4/80, respectively) was investigated in mice from all treatment groups (Figure 3). Significant immune cell infiltration was apparent in tumors present in all the treatment groups. Of note, there were high numbers of T cells and macrophages, indicating an active immune environment.

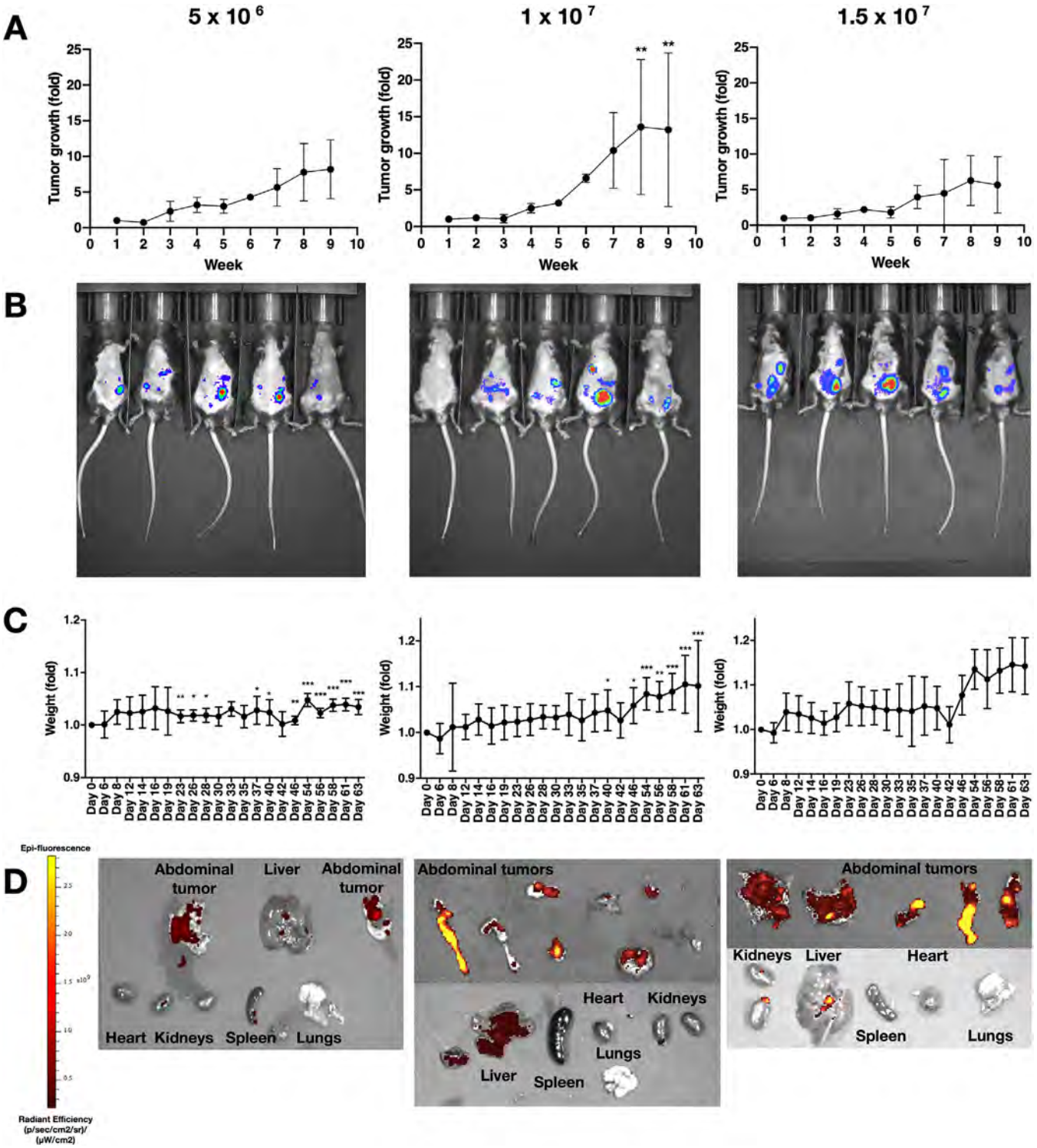

FIGURE 1 Tumor model generation and optimization. (A) Tumor growth signal quantification over a 9-week period by IVIS following injection of 5×10^6, 1×10^7, or 1.5×10^7 cells ($n = 5$). (B) Representative IVIS images of each tumor group taken after 6 weeks from tumor cells injection. (C) Mice weights (grams), expressed as fold change, during the 9-week experimental period ($n = 5$). (D) IVIS images of organs extracted from the mice abdomen 9 weeks after injection with 5×10^6, 1×10^7, or 1.5×10^7 ID8-Luc/GFP cells. Extracted organs include liver, spleen, kidneys, lungs, heart, peritoneal membranes, tumor nodules. Epi-fluorescent signals reflects the presence of ID8-Luc/GFP cells. Data are expressed as mean (SD) from 5 independent experiments. Data were analyzed by ANOVA and Dunnett's pairwise multiple comparison test; values differ from week 1 (A) or day 0 (C), $^*P < 0.05$, $^{**}P < 0.01$, $^{***}P < 0.001$

CLINICAL AND TRANSLATIONAL MEDICINE

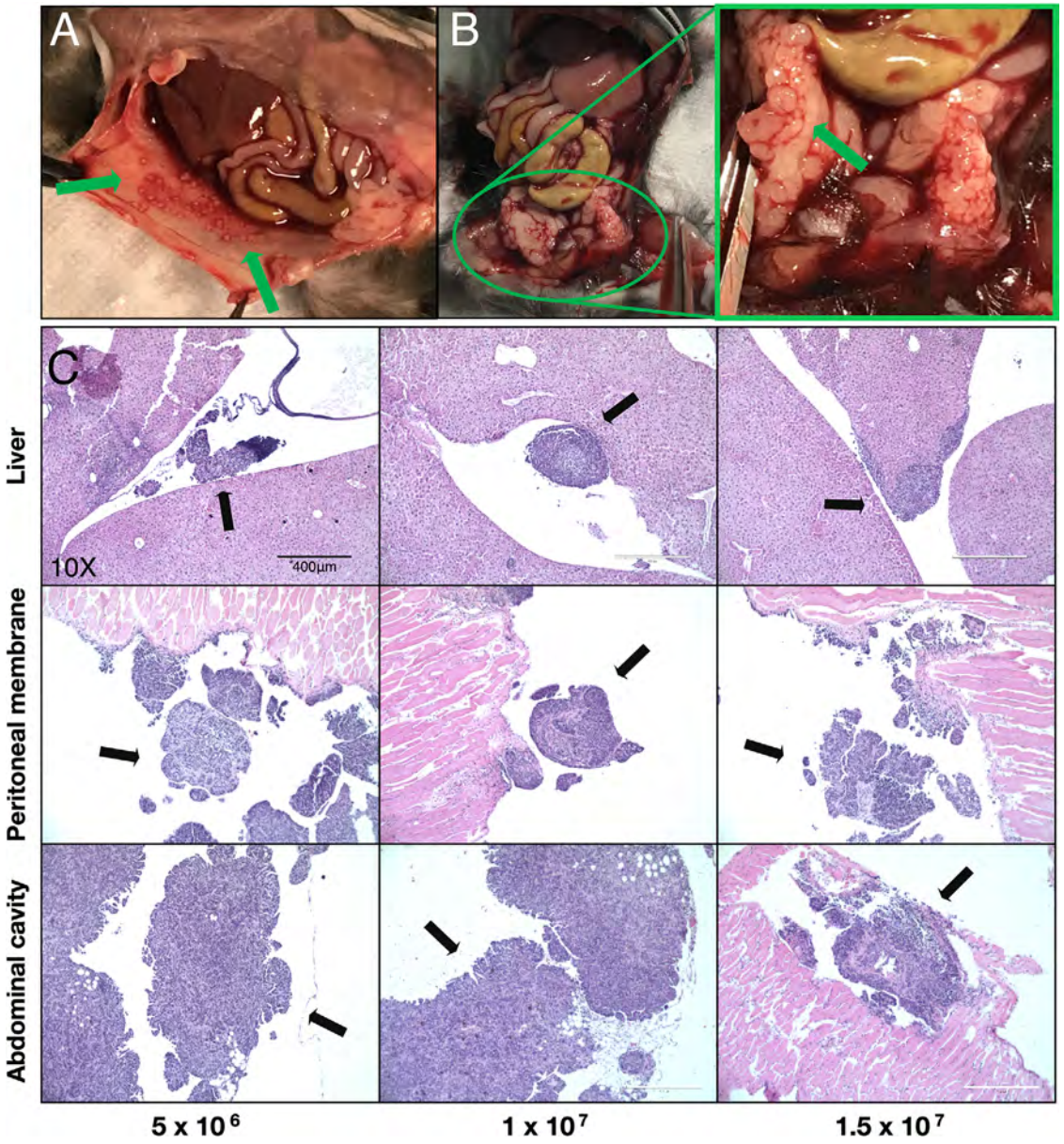

FIGURE 2 Histological assessment and localization of tumor nodules within the peritoneal cavity. (A) Representative images of tumor growth on the peritoneal membrane (green arrows). (B) Representative images of tumor growth within the lower abdominal cavity, indicated by the green arrow in the inset image. (C) H&E staining of tumor nodules found in the liver, peritoneal membrane, and abdominal cavity (black arrows). Magnification: 10×, scale bar: 400 μm

A similar trend of immune cells recruitment to the tumor masses was observed in the cancerous fragments extracted from different areas of the abdominal cavity. Figure 4 shows a strong presence of immune infiltrates despite the varied histological landscapes of the tissues examined.

3.4 | Immune characterization of ascites through mass cytometry (CyTOF)

To obtain a better understanding of the immune landscape of our metastatic OC model, immune cell populations within the ascites of tumor-bearing mice were analyzed by mass cytometry. Seventy days after tumor cell injection, ascitic fluid formation resulted in a swollen abdomen that was apparent and palpable (Figure 5A). Differential expression analysis of specific immune cell surface markers (Table 1) present on CD45+ cells within ascitic fluid was performed through mass cytometry (CyTOF) analysis. Results from this analysis are plotted onto a viSNE graph (Figure 5B) that plots CD45+ cells on a two-dimensional map and identifies individual cells by their expression of the specific immune cell markers chosen (for gating strategy, see Figure S1). From these data,

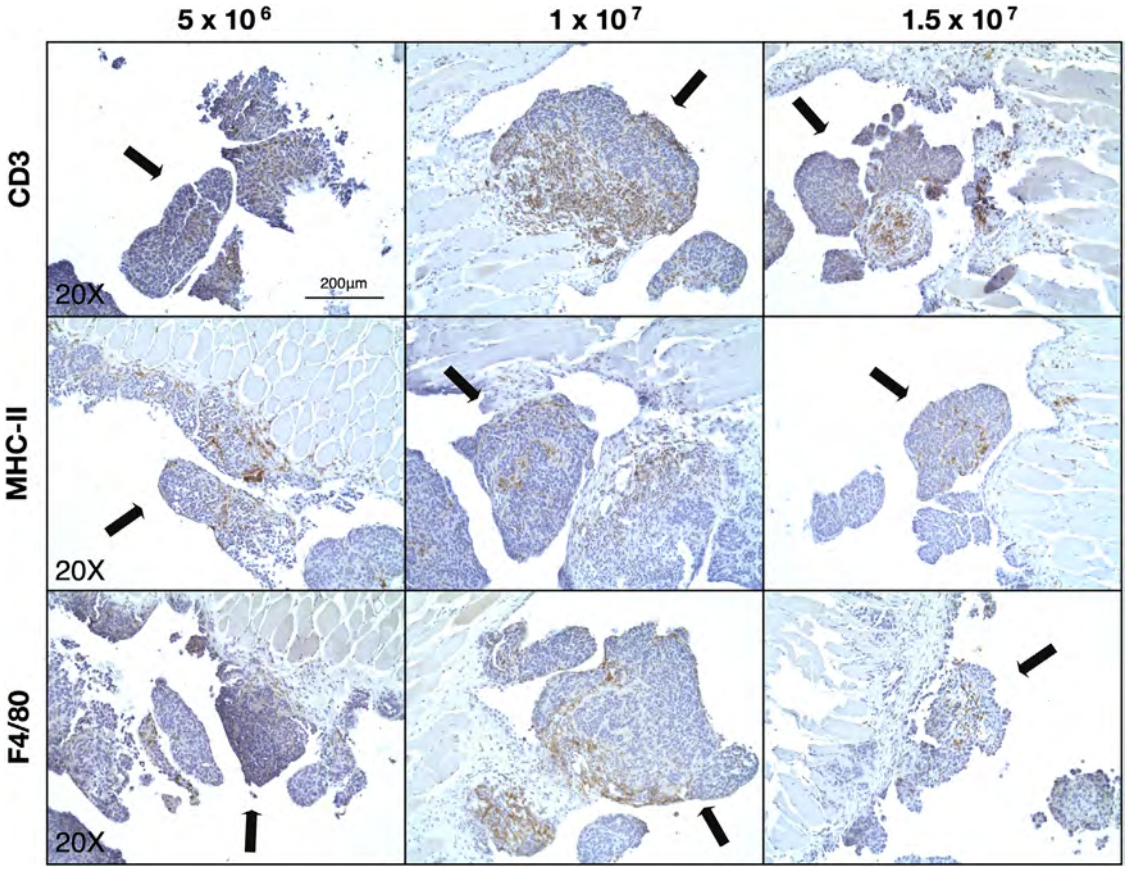

FIGURE 3 Identification of immune cell infiltration within tumors of the peritoneal membrane. Representative IHC images of each of the experimental groups showing the presence of CD3+, MHC-II+, and F4/80+ cells (T cells, APC, and macrophages, respectively) within tumors on the peritoneal membrane. Black arrows indicate the tumor masses. Magnification: 20×, scale bar: 200 μm

immune cell population percentages and numbers can be derived (Figure 5C) enabling a comprehensive analysis of the ascitic fluid immune cell population. Within the present study, the most abundant cell populations in the ascitic fluid of tumor-bearing mice were B cells (27.3.6% ± 9.6%), CD8+ T cells (38.5% ± 4.5%), and CD4+ T cells (20.7% ± 3.5%), with myeloid immune cells, including monocytes, macrophages, DCs, eosinophils, and neutrophils accounting for the remaining 15% of the total cell population.

Further characterization revealed the presence of specific subpopulations among CD8+ and CD4+ T cells (Figure 5D). Specifically, based on their expression of specific markers we identified the presence of (i) memory CD8+ T cells (Ly6C+/CD44+, 23.1% ± 12.1%), (ii) T helper cells (IFNγ+/CD4+, 22.2% ± 15.3%), and (iii) cytotoxic T lymphocytes (CTL, IFNγ+/CD8+, 12.5% ± 9.05%). In addition, low expression of PD1 in 8.03% ± 7.4% of CD4+ T cells and 2.3% ± 1.5% of CD8+ T cells was noted indicating a low level of T-cell exhaustion. The percentages of remaining CD8+ and CD4+ T cells with no identified subpopulations were 61.9% ± 24.3% and 69.7% ± 28.5%, respectively. The CD8+/CD4+ T-cell ratio was 1.65, indicating a prevalence of CD8+ T cells, while the relative percentages of T helper and CTL cells (4.6% ± 3.1% and 4.85% ± 3.4%, respectively) were similar.

Table 2 shows the list of all markers identified in each immune cell population and differentiates them based on the level of expression (see Section 2.6). For instance, the B-cell group is characterized by the high expression of the markers CD38, B220, MHC-II, CD19, and CD80. In addition, CD25, PD-L1, and PD-1 are found to be expressed by both B cells and CD4+ and CD8+ cells at high and low expression levels, respectively. CD4+ and CD8+ cells share high expression levels of TCRβ and IFN-γ (in addition to the cell specific markers CD4 and CD8α, respectively), with Ly6C, Tbet, CD25, and CD103 being specifically expressed by the CD8+ population. Treg cells express high levels of Foxp3, CD25, CD4, and CD44 markers among others, with CD44 being also present in eosinophils, NK cells, monocytes, macrophages, DCs, and neutrophils. Macrophages show high expression of F480 and share with monocytes the moderate to low expression of CD11b, TCRgt, CD64, and CD80. Similarly, the presence of CD11b, Ly6C, and Ly6G is observed in both, eosinophils, and neutrophils.

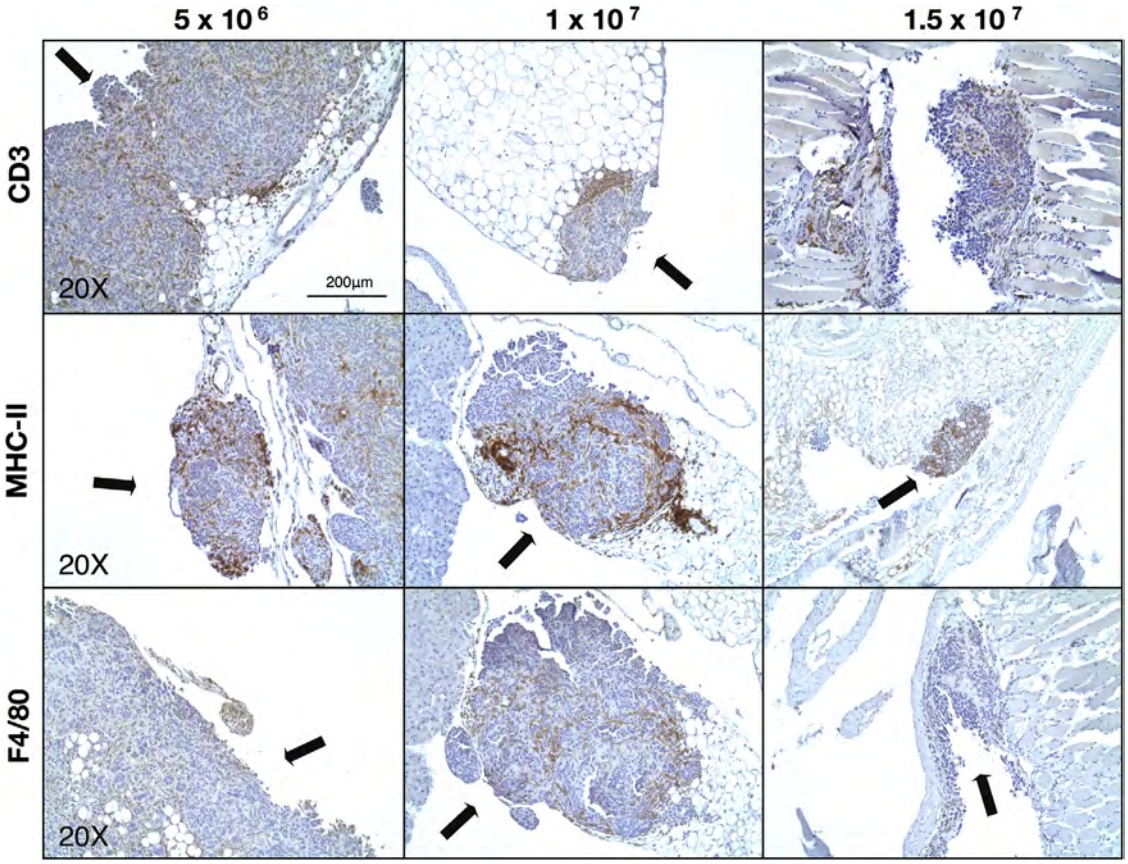

FIGURE 4 Identification of immune cell infiltrates within abdominal cavity tumors. Representative IHC images of CD3+, MHC-II+, F4/80+ cells (T cells, APC, and macrophages, respectively) within tumor nodules (indicated by black arrows) found within the abdominal cavity. Magnification: 20×, scale bar: 200 μm

To complement the information provided in Table 2 and visualize the immune cell marker expression, data from the CyTOF experiments were arranged into subgroups according to marker expression and their association with specific cell types (Figure 6). Several immune markers were associated with more than one cell population; however, the three main cell types identified were: B cells; CD4+ and CD8+ T cells; neutrophils, eosinophils, macrophages, monocytes, and dendritic cells. The expression of CD62L, iNOS, and CD206 was not apparent on any cell population.

4 | DISCUSSION

The treatment of advanced OC is challenging, especially considering the altered physical transport properties that create an immunosuppressive environment[27,28] and limit responsiveness to current immunotherapy strategies. Efforts to optimize animal models that comprehensively mimic cancer development in vivo and thus enable new therapeutic strategies to be tested are ongoing. In this context, the mouse ovarian surface epithelial cell line (ID8 cell line) is widely used to generate preclinical models of advanced OC. This is due to its capacity to closely reproduce the histopathological nuances that are characteristic of patients with advanced OC. These include tumor dissemination across the peritoneal cavity, a specific pattern of invasion and the formation of ascites, which further increases the metastatic process and hinders therapy effectiveness.[29] In addition, ID8 cells have been found to express Pax8,[30] a member of a transcription factor family that has also been linked to a role in OC development.[31] Lastly, the immunological nature of ID8-based OC models further increases their clinical relevance as they also allow for the testing of innovative immunotherapies with the potential to treat this malignancy. As such, ID8 cells have been widely used to test different hypotheses. For example, Wilson et al used the ID8 model to track nuclear factor-kappa B (NF-κB) signaling during cancer progression,[32] while Zhang et al used ID8 cells stably expressing the vascular endothelial growth factor to demonstrate increased tumor-progression rate and ascites formation.[33] However, some doubts about the stability of this cell line have been raised, since the onset of ascites has been reported to alter the efficacy of the bioluminescent signaling associated to

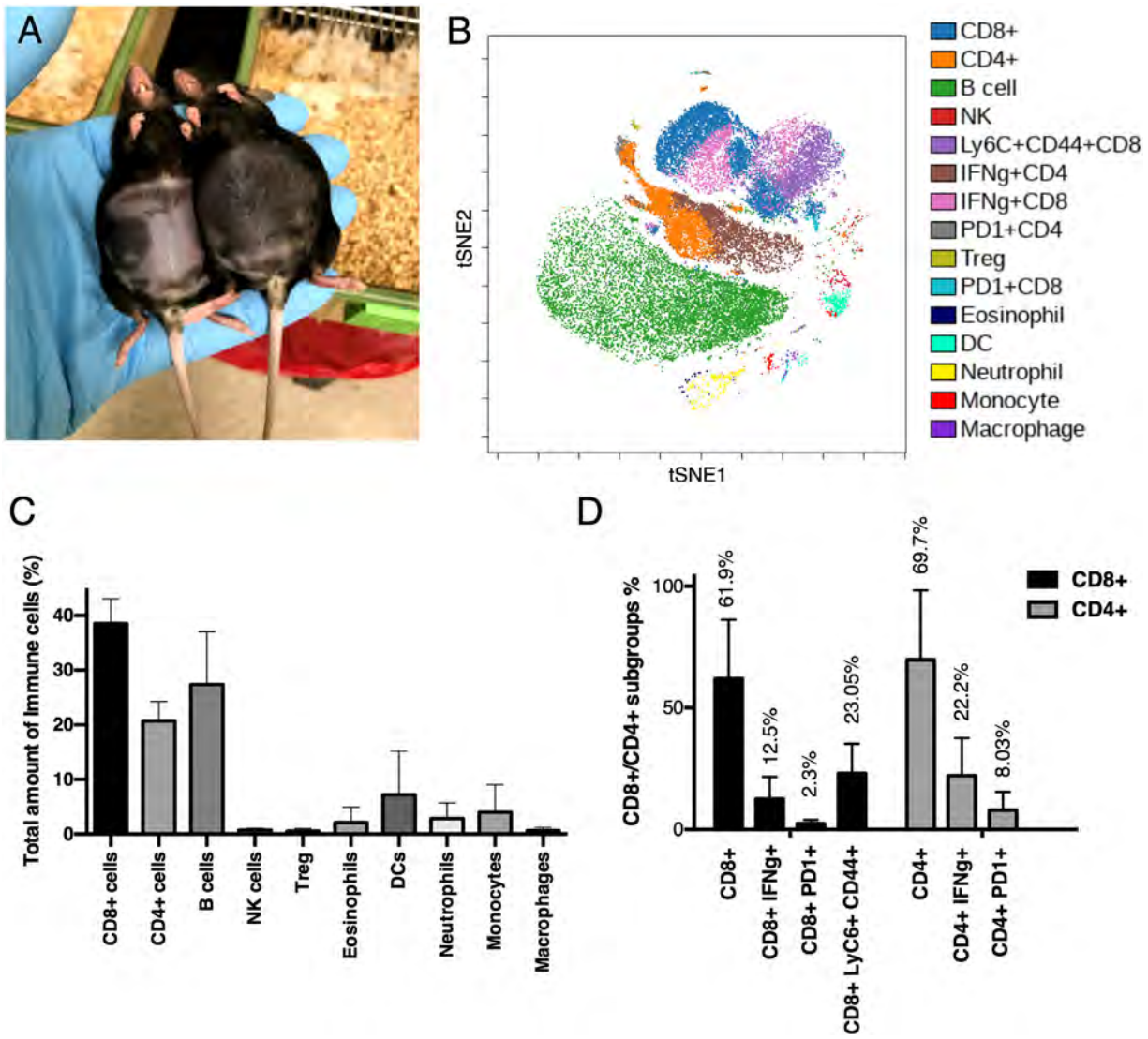

FIGURE 5 Characterization of immune cell populations in ascites. (A) Representative image of ascites formation in tumor-bearing C57BL/6 mice 70 days after tumor cell injection. (B) visNE plot obtained by mass cytometry depicting the most represented immune cell populations in ascites collected from tumor-bearing mice ($n = 3$). (C) Immune cell populations identified from the mass cytometry analysis as a percentage of the total cells. (D) Percentages of CD4+ and CD8+ T-cell subtypes, which are mainly CD4+/CD8+/IFNγ+, CD4+/CD8+/PD1+, or CD8+/LyC6+/CD44+. Data presented are mean (SD)

ID8-Luc/GFP cells.[34] Moreover, despite ID8 cells being considered the gold standard when generating advanced OC in immune competent mice,[35] the scientific community is yet to provide robust protocols, nor a consensus on optimal cell concentrations and incubation times for tumor development. In particular, the literature reports a wide range of ID8 cell concentrations being peritoneally injected (between 1×10^6 and 1×10^7),[32,36–39] and different incubation times required to develop a noticeable tumor and ascites in immunocompetent mice.[34,39]

In this work, we tested three concentrations of ID8-Luc/GFP cells (5×10^6, 1×10^7, or 1.5×10^7 cells) for their capacity to develop an advanced tumor in immune-competent mice after intraperitoneal injection, with the aim of identifying a robust, reproducible protocol for tumor development. The range of concentrations selected was based on the most remarkable results found in literature, that is, significant tumor and acsities development. Our results demonstrated significant tumor growth over a 9-week period for each of the cell concentrations tested, suggesting the suitability of these cell concentrations to reliably create a tumor in vivo. Additionally, the onset of ascites was confirmed between 70 and 80 days after cell injection, which was associated with increased mouse weight providing an indication of advanced stage disease.

H&E staining confirmed the presence of distinct tumor nodules on the liver, scattered across the abdominal cavity and lining the peritoneal membrane. No differences in

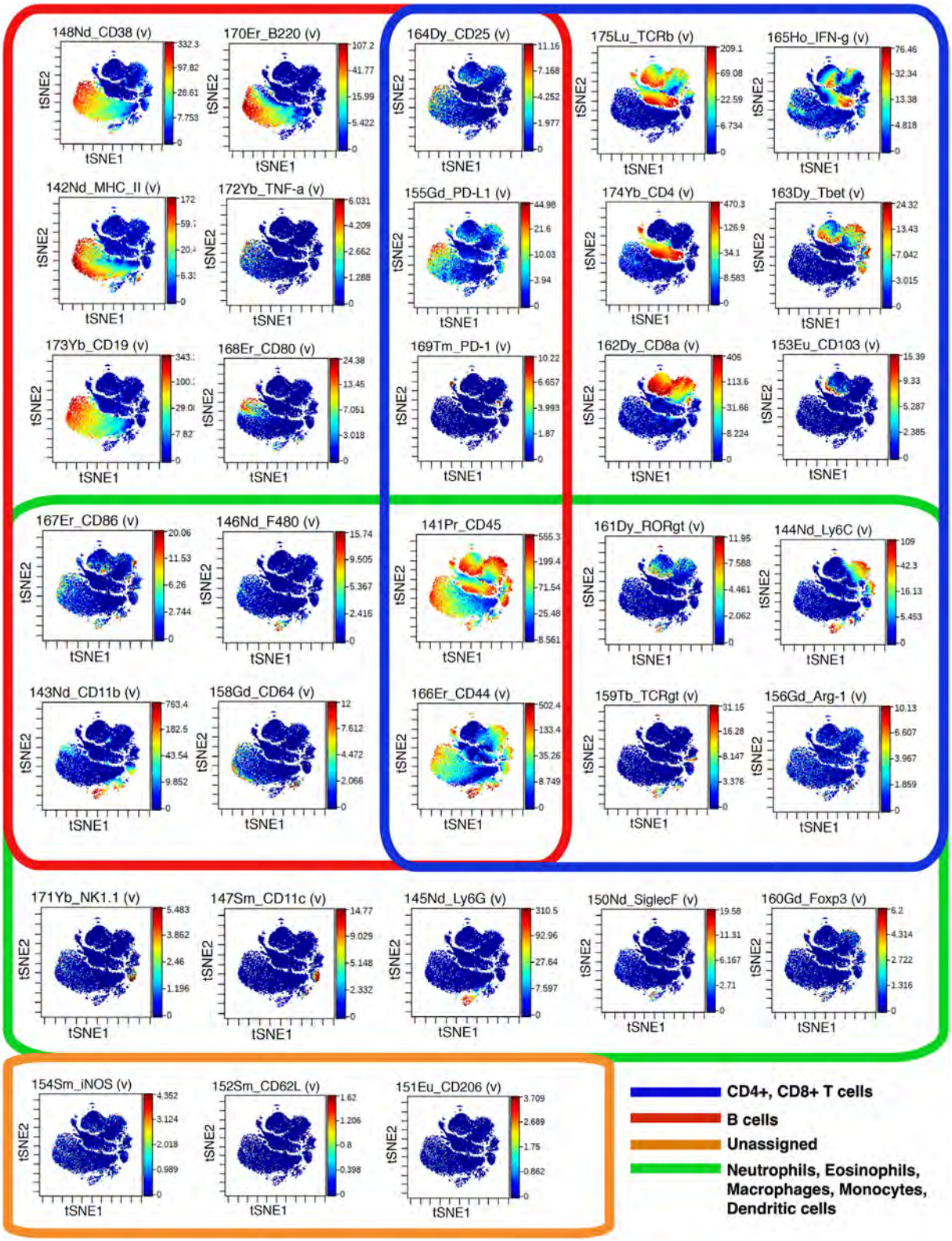

FIGURE 6 viSNE plots for 33 immune markers. From the CyTOF analysis of the 33 immune cell markers, three main immune cell populations were identified based on the coexpression of specific markers. B cells: CD38+/B220+/MHC-II+/TNFα+/CD19+/CD80+. T cells (CD4+ and CD8+): CD25+/PD-L1+/ PD-1+ have been colocalized on both, CD4+ and CD8+ cells, which also express subgroup-specific markers TCRβ, IFN-γ, CD4, CD8α, Tbet, and CD103. The third subgroup is represented by neutrophils, eosinophils, macrophages, monocytes, and dendritic cells, which are specifically positive for NK1.1, CD11c, Ly6G, SiglecF, and FoxP3. The markers CD86, F480, CD11b, and CD64 are shared with the B cells subgroup, whereas RORgtm Ly6C, TCRgt, and Arg-1 are shared with the CD4+/CD8+ cell subgroup

TABLE 2 Expression level of markers identified in each immune population found in the ascitic fluid

	B cells	CD8+ cells	CD4+ cells	T regulatory	NK cells	Monocytes	Neutrophils	Eosinophils	Macrophages	Dendritic cells
CD38	++	–	–	+	–	+	+	–	+	+
B220	++	–	–	–	–	–	–	–	–	–
CD25	+	+	–	++	–	–	–	–	–	–
TCRb	–	++	++	++	–	–	–	–	–	–
IFN-γ	+	++	++	–	–	–	–	–	–	+
MHC-II	++	–	–	+	–	–	–	–	+	+
TNF-α	+	–	–	–	–	–	–	–	–	–
PD-L1	++	+	+	+	–	–	–	–	+	+
CD4	–	–	++	++	–	–	–	–	–	–
Tbet	–	+	–	–	+	–	–	–	–	++
CD19	++	–	–	–	–	–	–	–	–	–
CD80	++	–	–	–	–	+	+	+	+	–
PD-1	+	+	+	+	–	–	–	–	–	–
CD8a	–	++	–	–	–	–	–	–	–	–
CD103	–	+	–	+	–	–	–	–	–	–
CD86	+	–	–	+	–	+	+	+	–	–
F480	–	–	–	–	–	+	+	+	++	–
CD45	–	–	–	–	–	–	–	–	–	–
RORgt	–	+	–	–	–	–	–	+	–	–
Ly6C	–	+	–	–	–	++	++	++	–	–
CD11b	+	–	–	–	–	+	++	++	+	++
CD64	–	–	–	–	–	+	–	–	+	–
CD44	++	++	+	++	++	++	++	++	++	++
TCRgt	–	–	–	–	–	+	+	+	+	–
Arg-1	–	–	–	–	–	–	–	–	–	–
NK 1.1	–	–	–	–	++	–	–	–	–	–
CD11c	–	–	–	–	+	–	–	–	–	++
Ly6G	–	–	–	–	–	–	++	++	–	–
SinglecF	–	–	–	–	–	–	–	++	–	–
Foxp3	–	–	–	++	–	–	–	–	–	–
iNOS	–	–	–	–	–	–	–	–	–	–
CD62L	–	–	–	–	–	–	–	–	–	–
CD206	–	–	–	–	–	–	–	–	–	–

The immune markers were assigned to each category of CD45+ cells according to their expression levels in that specific subpopulation. Marker intensity thresholds used to discern between high and low marker expression are reported in Section 2.6 of methods. ++: high expression, +: intermediate expression, –: lack of expression. iNOS, CD62L, and CD206 were not expressed on any cell population within the ascites.

the number or size of nodules between the experimental groups was evident microscopically. Thus, further characterization to assess the immune environment within the tumor nodules was undertaken. In agreement with the existing literature on immune cells present within the OC TME,[40] immunohistochemical analysis showed T cells and antigen presenting cells (macrophages and DCs) distributed throughout tumor nodules found on the surface of the peritoneal membrane and scattered within the abdomen. The presence of CD3+ tumor infiltrating lymphocytes (TILs) has been identified as an independent prognostic factor in patients with epithelial OC.[41–45] In addition, antigen presenting cells such as tumor associated macrophages (TAMs) and DCs have significant roles in the TME. In particular, TAMs, the most represented cell population,[46] have the potential to suppress or stimulate an anticancer response according to the effect the surrounding microenvironment exerts on them.[47,48]

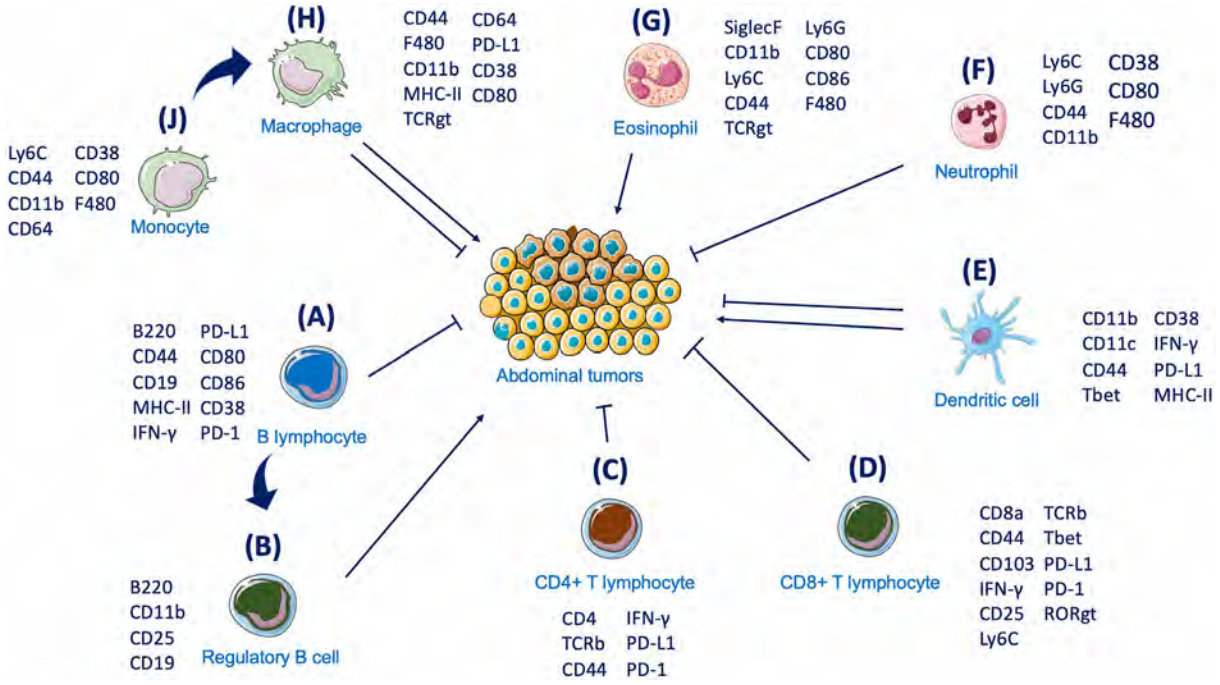

FIGURE 7 Schematic of ascites immune cells and their interactions with the tumor. The interactions between ascites immune cells and their potential effect on tumor cells. B220+/CD11b+/CD38+ B lymphocytes (A) and their CD25+/CD119+ regulatory B-cell subgroup (B) exert antitumor and protumor activity, respectively. The role of CD4+ (C) and CD8+ (D) T cells in exerting cytotoxic activity towards the tumor is linked to the antigen presenting capacity of CD11b+/CD11c+/CD44+ DCs (E). Eosinophils (G) and neutrophils (F) are linked to protumoral and antitumoral properties, respectively. In parallel, monocytes and macrophages (H-J) exert either a tumor promoting or suppressive effect according to the surrounding microenvironment

Focusing on the ascites, which is closely linked to an altered immune environment within the peritoneal cavity of advanced OC patients, further characterization was undertaken. To comprehensively analyze the immune landscape of the ascitic fluid collected from an ID8 ovarian cancer model, for the first time we exploited mass cytometry. The 33 immune cell markers analyzed allowed for the specific identification of distinct immune cell populations and their linkage to pivotal functions with respect to tumor progression. Compared to the review from Wertel et al mentioned above, our results showed similar overall percentages of CD8+ T cells, in contrast with the lower percentages of CD4+ T cells and B cells.[49] The CD8+/CD4+ T-cell ratio of 1.76 we identified was indicative of a higher overall presence of CD8+ T cells compared to CD4+ cells, which is associated with improved patient survival. This finding, together with the expression of IFNγ, suggests effective immune stimulation within the tumor and the development of cell-mediated immunity. In contrast, Giuntoli et al demonstrated that a high CD4+/CD8+ T-cell ratio is associated with poor outcome done in patients with ovarian, primary peritoneal or fallopian tube cancers, and that high concentrations of interleukins 6 (IL-6) and 10 (IL-10) can help establish an immunosuppressive climate that might lead to a decreased activation of ascites-derived T cells.[50]

In Figure 7, we summarize the possible interactions occurring between the immune cell populations identified within the ascites and their effect on the metastatic tumors in situ, based on cell-surface marker expression. The presence of CD45+B220+ B cells can be linked to both pro- and antitumor responses due to their phenotypical and functional variability, as confirmed by several other studies. Indeed, the B220+CD11b+MHC-II+ B-cell population (7A) can have a positive or neutral prognostic effect,[51,52] which can also be mediated by CD38 expression.[53] In contrast to this, the presence of CD25+CD19+ B regulatory cells (7B) is correlated with suppressed T cells responses and poorer patient survival.[54]

Two additional markers, PD-1 and PD-L1, present on both CD4+ (7C) and CD8+ T (7D) cells, have a pivotal role in establishing efficient immunotherapeutic approaches, after it was demonstrated that their inhibition can stop cancer progression.[55] Although clinical trials testing PD-1 and PD-L1 inhibitors have not yet yielded satisfactory results in OC as single treatment,[8,9] their use as combinatorial treatment still holds promise. The prognostic value of PD1+ TILs, when colocalized with PD-L1 on cancer cells

has been demonstrated supporting the PD-1 inhibitory pathway as one mechanism they use to silence the immune system during OC progression.[56] In particular, although tumors appear to be infiltrated by T cells at early stages, a progressive reduction in the frequency of CD8+ T cells and CD8:Treg ratio was noticed at more advanced advanced stages.[57] Our findings have also attributed the majority of PD-L1 expression to macrophages (**7H**) and, together with the presence of cytolytic and regulatory TIL subsets, link directly to survival potential.[58] Macrophages, identified through the coexpression of F4/80 and CD64, were also positive for MHC-II, CD44, and CD80, with the latter marker suggesting an M1 phenotype, which has been linked to increased inflammatory status[47] and is specifically correlated with a longer overall survival (OS) and progression-free survival (PFS) in serous OC patients.[59]

Neutrophils (**7F**), identified by the presence of the markers Ly6C and Ly6G (similar to other myeloid derived populations such as eosinophils (**7G**) and monocytes/macrophages), were also present.[60] Neutrophils have been connected to antitumor-promoting activity in OC. Indeed, neutrophils isolated from the ascites of a KRAS-ID8-induced mouse model showed KRAS-dependent CD8+ T-cell activation through increased recruitment of costimulatory molecules. On the contrary, neutrophil depletion (through administration of an anti-Ly6G monoclonal antibody) led to marked tumor progression.[37] More recently, however, Ly6G-positive neutrophils have been reported to promote a microenviroment that is conducive of metastases spreading and accumulation at specific sites.[61]

Dendritic cells, identified by the expression of CD11b+, CD11c+, CD44+, and MHC-II (**7E**), are paramount players in the activation of effective T-cell responses through their antigen-presenting activity. Indeed, CD44 was found to be pivotal in the formation of tight junctions between mature DCs and T cells and to play a role in T-cell activation as a consequence.[62] However, DCs can undergo tumor-mediated immunosupressive processes, such as the blockage of their activity through the tumor-induced upregulation of the unfolded protein response (UPR), as showed by Cubillos-Ruiz et al.[14] Moreover, Krempski et al also found that tumor infiltrating, PD-1+/PD-L1+ DCs within the ascites respond poorly to danger signal, suppress T-cell activity and decrease T-cell infiltration within the tumor masses.[63]

The immune cells identified within the ascites produced in this model of HGSOC are linked to both pro- and antitumoral activity, indicating that this model represents a balanced immune response to the tumor, or that the immunosuppressive effect of the tumor is yet to take hold. For instance, while expression of the integrin, CD103, and transcription factor, Tbet, associated with CD8+ T cells might indicate a better prognosis,[64–66] the high expression of Ly6C on monocytes is a strong indicator of a TAM phenotype with strong immunosuppressive potential and poor a prognosis.[67,68]

More generally, the presence of immune-active components within the tumor nodules and the ascites raises the question of why the therapeutic potential of immunotherapies is still limited in OC settings. In this case, additional factors should be considered, including the so-called tumor mutation burden (TMB). TMB results from the identification and quantification of driver genes mutations that are responsible for the production of neoantigens. The increasing presence of neoantigens has been associated to the activation of the antitumor immune response. For this reason, TBM plays an important role in the progression of a cancer with a high mutation load being associate to a better prognosis.[69] A recent investigation calculating TMB in 397 patients with OC in the TCGA database revealed that resting immune cells (B cells, B cells, CD4+ T cells, Tregs, monocytes, mast cells, and neutrophils) likely infiltrate tumors with low TMB, whereas activated immune cells (CD4+ T cells, follicle-assisted T cells, proinflammatory macrophages) infiltrate tumors with high TMB.[70] In other cases, some cell-based immunotherapies (such as CAR-T) targeting a single tumor antigen often lose their efficacy as the result of mutations occurring in tumor cells, which impair specific antigen expression thus hindering the effect of the therapy.[71] In addition, cell therapeutics often are subjected to the immunosuppressive environment they meet following administration, which limits their effectiveness in exerting an antitumor immune response.[28,72] The tryptophan catabolism offers another example relevant in this context, as the tryptophan-catabolizing enzyme indoleamine 2,3-dioxygenase (IDO) has been found to be hyperactive in OC and linked to the production of immunosuppressive catabolites and poor patient survival.[73] In addition, the cancer-induced acidic environment has been shown to have a role in tumor recurrence, metastasis, and prognosis of cancer patients (due to the high production of lactate).[74] Furthermore, lactate can also support cancer cell immune evasion by inhibiting T-cell activation[75] and dendritic cell antigen presenting capacities.[76]

This work is the first to provide a multiparametric and comprehensive characterization of the immune cell landscape of the ascites collected from a preclinical model of advanced OC. Published literature reports fragmented information, as only single populations (such as CD4+ and CD8+ T cells) have been so far identified and described.[50] A more complete description has been offered by Wertel et al who listed the percentages of the main cellular components found in the peritoneal fluid of advanced OC patients by merging the information collected from several

different studies.[49] More recently, the panorama of the ascites collected from HGSOC patients has been resolved by applying single cell-RNA sequencing (scRNA-seq).[77] In this study, the authors provided a broad view of the different cell types in the ascites ecosystem, with particular focus on malignant versus nonmalignant cells (analyzing samples partially depleted of CD45+ immune cells).

The potential strength of the data we identified is therefore to demonstrate that mass cytometry provides a platform for the comprehensive analysis of the immune cell landscape within ascites, which would allow periodical analysis of cellular and molecular changes in patients with OC. In this regard, CyTOF holds the promise of complementing personalized therapeutic approaches, and potentially enabling real time tracking of the efficacy of immunotherapeutics. Compared to scRNA-seq, CYTOF offers the advantage of a higher throughput for the evaluation of the TME in clinical samples, as it allows for a more accurate targeting of immune cell subsets through the use of >30 selected antigen markers. Moreover, CyTOF "narrow and distinct"[78,79] data are generated from the analysis of over 250 000 cells, whereas transcriptome-based platforms detect wider unbiased populations from several thousands of cells.[80,81]

5 | CONCLUSIONS

In this work, we provide, for the first time, a comprehensive characterization of the immune landscape of the ascites collected from tumor-bearing mice, unveiling its potential for clinical implementation. The continuous analysis of interactions between immune cells in a cancerous environment would significantly increase the number of therapeutic options for the treatment of this malignancy and offer a significant alternative for the evaluation of ongoing therapies. Data presented in this study prove mass cytometry as a promising tool to facilitate this process, with the potential to identify personalized therapeutic targets and establish improved immunotherapy strategies. In addition, the application of CyTOF on more complex and genetically modified mice models, as well as on patients' derived samples, will also unveil new insights into disease heterogeneity, pathology, and drug resistance, and will expand our understanding of HGSOC.

ACKNOWLEDGMENT

We thank the Houston Methodist Research Institute (HMRI) Immunomonitoring Core. BC acknowledges support through the Sêr Cymru II scheme, funded by the European Union's Horizon 2020 Research and Innovation Program under the Marie Skłodowska-Curie grant agreement No. 663830, the Welsh European Funding Office (WEFO) under the European Regional Development Fund (ERDF) and Houston Methodist Research Institute. SP is sponsored by the Swansea University Medical School (UK)/Houston Methodist Research Institute (US) joint PhD Initiative. Additional support for the study was provided by the Golfers Against Cancer Foundation.

COMPETING INTEREST

The authors declare that they have no competing interests.

ETHICS APPROVAL AND CONSENT TO PARTICIPATE

All animal studies were carried out in accordance with guidelines determined by the Animal Welfare Act and the Guide for the Care and Use of Laboratory Animals and complied with protocols approved by the Institutional Animal Care and Use Committee at the Houston Methodist Research Institute (AUP-0219-0013).

AUTHORS' CONTRIBUTIONS

Conceptualization and methodology: SP, BC; Formal analysis and data curation: SP, SL, FI, LM, OSV, GDH, RSC and BC; Validation and investigation: SP, SL, LM and BC; Original draft preparation and Writing: SP, LM, GDH and BC; Review and editing: SP, GDH, DG, RSC and BC; Approval of final manuscript: all authors read and approved the final manuscript.

AVAILABILITY OF DATA AND MATERIAL

All data relevant to the study are included in the article or uploaded as supplementary information.

ORCID

Simone Pisano https://orcid.org/0000-0002-5412-1241
Yajaira S. Jimenez https://orcid.org/0000-0003-4647-4546

REFERENCES

1. Siegel RL, Miller KD, Jemal A. Cancer statistics, 2020. *CA Cancer J Clin*. https://doi.org/10.3322/caac.21590. Published Online First: 2020.
2. Wu J, Sun H, Yang L, et al. Improved survival in ovarian cancer, with widening survival gaps of races and socioeconomic status: a period analysis. *J Cancer*. 2018;9:3548-3556. https://doi.org/10.7150/jca.26300.
3. Torre LA, Trabert B, DeSantis CE, et al. Ovarian cancer statistics, 2018. *CA Cancer J Clin*. https://doi.org/10.3322/caac.21456. Published Online First: 2018.
4. Lisio MA, Fu L, Goyeneche A, et al. High-grade serous ovarian cancer: basic sciences, clinical and therapeutic standpoints. *Int J Mol Sci*. 2019;20(4):952. https://doi.org/10.3390/ijms20040952.
5. Armstrong DK, Alvarez RD, Bakkum-Gamez JN, et al. NCCN Guidelines Insights: Ovarian Cancer, Version 1.2019. *J Natl*

Compr Cancer Netw. 2019;17(8):896-909. https://doi.org/10.6004/jnccn.2019.0039.

6. Garcia A, Singh H. Bevacizumab and ovarian cancer. *Ther Adv Med Oncol*. 2013;5(2):133-141. https://doi.org/10.1177/1758834012467661.
7. Vasey PA. Resistance to chemotherapy in advanced ovarian cancer: mechanisms and current strategies. *Br J Cancer*. 2003;89:S23–S28. https://doi.org/10.1038/sj.bjc.6601497. Published Online First: 2003.
8. Matulonis UA, Shapira-Frommer R, Santin AD, et al. Antitumor activity and safety of pembrolizumab in patients with advanced recurrent ovarian cancer: results from the phase II KEYNOTE-100 study. *Ann Oncol*. https://doi.org/10.1093/annonc/mdz135. Published Online First: 2019.
9. Bartl T, Paspalj V, Polterauer S, et al. Current state and perspectives of checkpoint inhibitors in ovarian cancer treatment. *Memo - Mag Eur Med Oncol*. 2020;13:202-206. https://doi.org/10.1007/s12254-020-00579-z.
10. Galon J, Bruni D. Approaches to treat immune hot, altered and cold tumours with combination immunotherapies. *Nat Rev Drug Discov*. 2019;18:197-218. https://doi.org/10.1038/s41573-018-0007-y.
11. Ghisoni E, Imbimbo M, Zimmermann S, et al. Ovarian cancer immunotherapy: turning up the heat. *Int J Mol Sci*. 2019;20(12):2927. https://doi.org/10.3390/ijms20122927.
12. Lanitis E, Dangaj D, Irving M, et al. Mechanisms regulating T-cell infiltration and activity in solid tumors. *Ann Oncol*. 2017;28(suppl_12):xii18-xii32. https://doi.org/10.1093/annonc/mdx238.
13. Scarlett UK, Rutkowski MR, Rauwerdink AM, et al. Ovarian cancer progression is controlled by phenotypic changes in dendritic cells. *J Exp Med*. https://doi.org/10.1084/jem.20111413. Published Online First: 2012.
14. Cubillos-Ruiz JR, Silberman PC, Rutkowski MR, et al. ER stress sensor XBP1 controls anti-tumor immunity by disrupting dendritic cell homeostasis. *Cell*. 2015;161(7):1527–1538. https://doi.org/10.1016/j.cell.2015.05.025. Published Online First: 2015.
15. Roane BM, Arend RC, Birrer MJ. Review: targeting the transforming growth factor-beta pathway in ovarian cancer. *Cancers (Basel)*. 2019;11(5):668. https://doi.org/10.3390/cancers11050668.
16. Kao JY, Gong Y, Chen C-M, et al. Tumor-derived TGF-β reduces the efficacy of dendritic cell/tumor fusion vaccine. *J Immunol*. https://doi.org/10.4049/jimmunol.170.7.3806. Published Online First: 2003.
17. Ahmed N, Stenvers KL. Getting to know ovarian cancer ascites: opportunities for targeted therapy-based translational research. *Front Oncol*. 2013;3:256. https://doi.org/10.3389/fonc.2013.00256.
18. Kipps E, Tan DSP, Kaye SB. Meeting the challenge of ascites in ovarian cancer: new avenues for therapy and research. *Nat Rev Cancer*. 2013;13(4):273-282. https://doi.org/10.1038/nrc3432.
19. Cohen M, Petignat P. The bright side of ascites in ovarian cancer. *Cell Cycle*. 2014;13(15):2319. https://doi.org/10.4161/cc.29951.
20. Tan DSP, Agarwal R, Kaye SB. Mechanisms of transcoelomic metastasis in ovarian cancer. *Lancet Oncol*. 2006;7(11):925-934. https://doi.org/10.1016/S1470-2045(06)70939-1.
21. Mocellin S, Wang E, Marincola FM. Cytokines and immune response in the tumor microenvironment. *J Immunother*. 2001;24:392-407. https://doi.org/10.1097/00002371-200109000-00002.
22. Moser M. Dendritic cells in immunity and tolerance—do they display opposite functions? *Immunity*. 2003;19:5-8. https://doi.org/10.1016/S1074-7613(03)00182-1.
23. Nelson BH. The impact of T-cell immunity on ovarian cancer outcomes. *Immunol Rev*. 2008;222:101-116. https://doi.org/10.1111/j.1600-065X.2008.00614.x.
24. Toker A, Nguyen LT, Stone SC, et al. Regulatory T cells in ovarian cancer are characterized by a highly activated phenotype distinct from that in melanoma. *Clin Cancer Res*. 2018;24(22):5685–5696. https://doi.org/10.1158/1078-0432.CCR-18-0554. Published Online First: 2018.
25. Toyoshimaa M, Tanaka Y, Matumoto M, et al. Generation of a syngeneic mouse model to study the intraperitoneal dissemination of ovarian cancer with in vivo luciferase imaging. *Luminescence*. https://doi.org/10.1002/bio.1112. Published Online First: 2009.
26. Fienberg HG, Simonds EF, Fantl WJ, et al. A platinum-based covalent viability reagent for single-cell mass cytometry. *Cytom Part A*. 2012;81 A:467-475. https://doi.org/10.1002/cyto.a.22067.
27. Pokhriyal R, Hariprasad R, Kumar L, et al. Chemotherapy resistance in advanced ovarian cancer patients. *Biomark Cancer*. 2019;11:1179299X19860815. https://doi.org/10.1177/1179299X19860815.
28. Nizzero S, Shen H, Ferrari M, et al. Immunotherapeutic transport oncophysics: space, time, and immune activation in cancer. *Trends Cancer*. 2020;6(1):40-48. https://doi.org/10.1016/j.trecan.2019.11.008.
29. Roby KF, Taylor CC, Sweetwood JP, et al. Development of a syngeneic mouse model for events related to ovarian cancer. *Carcinogenesis*. 2000;21(4):585-591. https://doi.org/10.1093/carcin/21.4.585.
30. Maniati E, Berlato C, Gopinathan G, et al. Mouse Ovarian Cancer Models Recapitulate the Human Tumor Microenvironment and Patient Response to Treatment. *Cell Rep*. 2020;30:525-540.e7. https://doi.org/10.1016/j.celrep.2019.12.034.
31. Soriano AA, De Cristofaro T, Palma Di, et al. PAX8 expression in high-grade serous ovarian cancer positively regulates attachment to ECM via Integrin β3. *Cancer Cell Int*. 2019;19(303):1-12. https://doi.org/10.1186/s12935-019-1022-8.
32. Wilson AJ, Barham W, Saskowski J, et al. Tracking NF-κB activity in tumor cells during ovarian cancer progression in a syngeneic mouse model. *J Ovarian Res*. 2013;6(1):63. https://doi.org/10.1186/1757-2215-6-63.
33. Zhang L, Yang N, Conejo Garcia JR, et al. Generation of a syngeneic mouse model to study the effects of vascular endothelial growth factor in ovarian carcinoma. *Am J Pathol*. 2002;161:2295-2309. https://doi.org/10.1016/S0002-9440(10)64505-1.
34. Baert T, Verschuere T, Van Hoylandt A, et al. The dark side of ID8-Luc2: pitfalls for luciferase tagged murine models for ovarian cancer. *J Immunother Cancer*. 2015;3:57. https://doi.org/10.1186/s40425-015-0102-0.
35. Gil M, Komorowski MP, Seshadri M, et al. CXCL12/CXCR4 blockade by oncolytic virotherapy inhibits ovarian cancer growth by decreasing immunosuppression and targeting cancer-initiating cells. *J Immunol*. 2014;193:5327-5337. https://doi.org/10.4049/jimmunol.1400201.

36. Cho S, Sun Y, Soisson AP, et al. Characterization and evaluation of pre-clinical suitability of a syngeneic orthotopic mouse ovarian cancer model. *Anticancer Res*. 2013;33(4):1317-1324.
37. Yoshida M, Taguchi A, Kawana K, et al. Intraperitoneal neutrophils activated by KRAS-induced ovarian cancer exert antitumor effects by modulating adaptive immunity. *Int J Oncol*. 2018;53:1580-1590. https://doi.org/10.3892/ijo.2018.4504.
38. Zhu X, Xu J, Cai H, et al. Carboplatin and programmed death-ligand 1 blockade synergistically produce a similar antitumor effect to carboplatin alone in murine ID8 ovarian cancer model. *J Obstet Gynaecol Res*. 2018;44:303-311. https://doi.org/10.1111/jog.13521.
39. Liao JB, Ovenell KJ, Curtis EEM, et al. Preservation of tumor-host immune interactions with luciferase-tagged imaging in a murine model of ovarian cancer. *J Immunother Cancer*. 2015;25(3):16. https://doi.org/10.1186/s40425-015-0060-6.
40. Cai DL, Jin LP. Immune cell population in ovarian tumor microenvironment. *J Cancer*. 2017;8(15):2915-2923. https://doi.org/10.7150/jca.20314.
41. Tomšová M, Melichar B, Sedláková I, et al. Prognostic significance of CD3+ tumor-infiltrating lymphocytes in ovarian carcinoma. *Gynecol Oncol*. 2008;108:415-420. https://doi.org/10.1016/j.ygyno.2007.10.016.
42. Stumpf M, Hasenburg A, Riener MO, et al. Intraepithelial CD8-positive T lymphocytes predict survival for patients with serous stage III ovarian carcinomas: relevance of clonal selection of T lymphocytes. *Br J Cancer*. 2009;101:1513-1521. https://doi.org/10.1038/sj.bjc.6605274.
43. Raspollini MR, Castiglione F, Degl'Innocenti DR, et al. Tumour-infiltrating gamma/delta T-lymphocytes are correlated with a brief disease-free interval in advanced ovarian serous carcinoma. *Ann Oncol*. 2005;16:590-596. https://doi.org/10.1093/annonc/mdi112.
44. Leffers N, Gooden MJM, De Jong RA, et al. Prognostic significance of tumor-infiltrating T-lymphocytes in primary and metastatic lesions of advanced stage ovarian cancer. *Cancer Immunol Immunother*. 2009;58(3):449-459. https://doi.org/10.1007/s00262-008-0583-5.
45. Zhang L, Conejo-Garcia JR, Katsaros D, et al. Intratumoral T cells, recurrence, and survival in epithelial ovarian cancer. *N Engl J Med*. 2003;348:203-213. https://doi.org/10.1056/NEJMoa020177.
46. Drakes ML, Stiff PJ. Regulation of ovarian cancer prognosis by immune cells in the tumor microenvironment. *Cancers (Basel)*. 2018;10(9):302. https://doi.org/10.3390/cancers10090302.
47. Allavena P, Sica A, Garlanda C, et al. The Yin-Yang of tumor-associated macrophages in neoplastic progression and immune surveillance. *Immunol Rev*. 2008;222:155-161. https://doi.org/10.1111/j.1600-065X.2008.00607.x.
48. Zhang M, He Y, Sun X, et al. A high M1/M2 ratio of tumor-associated macrophages is associated with extended survival in ovarian cancer patients. *J Ovarian Res*. 2014;7:19. https://doi.org/10.1186/1757-2215-7-19.
49. Wertel I, Nowicka A, Rogala E, et al. Peritoneal immune system in patients with advance epithelial ovarian cancer. *Int Rev Immunol*. 2011;30:87-101. https://doi.org/10.3109/08830185.2011.569902.
50. Giuntoli RL, Webb TJ, Zoso A, et al. Ovarian cancer-associated ascites demonstrates altered immune environment: implications for antitumor immunity. *Anticancer Res*. 2009;29:2875-2884. http://www.ncbi.nlm.nih.gov/pubmed/19661290.
51. Wouters MCA, Nelson BH. Prognostic significance of tumor-infiltrating B cells and plasma cells in human cancer. *Clin Cancer Res*. 2018;24:6125-6135. https://doi.org/10.1158/1078-0432.CCR-18-1481.
52. Gupta P, Chen C, Chaluvally-Raghavan P, et al. B cells as an immune-regulatory signature in ovarian cancer. *Cancers (Basel)*. 2019;11(7):894. https://doi.org/10.3390/cancers11070894.
53. Zhu Y, Zhang Z, Jiang Z, et al. CD38 predicts favorable prognosis by enhancing immune infiltration and antitumor immunity in the epithelial ovarian cancer microenvironment. *Front Genet*. 2020;11. https://doi.org/10.3389/fgene.2020.00369.
54. Wei X, Jin Y, Tian Y, et al. Regulatory B cells contribute to the impaired antitumor immunity in ovarian cancer patients. *Tumor Biol*. 2016;37(5):6581-6588. https://doi.org/10.1007/s13277-015-4538-0.
55. Gong J, Chehrazi-Raffle A, Reddi S, et al. Development of PD-1 and PD-L1 inhibitors as a form of cancer immunotherapy: a comprehensive review of registration trials and future considerations. *J Immunother Cancer*. 2018;6(1):8. https://doi.org/10.1186/s40425-018-0316-z.
56. Wang Q, Lou W, Di W, et al. Prognostic value of tumor PD-L1 expression combined with CD8+ tumor infiltrating lymphocytes in high grade serous ovarian cancer. *Int Immunopharmacol*. 2017;52:7-14. https://doi.org/10.1016/j.intimp.2017.08.017.
57. Duraiswamy J, Freeman GJ, Coukos G. Therapeutic PD-1 pathway blockade augments with other modalities of immunotherapy T-cell function to prevent immune decline in ovarian cancer. *Cancer Res*. 2013;73(23):6900–6912. https://doi.org/10.1158/0008-5472.CAN-13-1550. Published Online First: 2013.
58. Webb JR, Milne K, Kroeger DR, et al. PD-L1 expression is associated with tumor-infiltrating T cells and favorable prognosis in high-grade serous ovarian cancer. *Gynecol Oncol*. 2016;141:293-302. https://doi.org/10.1016/j.ygyno.2016.03.008.
59. Macciò A, Gramignano G, Cherchi MC, et al. Role of M1-polarized tumorassociated macrophages in the prognosis of advanced ovarian cancer patients. *Sci Rep*. 2020;10. https://doi.org/10.1038/s41598-020-63276-1.
60. Rose S, Misharin A, Perlman H. A novel Ly6C/Ly6G-based strategy to analyze the mouse splenic myeloid compartment. *Cytom Part A*. 2012;81 A:343-350. https://doi.org/10.1002/cyto.a.22012.
61. Lee WJ, Ko SY, Mohamed MS, et al. Neutrophils facilitate ovarian cancer premetastatic niche formation in the omentum. *J Exp Med*. 2019;216:176-194. https://doi.org/10.1084/jem.20181170.
62. Hegde VL, Singh NP, Nagarkatti PS, et al. CD44 mobilization in allogeneic dendritic cell-T cell immunological synapse plays a key role in T cell activation. *J Leukoc Biol*. https://doi.org/10.1189/jlb.1107752. Published Online First: 2008.
63. Krempski J, Karyampudi L, Behrens MD, et al. Tumor-infiltrating programmed death receptor-1 + dendritic cells mediate immune suppression in ovarian cancer. *J Immunol*. 2011;186:6905-6913. https://doi.org/10.4049/jimmunol.1100274.
64. Webb JR, Milne K, Watson P, et al. Tumor-infiltrating lymphocytes expressing the tissue resident memory marker cd103 are associated with increased survival in high-grade serous ovarian cancer. *Clin Cancer Res*. 2014;20(2):434-444. https://doi.org/10.1158/1078-0432.CCR-13-1877.

65. Xu Y, Chen L, Xu B, et al. Higher numbers of T-bet + tumor-infiltrating lymphocytes associate with better survival in human epithelial ovarian cancer. *Cell Physiol Biochem*. 2017;41:475-483. https://doi.org/10.1159/000456600.
66. Gacerez AT, Sentman CL. T-bet promotes potent antitumor activity of CD4+ CAR T cells. *Cancer Gene Ther*. 2018;25(5-6):117-128. https://doi.org/10.1038/s41417-018-0012-7.
67. Movahedi K, Laoui D, Gysemans C, et al. Different tumor microenvironments contain functionally distinct subsets of macrophages derived from Ly6C(high) monocytes. *Cancer Res*. 2010;70(14):5728-5739. https://doi.org/10.1158/0008-5472.CAN-09-4672.
68. Reinartz S, Schumann T, Finkernagel F, et al. Mixed-polarization phenotype of ascites-associated macrophages in human ovarian carcinoma: correlation of CD163 expression, cytokine levels and early relapse. *Int J Cancer*. 2014;134:32-42. https://doi.org/10.1002/ijc.28335.
69. Snyder A, Makarov V, Merghoub T, et al. Genetic basis for clinical response to CTLA-4 blockade in melanoma. *N Engl J Med*. 2014;371:2189-2199. https://doi.org/10.1056/nejmoa1406498.
70. Bi F, Chen Y, Yang Q. Significance of tumor mutation burden combined with immune infiltrates in the progression and prognosis of ovarian cancer. *Cancer Cell Int*. 2020;20:373. https://doi.org/10.1186/s12935-020-01472-9.
71. Mehta A, Kim YJ, Robert L, et al. Immunotherapy resistance by inflammation-induced dedifferentiation. *Cancer Discov*. 2018;8(8):935-943. https://doi.org/10.1158/2159-8290.CD-17-1178.
72. Corradetti B, Pisano S, Conlan RS, et al. Nanotechnology and immunotherapy in ovarian cancer: tracing new landscapes. *J Pharmacol Exp Ther*. 2019;370(3):636-646. https://doi.org/10.1124/jpet.118.254979.
73. Smith LP, Bitler BG, Richer JK, et al. Tryptophan catabolism in epithelial ovarian carcinoma. *Trends Cancer Res*. 2019;14:1-9. http://www.ncbi.nlm.nih.gov/pubmed/31736606.
74. Kato Y, Ozawa S, Miyamoto C, et al. Acidic extracellular microenvironment and cancer. *Cancer Cell Int*. 2013;13(89):1-8. https://doi.org/10.1186/1475-2867-13-89.
75. Fischer K, Hoffmann P, Voelkl S, et al. Inhibitory effect of tumor cell-derived lactic acid on human T cells. *Blood*. 2007;109(9):3812-3819. https://doi.org/10.1182/blood-2006-07-035972.
76. Gottfried E, Kunz-Schughart LA, Ebner S, et al. Tumor-derived lactic acid modulates dendritic cell activation and antigen expression. *Blood*. 2006;107:2013-2021. https://doi.org/10.1182/blood-2005-05-1795.
77. Izar B, Tirosh I, Stover EH, et al. A single-cell landscape of high-grade serous ovarian cancer. *Nat Med*. 2020;26:1271-1279. https://doi.org/10.1038/s41591-020-0926-0.
78. Kashima Y, Togashi Y, Fukuoka S, et al. Potentiality of multiple modalities for single-cell analyses to evaluate the tumor microenvironment in clinical specimens. *Sci Rep*. 2021;11:341. https://doi.org/10.1038/s41598-020-79385-w.
79. Schelker M, Feau S, Du J, et al. Estimation of immune cell content in tumour tissue using single-cell RNA-seq data. *Nat Commun*. 2017;8:2032. https://doi.org/10.1038/s41467-017-02289-3.
80. Bacher R, Kendziorski C. Design and computational analysis of single-cell RNA-sequencing experiments. *Genome Biol*. 2016;17(63). https://doi.org/10.1186/s13059-016-0927-y.
81. Ren X, Kang B, Zhang Z. Understanding tumor ecosystems by single-cell sequencing: promises and limitations 11 medical and health sciences 1112 oncology and carcinogenesis 06 biological sciences 0604 genetics. *Genome Biol*. 2018;19(211). https://doi.org/10.1186/s13059-018-1593-z.

SUPPORTING INFORMATION

Additional supporting information may be found online in the Supporting Information section at the end of the article.

DOI: 10.1002/eji.202149329 Eur. J. Immunol. 2022. 52: 96–108

Clinical

European Journal of Immunology

Systems immunology

Research Article

Systematic analysis of CD39, CD103, CD137, and PD-1 as biomarkers for naturally occurring tumor antigen-specific TILs

Monika A. Eiva[1,2,3], *Dalia K. Omran*[1], *Jessica A. Chacon*[4] *and Daniel J. Powell Jr.*[1,2,3]

[1] Ovarian Cancer Research Center, Department of Obstetrics and Gynecology, Perelman School of Medicine, University of Pennsylvania, Philadelphia, Pennsylvania, USA
[2] Center for Cellular Immunotherapies, Abramson Cancer Center, University of Pennsylvania, Philadelphia, Pennsylvania, USA
[3] Department of Pathology and Laboratory Medicine, Abramson Cancer Center, Perelman School of Medicine, University of Pennsylvania, Philadelphia, Pennsylvania, USA
[4] Paul L Foster School of Medicine and Woody L. Hunt School of Dental Medicine, Texas Tech University Health Sciences Center, El Paso, Texas, USA

The detection of tumor-specific T cells in solid tumors is integral to interrogate endogenous antitumor responses and to advance downstream therapeutic applications. Multiple biomarkers are reported to identify endogenous tumor-specific tumor-infiltrating lymphocytes (TILs), namely CD137, PD-1, CD103, and CD39; however, a direct comparison of these molecules has yet to be performed. We evaluated these biomarkers in primary human ovarian tumor samples using single-cell mass cytometry to compare their relative phenotypic profiles, and examined their response to autologous tumor cells ex vivo. PD-1$^+$, CD103$^+$, and CD39$^+$ TILs all contain a CD137$^+$ cell subset, while CD137$^+$ TILs highly co-express the aforementioned markers. CD137$^+$ TILs exhibit the highest expression of cytotoxic effector molecules compared to PD-1$^+$, CD103$^+$, or CD39$^+$ TILs. Removal of CD137$^+$ cells from PD-1$^+$, CD103$^+$, or CD39$^+$ TILs diminish their IFN-γ secretion in response to autologous tumor cell stimulation, while CD137$^+$ TILs maintain high HLA-dependent IFN-γ secretion. CD137$^+$ TILs exhibited an exhausted phenotype but with CD28 co-expression, suggesting possible receptiveness to reinvigoration via immune checkpoint blockade. Together, our findings demonstrate that the antitumor abilities of PD-1$^+$, CD103$^+$, and CD39$^+$ TILs are mainly derived from a subset of CD137-expressing TILs, implicating CD137 as a more selective biomarker for naturally occurring tumor-specific TILs.

Keywords: CD39 · CD103 · CD137 · PD-1 · tumor-infiltrating lymphocytes

Additional supporting information may be found online in the Supporting Information section at the end of the article.

Correspondence: Daniel J. Powell Jr.
e-mail: poda@pennmedicine.upenn.edu

Introduction

The intratumoral abundance of tumor-infiltrating lymphocytes (TILs) is a positive prognostic factor for increased survival in most solid cancers, indicating that TILs are integral to endogenous antitumor immunity and play a role in controlling cancer progression [1, 2]. However, only a small percentage of TILs respond against tumor antigens and their antitumor response can be hindered by multiple mechanisms of immunosuppression [3, 4]. The challenges of detecting TILs capable of responding to tumor antigens have led to great interest in identifying biomarkers of tumor-specific TILs in solid tumors. Biomarkers that identify tumor-specific TILs are integral for downstream applications, such as enriching tumor-specific TILs for use in adoptive cellular therapy, investigating endogenous antitumor immunity, studying mechanisms of effective immunotherapy, identifying antigen-specific T-cell receptors or neoantigens, and exploring the immunobiology of these cells [5–8]. The need for effective biomarkers to detect T cells is further underscored by the fact that many cancers, such as ovarian cancer, do not have well-defined shared tumor-specific antigens capable of initiating a tumor-specific T cell response. The paucity of shared tumor-specific antigens is in contrast to other cancers, such as melanoma, where some patients mount spontaneous responses against the melanocyte differentiation antigen, MART-1, which can be used to rapidly identify tumor-specific T cells in melanoma patients using peptide/MHC detection agents [9]. Furthermore, many cancers including ovarian cancer, have limited numbers of T cells that naturally respond to tumor-specific antigens, making their examination challenging. Identifying robust biomarkers for tumor-specific TILs can address this issue.

Various biomarkers are used to detect endogenous tumor-specific T cells from solid tumors, such as the co-stimulatory receptor CD137 (also known as 4-1BB and TNFRSF9), the negative immunoregulatory receptor PD-1, the lymphocyte-retention mediating integrin CD103, and the co-expression of both the ectonucleotidase CD39 and CD103 [10–13]. Identifying a singular, accurate biomarker for tumor-specific TILs would streamline downstream research and clinical applications, but it is unknown which singular biomarker is most effective at identifying the tumor-specific TIL subset, as a direct comparison of these reported biomarkers has not been performed. Addressing this knowledge gap is particularly important, because TILs frequently co-express these markers and each biomarker can be differentially expressed across the TIL population, therefore, a biomarker comparison is needed to identify the marker that most accurately discerns tumor-specific TILs [14, 15].

Here, we compared the expression of CD137, PD-1, CD103, and CD39 on TILs in human ovarian cancer, as these are leading biomarkers used to identify tumor-specific TILs. We hypothesized that a comparative interrogation of TILs in human tumors would reveal which biomarker is most discriminating for tumor-specific TILs with autologous antitumor activity.

Results

A subset of TILs express effector molecules

To investigate the phenotype of TILs harbored within infiltrated tumors, the algorithms viSNE and PhenoGraph metaclustering [16, 17] were used to co-map $CD3^+CD45^+$ TILs in enzyme-digested ovarian tumors analyzed by single-cell mass cytometry. To address patient-specific variability and to understand TIL dynamics shared between samples, PhenoGraph clusters were merged using the metaclustering algorithm in the interactive *cyt* tool [16]. Metaclustering analysis identified seven major TIL populations (Fig. 1A). Metaclusters (MCs) 1, 5, 6, and 7 were generally conserved among all samples tested, while MCs 2, 3, and 4 had greater variability (Fig. 1B). MC5 (mean = 1.51, 95% CI = -0.37 to 3.39) and MC6 (mean = 2.21, 95% CI = -0.83 to 5.24) were the rarest subsets in all samples, and MC5 was consistently enriched for cells expressing activation, proliferation, and effector molecules (Fig. 1B,C). Compared to the other metaclustered groups, only MC5 highly expressed effector molecules associated with antitumor responses, including IL-2, IFN-γ, perforin, TNF-α, and Granzyme B (Fig. 1C).

A series of activation-associated, cell surface markers have recently been described to identify, characterize and utilize naturally occurring tumor-specific T cells in human tumors. CD137, PD-1, CD103, and CD39 are most commonly utilized as biomarkers of TILs with tumor-specificity [10–13, 18]. MC5, which highly expresses effector molecules, was enriched for TILs expressing high levels of CD137 as well as the co-stimulatory receptor OX40, another TNFR family member upregulated upon T cell activation. MC5 moderately expressed CD103, PD-1, and CD39, as well as activation markers CD69 and CD25 (Fig. 1D), indicating that cells in MC5 are enriched for an activated T cell population.

$CD137^+$ TILs preferentially express effector molecules and co-express biomarkers of tumor-specificity

To gain a further understanding of which biomarkers are most selective in identifying TILs expressing effector molecules within human cancer, we examined viSNE plots of activation and tumor-specific biomarkers, which revealed the heterogeneity of their expression patterns. Similar to what was observed in the metaPhenoGraph heat map results (Fig. 1D), CD137 expression was primarily detected in the MC5 region, was expressed by both $CD4^+$ and $CD8^+$ TILs, and had co-expression of OX40, CD103, CD39, and PD-1 (Fig. 2A). PD-1 and CD69 expression were common, broadly distributed, with overlapping expression of CD25, OX40, CD103, CD39, and CD137. CD25 and OX40 expression were dominated by $CD4^+$ TILs and commonly co-expressed with CD39, while $CD103^+$ TILs were mainly $CD8^+$, a portion of which expressed CD39. Overall, few TILs expressed effector

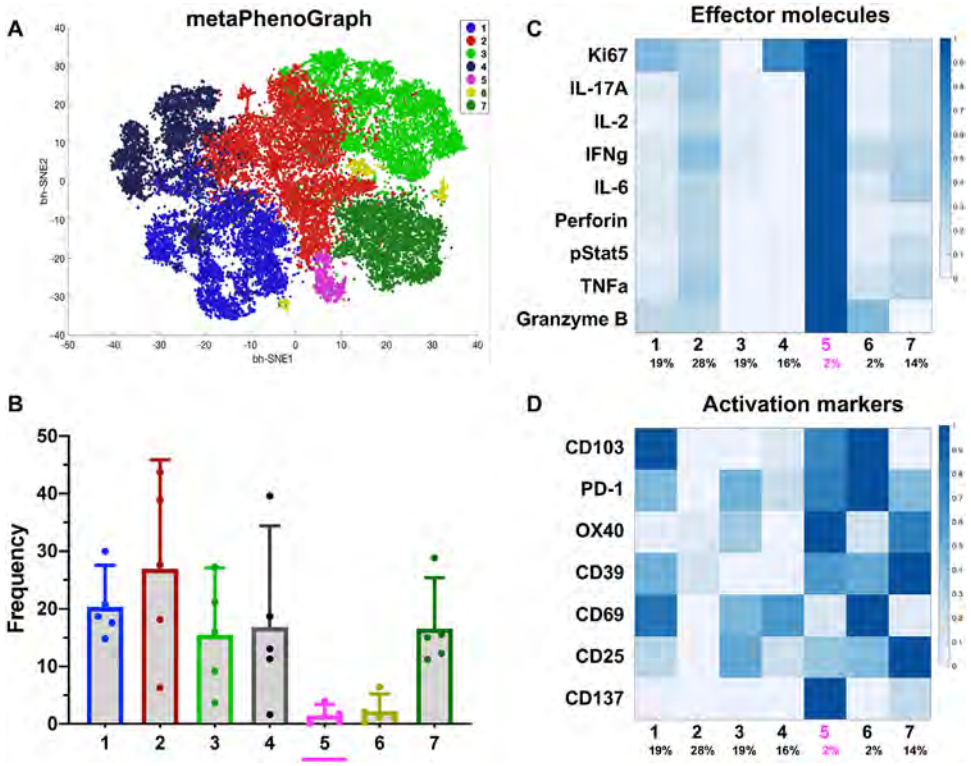

Figure 1. A small population of patient TILs positive for activation, tumor-specific markers also co-express effector molecules. CyTOF was performed on human ovarian tumor digests and analyzed using metaPhenoGraph. Experiment was repeated twice for a total of 5 samples (A) Metaclustering analysis identified 7 metaPhenoGraph metaclusters for ovarian cancer patient $CD3^+CD45^+$ TILs ($n = 5$). (B) Bar plot represents metacluster frequency per patient. Error bars represent the 95% confidence interval ($n = 5$). (C) metaPhenoGraph cluster results are represented as a heatmap, showing expression of Ki67, CD4, CD8, and effector markers ($n = 5$). (D) metaPhenoGraph heatmap displaying activation/tumor-specific markers ($n = 5$).

molecules, such as IFN-γ, IL-2, and TNF-α, and their MMI was low, compared to the level of activation and tumor-specific biomarkers. However, the few TILs that expressed effector molecules such as IFN-γ, IL-2, and TNF-α, were positive for CD137 in the MC5 region, suggestive of $CD137^+$ TIL polyfunctionality, and CD137 expression was more focal than other tumor-specific biomarkers (Fig. 2A). Since viSNE plot analyses indicated that CD137 expression overlapped more with effector molecule expression than other biomarkers, we compared effector molecule expression within the $CD137^+$ TIL population to expression in TILs expressing other tumor-specific and activation markers (Supporting Information Fig. 1). Generally, $CD137^+$ TILs exhibited the greatest frequency of cells expressing IFN-γ, TNF-α, Granzyme B, perforin, and IL-2, compared to other biomarkers expressing TILs (Fig. 2B). $CD137^+$ TILs had greater expression of IFN-γ (P-value = 0.0008), Granzyme B (P-value = 0.01), perforin (P-value = 0.003), and IL-2 (P-value = 0.002) than $CD103^+$ TILs, but similar levels of TNF-α expression (Fig. 2B). $CD137^+$ TILs and $OX40^+$ TILs were similar with the exception of $CD137^+$ TILs expressing greater frequencies of IFN-γ (P-value = 0.008) and Granzyme B (P-value = 0.01; Fig. 2B). While this study focuses on comparing single biomarkers, dual expression of $CD103^+CD39^+$ was reported to identify $CD8^+$ tumor-specific TILs [13]. When comparing $CD103^+CD39^+$ TILs to $CD137^+$ TILs, CD137 expression was more selective for identifying total $CD3^+$ and $CD8^+$ TILs expressing effector molecules (Supporting Information Fig. 2A,B) with no differences observed when comparing $CD4^+$ TILs (data not shown).

Although $CD137^+$ TILs exhibited the highest expression of effector molecules, the frequency of these cells was low (mean = 4.1%, 95% CI = 1.87 to 6.36) compared to TILs expressing other biomarkers (Fig. 3A). Since viSNE and PhenoGraph analyses (Fig. 1) revealed that $CD137^+$ TILs often co-express tumor-specific biomarkers, we next examined the frequency of $CD137^+$ TILs within TIL populations expressing other tumor-specific biomarkers using biaxial gating (Fig. 3B). $CD137^+$ TILs commonly co-expressed PD-1 (mean = 54.9%, 95% CI = 39.47 to 70.31]), CD103 (mean = 37.6%, 95% CI = 24.64 to 48.78), and CD39 (mean = 76.8%, 95% CI = 64.55 to 88.95). In contrast, only a small portion of $PD\text{-}1^+$ (mean = 6.2%, 95% CI = 4.36 to 8.07), $CD103^+$ (mean = 6.2%, 95% CI = 3.13 to 9.17), or $CD39^+$ (mean = 6.7%, 95% CI = 3.45 to 10.02) TILs co-expressed CD137. These results, combined with effector molecule expression data (Fig. 2), indicate that CD137 is the more selective marker for identifying tumor-specific TILs (Fig. 3C).

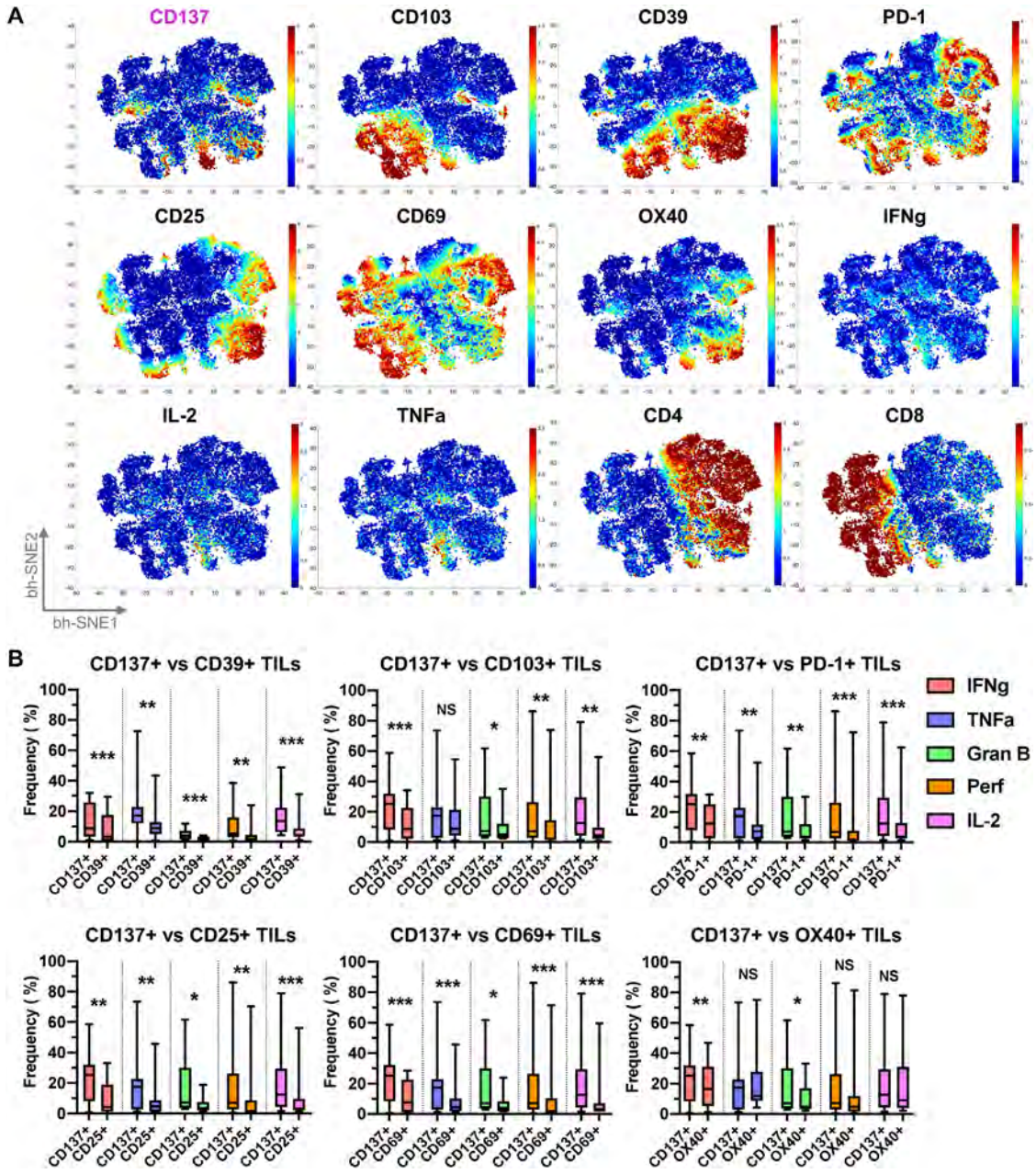

Figure 2. TILs positive for CD137 have enhanced expression of effector molecules compared to other markers indicative of tumor-specificity. CyTOF analysis was performed on human ovarian tumor digests and analyzed via viSNE (A) or traditional biaxial gating (B). (A) viSNE plots of tumor-specific markers used in the literature (CD137, CD103, PD-1, CD39), activation markers (CD25, CD69), a TNFR family member (OX40), and effector molecules IFN-γ and TNF-α. CD4 and CD8 TILs are represented as well. Experiment was conducted twice for a total of 5 samples. (B) Plots comparing frequency of effector molecule expression between activation and markers of tumor-specificity ($n = 15$). Experiment was independently performed four times, with the exception of CD39 where the experiment was repeated three times. The Student's two-tailed, paired *t*-test was run to determine statistical significance. NS represents a *P*-value >0.050, (*) represents a *P*-value ≤ 0.050, (**) represents a *P*-value <0.01, (***) represents a *P*-value < 0.001, (****) represents a *P*-value < 0.0001, boxplots depict the median, quartiles, with whiskers representing the min and max, error bars are 95% confidence interval.

CD137$^+$ TILs are a subset of PD-1$^+$, CD103$^+$, and CD39$^+$ TILs that exhibit antitumor activity

We next investigated whether the CD137$^+$ TIL subset contained within other biomarker populations are enriched for effector molecules. Decreased IFN-γ expression was observed in CD39$^+$ (*P*-value = 0.001), CD103$^+$ (*P*-value < 0.001), and PD-1$^+$ (*P*-value = 0.002) TILs when CD137$^+$ TILs were selectively gated out (Supporting Information Fig. 2C) prior to analysis in Fig. 4A. This effect was also observed in TILs expressing CD25 (*P*-value = 0.001), CD69 (*P*-value = 0.001), or OX40 (*P*-value = 0.003; Fig. 4A). Granzyme B expression similarly decreased (Fig. 4B),

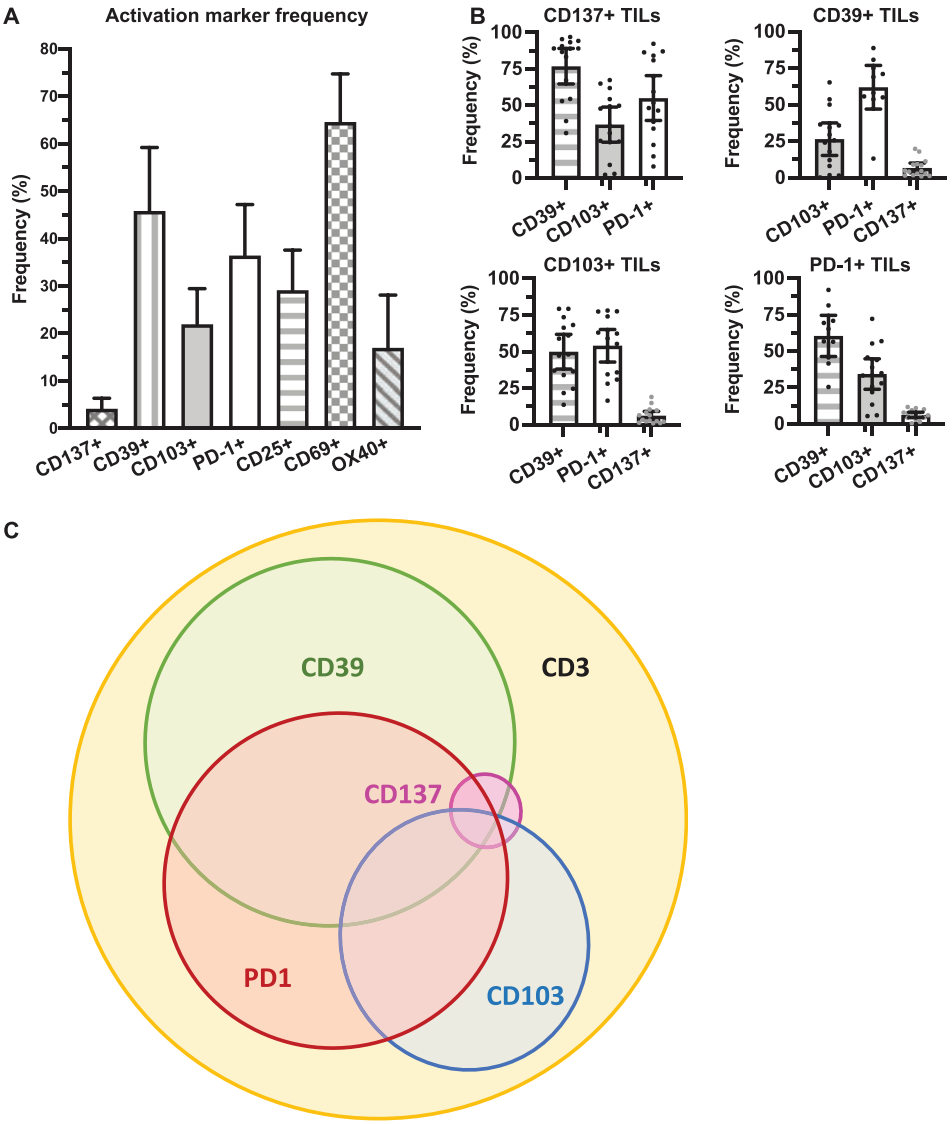

Figure 3. CD137$^+$ TILs are rare and highly co-express PD-1, CD103, and CD39. Human ovarian tumor digests were interrogated using CyTOF and analyzed using traditional biaxial gating. Experiment was conducted a total of four times, with the exception of CD39 which was performed three times independently. (A) Frequency of activation and tumor-specific markers within CD3$^+$CD45$^+$ TILs ($n = 15$). (B) Co-expression patterns of CD137$^+$, PD-1$^+$, CD103$^+$, and CD39$^+$ TILs ($n = 15$ with the exception of CD39$^+$ TIL co-expression for PD-1, $n = 10$). (C) Schematic of CD137, PD-1, CD103, and CD39 predicted T cell expression according to phenotypic findings. The Student's two-tailed, paired *t*-test was run to determine statistical significance. NS represents a *P*-value > 0.050, (*) represents a *P*-value ≤ 0.050, (**) represents a *P*-value < 0.01, (***) represents a *P*-value < 0.001, (****) represents a *P*-value < 0.0001, error bars are 95% CI with center values representing the mean.

leading us to hypothesize that the CD137$^+$ TIL subset may account for the reactivity observed in other biomarker-expressing tumor-specific TIL populations [10–13].

We next tested whether functional reactivity of TILs was restricted to the CD137$^+$ TIL subset in co-culture assays where CD137$^+$ TILs were first sorted out of the bulk TIL, and then other biomarker expressing TIL subsets were sorted prior to co-culture with autologous tumor cells (Supporting Information Fig. 2D). Compared to the PD-1$^+$, CD103$^+$, and CD39$^+$ TIL populations depleted of CD137$^+$ cells, the CD137$^+$ TIL subset produced the highest levels of IFN-γ in response to autologous tumor cells exposure in three independent donor samples. Production of IFN-γ by CD137$^+$ TILs upon autologous tumor co-culture was HLA-dependent, indicating tumor-antigen specificity, as IFN-γ decreased upon HLA blocking of MHC class I and class II with antibodies (Fig. 4C). In all tested TIL samples, the CD137$^+$ subset secreted IFNγ levels twice as high as that of unstimulated TILs alone. These results indicate that effector molecule expression is enriched within the CD137$^+$ TIL fraction, and that CD137$^+$ TILs account for the majority of antitumor reactivity observed within PD-1$^+$, CD39$^+$, and CD103$^+$ TIL populations.

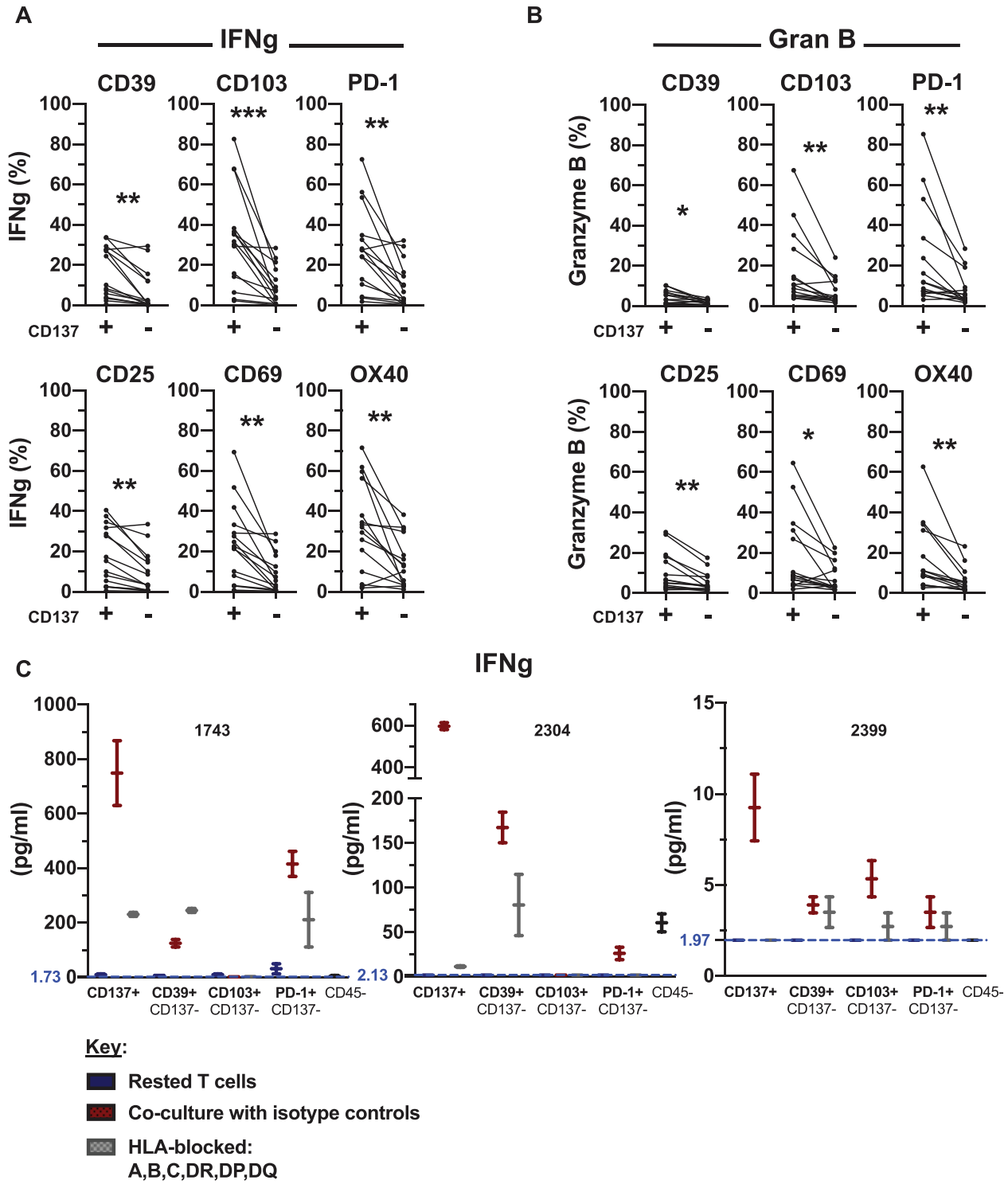

Figure 4. Removal of CD137$^+$ T cells decreases effector molecule production in other biomarker subsets. (A and B) CyTOF analysis was run on human ovarian tumor digests and analyzed via biaxial gating. (C) TIL subsets were co-cultured with autologous tumor cells and supernatants were analyzed after 24 h by LEGENDplax. (A) Expression of IFN-γ and (B) Granzyme B within CD137$^+$ and CD137$^-$ subpopulation within tumor-specific and activation markers ($n = 15$). Experiment was conducted four times, for a total of total of 15 samples, with the exception of the CD39 plot where the experiment was repeated three times for a total of 15 samples. Representative gating is shown in Supporting Information Figure 2C. (C) IFN-γ secretion following autologous tumor co-culture in three different ovarian patient samples. Blue dashed and blue number on the y-axis indicates the lowest sensitivity of the assay according to the standard curve. Assay flow setup is represented in Supporting Information Figure 2D. Experimented was conducted three times, with one patient ran at a time. The Student's two-tailed, paired *t*-test was run to determine statistical significance. NS represents a *P*-value > 0.050, (*) represents a *P*-value ≤ 0.050, (**) represents a *P*-value < 0.01, (***) represents a *P*-value < 0.001, (****) represents a *P*-value < 0.0001, error bars are 95% confidence interval with center values representing the mean.

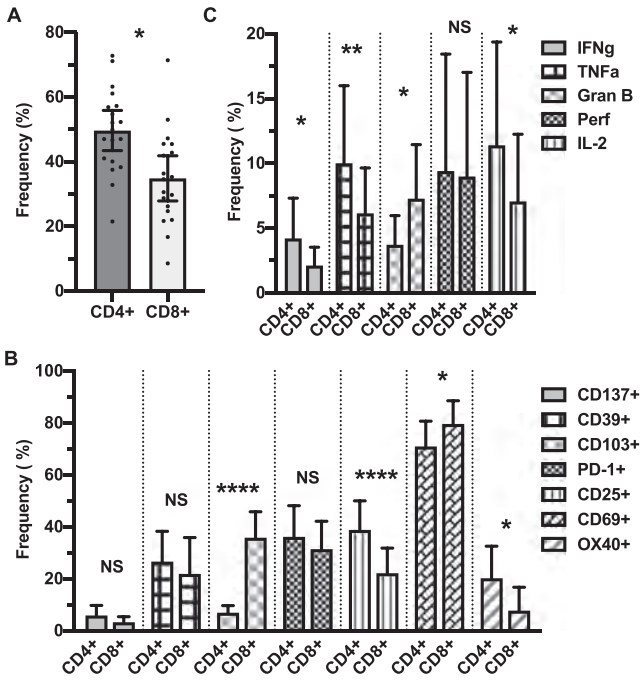

Figure 5. Both CD4$^+$ and CD8$^+$ TILs express markers indicative of antitumor reactivity. Human ovarian tumor digests were interrogated by CyTOF and analyzed via biaxial gating. Experiment was independently run four times, with the exception for CD39 which was repeated three times. (A) Frequency of CD4$^+$ and CD8$^+$ TILs in live CD3$^+$CD45$^+$ TILs ($n = 19$). (B) Frequency of tumor-specific markers within CD4$^+$ and CD8$^+$ TILs. Sample size per group: CD137 ($n = 19$), CD39 ($n = 14$), CD103, PD-1, CD25, CD69, and OX40 ($n = 18$). (C) Frequency of effector molecules within CD4$^+$ and CD8$^+$ TILs. The Student's two-tailed, paired *t*-test was run to determine statistical significance. NS represents a P-value > 0.050, (*) represents a P-value ≤ 0.050, (**) represents a P-value < 0.01, (***) represents a P-value < 0.001, (****) represents a P-value < 0.0001, error bars are 95% confidence interval with center values representing the mean.

Both CD4$^+$ and CD8$^+$ TILs express markers of antitumor reactivity

Having analyzed co-expression and effector profiles of tumor-specific marker expressing populations within overall CD3$^+$CD45$^+$ TILs, we next examined the biomarker profiles of CD4$^+$ or CD8$^+$ TIL subsets in ovarian cancer samples. There were more CD4$^+$ TILs (mean = 49.6%, 95% CI = 43.43 to 55.86) than CD8$^+$ TILs (*P*-value = 0.02, mean = 34.9%, 95% CI = 27.88 to 41.85) (Fig. 5A). CD137 expression within the CD4$^+$ (mean = 5.9%, 95% CI = 2.12 to 9.75) and CD8$^+$ (mean = 3.32%, 95% CI = 5.46 to 1.19) TIL subsets did not statistically differ, suggesting that both CD4$^+$ and CD8$^+$ T cells harbor tumor-specific TILs and that both subsets may contribute to antitumor activity in ovarian cancer. More CD8$^+$ TILs expressed CD103 (*P*-value < 0.001) and CD69 (*P*-value = 0.01). A higher percentage of CD4$^+$ TILs expressed CD25 (*P*-value < 0.001) and OX40 (*P*-value = 0.01), but there was no significant differences in CD39 or PD-1 expression (Fig. 5B). When comparing effector molecule expression, an increased frequency of IFN-γ (*P*-value = 0.04), TNF-α (*P*-value = 0.01), and IL-2 (*P*-value = 0.01) expressing cells was detected in CD4$^+$ TILs. CD8$^+$ TILs contained greater frequencies of cells expressing Granzyme B (*P*-value = 0.03), and no difference was detected in perforin expression (Fig. 5C). These results support the notion that both CD4$^+$ and CD8$^+$ TILs can express effector molecules, which can be divergent and together may play integral roles in immune responses against tumor cells.

Tumor-specific TILs display a phenotype indicative of restorable exhaustion

Since our findings indicate that CD137$^+$ TILs express effector molecules and other molecules indicative of activation, we queried whether these tumor-specific TILs displayed features of exhaustion, which is commonly associated with chronic tumor-antigen stimulation [19]. We examined to what degree TILs in meta-cluster 5 (MC5) (Figs. 1 and 2), which harbored the highest frequency of CD137$^+$ and effector molecule-expressing TILs, exhibit phenotypic hallmarks of exhaustion. T cells in the MC5 population expressed multiple markers indicative of exhaustion, specifically CTLA-4, Tim-3, PD-1, CD39, CD244, EOMES, Lag-3, TIGIT, and CD160. (Fig. 6A). MC5 TILs expressed PD-1, albeit at overall lower levels than MC6. MC5 TILs uniquely co-expressed PD-1 and the costimulatory molecule CD28, whose signaling is required for rescue of CD8$^+$ T cell activity in anti-PD-1 therapy for cancer [20]. Exhaustion-associated marker expression in CD137$^+$ TILs was compared to other TIL populations by examining TIGIT, EOMES, and CD39 expression in CD137$^+$ or CD137$^-$ subsets. CD137$^+$ TILs expressed higher levels of the exhaustion-associated markers TIGIT (*P*-value < 0.001), EOMES (*P*-value < 0.001), and CD39 (*P*-value < 0.001), compared to CD137$^-$ TILs (Fig. 6B). Since the aforementioned markers can be upregulated by both activated and exhausted T cells, we assessed whether CD137$^+$ TILs are skewed towards a EOMES^{hi}T-bet^{dim} phenotype associated with dampened effector functions [21] or toward a more functional EOMES^{dim}T-bet^{hi} phenotype. CD137$^+$ TILs were more skewed towards an EOMES^{hi}T-bet^{dim} (*P*-value = 0.004) phenotype than their CD137$^-$ counterparts, supporting the notion that CD137$^+$ TILs are exhausted (Fig. 6C, D). As CD137$^+$ TILs appear exhausted but also harbor tumor-specific TILs that express effector molecules and co-express CD28, our results suggest that CD137$^+$ TILs have the greatest potential for reinvigoration [20]; however, studies designed to disentangle functional T cell exhaustion from activity in CD137-expressing TILs would be necessary to validate this supposition.

Discussion

TILs are a heterogeneous population of immune cells that can differ in specificity, differentiation, and function. Biomarkers that identify endogenous tumor-specific TIL subsets are fundamental to immunobiology research, studying mechanisms of endogenous antitumor immunity, isolating tumor-specific T-cell receptors, and optimizing cellular therapies [5–8]. We observed

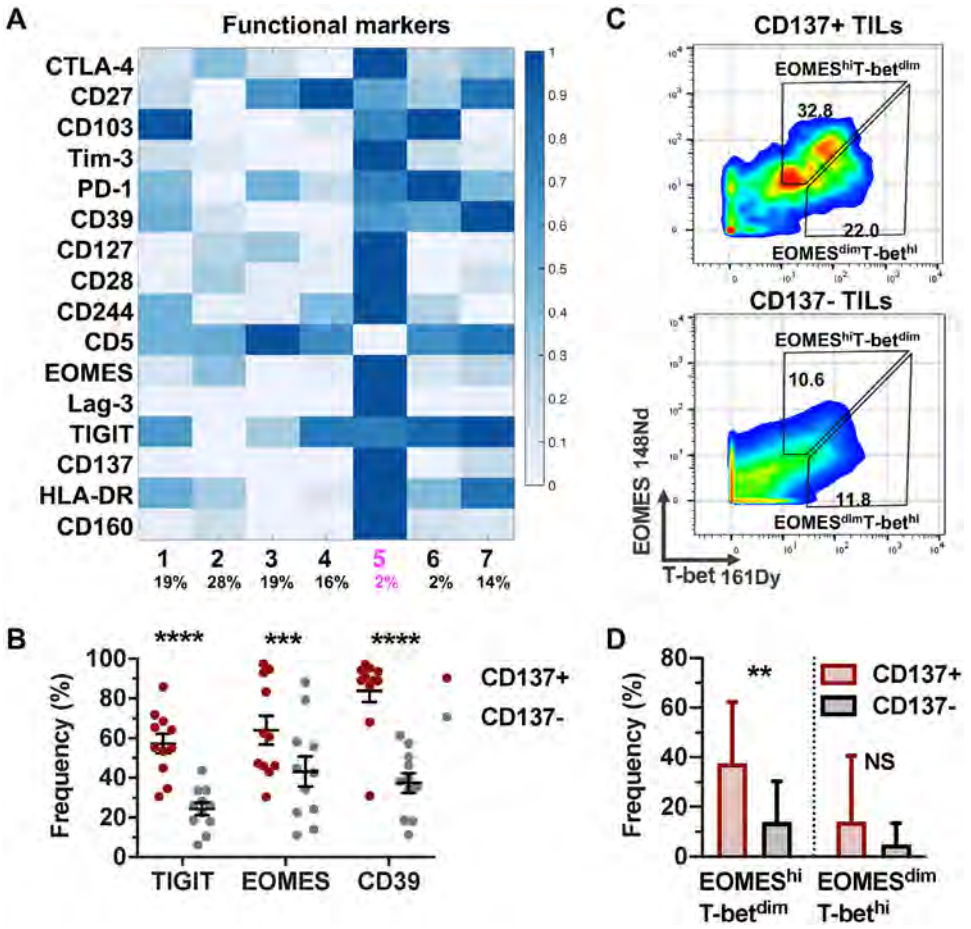

Figure 6. CD137$^+$ TILs within the ovarian cancer tumor microenvironment have a phenotype indicative of exhaustion. CyTOF analysis was performed on human ovarian tumor digests and analyzed via biaxial gating. (A) metaPhenoGraph heatmap (same samples and setup as in Figure 1) displaying markers mainly of activation, co-stimulation, and exhaustion. Experiment was conducted twice ($n = 5$). (B) Frequencies of exhaustion markers TIGIT, EOMES, and CD39 in CD137$^+$ versus CD137$^-$ TILs ($n = 11$). Experiment was repeated three times. (C) Representative gating of EOMES^{hi}T–bet^{lo} and EOMES^{hi} T-bet^{lo} in CD137$^+$ and CD137$^-$ live CD3$^+$CD45$^+$ TILs. (D) EOMES^{hi}T–bet^{lo} and EOMES^{hi} T-bet^{lo} frequencies in CD137$^+$ and CD137$^-$ TILs ($n = 7$). Experiment was performed independently twice. The Student's two-tailed, paired *t*-test was run to determine statistical significance. NS represents a *P*-value > 0.050, (*) represents a *P*-value ≤ 0.050, (**) represents a *P*-value <0.01, (***) represents a *P*-value < 0.001, (****) represents a *P*-value < 0.0001, error bars are 95% confidence interval with center values representing the mean.

that TILs expressing effector molecules often co-expressed other biomarkers used to identify tumor-specific TILs. Earlier studies of TILs expressing a single biomarker reported levels of secondary biomarker co-expression, but a direct comparison between various biomarker-expressing TIL subsets had yet to be conducted [10–13]. We found that a small subset of PD-1$^+$, CD103$^+$, and CD39$^+$ TILs reproducibly co-express CD137. In contrast, most CD137$^+$ TILs highly co-express the aforementioned biomarkers, and preferentially express effector molecules, indicating that CD137 more selectively identifies tumor-specific TILs. Further, removing CD137$^+$ TILs from other biomarker-expressing TIL subsets reduced their functional activity in response to autologous tumor stimulation, indicating that while PD-1, CD103, and CD39 markers can be used to identify tumor-specific TILs, CD137 expression is a more discriminatory tumor-specific TIL biomarker.

The finding that CD137 expression is a highly selective marker for endogenous tumor-specific TIL identification is supported by previous findings from our laboratory [9, 10], and later studies that used CD137 to enrich tumor-specific TILs [7,10,22]. Our findings contradict results reported by Gros and colleagues showing that both PD-1$^+$ and CD137$^+$ TIL subsets were tumor-reactive but with PD-1 better identifying tumor-reactive T cells [11]. Interesting, activation-induced expression of CD137 was used to define tumor-reactivity in many of the assays used in that study. The discrepancy between our findings and those reported by Gros et al. may be explained by differences in the cancer type studied as well as the methodology applied. Gros et al. solely focused on CD8$^+$ TILs and did not include CD4$^+$ TILs. In contrast, the present study, and our previous study that first defined CD137 as a biomarker for tumor-specific TILs [10] included CD4$^+$ TILs in the analysis. This alone does not account for the discrepancy, since CD137 still served as a better biomarker for tumor-specific CD8$^+$ TILs. Identifying endogenous tumor-antigen-specific TIL biomarkers in patients has been heavily CD8$^+$ T-cell-centric [11–13, 23],

but there is growing appreciation for the role of $CD4^+$ T cells in promoting antitumor immunity and immunotherapy efficacy [24–27]. This is emphasized by our findings that $CD4^+$ TILs dominate the ovarian tumor environment and have equivalent expression of CD137 as $CD8^+$ TILs. Also, with the exception of Granzyme B, $CD4^+$ TILs had either equivalent or greater positivity for IFN-γ, TNF-α, perforin, and IL-2. Our results support the idea that both $CD8^+$ and $CD4^+$ TILs have integral roles in driving antitumor immune responses and may have divergent antigen-specific responses.

A separate study by Duhen et al. demonstrated that co-expression of CD39 and CD103 TILs can identify tumor-specific TILs within solid tumors. Similar to Gros et al., the work focused on $CD8^+$ TILs [13]. Supporting our finding that $CD137^+$ TILs often co-express other commonly used tumor-specific TIL biomarkers, both Gros et al. and Duhen et al., used CD137 upregulation as a measure to assess tumor-cell recognition by $PD\text{-}1^+$ or $CD39^+CD103^+$ $CD8^+$ TILs in co-culture experiments. Notably, only a subset of enriched $PD\text{-}1^+$ or $CD39^+CD103^+$ $CD8^+$ TILs upregulated CD137 expression after autologous tumor recognition. Unlike Gros et al. and Duhen et al. studies, we examined TILs from tumor digests without the addition of cytokines, establishment of T cell clones, or bulk-expansion. It bears consideration that this methodology may better preserve TIL natural reactivities to autologous tumor antigens with minimal manipulation of TIL biomarker expression.

Immune checkpoint blockade has shown great promise in numerous solid tumors, and successful antitumor responses are thought to rely upon reinvigorated responses by tumor- specific T cells [19, 28, 29]. The phenotypic profile of $CD137^+$ TILs suggests that they have potential for reinvigoration via checkpoint blockade. $CD137^+$ TILs highly expressed multiple co-inhibitory receptors, including PD-1, and were skewed towards a phenotype characteristic of exhausted T cells [21] and co-expressed CD28. Expression of CD28 by $CD137^+$ TILs is important because restoring exhausted T cell function is dependent on CD28 co-stimulation [20, 30]. However, many cancers, including ovarian cancer, have low response rates to PD-1/PDL1 blockade [31]. Our data may suggest that one potential explanation is that most patients have too few $CD137^+$ TILs to reinvigorate for an effective antitumor response. It is intriguing to hypothesize that the response rate to PD-1/PDL1 blockade may be increased by promoting CD28 signaling to TILs, such as through CTLA-4 blockade. Both CTLA-4 and CD28 bind to CD80 and CD86 on antigen-presenting cells, but CTLA-4 binds CD80 and CD86 with greater affinity and avidity than CD28, enabling it to outcompete CD28 for these ligands. The response rate to anti-PD-1 antibody treatment in ovarian cancer nearly triples when a CTLA-4 blocking antibody is added to the treatment regimen [32]. Furthermore, agonizing CD137 may aid in promoting antitumor responses in patients, and although CD137 agonism in the clinic has had toxicities [33, 34], dual bispecific antibodies that agonize CD137 are being developed in order to enhance T cell proliferation and antitumor activity in human cancer without the safety limitations observed in the clinic [35, 36]. The recently developed CD137/OX40 bispecific antibody [35] may be promising to test in an ovarian cancer model, as we observed that effector molecule expressing $CD137^+$ TILs also co-expressed OX40 (Fig. 2A). Future studies are needed to determine if $CD137^+$ TILs are reinvigorated by anti-PD-1 therapy, whether they require CD28 signaling, and how they contribute to successful immune checkpoint blockade monotherapy or combinatorial immunotherapy strategies [35, 36].

Collectively, this work clarifies the differential expression of biomarkers for tumor-specific TILs and demonstrates that CD137 is a more selective biomarker for identifying naturally occurring, tumor-specific TILs than PD-1, CD103, or CD39 within human ovarian tumors. This work corroborates our original finding that CD137 accurately identifies tumor-specific TILs[10]. Furthermore, our findings explain why the addition of an agonistic antibody to TIL cultures results in preferential expansion of tumor-specific TILs in melanoma [37]. We acknowledge there are limitations to this analysis. Our study entirely used ovarian cancer specimens, and results may differ in other cancer types. Also, due to limited cell numbers, we were unable to independently test $CD4^+$ and $CD8^+$ TILs for TIL subset reactivity, or test restorable exhaustion on $PD\text{-}1^+$ T cells. Furthermore, PD-1 blockade has low efficacy in in vitro assays, and would require sophisticated in vivo models and large cell numbers. Nevertheless, we conclude that this work disentangles the differential expression of tumor-specific biomarkers by TILs and demonstrates that CD137 is an ideal singular biomarker for identifying tumor-specific TILs, which provides a deeper understanding of human TILs that may pave a route towards improving immunotherapeutic strategies for cancer.

Materials and methods

Tumor Samples

Viably frozen, human high-grade serous ovarian tumor samples were purchased from the Penn Ovarian Cancer Research Center (OCRC) Tumor BioTrust Collection. Ethics statement: All donor samples used in this study were de-identified and approved for use by the UPenn Institutional Review Board (IRB 702679, UPCC 17909). Sex and weight are not a biological variable as all tumor samples are from females. As samples are de-identified, age and weight are not known. Surgically resected tumors were procured from the operating room in an aseptic manner. Tissue was mechanically processed into fragments and added to an enzyme digest solution. A 10× stock solution of the enzyme digest buffer contains 2 mg/mL collagenase (Sigma–Aldrich) and 0.3 kU/mL DNase I Type IV (Sigma–Aldrich); solution was diluted to a 1× solution with RPMI 1640 at the time of digestion. Tissue was incubated in the enzyme digest buffer overnight at room temperature on a rotator. Dissociated tumor tissue was subsequently filtered through sterile 100μm nylon mesh, centrifuged, and washed twice with dPBS (Dulbecco's Phosphate Buffered Saline). Resultant tumor cell digests were cryopreserved in 10%

dimethyl sulfoxide (DMSO) (Sigma Aldrich) and human serum (Valley Biomedical, Inc., Product #HS1017). Samples were frozen at -80°C and banked at -150°C until further use.

Mass Cytometry staining

CyTOF antibodies were purchased from Fluidigm as pre-conjugated metal tagged antibodies or were conjugated in-house using the Maxpar Fluidigm kit and protocol. All antibodies were titrated to determine optimal concentrations for staining samples. The panel used to initially investigate tumor-specific markers, before inclusion of CD39 in the aforementioned panel, had the following surface markers: CD3, CD45, CD4, CD8, CD244, CD69, OX40, Lag-3, CD103, Tim-3, TIGIT, PD-1, CD137, CD28, CD127, CD27, GITR, CD25, HLA-DR, and CD160. Intracellular antibodies included: CTLA-4, pStat5, IL-17A, IL-2, IFNg, Granzyme B, Ki67, and Perforin. No additional polyclonal stimulation or protein transport inhibitors were added to preserve the natural phenotype and activation state of the T cells. We subsequently designed a panel to include CD39 and all other tumor-specific markers of interest. The following panel included CD39 and was used for downstream viSNE, metaPhenoGraph, and biaxial analysis. Anti-human surface markers for the panel were: CD3, CD45, CD4, CD8, CD103, PD-1, OX40, CD39, CD69, CD25, CD137, CD27, Tim-3, CD127, CD28, CD244, CD5, Lag-3, TIGIT, HLA-DR, and CD160. Intracellular markers included: Ki67, IL-17A, IL-2, IFN-γ, IL-6, Perforin, pStat5, TNF-α, Granzyme B, CTLA-4, and EOMES. The initial panel to compare CD39 and CD137 positive TILs had the following surface antibodies interrogated: CD3, CD45, CD4, CD8, CD137, CD39, CD25, HLA-DR, and CD127. Intracellular antibodies detected were: IL-2, pStat5, EOMES, T-bet, IL-17A, IFN-γ, Granzyme B, Ki67, and Perforin. The last panel used in this study was designed to focus on TIL exhaustion. Surface antibodies used were: CD3, CD45, CD4, CD8, OX40, CD103, TIGIT, CD137, CD39, CD25, CD3, HLA-DR, and CD127. Intracellular antibodies were: IL-2, pStat5, EOMES, T-bet, and Ki67. For all panels, cell identifier stain Iridium191/193, live identifier 127IdU (Fluidigm) were used. To discriminate dead cells, cisplatin purchased from Fluidigm or dead stain maleimido-mono-amine-DOTA (mm-DOTA) from Macrocyclics was used. Viably frozen ovarian human tumor digests obtained from the Tumor BioTrust collection, processed as described in the Tumor Samples section above, were thawed in batches and stained for CyTOF following the same methodology as Bengsch et al. [38]. Data acquisition was performed on a CyTOF Helios (Fluidigm CyTOF Helios Mass Cytometer, RRID:SCR_019916) by the CyTOF Mass Cytometer Core at UPenn. The core performed bead-based normalization for all samples.

Fluorescent-activated cell sorting

Tumor samples were thawed and washed twice with staining buffer (PBS, 5% fetal bovine serum) to remove DMSO. Samples were subsequently stained with Zombie aqua (BioLegend Cat# 423102) for 10 minutes to discriminate live and dead cells. Samples were washed twice to remove Zombie aqua, then incubated at 4°C for 30 min in 50 μl of an antibody cocktail to label human surface markers. Following surface staining, samples were washed three times. Samples were sent to the Flow Cytometry Facility at the Wistar Institute for fluorescent-activated cell sorting (FACS) on a MoFlo Astrios or to the Flow Cytometry Core at the Children's Hospital of Philadelphia and sorted on an Aria, and adhered to the guidelines for the use of flow cytometry and cell sorting in immunological studies [39]. All antibodies were purchased from BioLegend. For all analyses, singlets were detected using FSC-H versus FSC-A followed by SSC-H versus SSC-A. Cells negative for Zombie aqua, were identified as live cells. Anti-human-anti-CD3-PerCpCy5.5 (BioLegend Cat# 317336, RRID:AB_2561628) was used to detect T cells and the following anti-human antibodies were used to identify T cell subsets $CD137^{+}$, $PD\text{-}1^{+}CD137^{-}$, $CD39^{+}CD137^{-}$, $CD103^{+}CD137^{-}$: anti-CD137-PeCY7 (BioLegend Cat# 309818, RRID:AB_2207741), anti-CD103-BV605 (BioLegend Cat# 350218, RRID:AB_2564283), anti-CD39-APC (BioLegend Cat# 328210, RRID:AB_1953234), and anti-PD-1-APCCy7 (BioLegend Cat# 329922, RRID:AB_10933429).

Mass cytometry biaxial analyses

Traditional biaxial analysis, on bead-normalized fcs files, was performed using Flowjo V10 software (FlowJo, RRID:SCR_008520). Intact single cells were identified using event-length and Iridium. Cells were live-gated according to 127IdU and mm-DOTA, where dead cells are positive for mm-DOTA. CD3 and CD45 positivity identified T-cells. Sequential gating analysis was performed for all analyzed markers. The resulting values were used to determine population frequencies.

viSNE and metaPhenoGraph analyses

High-dimensional analysis was conducted using the algorithm viSNE, which uses the Barnes-Hut t-SNE (bh-SNE) implementation, from *cyt* a visualization tool written in Matlab (R2016b, MATLAB,RRID:SCR_001622) downloaded in 2015 and available at https://www.c2b2.columbia.edu/danapeerlab/html/cyt-download.html. Live, single, $CD3^{+}CD45^{+}CD137^{+/-}$ exported fcs data from five donor samples were imported into *cyt*, arcsinh5-transformed, and run as described by Amir et al., 2013 [16] to create viSNE plots. The following parameters were used for bh-SNE mapping analysis: Ki67, IL-17A, IL-2, IFN-γ, CD103, PD-1, IL-6, OX40, CD39, Perforin, CD69, CD4, CD8, pStat5, TNF-α, GITR, CD25, Granzyme B, and CD137. The PhenoGraph algorithm was run, as described by Levin et al. [17], with the nearest neighbor input of $k = 30$ and a Euclidean distance metric. Markers used for PhenoGraph clustering were the following: Ki67, IL-17A, IL-2, IFN-γ, CD103, PD-1, IL-6, OX40, CD39, Perforin, CD69, CD4, CD8, pStat5, TNF-α, GITR, CD25, Granzyme B, and

CD137. PhenoGraph was metaclustered, as described by Levine et al., using a $k = 15$ and a Euclidean distance metric. viSNE, PhenoGraph, metaPhenoGraph plots, and heatmaps were created by *cyt*.

Co-culture experiment

The following live T cell subsets were FACS sorted from thawed cryopreserved patient tumor samples: $CD137^+$, $CD39^+CD137^-$, $CD103^+CD137^-$, and PD-1^+CD137- using the staining protocol specified in the FACs sorting section. T cells were rested overnight in RPMI 1640 media supplemented with 10% FBS and supernatants were collected the following day. $CD45^+$ cells were depleted from the same patient sample to obtain $CD45^-$ cells for co-culture using the EasySep Human CD45 Depletion Kit from StemCell Technologies Cat# 17898. T cell subsets were co-cultured, with 10ug/ml HLA-blocking Class I (BioLegend Cat# 311402, RRID:AB_314871) & II (BioLegend Cat# 361702, RRID:AB_2563139) or isotype (BioLegend Cat# 400202) antibodies, at a 1:2 ratio of T cells to autologous tumor cells in 100ul of media in a 96-ubottom plate. The number of T cells added to co-culture were as follows; 30,000 cells for sample 1743; 14,500 cells for 2304 and 6125 cells for 2399. Following 24 h co-culture, samples were spun down at 1300 rpm, and supernatants were collected and stored at -80°C until use. To analyze cytokines within the supernatants, the manufacture's protocol of the LEGENDplex Human CD8/NK Panel kit (BioLegend Cat# 740267) was followed, and two technical replicates were analyzed per sample.

Statistical analysis

The Student's two-tailed, paired *t*-test was run to determine statistical significance. NS represents a *P*-value > 0.050, "*" represents a *P*-value ≤ 0.050, "**" represents a *P*-value < 0.01, "***" represents a *P*-value < 0.001, "****" represents a *P*-value < 0.0001, error bars represent 95% confidence Interval.

Acknowledgements: The authors acknowledge the Ovarian Cancer Translational Center for Excellence in the Abramson Cancer Center for support of tumor banking operations through the Tumor BioTrust Collection. The authors thank Dr. Bertram Bengsch and the E. John Wherry laboratory at the University of Pennsylvania, for aid in the development of CyTOF antibody panels and insights on data analysis, as well Takuya Ohtani of the UPenn CyTOF Core for running mass cytometry samples. The authors also acknowledge the personnel of the Wistar Institute's Flow Cytometry Facility and the Flow Cytometry Core Laboratory at the Children's Hospital of Philadelphia Research Institute for their aid and expertise in sorting cells. This work was supported in part by an NIH/NCI pilot grant P50 CA228991 awarded to Daniel J. Powell Jr., and partly by BMS grant CA186-113 awarded to Jessica A. Chacon and Daniel J. Powell Jr. The funding sources had no role in the design, collection, analysis, interpretation, writing, or decision to submit the manuscript for publication.

Data availability statement: The data supporting the findings of this study are available from the corresponding author upon reasonable request.

Peer review: The peer review history for this article is available at https://publons.com/publon/10.1002/eji.202149329

Ethics approval statement

De-identified human ovarian cancer samples were obtained from the Penn Ovarian Cancer Research Center (OCRC) Tumor BioTrust Collection (UPCC 17909, IRB 702679).

Author contributions

M.A.E. and D.J.P were associated with conceptualization, methodology, project administration, and writing; D.J.P. was associated with supervision and resources. D.J.P and J.C. were associated with funding acquisition. M.A.E. was associated with formal analysis, visualization, investigation, and validation; D.K.O. was associated with resources and writing; J.C. reviewed and edited the final manuscript.

Conflict of interest: D.J.P. holds a patent on CD137 enrichment for efficient tumor infiltrating lymphocyte selection (U.S. Pat. No. 10,233,425) and receives fees for advisory services from InsTIL Bio on TIL therapy. All other authors have no commercial or financial conflicts of interests.

References

1 **Zhang, L., Conejo-Garcia, J. R., Katsaros, D., Gimotty, P. A., Massobrio, M., Regnani, G., Makrigiannakis, A.** et al., Intratumoral T cells, recurrence, and survival in epithelial ovarian cancer. *N. Engl. J. Med.* 2003; **348**: 203–213.

2 **Geng, Y., Shao, Y., He, W., Hu, W., Xu, Y., Chen, J., Wu, C.** et al., Prognostic role of tumor-infiltrating lymphocytes in lung cancer: a meta-analysis. *Cell. Physiol. Biochem. Int. J. Exp. Cell. Physiol. Biochem. Pharmacol.* 2015; **37**: 1560–1571.

3 **Chen, M.-L., Pittet, M. J., Gorelik, L., Flavell, R. A., Weissleder, R., von Boehmer, H.** and **Khazaie, K.**, Regulatory T cells suppress tumor-specific CD8 T cell cytotoxicity through TGF-beta signals in vivo. *Proc. Natl. Acad. Sci. U. S. A.* 2005; **102**: 419–424.

4 **Rabinovich, G. A., Gabrilovich, D.** and **Sotomayor, E. M.**, Immunosuppressive strategies that are mediated by tumor cells. *Annu. Rev. Immunol.* 2007; **25**: 267–296.

5 **Rosenberg, S. A.**, **Restifo, N. P.**, **Yang, J. C.**, **Morgan, R. A.** and **Dudley, M. E.**, Adoptive cell transfer: a clinical path to effective cancer immunotherapy. *Nat. Rev. Cancer.* 2008; **8**: 299–308.

6 **Yossef, R.**, **Tran, E.**, **Deniger, D. C.**, **Gros, A.**, **Pasetto, A.**, **Parkhurst, M. R.**, **Gartner, J. J.** et al., Enhanced detection of neoantigen-reactive T cells targeting unique and shared oncogenes for personalized cancer immunotherapy. *JCI Insight*. 3.

7 **Parkhurst, M.**, **Gros, A.**, **Pasetto, A.**, **Prickett, T.**, **Crystal, J. S.**, **Robbins, P.** and **Rosenberg, S. A.**, Isolation of T-cell receptors specifically reactive with mutated tumor-associated antigens from tumor-infiltrating lymphocytes based on CD137 expression. *Clin Cancer Res*. 2017; **23**: 2491–2505.

8 **Leung, W.** and **Heslop, H. E.**, Adoptive immunotherapy with antigen-specific T cells expressing a native TCR. *Cancer Immunol. Res.* 2019; **7**: 528–533.

9 **Ramirez-Montagut, T.**, **Andrews, D. M.**, **Ihara, A.**, **Pervaiz, S.**, **Pandolfi, F.**, **Van Den Elsen, P. J.**, **Waitkus, R.** et al., Melanoma antigen recognition by tumour-infiltrating T lymphocytes (TIL): effect of differential expression of Melan-A/MART-1. *Clin. Exp. Immunol.* 2000; **119**: 11–18.

10 **Ye, Q.**, **Song, D.-G. G.**, **Poussin, M.**, **Yamamoto, T.**, **Best, A.**, **Li, C.**, **Coukos, G.** et al., CD137 accurately identifies and enriches for naturally occurring tumor-reactive T cells in tumor. *Clin Cancer Res*. 2014; **20**: 44–55.

11 **Gros, A.**, **Robbins, P. F.**, **Yao, X.**, **Li, Y. F.**, **Turcotte, S.**, **Tran, E.**, **Wunderlich, J. R.** et al., PD-1 identifies the patient-specific CD8$^+$ tumor-reactive repertoire infiltrating human tumors. *J Clin Invest*. 2014; **124**: 2246–2259.

12 **Djenidi, F.**, **Adam, J.**, **Goubar, A.**, **Durgeau, A.**, **Meurice, G.**, **de Montpréville, V.** and **Validire, P.** et al., CD8+CD103+ tumor–infiltrating lymphocytes are tumor-specific tissue-resident memory T Cells and a Prognostic factor for survival in lung cancer patients. *J. Immunol.* 2015; **194**: 3475–3486.

13 **Duhen, T.**, **Duhen, R.**, **Montler, R.**, **Moses, J.**, **Moudgil, T.**, **Miranda, de N. F.**, **Goodall, C. P.** et al., Co-expression of CD39 and CD103 identifies tumor-reactive CD8 T cells in human solid tumors. *Nat. Commun.* 2018; **9**: 2724.

14 **Kamada, T.**, **Togashi, Y.**, **Tay, C.**, **Ha, D.**, **Sasaki, A.**, **Nakamura, Y.**, **Sato, E.** et al., PD-1+ regulatory T cells amplified by PD-1 blockade promote hyperprogression of cancer. *Proc. Natl. Acad. Sci.* 2019; **116**: 9999–10008.

15 **Lowther D. E.**, **Goods B. A.**, **Lucca L. E.**, **Lerner B. A.**, **Raddassi K.**, **van Dijk D.**, **Hernandez A. L.** et al., PD-1 marks dysfunctional regulatory T cells in malignant gliomas. *JCI Insight*. 2016;**1**: (5): http://doi.org/10.1172/jci.insight.85935

16 **Amir, ED l-AD**, **Davis, K. L.**, **Tadmor, M. D.**, **Simonds, E. F.**, **Levine, J. H.**, **Bendall, S. C.**, **Shenfeld, D. K.** et al., viSNE enables visualization of high dimensional single-cell data and reveals phenotypic heterogeneity of leukemia. *Nat Biotechnol*. 2013; **31**: 545–552.

17 **Levine, J.**, **Simonds, E.**, **Bendall, S.** and **Davis, K.**, Data-driven phenotypic dissection of AML reveals progenitor-like cells that correlate with prognosis. *Cell* 2015;**162**: 184–197.

18 **Lee, Y.**, **Park, J.**, **Park, S.-H.** and **Shin, E.-C.**, CD39+CD8+ T cells exhibit a distinct phenotype among tumor-infiltrating tumor-antigenspecific CD8+ T cells. *J. Immunol.* 2019; **202**: 195.2–195.2.

19 **Pauken, K. E.** and **Wherry, E. J.**, Overcoming T cell exhaustion in infection and cancer. *Trends Immunol* 2015;**36**: 265–276.

20 **Kamphorst, A. O.**, **Wieland, A.**, **Nasti, T.**, **Yang, S.**, **Zhang, R.**, **Barber, D. L.**, **Konieczny, B. T.** et al., Rescue of exhausted CD8 T cells by PD-1–targeted therapies is CD28-dependent. *Science* 2017; **355**: 1423–1427.

21 **Wherry, E.** and **Kurachi, M.**, Molecular and cellular insights into T cell exhaustion. *Nat Rev Immunol*. 2015; **15**: 486–499.

22 **Seliktar-Ofir, S.**, **Merhavi-Shoham, E.**, **Itzhaki, O.**, **Yunger, S.**, **Markel, G.**, **Schachter, J.** and **Besser, M. J.**, Selection of shared and neoantigen-reactive T cells for adoptive cell therapy based on CD137 separation. *Front. Immunol.* 2017; **8**: 1211.

23 **Wolfl M.**, **Kuball J.**, **Ho W. Y.**, **Nguyen H.**, **Manley T. J.**, **Bleakley M.**, **Greenberg P. D.** Activation-induced expression of CD137 permits detection, isolation, and expansion of the full repertoire of CD8+ T cells responding to antigen without requiring knowledge of epitope specificities. *Blood*. 2007;**110**: (1):201–210.

24 **Borst, J.**, **Ahrends, T.**, **Bąbała, N.**, **Melief, C. J. M.** and **Kastenmüller, W.**, CD4 + T cell help in cancer immunology and immunotherapy. *Nat. Rev. Immunol.* 2018; **18**: 635–647.

25 **Friedman, K. M.**, **Prieto, P. A.**, **Devillier, L. E.**, **Gross, C. A.**, **Yang, J. C.**, **Wunderlich, J. R.**, **Rosenberg, S. A.** et al., Tumor-specific CD4+ melanoma tumor-infiltrating lymphocytes. *J. Immunother.* 2012; **35**: 400–408.

26 **Hunder, N. N.**, **Wallen, H.**, **Cao, J.**, **Hendricks, D. W.**, **Reilly, J. Z.**, **Rodmyre, R.**, **Jungbluth, A.** et al., Treatment of metastatic melanoma with autologous CD4+ T cells against NY-ESO-1. *N. Engl. J. Med.* 2008; **358**: 2698–2703.

27 **Tran E.**, **Turcotte S.**, **Gros A.**, **Robbins P. F.**, **Lu Y.-C.**, **Dudley M. E.**, **Wunderlich J. R.** et al., Cancer Immunotherapy Based on Mutation-Specific CD4+ T Cells in a Patient with Epithelial Cancer. *Science*. 2014;**344**: (6184):641–645.

28 **Simon, S.** and **Labarriere, N.**, PD-1 expression on tumor-specific T cells: Friend or foe for immunotherapy? *Oncoimmunology*. 2017; **7** (1): https://www.ncbi.nlm.nih.gov/pmc/articles/PMC5739549/ [Accessed April 7, 2020]. https://doi.org/10.1080/2162402X.2017.1364828.

29 **Thommen, D. S.** and **Schumacher, T. N.**, T Cell Dysfunction in Cancer. *Cancer Cell*. 2018; **33**: 547–562.

30 **Kamphorst, A. O.**, **Pillai, R. N.**, **Yang, S.**, **Nasti, T. H.**, **Akondy, R. S.**, **Wieland, A.**, **Sica, G. L.** et al., Proliferation of PD-1+ CD8 T cells in peripheral blood after PD-1–targeted therapy in lung cancer patients. *Proc. Natl. Acad. Sci.* 2017; **114**: 4993–4998.

31 **Longoria, T. C.** and **Eskander, R. N.**, Immune checkpoint inhibition: therapeutic implications in epithelial ovarian cancer. *Recent Patents Anticancer Drug Discov*. 2015; **10**: 133–144.

32 **Zamarin, D.**, **Burger, R. A.**, **Sill, M. W.**, **Powell, D. J.**, **Lankes, H. A.**, **Feldman, M. D.**, **Zivanovic, O.** et al., Randomized Phase II trial of nivolumab versus nivolumab and ipilimumab for recurrent or persistent ovarian cancer: an NRG oncology study. *J. Clin. Oncol.* 2020; **38**: 1814–1823.

33 **Segal, N. H.**, **Logan, T. F.**, **Hodi, F. S.**, **McDermott, D.**, **Melero, I.**, **Hamid, O.**, **Schmidt, H.** et al., Results from an Integrated Safety Analysis of Urelumab, an Agonist Anti-CD137 Monoclonal Antibody. *Clin. Cancer Res. Off. J. Am. Assoc. Cancer Res.* 2017; **23**: 1929–1936.

34 **Segal, N. H.**, **He, A. R.**, **Doi, T.**, **Levy, R.**, **Bhatia, S.**, **Pishvaian, M. J.**, **Cesari, R.** et al., Phase I study of single-agent Utomilumab (PF-05082566), a 4-1BB/CD137 agonist, in patients with advanced cancer. *Clin. Cancer Res. Off. J. Am. Assoc. Cancer Res.* 2018; **24**: 1816–1823.

35 **Gaspar, M.**, **Pravin, J.**, **Rodrigues, L.**, **Uhlenbroich, S.**, **Everett, K. L.**, **Wollerton, F.**, **Morrow, M.** et al., CD137/OX40 bispecific antibody induces potent antitumor activity that is dependent on target coengagement. *Cancer Immunol. Res.* 2020; **8**: 781–793.

36 **Lakins, M. A.**, **Koers, A.**, **Giambalvo, R.**, **Munoz-Olaya, J.**, **Hughes, R.**, **Goodman, E.**, **Marshall, S.** et al., FS222, a CD137/PD-L1 tetravalent bispecific antibody, exhibits low toxicity and antitumor activity in colorectal cancer models. *Clin. Cancer Res.* 2020; **26**: 4154–4167.

37 **Chacon, J. A.**, **Wu, R. C.**, **Sukhumalchandra, P.**, **Molldrem, J. J.**, **Sarnaik, A.**, **Pilon-Thomas, S.**, **Weber, J.** et al., Co-stimulation through 4-1BB/CD137 improves the expansion and function of CD8(+) melanoma tumor-infiltrating lymphocytes for adoptive T-cell therapy. *PloS One*. 2013; **8**: e60031.

38 **Bengsch, B.**, **Ohtani, T.**, **Khan, O.**, **Setty, M.**, **Manne, S.**, **O'Brien, S.**, **Gherardini, P. F.** et al., Epigenomic-guided mass cytometry profiling reveals disease-specific features of exhausted CD8 T cells. *Immunity*. 2018; **48**: 1029–1045.e5.

39 **Cossarizza, A.**, **Chang, H.-D.**, **Radbruch, A.**, **Acs, A.**, **Adam, D.**, **Adam-Klages, S.**, **Agace, W. W.** et al., Guidelines for the use of flow cytometry and cell sorting in immunological studies (second edition). *Eur. J. Immunol.* 2019; **49**: 1457–1973.

Abbreviations: **CI:** confidence interval · **MC:** metacluster · **TILs:** tumor-infiltrating lymphocytes

Full correspondence: Daniel J. Powell Jr., PhD, University of Pennsylvania, 3400 Civic Center Blvd., Bldg. 421, TRC Rm 8-103, Philadelphia, PA 19104-5156, USA.
e-mail: poda@pennmedicine.upenn.edu

Received: 29/4/2021
Revised: 7/7/2021
Accepted: 10/9/2021
Accepted article online: 10/9/2021

Clinical & Translational Immunology

Australian and New Zealand Society for Immunology Inc.

Clinical & Translational Immunology 2020; e1132. doi: 10.1002/cti2.e1132
www.wileyonlinelibrary.com/journal/cti

ORIGINAL ARTICLE

Identification of the immune checkpoint signature of multiple myeloma using mass cytometry-based single-cell analysis

Jinheng Wang[1], Yongjiang Zheng[2], Chenggong Tu[1], Hui Zhang[1], Karin Vanderkerken[3], Eline Menu[3] & Jinbao Liu[1]

[1]Affiliated Cancer Hospital & Institute of Guangzhou Medical University, Guangzhou Municipal and Guangdong Provincial Key Laboratory of Protein Modification and Degradation, State Key Laboratory of Respiratory Disease, School of Basic Medical Sciences, Guangzhou Medical University, Guangzhou, China
[2]Department of Hematology, The Third Affiliated Hospital of Sun Yat-Sen University, Guangzhou, China
[3]Department of Hematology and Immunology, Myeloma Center Brussels, Vrije Universiteit Brussel, Brussels, Belgium

Correspondence
J Wang or J Liu, Affiliated Cancer Hospital & Institute of Guangzhou Medical University, Guangzhou Municipal and Guangdong Provincial Key Laboratory of Protein Modification and Degradation, State Key Laboratory of Respiratory Disease, School of Basic Medical Sciences, Guangzhou Medical University, 510095 Guangzhou, China.
E-mails: wangjh89@gzhmu.edu.cn (JW); jliu@gzhmu.edu.cn (JL)

Received 18 January 2020;
Revised 5 April 2020;
Accepted 6 April 2020

doi: 10.1002/cti2.e1132

Clinical & Translational Immunology
2020; **9**: e1132

Abstract

Objectives. New targets or strategies are needed to increase the success of immune checkpoint-based immunotherapy for multiple myeloma (MM). However, immune checkpoint signals in MM microenvironment have not been fully elucidated. Here, we aimed to have a broad overview of the different immune subsets and their immune checkpoint status, within the MM microenvironment, and to provide novel immunotherapeutic targets to treat MM patients. **Methods.** We performed immune checkpoint profiling of bone marrow (BM) samples from MM patients and healthy controls using mass cytometry. With high-dimensional single-cell analysis of 30 immune proteins containing 10 pairs of immune checkpoint axes in 0.55 million of BM cells, an immune landscape of MM was mapped. **Results.** We identified an abnormality of immune cell composition by demonstrating a significant increase in activated CD4 T, CD8 T, $CD8^+$ natural killer T-like and NK cells in MM BM. Our data suggest a correlation between MM cells and immune checkpoint phenotypes and expand the view of MM immune signatures. Specifically, several critical immune checkpoints, such as programmed cell death 1 (PD-1)/PD ligand 2, galectin-9/T-cell immunoglobulin mucin-3, and inducible T-cell costimulator (ICOS)/ICOS ligand, on both MM and immune effector cells and a number of activated $PD\text{-}1^+$ CD8 T cells lacking CD28 were distinguished in MM patients. **Conclusion.** A clear interaction between MM cells and the surrounding immune cells was established, leading to immune checkpoint dysregulation. The analysis of the immune landscape enhances our understanding of the MM immunological milieu and proposes novel targets for improving immune checkpoint blockade-based MM immunotherapy.

Keywords: immune checkpoint, immunotherapy, mass cytometry, multiple myeloma, single-cell analysis

INTRODUCTION

Multiple myeloma (MM) is a cancer of clonal plasma cells preferentially localised in the bone marrow (BM). The proliferation of MM cells, together with an MM cell-changed BM microenvironment, suppresses local and systemic immunity, eventually leading to an escape from immune surveillance.[1] Mechanisms involved in MM-induced immunosuppression include dysfunction of T and natural killer (NK) cells,[2] disruption of antigen presentation processes,[3] activation of immunosuppressive cells,[3,4] upregulation of inhibitory immune checkpoints[5,6] and release of immunosuppressive mediators.[7] Comprehensively uncovering the immune status in the BM microenvironment of MM patients will largely facilitate the understanding of the ongoing process of immunosuppression in MM progression and therefore promote the development of novel immunotherapeutic strategies.

Immunotherapy that involves stimulating and provoking a patients' own immune system against cancer has proven to be very encouraging as dramatic and durable anticancer responses are well documented in many cancer types.[8,9] Blocking inhibitory immune checkpoints on immune effector cells results in the reactivation of anticancer immunity.[10] Immune checkpoints contain a series of costimulatory and coinhibitory receptors or ligands expressed on T, NK or antigen-presenting cells and mainly function as switches of immune activation or suppression.[11] Under normal physiological conditions, immune checkpoints maintain self-tolerance and immune homeostasis, whereas malignant cells take advantage of these molecules to achieve immune evasion.[12] The most prominent immune checkpoint blocking strategies, such as targeting cytotoxic T lymphocyte-associated protein 4 (CTLA-4) and blocking the interaction between programmed cell death 1 (PD-1) and PD ligand 1 (PD-L1), are able to enlist and strengthen the immune system to attack cancer cells and have achieved clinical success in several cancer types, even in metastatic and chemoresistant cancer.[13,14] However, these immunotherapies are unable to control malignancy in a significant proportion of patients, largely because of the fact that inhibitory signals inducing the exhaustion and dysfunction of anticancer immune cells are not fully and sustainably blocked.[10,15] Indeed, as reported by a phase 1b clinical study, PD-1/PD-L1 axis-based immune checkpoint blockade failed to control MM progression,[16,17] suggesting that this checkpoint may not be the major mediator of failing anti-MM immunity. Besides PD-1 and CTLA-4, many other immune checkpoints have been discovered and are used for improved immune checkpoint-based immunotherapy.[18] However, immune checkpoint signals in the MM microenvironment have not been fully elucidated. The analysis of immune checkpoints will help us to better understand the mechanism of immune evasion of MM cells and would allow the development of potent strategies, focused on the checkpoint signals that are actually used by MM cells to evade the immune system.

The most commonly used technique for immune phenotyping, flow cytometry, suffers from the limited detection channels (generally < 15) and cumbersome compensation because of spectral overlap, making it difficult to simultaneously detect all immune checkpoint phenotypes. As a cutting-edge single-cell technology, current mass cytometry merging mass spectrometry with flow cytometry permits up to 50 metal isotope tags to be measured simultaneously on a single cell with minimal/no compensation.[19,20] Such high multiparametric detection provides an unprecedented opportunity for deep phenotyping of the tumor immune microenvironment at the single-cell level. For now, this powerful innovation has offered insights into the heterogeneity and complexity of biology and has been used to understand the complex processes in cellular development,[21] differentiation[22] and tumor immunology,[23-25] and to explore the potential immunotherapeutic targets.[23]

In this study, 0.55 million BM cells from 10 MM patients and five healthy donors (HD) were analysed using mass cytometry to elucidate the phenotypic diversity and immune checkpoint signature in MM BM ecosystems. Our data reveal vast phenotypic heterogeneity among both malignant and immune cells, identify an abnormality of immune cell composition and

suggest links between MM cells and immune checkpoint phenotypes. Through in-depth analyses of 10 pairs of immune checkpoint axes in 12 identified immune cell types at the single-cell level, a picture of the immune checkpoint interaction network that exists in the MM BM microenvironment of these patients was established. Several critical immune checkpoints were identified in the MM BM and may serve as novel targets for developing more potent and efficacious checkpoint blockade-based MM immunotherapeutic strategies.

RESULTS

In-depth immune checkpoint phenotyping of MM cells using mass cytometry

To map the immune checkpoint signatures in the BM microenvironment of MM patients, we implemented a clinical high-dimensional single-cell profiling study of freshly collected BM from newly diagnosed and untreated MM patients using mass cytometry. Ten MM BM samples and five healthy BM samples were included for a large-scale mass cytometry analysis (Figure 1a). We stained prebarcoded BM cells with 30 antibodies to simultaneously determine the expression of 30 markers used to define cell populations and immune checkpoint phenotypes at the single-cell level (Figure 1b). As the loss of CD138 caused by the cold storage and processing frequently occurs,[26,27] cells with a $CD38^{++}CD45^{-/dim}$ phenotype were defined as malignant MM cells (Figure 1c). To comprehensively view the immune checkpoint profile of MM cells from all patients, we generated a single-cell viSNE map to visualise high-dimensional data in two dimensions.[28] This analysis demonstrated a clear heterogeneity of MM cells among patients (Figure 1c). On the viSNE map, clear expression of multiple immunoregulatory proteins, including CTLA-4, CD56, inducible T-cell costimulator (ICOS), galectin-9 (GAL9), CD86, ICOS ligand (ICOSL), OX40 and HLA-DR, was observed in different MM cell clusters (Figure 1d). Large proportion of $CD56^+$ MM cells were detected in 8 of 10 patients, and GAL9 and ICOSL expressions were widely found in MM cells from all patients (Figure 1e), whereas high PD-L1 or PD-L2 expressions were only observed in few MM cells (Supplementary figure 1a). These 10 BM samples with 7–41% MM cells displayed diverse phenotypes in the expression of immune checkpoint proteins. Important immune checkpoint ligands, including GAL9, ICOSL, HLA-DR, CD86, PD-L2, and 4-1BBL, were expressed by more than 10% of MM cells in average (Figure 1f and Supplementary figure 1b). We next performed correlation analyses to systematically quantify the underlying relationships between overall MM burden and MM cells with different immune checkpoint phenotypes. Multiple robust either positive or negative relationships were identified (Figure 1g). Among the positive relationships, GAL9 expression was most strongly related to MM burden. Also, the expression of different immune checkpoint ligands correlated significantly with each other, such as PD-L2 expression, which correlated with 4-1BBL and CD56 expressions with ICOSL (Supplementary figure 1c).

Immune cell signature in MM BM microenvironment

Next, we used viSNE to visualise the distribution of the immune cells in the HD and MM BM samples (equal cell number from each individual) and demonstrated a large heterogeneity among MM patients and healthy controls (Figure 2a). According to the standardised immunophenotyping for human immunology[29] and the expression of 15 surface markers in HD and MM BM $CD45^+$ cells displayed on the viSNE map (Figure 2b), 12 major immune cell populations were gated on the map (Figure 2c). Natural killer T (NKT) cells are identified with a $CD3^+CD56^+$ phenotype in many studies.[30-32] However, only a small proportion of $CD3^+CD56^+$ are CD1d-restricted, which is a unique feature of invariant NKT (iNKT) cells. Thus, this population is frequently referred to as 'NKT-like'.[32] Here, we gated two $CD3^+CD56^+$ cell subsets, namely NKT-like and $CD8^+$ NKT-like cells, after excluding CD4, CD8 and double-negative (DN) T cells from all $CD3^+$ cells. As shown by heatmap, the expression of surface markers in each population was identical to the phenotype of indicated immune lineages (Figure 2d). After gating on viSNE map, the immune lineages in individual samples were analysed (Figure 2e), which revealed a heterogeneity across HD or MM patients. Although wide variation existed in the frequencies of each immune cell type in different individuals, several significant changes between HD and MM patients were detected. In the BM of

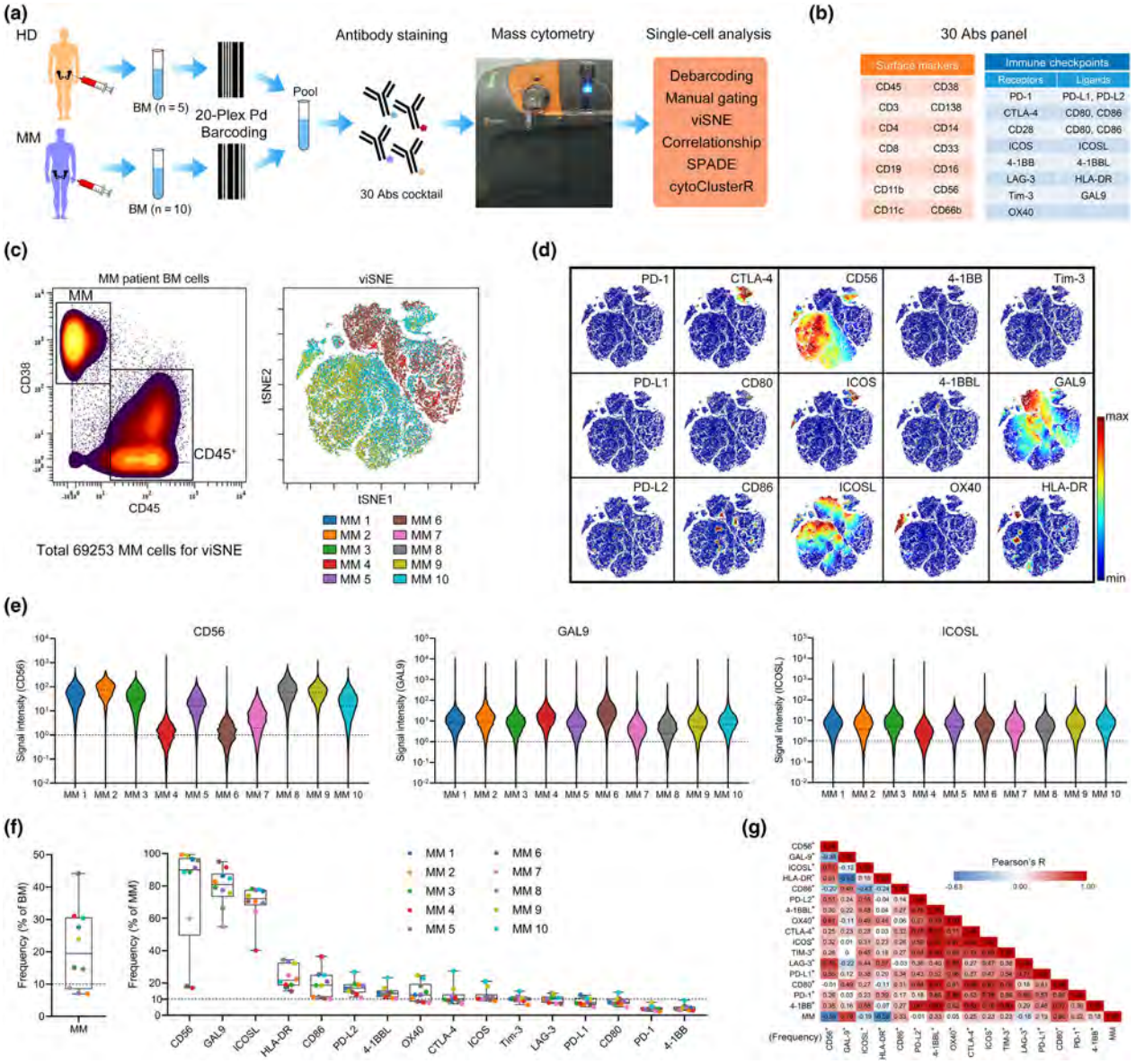

Figure 1. Characterisation of immune checkpoints of MM cells. **(a)** The experimental workflow used in this study. **(b)** Markers used to define cell populations and immune checkpoint phenotypes. **(c)** Gating of MM and CD45$^+$ cells (left panel). viSNE map showing 69 253 MM cells from the BM of MM (n = 10) patients coloured by individual. **(d)** Cells coloured by normalised expression of indicated immune checkpoint markers on the viSNE map. **(e)** A violin plot showing the signal intensity of CD56, GAL9 and ICOSL in MM cells of individual patients. **(f)** Dot plots showing the frequency of MM cells among BM cells (left panel) and indicated markers' positive cells among MM cells for each MM BM sample (right panel). Dots are coloured by individual. **(g)** A heatmap showing the Pearson correlation coefficients for relationships between the frequencies of indicated cell populations. Abs, antibodies; BM, bone marrow; HD, healthy donor; MM, multiple myeloma. MM, n = 10.

MM patients, the proportion of CD4 T, CD8 T, CD16$^+$ NK and CD8$^+$ NKT-like cells in CD45$^+$ immune cells was significantly increased along with the significant decrease in granulocytes, as compared to those in HD BM cells (Figure 2f). The average percentage of CD8 T cells increased from 7.77% in HD to 14.82% in MM and that of CD4 T cells rose from 9.49% to 15.36%. Importantly, CD8$^+$ NKT-like cells only accounted for 0.92% of HD BM immune cells in average, whereas it increased to 4.86% in MM patients (Figure 2f). iNKT cells have been shown to be associated with MM and are important for antitumor immunity.[33] We also examined the proportion of iNKT cells

with the T-cell receptor Va24Ja18 antibody. We found that they constitute a minor fraction of BM T cells and there is no significant difference in their percentages between HD and MM patients (Supplementary figure 2a). Moreover, the MM burden was positively correlated with the frequency of CD8 T cells in MM patients and negatively correlated with the frequency of $CD16^+$ NK cells with a trend close to significance (Supplementary figure 2b).

The immune checkpoint landscape of MM BM T cells

To characterise the immune checkpoint phenotype in MM BM immune cells, we assessed the expression of all detected immune checkpoint proteins in $CD45^+$ cells on the viSNE map. ICOSL, CD28, CD86 and GAL9 expressions were clearly observed in several cell subsets (Figure 3a). In contrast, no clear accumulative expression of the other immune checkpoints appeared on the viSNE map. However, the normalised mean expression of these proteins was distinct among the 12 gated immune cell populations clustered from viSNE map (Figure 3b), suggesting the presence of heterogeneous subgroups with high immune checkpoint expression in these populations. Thus, we first compared the frequencies of immune checkpoint-positive cells in all cell populations of HD BM with those of MM patients (Figure 3c and Supplementary figure 3). In BM CD4 T-cell subsets, the proportions of PD-$L1^+$, PD-$L2^+$, CTLA-4^+, 4-$1BB^+$ and 4-$1BBL^+$ cells were consistently $< 20\%$, but were significantly higher in MM patients than those in HD. The percentages of $CD28^+$ and $ICOS^+$ CD4 T cells were also significantly higher in MM patients than in HD (Figure 3d and Supplementary figure 4a). Moreover, PD-1^+, PD-$L2^+$, $ICOS^+$, T-cell immunoglobulin mucin-3 (Tim-$3)^+$ and lymphocyte activating 3 (LAG-$3)^+$ CD8 T cells were significantly increased in the BM of MM patients (Figure 3e and Supplementary figure 4b). Additionally, several immune checkpoints were also significantly increased in other T-cell types, such as the number of PD-$L2^+$ cells in $CD8^+$ NKT-like cells; PD-$L2^+$, $OX40^+$ and Tim-3^+ cells in NKT-like cells; and CTLA-4^+ and the number of Tim-3^+ cells in DNT cells. By contrast, some decreases in the number of immune checkpoint-positive cells were observed as well, such as $CD28^+$ and $ICOSL^+$ cells in $CD8^+$ NKT-like cells (Figure 3f and Supplementary figure 4c–e). We also compared the intensity of the expression of these checkpoints in the corresponding positive cells. The expression of CD28 was significantly stronger in $CD28^+$ CD4 T, CD8 T and DNT cells of MM patients. In PD-1^+ $CD8^+$ NKT-like and CD8 T cells, the PD-1 expression was also significantly increased in MM patients. Many significant changes in the expression of immune checkpoints in CD4 T, CD8 T, NKT-like or $CD8^+$ NKT-like cells were discovered (Figure 3g).

The immune checkpoint atlas of MM BM non-T cells

The frequencies of PD-1^+, PD-$L2^+$, CTLA-4^+, $ICOS^+$, 4-$1BBL^+$, $OX40^+$ and Tim-3^+ cells in granulocytes were significantly increased in MM patients, although most of them were $< 10\%$ (Figure 4a and b). Granulocytes accounted for the major provider of ICOSL as more than 85% of them express ICOSL in both HD and MM patients. The frequencies of PD-1^+ and 4-$1BB^+$ cells in undefined (the rest of) $CD45^+$, Tim-3^+ cells in DC, LAG-3^+ cells in $CD16^-$ NK cells, and PD-$L2^+$ cells in $CD16^+$ NK cells were also significantly increased in MM patients (Figure 4c–e and Supplementary figure 5a–c). Although significant differences in the percentages of immune checkpoint-positive cells were not detected in many cell types, the intensity of their expression in several immune cell populations was significantly altered in MM patients (Figure 4f and g).

Activation signature of T and NK cells in MM BM microenvironment

CD8 T and NK cells are major contributors to anticancer immunity and the main targets to be reinvigorated by immune checkpoint blockade-based immunotherapy. HLA-DR appears at the late stages of activated T and NK cells and has been widely used as an activation marker.[34-36] CD38 and HLA-DR are also primarily regarded as biomarkers for identifying activated T cells.[29,37] Here, the activation status of T- and NK cell subsets was systematically quantified using these markers. In the MM BM cells, significant increase in activated ($HLA\text{-}DR^+CD38^+$) cells was found in CD4 T, CD8 T, NKT-like and $CD8^+$ NKT-like cells (Figure 5a). Specifically, the average frequency of activated cells in CD8 T cells was dramatically elevated from 11.66% in HD to 40.94% in MM patients (Figure 5b). Similarly, activated NK cells in

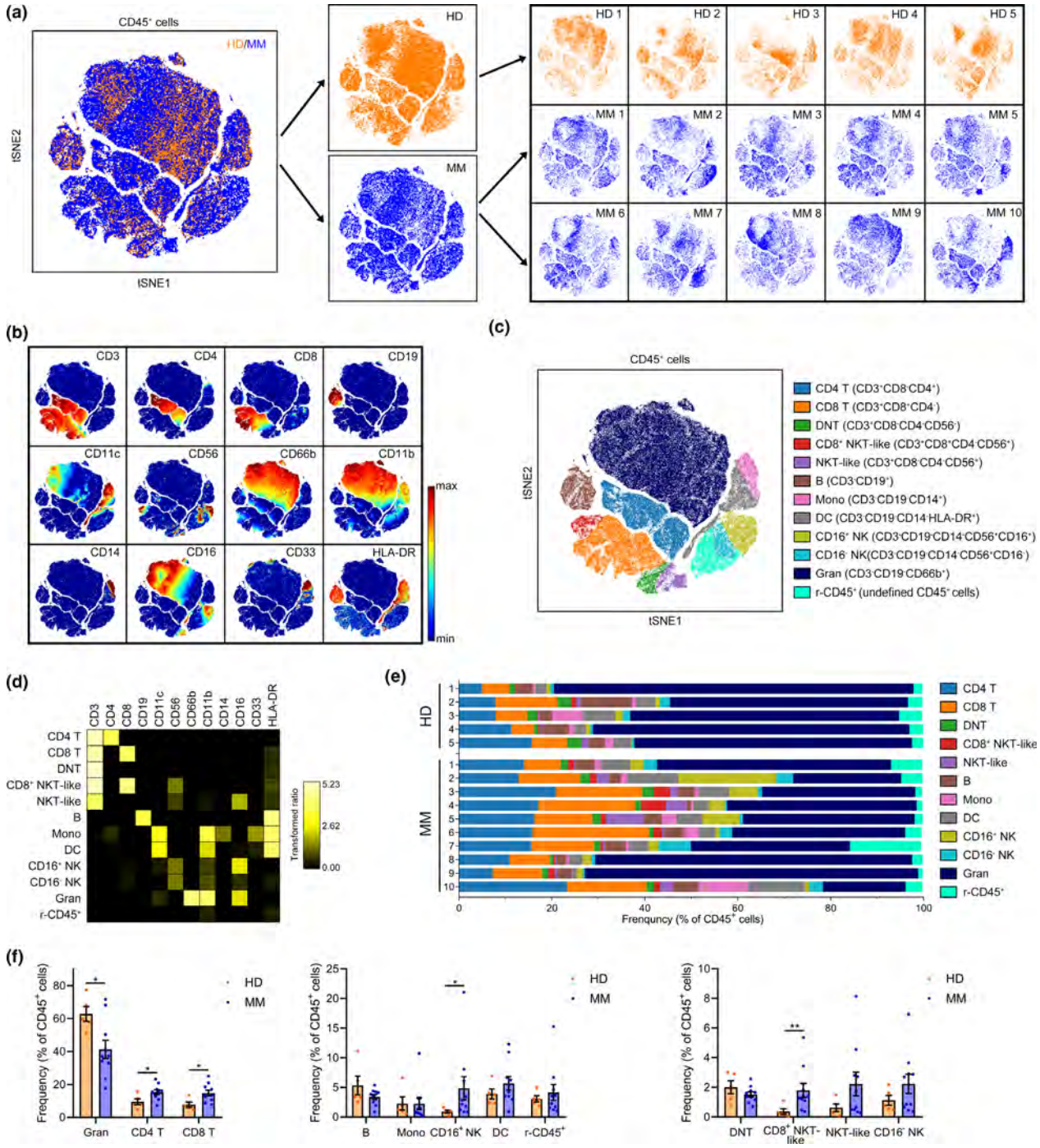

Figure 2. Immune cell population changes in the BM of MM patients. **(a)** A viSNE map displaying gated CD45$^+$ BM cells of five HD and 10 MM patients coloured by groups. **(b)** A viSNE map coloured by the normalised expression of indicated markers. **(c)** A viSNE map coloured by 12 main cell populations after clustering. **(d)** A heatmap showing the normalised median expression of 12 indicated markers in 12 cell populations. **(e)** Frequencies of 12 cell populations in CD45$^+$ cells for each BM sample. Cell types are indicated by colour. **(f)** Bar plots showing the frequencies of indicated populations in BM CD45$^+$ cells of HD and MM patients. HD, $n = 5$; MM, $n = 10$. DC, dendritic cells; DNT, double-negative T; Gran, granulocytes; Mono, monocytes; NK, natural killer; r-CD45$^+$, the rest of CD45$^+$. *$P < 0.05$ and **$P < 0.01$.

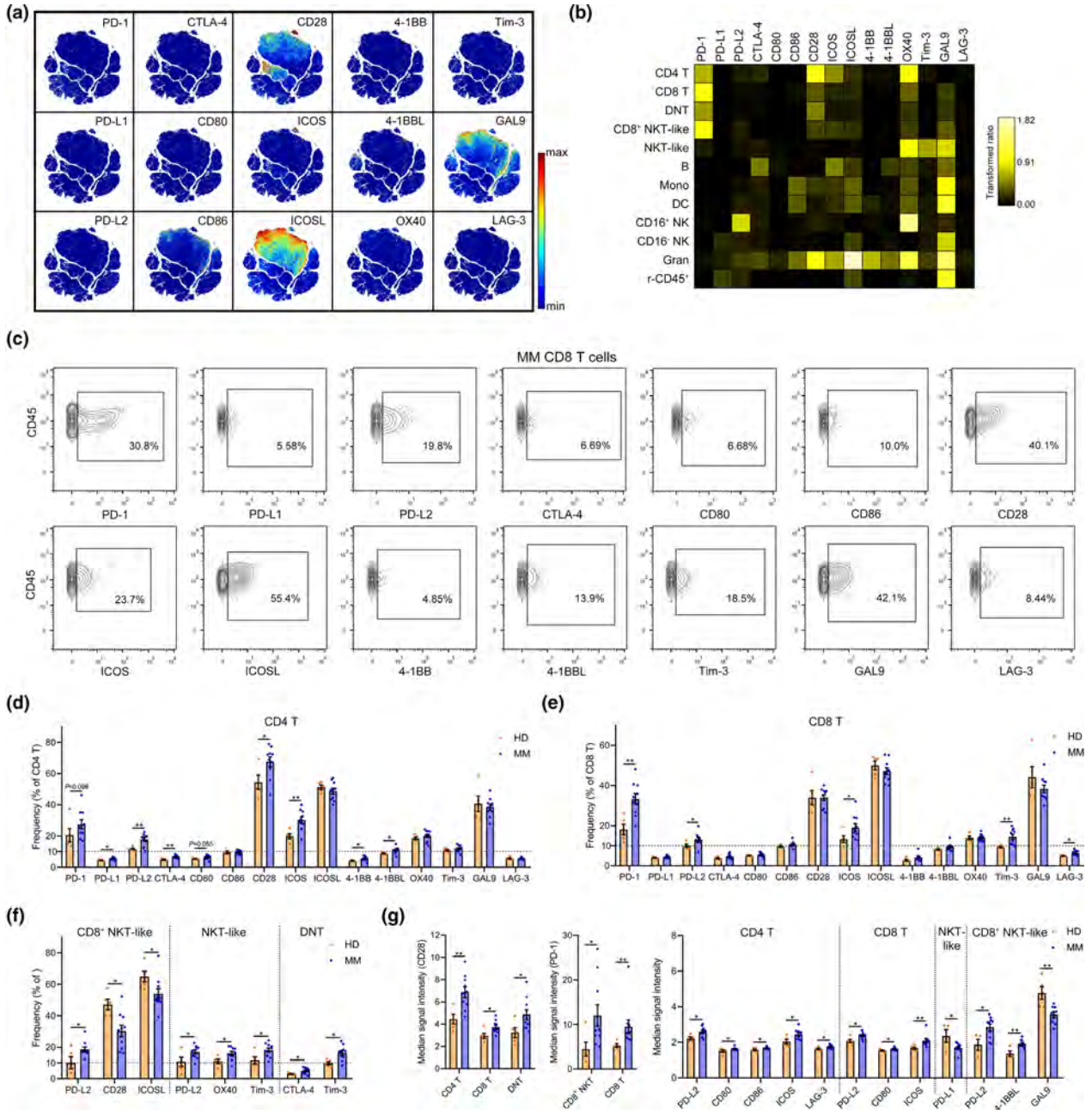

Figure 3. Immune checkpoint changes in MM BM T cells. **(a)** A viSNE map coloured by the normalised expression of 15 immune checkpoint markers. **(b)** Heatmaps showing the normalised mean expression of 15 immune checkpoint markers in all cell populations (normalised to the column's minimum). **(c)** Contour plots showing the gating strategy and the expression of indicated checkpoint molecules in CD8 T cells of one representative MM patient. **(d, e)** Bar plots showing the frequencies of indicated markers' positive cells in BM **(d),** CD4 and **(e)** CD8 T cells of HD and MM patients. **(f)** Bar plots showing the significantly changed frequencies of indicated markers' positive cells in $CD8^+$ NKT-like, NKT-like and DNT cells of HD and MM patients. **(g)** Bar plots showing the significantly changed median signal intensity of indicated markers in corresponding positive T-cell subsets of HD and MM patients. HD, $n = 5$; MM, $n = 10$. $*P < 0.05$ and $**P < 0.01$.

the BM were also increased in MM patients (Figure 5c). A number of strong positive or negative correlations were revealed between the frequencies of activated T- or NK cell subsets and indicated immune checkpoint protein-expressing MM cells in all patients (Supplementary figure 6a). In activated ($HLA\text{-}DR^+$) T- or NK cell subsets, several changes in immune checkpoint phenotype

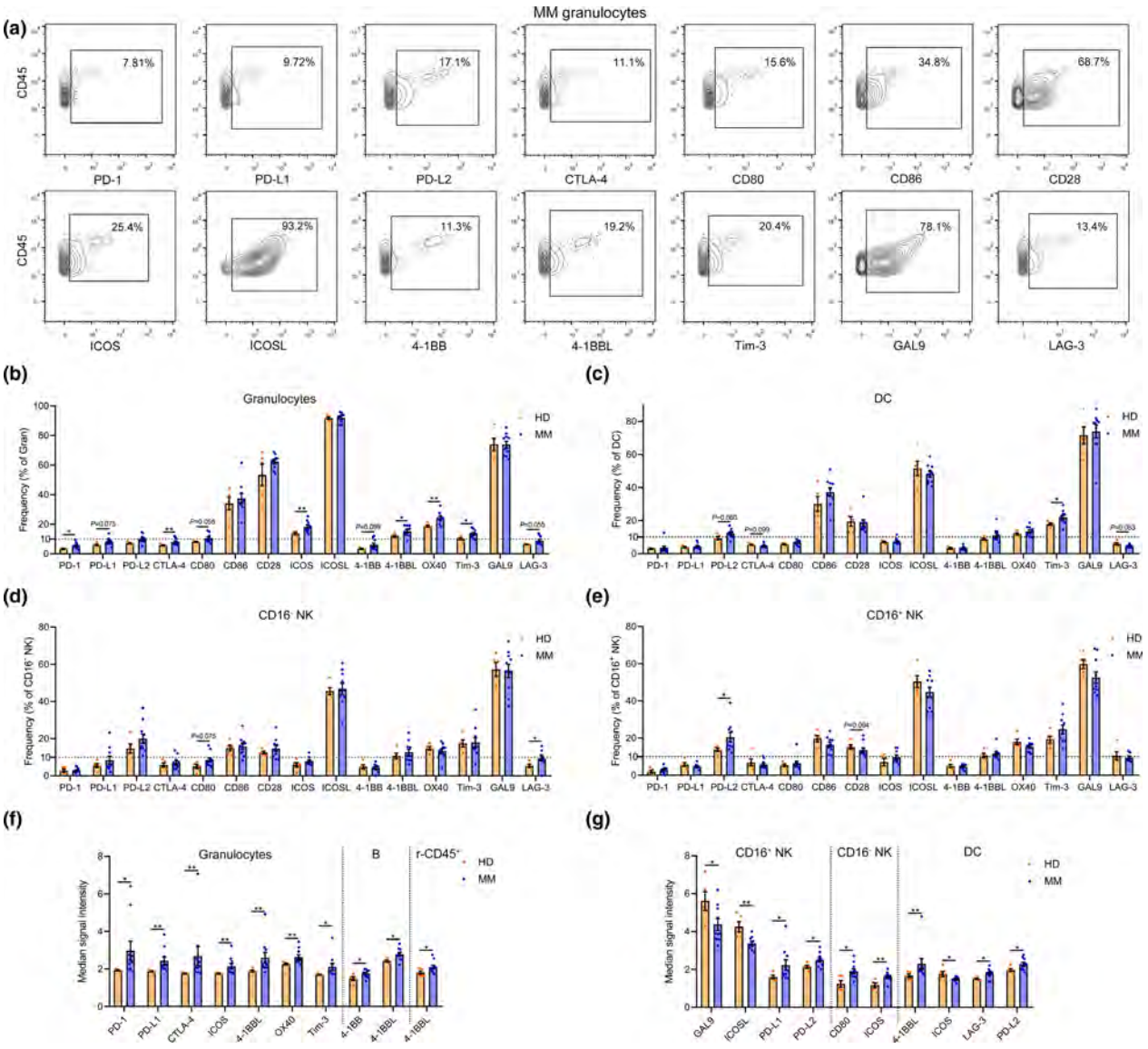

Figure 4. Immune checkpoint changes in MM BM non-T immune cells. **(a)** Contour plots showing the gating strategy and the expression of indicated checkpoint molecules in granulocytes of one representative MM patient. **(b–e)** Bar plots showing the frequencies of indicated markers' positive cells in BM **(b)** granulocytes, **(c)** DC, **(d)** $CD16^-$ NK and **(e)** $CD16^+$ NK cells of HD and MM patients. **(f, g)** Bar plots showing the significantly changed median signal intensity of indicated markers in corresponding positive **(f)** granulocytes, B and r-$CD45^+$, and **(g)** DC, $CD16^+$ and $CD16^-$ NK cells of HD and MM patients. HD, $n = 5$; MM, $n = 10$. $^*P < 0.05$ and $^{**}P < 0.01$.

appeared in MM patients compared with those in HD (Figure 5d–f), changes were also found in inactivated (HLA-DR^-) T cells (Supplementary figure 6b and c). In addition, the expression of important immune checkpoints, including PD-1, CD28 and ICOS, was changed in activated (HLA-DR^+) CD4 and CD8 T cells (Figure 5g). Coexpression of CD39 and CD103 has been used to identify the tumor-specific $CD8^+$ T cells in human tumors.[38,39] Here, we introduced these two markers to examine whether increased CD8 T cells in the BM are specific against MM cells. However, above 90% of CD8 T or activated CD8 T cells are $CD39^-$ and $CD103^-$negative (Supplementary figure 6d), suggesting that bystander T cells instead of tumor-specific CD8 T cells are abundant in MM BM. To identify the immune checkpoint phenotypes in activated cells, we compared the frequencies of the immune marker-expressing cells in inactivated with

activated T or NK cells. Activated CD4 T cells expressed more Tim-3, PD-1, GAL9, CTLA-4, ICOS and 4-1BB than inactivated cells in both HD and MM patients. More activated CD8 T cells expressed PD-1, GAL9, ICOS, CTLA-4 and Tim-3 (Figure 5h). Moreover, compared with inactivated cells, more activated NKT-like cells expressed CTLA-4; more activated $CD16^{-}$ NK cells expressed CTLA-4, Tim-3 and GAL9; and more activated $CD16^{+}$ NK cells expressed 4-1BB (Supplementary figure 6e).

In-depth and systematic analyses of the immune checkpoint profile of MM BM T cells

As T cells are the primary anticancer contributor, we next systematically analysed the immune checkpoint phenotype of all possible exclusively and significantly changed T-cell clusters. From the viSNE containing all CD3 T cells, we observed a huge heterogeneity of the T-cell compartments, regarding the expression of immune modulatory proteins (Supplementary figure 7a). We next introduced spanning-tree progression analysis of density-normalised events (SPADE) analysis[40] to divide all T cells into 100 minor clusters (nodes) containing cells with similar phenotypes. On the SPADE tree, we were able to characterise the immune checkpoint phenotype of each cluster and clearly observe the differences in these clusters in each individual (Figure 6a and Supplementary figure 7b). Using cytoClusterR, the heterogeneity of immune checkpoint receptor signatures across 100 T-cell clusters from all 10 MM patients or five HD was obviously revealed on heatmaps (Figure 6b). Clusters 82, 92, 89, 68 and 42 were specifically presented in MM patients. In each cluster, different median expressions of immune checkpoint protein are summarised (Figure 6b). Among these 100 T-cell clusters, the frequencies of 42 clusters in MM patients were significantly different from those in HD (Figure 6c and Supplementary figure 7c). Twenty-eight clusters displayed an activated phenotype ($HLA\text{-}DR^{+}$) and were significantly increased in MM patients (Figure 6c), indicating that these T-cell clusters may play pivotal roles in remodelling the MM BM immune microenvironment. Among these 28 clusters, eight CD8 T-cell clusters, including clusters 37, 32, 39, 21, 73, 89, 68 and 42, were activated and $PD\text{-}1^{+}$, whereas all these clusters were deficient in CD28 expression, except cluster 89 (Figure 6d). In addition, MM burden was significantly correlated with the frequencies of clusters 32, 48, 76, 82, 92 and 96 in MM patients (Figure 6e), indicating that the changes in these T-cell clusters are MM cell-dependent.

Immune checkpoint network in the MM BM microenvironment

We summarised the top 3 cell types providing immune checkpoint-related receptors or ligands in MM patients (Figure 7a). Based on these main providers and the expression of immune checkpoint molecules in MM cells, a list and a network describing the interactions among MM and immune cells through immune checkpoints were established (Figure 7b and c). Considering the large heterogeneity among MM patients, we also built an immune checkpoint network for each MM patient (Supplementary figure 8).

DISCUSSION

The BM contains a complex environment and is filled with numerous kinds of immunoregulatory signal from both immune and non-immune cells. In the MM BM microenvironment, non-immune cells, such as stromal cells, regulate immunosuppression through cell-to-cell contact and release extracellular vesicles and thus favor immune evasion of MM cells.[41] Immune checkpoints expressed on immune cells maintain the immune homeostasis, whereas MM cells enhance the suppression signal to escape from immune surveillance. Immune checkpoint blockade can break this malignant cell-induced inhibitory communication and thus lead to the reinvigoration of anticancer immunity. Success of immune checkpoint therapies largely relies on the targets responsible for cancer-induced immune suppression. To improve our understanding of the immune signature and immune checkpoint abnormalities in the MM BM microenvironment, we performed a high-dimensional single-cell analysis of the immune checkpoint molecules in healthy and MM BM samples. This high-quality data set identifies an unambiguous immune checkpoint network in the MM immunologic milieu of these patients (Figure 7b and c) and establishes a powerful new level of insights into MM checkpoint immunotherapy.

Mass cytometry has been recently used to identify T-cell heterogeneity and early alterations

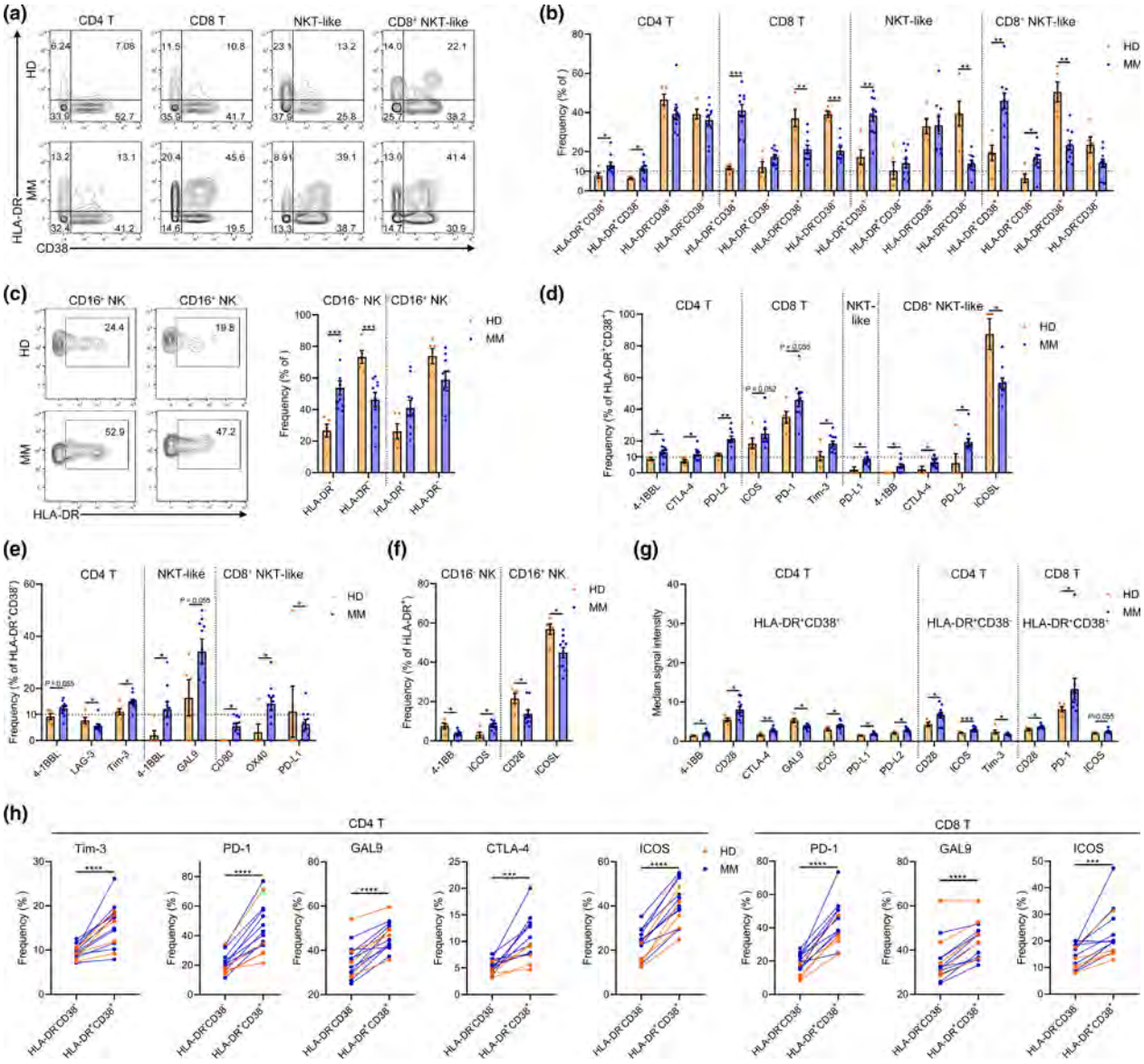

Figure 5. Changes in T-cell activation status in the BM of MM patients. **(a)** Contour plots showing the expression of CD38 and HLA-DR in 4 T-cell subsets of one representative HD or MM patient. **(b)** Bar plots showing the frequencies of indicated cell clusters in BM T-cell subsets of HD and MM patients. **(c)** Contour plots showing the expression of HLA-DR in NK cell subsets of one representative HD or MM patient (left panel). Bar plots showing the frequencies of indicated clusters in BM NK cell subsets of HD and MM patients (right panel). **(d)** Bar plots showing the significantly changed frequencies of indicated markers' positive cells in HLA-DR$^+$CD38$^+$ T-cell subsets of HD and MM patients. **(e)** Bar plots showing the significantly changed frequencies of indicated markers' positive cells in HLA-DR$^+$CD38$^-$ T-cell subsets of HD and MM patients. **(f)** Bar plots showing the significantly changed frequencies of indicated markers' positive cells in HLA-DR$^+$ NK cell subsets of HD and MM patients. **(g)** Bar plots showing the significantly changed median signal intensity of indicated markers in corresponding positive HLA-DR$^+$CD38$^+$ CD4 T, HLA-DR$^+$CD38$^-$ CD4 T and HLA-DR$^+$CD38$^+$ CD8 T cells of HD and MM patients. **(h)** Dot plots showing the significantly changed frequencies of the indicated markers' positive cells in HLA-DR$^-$CD38$^-$ and HLA-DR$^+$CD38$^+$ T-cell subsets of the individual. HD, $n = 5$; MM, $n = 10$. *$P < 0.05$, **$P < 0.01$, ***$P < 0.001$ and ****$P < 0.0001$.

in resident T cells, and innate and myeloid cells in the BM of MM.[42,43] Kourelis *et al.*[42] have evaluated 33 immune markers, including five immune checkpoint molecules, in BM samples from dysproteinaemia patients, including MGUS, MM and AL amyloidosis, at diagnosis and after chemotherapy, and autologous stem cell transplant using mass cytometry. Similar to our

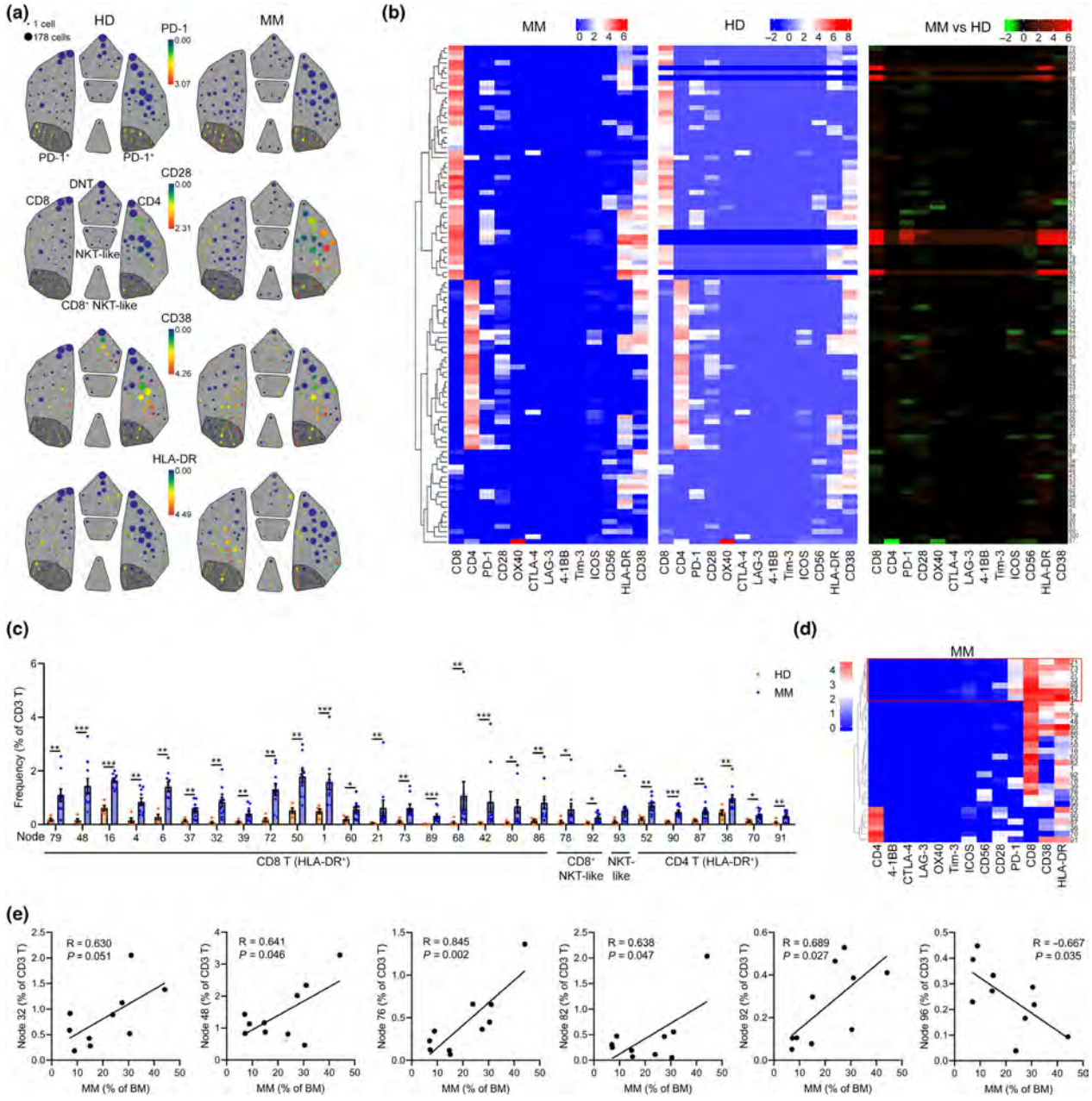

Figure 6. Identification of the immune checkpoint signature of T cell in MM patients. **(a)** A SPADE tree describing 100 small T-cell clusters of one representative HD or MM patient coloured by the median expression of indicated markers. T-cell subpopulations are gated with a grey colour, and PD-1$^+$ subsets are gated with a deep grey area. **(b)** Heatmaps showing the normalised median expression of indicated markers in 100 small T-cell clusters of all MM patients and all HD and displaying the differences in markers' expression between T-cell clusters of MM patients and HD (right panel). **(c)** Bar plots showing the significantly changed frequencies of T-cell clusters (nodes) of HD and MM patients. **(d)** A heatmap showing the normalised median expression of indicated markers in significantly changed HLA-R$^+$ T-cell clusters of MM patients. Red boxes indicate PD-1$^+$HLA-DR$^+$CD38$^+$ CD8 T-cell clusters. **(e)** Dot plots showing the Pearson correlation coefficients for relationships between the frequencies of MM cells and indicated T-cell clusters. HD, n = 5; MM, n = 10. *P < 0.05, **P < 0.01 and ***P < 0.001.

results, they also found a very low level of CTLA-4 in both CD4 and CD8 T cells and that PD-1 is expressed by several T-cell clusters, but not by all T cells. All identified BM cell types, except myeloid DC, express very low level of PD-L1, further confirming the lack of PD-1/PD-L1 checkpoint signalling. The other recent study also analysed the BM T cells from 7 HD and 10 MM patients and

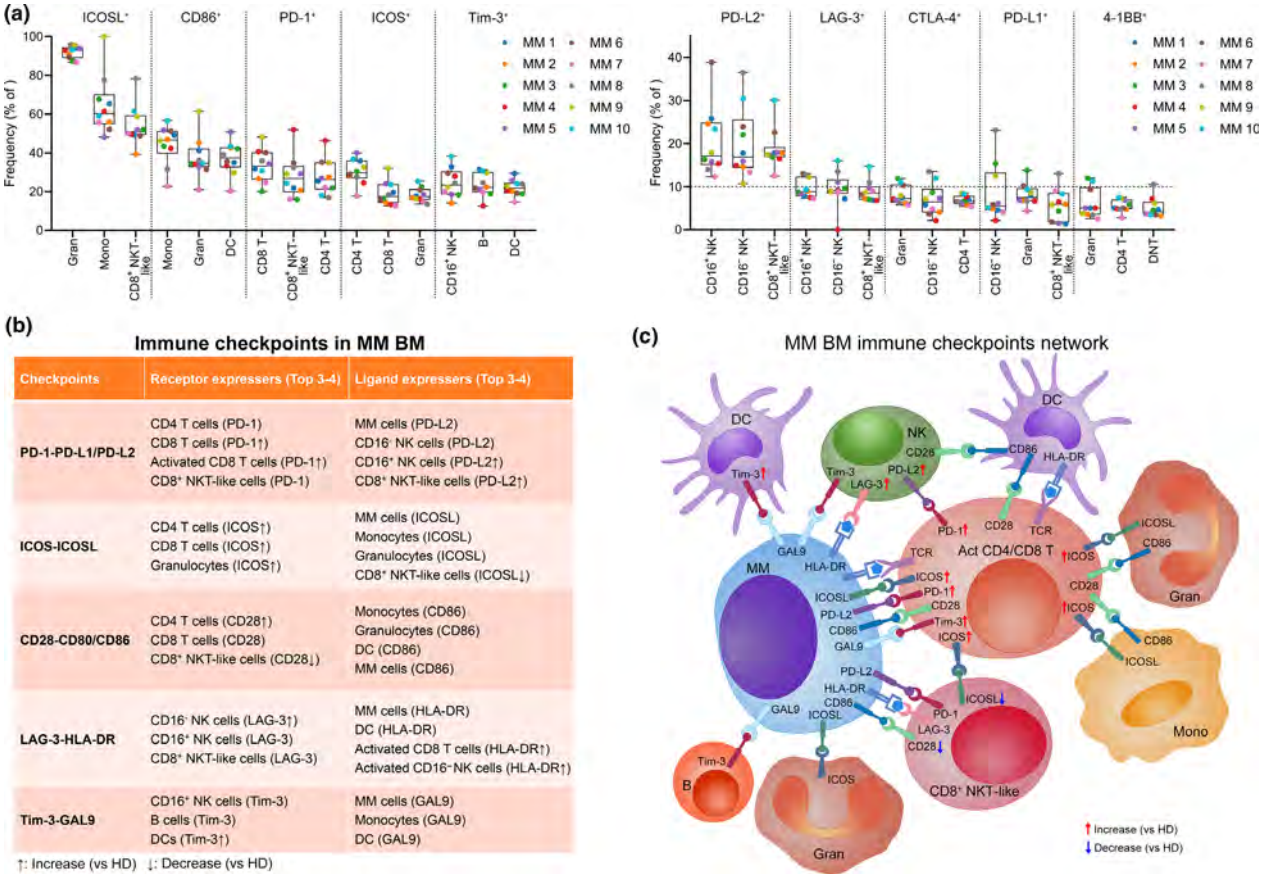

Figure 7. The immune checkpoint network in the MM BM microenvironment. **(a)** Dot plots showing the top 3 frequencies of indicated markers' positive cells in immune cell types. Dots are coloured by individual. **(b)** A table listing all the important checkpoints and their top 3 or 4 providers. **(c)** A schematic diagram showing the main provider cells of immune checkpoint ligands and receptors, and the network among them in the MM BM microenvironment. Act, activated. MM, $n = 10$.

the BM myeloid cells from 4 HD and 8 MM patients using mass cytometry.[43] They discovered greater terminal effector differentiation in memory T cells and an increased PD-L1 expression on myeloid cells from MM patients than healthy donors. However, detailed status of immune checkpoints, as well as the cell types providing checkpoint signals, has not been identified in these previous studies. Here, we devoted to systemically delineate the immune checkpoint signature of MM by measuring 10 pairs of immune checkpoint axes in freshly isolated BM samples from MM patients without treatment and our data would maximally reflect the real immune status of MM BM microenvironment.

Malignant cells offer a variety of immune checkpoint ligands to match receptors on immune cells and thus regulate anticancer immunity. With the successful application of PD-1/PD-L1 axis inhibitors in solid tumor immunotherapy, this blocking strategy has also become a focus of MM immunotherapy and plenty of clinical trials are conducted.[44] However, single-agent therapy with PD-1 inhibitors fails to induce significant clinical responses in a phase 1b study,[16] suggesting that PD-1 blockade alone is insufficient to reinvigorate a clinically meaningful anti-MM immunity. Discrepant results concerning PD-L1 expression on MM cells have been reported.[45] Several studies have confirmed the limited expression of PD-L1 on MM cells[46-48]; in contrast, higher PD-L1 has been also found in MM cells than plasma cells from HD.[5,49] Our comprehensive data revealed a low frequency (< 12%) of PD-L1 expression in MM cells from all 10 MM patients. However, the expression of PD-L2, another ligand for PD-1, on MM cells was relatively higher than PD-L1. Anyhow, ligands of PD-1 were not widely expressed by MM cells, implicating the existence of other possible participants in inhibitory immunity. We validated

here that several immune checkpoint ligands, including GAL9, ICOSL, HLA-DR, CD86, PD-L2 and 4-1BBL, were more generally presented on MM cells and these ligands are able to largely influence the immune response through binding to their receptors on immune effector cells.

A significant positive correlation between MM burden and GAL9 expression, together with the high frequency of GAL9 expression on MM cells, emphasises the possible contribution of this ligand to the MM immune microenvironment. In addition, Tim-3, a receptor of GAL9,[50] was expressed by activated CD8 T, NKT-like, DNT cells and DC in MM patients. Tim-3-GAL9 axis provides inhibitory immune signals to activated T cells,[51] and immunotherapy targeting Tim-3 and PD-1 pathways enables the reversion of T-cell exhaustion and restoration of antitumor immunity,[52] thus suggesting a possible use of this strategy to reconstruct anti-MM immunity.

ICOSL was also expressed by most of MM cells, and its receptor ICOS was increasingly detected in 20–40% of CD4 or CD8 T cells of MM patients. Being in line with this mechanism, a higher percentage of $ICOS^+$ cells in follicular helper T cells has been found in MM patients than healthy controls.[53] The ICOS/ICOSL signal can mediate helper T-cell immunity and regulate effector T-cell differentiation.[54] *In vitro*, ICOS/ICOSL blockade significantly reduced the generation of MM cell-induced inhibitory $CD4^+$ Treg cells,[55,56] and lenalidomide, a clinically approved anti-MM immunomodulatory drug, could inhibit ICOSL expression in MM cells[57] and enhance PD-1/PD-L1 blockade-induced anticancer immunity in MM patients.[58] These evidences, together with our results, underline ICOS/ICOSL blockade as a possible enhancer for anti-MM immunotherapeutic strategies.

T and NK cells are at the forefront of anticancer immune responses, and quantitative and functional abnormalities in these cells' subsets have been well identified in the MM BM microenvironment.[2,59,60] The discovery of significant increases in CD4 T, CD8 T, $CD16^+$ NK and $CD8^+$ NKT-like cells in MM BM compared with HD BM confirms an abnormal immune cell composition induced by MM cells. Remarkably, these increased T or NK cells are activated in the MM samples, but with a suppressive phenotype as several inhibitory receptors, such as PD-1 and Tim-3, were increased. Because of the fact that CTLA-4, 4-1BB and LAG-3 were expressed only by very few CD8 T cells, targeting those checkpoints might be less effective. Deep analysis of T-cell profiling identified several specifically activated CD8 T-cell clusters highly expressing PD-1 in MM patients, whereas most of them are deficient in CD28 expression, a critical T-cell costimulatory receptor that binds to B7 molecules, including CD80 and CD86.[61] The failure of PD-1 inhibitors in MM immunotherapy may result from the deficiency of CD28 in activated $CD8^+$ T cells as substantial evidences have demonstrated that successful reinvigoration of exhausted $CD8^+$ T cells by PD-1/PD-L1 blockade is dependent on CD28.[62,63] Most likely, once CD28 signalling is restored in these increased numbers of activated $CD8^+$ T cells, strong anti-MM immunity will be achieved for controlling MM growth.

New targets or strategies are needed to increase the success of immune checkpoint-based immunotherapy for MM. By fine-grained analysis of the immune cells in the MM BM microenvironment, this study provides a detailed atlas of the infiltrating immune cells in MM, identifies immune checkpoints change that are unique to the MM immunologic milieu, and reveals distinct immune subsets that may be responsible for anti-MM immunosuppression. These data will be a valuable resource for future research to explore more efficient immunotherapy strategies tailored to restore anti-MM immunity through inhibition of immune checkpoints. The large individual heterogeneity in immune checkpoint networks among MM patients also emphasises the necessity of personalised strategies for a successful MM immunotherapy. Our findings demonstrating several potential immune checkpoint targets warrant further functional investigation into developing novel strategies for MM immunotherapy. In addition, non-immune cell components, such as stromal cells and extracellular vesicles, which also play an important role in regulating immunosuppression in the MM BM, also need to be taken into account in discovering novel targets for MM treatment in future.

METHODS

Human specimens

Multiple myeloma BM samples were collected from MM patients undergoing BM biopsy for diagnosis, and healthy BM samples were obtained from donors undergoing BM biopsy for BM donation. Informed consents in accordance with the Declaration of Helsinki were obtained from all participants. All participants were recruited at the Third

Affiliated Hospital of Sun Yat-sen University. All protocols were reviewed and approved by the Hospital Ethics Committee. The clinical characteristics of all participants are listed in Supplementary table 1.

Sample processing

Bone marrow samples were collected into sodium heparin tubes. To maximally maintain the immune profile, freshly isolated BM cells were directly fixed using an optimised and well-established fixing method with minimal effects on target epitope.[64] About 1–2 mL of BM samples was fixed with Fix I Buffer (Fluidigm, South San Francisco, CA, USA) for 10 min at RT, and red blood lysis buffer was used to fully remove the erythrocytes. Cells were then resuspended in cell staining buffer (CSB) and Dulbecco's phosphate-buffered saline, supplemented with 0.5% bovine serum albumin and 0.02% sodium azide, containing 10% dimethyl sulphoxide, and stored at −80°C until cell staining was performed.

Barcoding

To eliminate sample-specific staining variation, all samples were barcoded first and then stained, processed and acquired as one multiplexed sample. A total of 0.5×10^6 fixed cells from each samples were washed thrice with CSB and washed twice with 1× Barcode Perm Buffer (Fluidigm). These samples were then barcoded using a 20-Plex Pd Barcoding Kit (Fluidigm). Each sample was washed thrice with CSB after incubation with different barcodes for 30 min at RT, and all samples were combined together into one tube for antibody staining.

Antibody staining

Combined samples were washed once with CSB and incubated with Human Fc Receptor Binding Inhibitor Antibody (Thermo Fisher, Waltham, MA, USA) for 10 min at RT to lower non-specific binding. Anti-human ICOSL-biotin (BioLegend, San Diego, CA, USA) was added to the samples for incubation for another 30 min at RT. These cells were washed twice with CSB and stained with 29 metal isotope-tagged antibodies and 1 metal-labelled antibody against biotin (Supplementary table 2) for 30 min at RT. These stained cells were washed thrice with CSB and incubated with 1 mL Fix & Perm Buffer (Fluidigm) containing 125 nM Intercalator-Ir (Fluidigm) overnight at 4°C.

CyTOF data acquisition

Samples were washed twice with CSB and twice with ultrapure water. Immediately prior to data acquisition, the sample was resuspended in ultrapure water containing 15% EQ Four Element Calibration Beads (Fluidigm) and filtered through a 38-μm cell strainer. The sample was acquired on a Helios mass cytometer (Fluidigm) at an acquisition rate of < 500 events/s. Bead-based normalisation and debarcoding were completed using CyTOF software 6.7 (Fluidigm).

Data analysis

Individual debarcoded files were uploaded to an online single-cell analyser, Cytobank (Beckman Coulter, Brea, CA, USA).[65] Beads, debris and doublets were excluded from the events, and the single-cell data were subsequently used for high-dimensional analyses. Contour plots, viSNE, SPADE and heatmaps were implemented using Cytobank. The frequency of positive cells in each gated population was determined using FlowJo (FlowJo LLC, Ashland, OR, USA). Bar plot, violin plot and heatmap of correlationship were generated using the GraphPad Prism software (GraphPad, San Diego, CA, USA). The comparison of HD and MM SPADE node was implemented using the cytoClustR R package developed in Kordasti Lab from King's College London. SPSS 20.0 software (IBM, Armonk, NY, USA) was used for the Pearson correlation analyses.

Statistical analysis

The Mann–Whitney *U*-test was used to determine the statistical significance between the two groups. A paired *t*-test was performed on the frequencies of different cell subsets in individuals. Error bars represent mean ± standard error of mean (sem). A *P*-value < 0.05 was considered as statistically significant.

ACKNOWLEDGMENTS

This work was supported by the National Natural Science Foundation of China (Grant No. 81700203), the Guangdong Basic and Applied Basic Research Foundation (2019A1515011126), the National Funds for Developing Local Colleges and Universities (Grant No. B16056001) and the Natural Science Foundation Research Team of Guangdong Province (Grant No. 2018B030312001). We thank all patients or healthy donors for supporting this work.

CONFLICT OF INTEREST

The authors declare no conflict of interest.

AUTHORS' CONTRIBUTION

JW and JL conceived the idea and supervised the experiments. YZ obtained the informed consents and collected samples. JW, CT and HZ implemented the experiments. JW analysed the data and wrote the manuscript. KV, EM and JL provided critical suggestions and revised the manuscript. All authors read and approved the final manuscript.

Data availability statement

Mass cytometry data that support the findings of this study are deposited in the FlowRepository database (No. FR-FCM-Z29D).

REFERENCES

1. Wang J, Hendrix A, Hernot S *et al*. Bone marrow stromal cell-derived exosomes as communicators in drug resistance in multiple myeloma cells. *Blood* 2014; **124**: 555–566.
2. Dosani T, Carlsten M, Maric I, Landgren O. The cellular immune system in myelomagenesis: NK cells and T cells in the development of myeloma and their uses in immunotherapies. *Blood Cancer J* 2015; **5**: e306.
3. Ghobrial I, Cruz CH, Garfall A *et al*. Immunotherapy in multiple myeloma: accelerating on the path to the patient. *Clin Lymphoma Myeloma Leuk* 2019; **19**: 332–344.
4. Ramachandran IR, Martner A, Pisklakova A *et al*. Myeloid-derived suppressor cells regulate growth of multiple myeloma by inhibiting T cells in bone marrow. *J Immunol* 2013; **190**: 3815–3823.
5. Liu J, Hamrouni A, Wolowiec D *et al*. Plasma cells from multiple myeloma patients express B7–H1 (PD-L1) and increase expression after stimulation with IFN-γ and TLR ligands via a MyD88-, TRAF6-, and MEK-dependent pathway. *Blood* 2007; **110**: 296–304.
6. Lucas F, Pennell M, Huang Y *et al*. T cell transcriptional profiling and immunophenotyping uncover LAG3 as a potential significant target of immune modulation in multiple myeloma. *Biol Blood Marrow Transplant* 2020; **26**: 7–15.
7. Wang J, De Veirman K, Faict S *et al*. Multiple myeloma exosomes establish a favourable bone marrow microenvironment with enhanced angiogenesis and immunosuppression. *J Pathol* 2016; **239**: 162–173.
8. Jelinek T, Mihalyova J, Kascak M, Duras J, Hajek R. PD-1/PD-L1 inhibitors in haematological malignancies: update 2017. *Immunology* 2017; **152**: 357–371.
9. Minn AJ, Wherry EJ. Combination cancer therapies with immune checkpoint blockade: convergence on interferon signaling. *Cell* 2016; **165**: 272–275.
10. Pitt JM, Vetizou M, Daillere R *et al*. Resistance mechanisms to immune-checkpoint blockade in cancer: tumor-intrinsic and -extrinsic factors. *Immunity* 2016; **44**: 1255–1269.
11. Syn NL, Teng MWL, Mok TSK, Soo RA. De-novo and acquired resistance to immune checkpoint targeting. *Lancet Oncol* 2017; **18**: e731–e741.
12. Topalian SL, Taube JM, Anders RA, Pardoll DM. Mechanism-driven biomarkers to guide immune checkpoint blockade in cancer therapy. *Nat Rev Cancer* 2016; **16**: 275–287.
13. Wilson RAM, Evans TRJ, Fraser AR, Nibbs RJB. Immune checkpoint inhibitors: new strategies to checkmate cancer. *Clin Exp Immunol* 2018; **191**: 133–148.
14. Brunner-Weinzierl MC, Rudd CE. CTLA-4 and PD-1 control of T-cell motility and migration: implications for tumor immunotherapy. *Front Immunol* 2018; **9**: 2737.
15. Jenkins RW, Barbie DA, Flaherty KT. Mechanisms of resistance to immune checkpoint inhibitors. *Br J Cancer* 2018; **118**: 9–16.
16. Suen H, Brown R, Yang S *et al*. The failure of immune checkpoint blockade in multiple myeloma with PD-1 inhibitors in a phase 1 study. *Leukemia* 2015; **29**: 1621–1622.
17. Lesokhin AM, Ansell SM, Armand P *et al*. Nivolumab in patients with relapsed or refractory hematologic malignancy: preliminary results of a phase Ib study. *J Clin Oncol* 2016; **34**: 2698–2704.
18. Pardoll DM. The blockade of immune checkpoints in cancer immunotherapy. *Nat Rev Cancer* 2012; **12**: 252–264.
19. Bendall SC, Simonds EF, Qiu P *et al*. Single-cell mass cytometry of differential immune and drug responses across a human hematopoietic continuum. *Science* 2011; **332**: 687–696.
20. Bodenmiller B, Zunder ER, Finck R *et al*. Multiplexed mass cytometry profiling of cellular states perturbed by small-molecule regulators. *Nat Biotechnol* 2012; **30**: 858–867.
21. Bendall SC, Davis KL, el Amir AD *et al*. Single-cell trajectory detection uncovers progression and regulatory coordination in human B cell development. *Cell* 2014; **157**: 714–725.
22. Porpiglia E, Samusik N, Ho ATV *et al*. High-resolution myogenic lineage mapping by single-cell mass cytometry. *Nat Cell Biol* 2017; **19**: 558–567.
23. Lavin Y, Kobayashi S, Leader A *et al*. Innate immune landscape in early lung adenocarcinoma by paired single-cell analyses. *Cell* 2017; **169**: 750–765.e17.
24. Chevrier S, Levine JH, Zanotelli VRT *et al*. An immune atlas of clear cell renal cell carcinoma. *Cell* 2017; **169**: 736–749.e18.
25. Wagner J, Rapsomaniki MA, Chevrier S *et al*. A single-cell atlas of the tumor and immune ecosystem of human breast cancer. *Cell* 2019; **177**: 1330–1345.e18.
26. Lin P, Owens R, Tricot G, Wilson CS. Flow cytometric immunophenotypic analysis of 306 cases of multiple myeloma. *Am J Clin Pathol* 2004; **121**: 482–488.
27. Reid S, Yang S, Brown R *et al*. Characterisation and relevance of CD138-negative plasma cells in plasma cell myeloma. *Int J Lab Hematol* 2010; **32**: e190–e196.
28. el Amir AD, Davis KL, Tadmor MD *et al*. viSNE enables visualization of high dimensional single-cell data and reveals phenotypic heterogeneity of leukemia. *Nat Biotechnol* 2013; **31**: 545–552.
29. Maecker HT, McCoy JP, Nussenblatt R. Standardizing immunophenotyping for the human immunology project. *Nat Rev Immunol* 2012; **12**: 191–200.
30. Chan WK, Rujkijyanont P, Neale G *et al*. Multiplex and genome-wide analyses reveal distinctive properties of KIR^+ and $CD56^+$ T cells in human blood. *J Immunol* 2013; **191**: 1625–1636.
31. Campbell JJ, Qin S, Unutmaz D *et al*. Unique subpopulations of $CD56^+$ NK and NK-T peripheral blood lymphocytes identified by chemokine receptor expression repertoire. *J Immunol* 2001; **166**: 6477–6482.
32. Krijgsman D, Hokland M, Kuppen PJK. The role of natural killer T cells in cancer-a phenotypical and functional approach. *Front Immunol* 2018; **9**: 367.
33. Tiwary S, Berzofsky JA, Terabe M. Altered lipid tumor environment and its potential effects on NKT cell function in tumor immunity. *Front Immunol* 2019; **10**: 2187.
34. Arruvito L, Payaslian F, Baz P *et al*. Identification and clinical relevance of naturally occurring human $CD8^+$HLA-DR^+ regulatory T cells. *J Immunol* 2014; **193**: 4469–4476.
35. Evans JH, Horowitz A, Mehrabi M *et al*. A distinct subset of human NK cells expressing HLA-DR expand in response to IL-2 and can aid immune responses to BCG. *Eur J Immunol* 2011; **41**: 1924–1933.

36. Christopoulos P, Pfeifer D, Bartholome K *et al*. Definition and characterization of the systemic T-cell dysregulation in untreated indolent B-cell lymphoma and very early CLL. *Blood* 2011; **117**: 3836–3846.
37. McElroy AK, Akondy RS, Davis CW *et al*. Human Ebola virus infection results in substantial immune activation. *Proc Natl Acad Sci USA* 2015; **112**: 4719–4724.
38. Simoni Y, Becht E, Fehlings M *et al*. Bystander $CD8^+$ T cells are abundant and phenotypically distinct in human tumour infiltrates. *Nature* 2018; **557**: 575–579.
39. Duhen T, Duhen R, Montler R *et al*. Co-expression of CD39 and CD103 identifies tumor-reactive CD8 T cells in human solid tumors. *Nat Commun* 2018; **9**: 2724.
40. Qiu P, Simonds EF, Bendall SC *et al*. Extracting a cellular hierarchy from high-dimensional cytometry data with SPADE. *Nat Biotechnol* 2011; **29**: 886–891.
41. Wang J, De Veirman K, De Beule N *et al*. The bone marrow microenvironment enhances multiple myeloma progression by exosome-mediated activation of myeloid-derived suppressor cells. *Oncotarget* 2015; **6**: 43992–44004.
42. Kourelis TV, Villasboas JC, Jessen E *et al*. Mass cytometry dissects T cell heterogeneity in the immune tumor microenvironment of common dysproteinemias at diagnosis and after first line therapies. *Blood Cancer J* 2019; **9**: 72.
43. Bailur JK, McCachren SS, Doxie DB *et al*. Early alterations in stem-like/resident T cells, innate and myeloid cells in the bone marrow in preneoplastic gammopathy. *JCI Insight* 2019; **5**: 127807.
44. Lesokhin AM, Bal S, Badros AZ. Lessons learned from checkpoint blockade targeting PD-1 in multiple myeloma. *Cancer Immunol Res* 2019; **7**: 1224–1229.
45. Jelinek T, Paiva B, Hajek R. Update on PD-1/PD-L1 inhibitors in multiple myeloma. *Front Immunol* 2018; **9**: 2431.
46. Paiva B, Azpilikueta A, Puig N *et al*. PD-L1/PD-1 presence in the tumor microenvironment and activity of PD-1 blockade in multiple myeloma. *Leukemia* 2015; **29**: 2110–2113.
47. Kelly KR, Espitia CM, Zhao W *et al*. Oncolytic reovirus sensitizes multiple myeloma cells to anti-PD-L1 therapy. *Leukemia* 2018; **32**: 230–233.
48. Favreau M, Venken K, Faict S *et al*. Both mucosal-associated invariant and natural killer T-cell deficiency in multiple myeloma can be countered by PD-1 inhibition. *Haematologica* 2017; **102**: e266–e270.
49. Tamura H, Ishibashi M, Yamashita T *et al*. Marrow stromal cells induce B7–H1 expression on myeloma cells, generating aggressive characteristics in multiple myeloma. *Leukemia* 2013; **27**: 464–472.
50. Zhu C, Anderson AC, Schubart A *et al*. The Tim-3 ligand galectin-9 negatively regulates T helper type 1 immunity. *Nat Immunol* 2005; **6**: 1245–1252.
51. Perez-Gracia JL, Labiano S, Rodriguez-Ruiz ME, Sanmamed MF, Melero I. Orchestrating immune check-point blockade for cancer immunotherapy in combinations. *Curr Opin Immunol* 2014; **27**: 89–97.
52. Sakuishi K, Apetoh L, Sullivan JM *et al*. Targeting Tim-3 and PD-1 pathways to reverse T cell exhaustion and restore anti-tumor immunity. *J Exp Med* 2010; **207**: 2187–2194.
53. Zhou DM, Xu YX, Zhang LY *et al*. The role of follicular T helper cells in patients with malignant lymphoid disease. *Hematology* 2017; **22**: 412–418.
54. Wikenheiser DJ, Stumhofer JS. ICOS co-stimulation: friend or foe? *Front Immunol* 2016; **7**: 304.
55. Feyler S, Scott GB, Parrish C *et al*. Tumour cell generation of inducible regulatory T-cells in multiple myeloma is contact-dependent and antigen-presenting cell-independent. *PLoS One* 2012; **7**: e35981.
56. Raja KRM, Hajek R. Contribution of regulatory T cells to immunosuppression and disease progression in multiple myeloma patients. *Oncoimmunology* 2013; **2**: e25619.
57. Scott GB, Carter C, Parrish C, Wood PM, Cook G. Downregulation of myeloma-induced ICOS-L and regulatory T cell generation by lenalidomide and dexamethasone therapy. *Cell Immunol* 2015; **297**: 1–9.
58. Gorgun G, Samur MK, Cowens KB *et al*. Lenalidomide enhances immune checkpoint blockade-induced immune response in multiple myeloma. *Clin Cancer Res* 2015; **21**: 4607–4618.
59. Perez-Andres M, Almeida J, Martin-Ayuso M *et al*. Characterization of bone marrow T cells in monoclonal gammopathy of undetermined significance, multiple myeloma, and plasma cell leukemia demonstrates increased infiltration by cytotoxic/Th1 T cells demonstrating a squed TCR-Vβ repertoire. *Cancer* 2006; **106**: 1296–1305.
60. Tamura H. Immunopathogenesis and immunotherapy of multiple myeloma. *Int J Hematol* 2018; **107**: 278–285.
61. Esensten JH, Helou YA, Chopra G, Weiss A, Bluestone JA. CD28 costimulation: from mechanism to therapy. *Immunity* 2016; **44**: 973–988.
62. Kamphorst AO, Wieland A, Nasti T *et al*. Rescue of exhausted CD8 T cells by PD-1-targeted therapies is CD28-dependent. *Science* 2017; **355**: 1423–1427.
63. Hui EF, Cheung J, Zhu J *et al*. T cell costimulatory receptor CD28 is a primary target for PD-1-mediated inhibition. *Science* 2017; **355**: 1428–1433.
64. Krutzik PO, Clutter MR, Nolan GP. Coordinate analysis of murine immune cell surface markers and intracellular phosphoproteins by flow cytometry. *J Immunol* 2005; **175**: 2357–2365.
65. Kotecha N, Krutzik PO, Irish JM. Web-based analysis and publication of flow cytometry experiments. *Curr Protoc Cytom* 2010; **Chapter 10**: Unit10.17.

Supporting Information

Additional supporting information may be found online in the Supporting Information section at the end of the article.

Original Article

A Phase 1b/2 Study of Azacitidine With PD-L1 Antibody Avelumab in Relapsed/Refractory Acute Myeloid Leukemia

Kapil Saxena, MD [1]; Shelley M. Herbrich, PhD[1]; Naveen Pemmaraju, MD [1]; Tapan M. Kadia, MD [1]; Courtney D. DiNardo, MD [1]; Gautam Borthakur, MD[1]; Sherry A. Pierce, BA, BS, RN[1]; Elias Jabbour, MD [1]; Sa A. Wang, MD[2]; Carlos Bueso-Ramos, MD, PhD[2]; Sanam Loghavi, MD[2]; Guillin Tang, MD, PhD[2]; Cora M. Cheung, RN[1]; Lynette Alexander, BA, RN[1]; Steven Kornblau, MD[1]; Michael Andreeff, MD, PhD[1]; Guillermo Garcia-Manero, MD [1]; Farhad Ravandi, MD[1]; Marina Y. Konopleva, MD, PhD[1]; and Naval Daver, MD [1]

BACKGROUND: Patients with relapsed/refractory (R/R) acute myeloid leukemia (AML) have limited treatment options. In preclinical models of AML, inhibition of the PD-1/PD-L1 axis demonstrated antileukemic activity. Avelumab is an anti–PD-L1 immune checkpoint inhibitor (ICI) approved in multiple solid tumors. The authors conducted a phase 1b/2 clinical trial to assess the safety and efficacy of azacitidine with avelumab in patients with R/R AML. **METHODS:** Patients aged ≥18 years who had R/R AML received azacitidine 75 mg/m^2 on days 1 through 7 and avelumab on days 1 and 14 of 28-day cycles. **RESULTS:** Nineteen patients were treated. The median age was 66 years (range, 22-83 years), 100% had European LeukemiaNet 2017 adverse-risk disease, and 63% had prior exposure to a hypomethylating agent. Avelumab was dosed at 3 mg/kg for the first 7 patients and at 10 mg/kg for the subsequent 12 patients. The most common grade ≥3 treatment-related adverse events were neutropenia and anemia in 2 patients each. Two patients experienced immune-related adverse events of grade 2 and grade 3 pneumonitis, respectively. The overall complete remission rate was 10.5%, and both were complete remission with residual thrombocytopenia. The median overall survival was 4.8 months. Bone marrow blasts were analyzed for immune-related markers by mass cytometry and demonstrated significantly higher expression of PD-L2 compared with PD-L1 both pretherapy and at all time points during therapy, with increasing PD-L2 expression on therapy. **CONCLUSIONS:** Although the combination of azacitidine and avelumab was well tolerated, clinical activity was limited. High expression of PD-L2 on bone marrow blasts may be an important mechanism of resistance to anti–PD-L1 therapy in AML. ***Cancer* 2021;127:3761-3771**. © *2021 American Cancer Society*.

LAY SUMMARY:

- This report describes the results of a phase 1b/2 study of azacitidine with the anti–PD-L1 immune checkpoint inhibitor avelumab for patients with relapsed/refractory acute myeloid leukemia (AML).
- The clinical activity of the combination therapy was modest, with an overall response rate of 10.5%.
- However, mass cytometry analysis revealed significantly higher expression of PD-L2 compared with PD-L1 on AML blasts from all patients who were analyzed at all time points.
- These data suggest a novel potential role for PD-L2 as a means of AML immune escape.

KEYWORDS: avelumab, azacitidine, checkpoint inhibitor, mass cytometry, PD-1, PD-L1, PD-L2.

INTRODUCTION

Over the past 4 years, multiple new therapies have been US Food and Drug Administration-approved for the treatment of acute myeloid leukemia (AML).[1] Despite these advancements, outcomes for the majority of patients with AML who do not undergo allogeneic stem cell transplantation (allo-SCT) remain dismal, especially for those patients with relapsed/refractory (R/R) disease who have an expected median overall survival (OS) of 4 to 7 months.[2-4]

Since the initial approval of the anti–CTLA-4 antibody ipilimumab in 2011 for melanoma, multiple immune checkpoint inhibitors (ICIs) targeting CTLA-4, PD-1, and PD-L1 have dramatically improved outcomes and have been approved in many solid tumors.[5] Efficacy of ICIs for hematologic malignancies has generally been less impressive, with US Food and Drug Administration approvals limited thus far to Hodgkin lymphoma and primary mediastinal B-cell lymphoma.[6] No ICI has received approval for leukemia, and trials assessing ICI-based therapy for AML have only recently been presented and published, with acceptable safety profiles but generally modest

Corresponding Author: Naval Daver, MD, Department of Leukemia, The University of Texas MD Anderson Cancer Center, 1515 Holcombe Boulevard, Unit 0428, Houston, TX 77030 (ndaver@mdanderson.org).

[1]Department of Leukemia, The University of Texas MD Anderson Cancer Center, Houston, Texas; [2]Department of Hematopathology, The University of Texas MD Anderson Cancer Center, Houston, Texas

The first 2 authors contributed equally to this article.

Additional supporting information may be found in the online version of this article.

DOI: 10.1002/cncr.33690, **Received:** February 1, 2021; **Revised:** April 17, 2021; **Accepted:** May 3, 2021, **Published online** June 25, 2021 in Wiley Online Library (wileyonlinelibrary.com)

efficacy.[7-12] Several reasons have been postulated for the limited efficacy of ICIs in AML compared with that in solid tumors and Hodgkin lymphoma. The protective bone marrow (BM) microenvironment might exert an immunosuppressive influence by preventing access of T cells to AML blasts or by secretion of immune-dampening metabolites such as IDO or arginine.[13-16] ICI efficacy typically correlates with the tumor mutational burden.[17] The tumor mutational burden of AML is logarithmically lower compared with that of many solid tumor malignancies.[18] However, a critical role for T-cell activity in the control of AML has been leveraged for over 40 years since early demonstrations of a graft-versus-leukemia effect with allo-SCT and subsequently with donor lymphocyte infusions post-SCT.[19-21] This suggests that a broad and comprehensive evaluation of immune strategies is warranted before final conclusions regarding the efficacy and applicability of various immune modalities in AML can be drawn.

Immune evasion in AML is likely a multifaceted process.[22] ICI therapy for AML was first reported as part of a phase 1/1b clinical trial, with striking antileukemic efficacy observed (especially for extramedullary disease) in a subset of patients with AML who had post–allo-SCT relapse treated with high-dose ipilimumab.[8] Human AML cells express various amounts of transcripts for the PD-1 ligands PD-L1 and PD-L2, and higher messenger RNA (mRNA) expression of *PD-L1* and *PD-L2* is correlated with inferior OS in patients with AML.[23-26] In a murine model of AML, both PD-1 gene knockout as well as anti–PD-L1 murine ICI led to decreased leukemic burden and improved survival.[27-29] In patients with AML, BM-infiltrating T-cell populations appeared to be preserved compared with BMs from healthy individuals, with an increased frequency of immune inhibitory and activating coreceptors (especially in relapsed AML), including PD-1, OX40, and TIM3.[30,31] Further treatment with the commonly used hypomethylating agent (HMA) azacitidine increased expression of *PD-1*, *PD-L1*, and *PD-L2* in patients with myeloid malignancies.[25,32] On the basis of these data, a phase 2 trial evaluated the efficacy of azacitidine with nivolumab, an anti–PD-1 ICI, in patients with R/R AML.[7] In that study of 70 patients who had R/R AML, the overall response rate (ORR) was 33%. The median OS was especially encouraging in salvage 1 patients (10.5 months), which was superior to matched historical controls. Although PD-1 and PD-L1 participate in the same axis, blockade of the tumor cell ligand (PD-L1) rather than the effector T-cell receptor (PD-1) may lead to different efficacy profiles.[5,33] The current phase 1b/2 study was designed to assess the combination of azacitidine with avelumab, an anti–PD-L1 ICI, in patients with R/R AML.

MATERIALS AND METHODS

Patient Eligibility

Patients who had AML that was refractory (up to 3 prior therapies for AML) or relapsed (up to salvage 3 status) who were aged ≤18 years with an Eastern Cooperative Oncology Group performance status ≤2 and adequate organ function, defined as total bilirubin ≤1.5 × the upper limit of normal (ULN) (≤3 × ULN if considered caused by leukemic involvement or Gilbert syndrome), aspartate aminotransferase and alanine aminotransferase levels ≤2.5 × ULN (≤5 × ULN if considered caused by leukemic involvement), and an estimated creatinine clearance >30 mL per minute (as calculated by the Cockcroft-Gault formula or similar institutional standard method), were eligible. Prior therapy for myelodysplastic syndrome (MDS), chronic myelomonocytic leukemia, or a myeloproliferative neoplasm was not considered as prior AML therapy. Key exclusion criteria included known severe hypersensitivity to monoclonal antibodies, uncontrolled asthma, known history of severe interstitial lung disease or pneumonitis, prior exposure to another PD-1/PD-L1 inhibitor in combination with azacitidine, any active autoimmune disease that could deteriorate with treatment, and prior organ allograft (with the exception of prior allo-SCT >3 months from initiation of protocol therapy). The study was conducted in accordance with the Declaration of Helsinki, and all participants signed a written informed consent document (ClinicalTrials.gov identifier NCT02953561). The complete protocol is attached as Supporting Materials.

Study Design and Objectives

This was a phase 1b/2, nonrandomized, single-center, open-label study evaluating the safety and efficacy of avelumab in combination with azacitidine for patients with R/R AML. Patients were recruited between February 2017 and May 2018. The data cutoff date was June 1, 2020. The primary objective of the phase 1b portion was to determine the maximum tolerated dose (MTD) and dose-limiting toxicity (DLT) of the combination. Definitions for DLTs and immune-related adverse events (irAEs) are outlined in the clinical protocol in sections 5.2.1.3 and 5.3.5, respectively (see

Supporting Materials). The primary objective of the phase 2 portion of the study was to define the ORR, defined as complete remission (CR) + CR with incomplete platelet recovery (CRp) + CR with incomplete blood count recovery (CRi) + morphologic leukemia-free state according to the AML International Working Group (IWG) 2003 response criteria.[34] Secondary objectives included the number of patients who achieved >50% reduction in BM blast percentage while on therapy, event-free survival (EFS), and OS. Exploratory objectives included evaluation of minimal residual disease by multiparametric flow cytometry and longitudinal analysis of immunological markers on peripheral blood (PB) and BM aspirate AML blasts. AML blasts were assessed for expression of multiple markers (including PD-L1, PD-L2, PD-1, CTLA-4, TIGIT, OX40, TIM3, CD200, LAG3, 4-1BB) with a mass cytometry/cytometry by time-of-flight (CyTOF) panel of antibodies designed and conjugated for this study (see Supporting Methods), as described below.

Treatment Regimen and Safety Assessment

Azacitidine was administered on days 1 through 7 intravenously or subcutaneously at a dose of 75 mg/m^2, and avelumab was administered on days 1 and 14 intravenously of each 28-day cycle. In the phase 1b dose-escalation portion, cohorts of 6 patients were enrolled in progressively increasing doses of avelumab with standard dose azacitidine to identify the MTD and the recommended phase 2 dose (RP2D) for the phase 2 portion. Avelumab was initially administered at a −1 dose of 3 mg/kg with standard-dose azacitidine to the first 7 patients enrolled, of whom 6 were evaluable for DLTs for 28 days, as specified in the protocol. Because no DLTs were identified, the subsequent 6 patients received avelumab 10 mg/kg with standard-dose azacitidine, again with no DLTs, and this was identified as the MTD and selected as the RP2D for the combination. Up to 40 additional patients (excluding patients treated at the RP2D from the lead-in part) could be recruited for the phase 2 part. However, only an additional 6 patients were enrolled in the expansion phase 2 at the RP2D, for a total of 12 patients (6 from the DLT evaluation phase 1b and 6 in the expansion phase 2) who received azacitidine with avelumab 10 mg/kg. The study was terminated early because of modest efficacy and other competing protocol priorities within the institution. Dose interruptions of both azacitidine and avelumab were permitted, as were dose reductions or modifications of azacitidine (for details of the full protocol, see the Supporting Materials). Adverse events (AEs) were defined according to the Common Terminology Criteria for Adverse Events, version 4.03.

Statistical Methods

Futility and toxicity were assessed using the Bayesian approach of Thall and Sung.[35] Patient demographics were analyzed using descriptive statistics, and survival analyses were performed using Kaplan-Meier methodology. EFS was calculated as time from treatment initiation to change in AML therapy, patient death from any cause, or loss to follow-up. OS was calculated as the time from treatment initiation to death from any cause. For comparisons of PD-L1 and PD-L2 blast expression, statistical analyses were performed using the Wilcoxon matched-pairs signed-rank test. For comparisons of OS based on salvage status and prior HMA exposure, statistical analyses were performed using the Mann-Whitney test.

Immunophenotyping of BM and PB Samples by Mass Cytometry

Frozen primary BM samples were thawed and immediately incubated in thawing media (10 mL Eagle's minimum essential medium, α modification; Sigma Life Science) with 20% heat-inactivated fetal bovine serum (GenDEPOT), 10 mM MgSO4, 100 μg/mL heparin, and DNAse for 15 minutes at 37 °C before CyTOF staining. Sample barcoding and metal-conjugated antibody staining were performed according to Fluidigm protocols (for additional details, including the customized panel of antibodies used, see Supporting Methods).

Mass Cytometry Data Analysis

Data were first demultiplexed using Fluidigm Debarcoder software. Individual mass cytometry data files (.fcs) were then filtered using FlowJo to remove the normalization beads, debris, doublets, and dead cells. Remaining analyses were performed in R (version 3.6.1; The R Foundation for Statistical Computing) using the R packages *cytofkit*[36] and *flowcore*.[37] Processed data were subjected to negative value-pruned, inverse hyperbolic sine transformation and clustered based on the PhenoGraph algorithm (k = 22) using all cell surface markers.[38] Dimensionality reduction was performed using the uniform manifold approximation and projection method.[39]

RESULTS

Patient Characteristics and Treatment

Between February 2017 and May 2018, 19 patients with R/R AML were enrolled and treated. These included 6 patients in the safety cohort. Patient characteristics are

TABLE 1. Baseline Patient Characteristics at the Time of Treatment Initiation, N = 19

Characteristic	No. of Patients (%) or Median [Range]
Age, y	66 [22-83]
≥60 y	14 (74)
Sex	
Women	9 (47)
Diagnosis	
De novo AML	6 (32)
Secondary AML	13 (68)
Prior HMA exposure for MDS or AML	12 (63)
No. of prior regimens for AML[a]	1 [1-3]
Prior regimens for AML	
HMA-based	6 (32)
HiDAC	8 (42)
IDAC	10 (53)
Targeted therapies[b]	7 (37)
Prior allogeneic SCT	3 (16)
BM blasts, %	40 [7-88]
White blood cell count, $\times 10^9$/L	2.4 [0.7-39.4]
Platelets, $\times 10^9$/L	22 [2-67]
ELN risk classification: Cytogenetics and mutations	
Favorable	0 (0)
Intermediate	0 (0)
Adverse	19 (100)
Cytogenetics by ELN classification	
Favorable	0 (0)
Intermediate	5 (26)
Adverse	14 (74)
Molecular mutational panel[c]	
TP53	7 (37)
TET2	5 (26)
ASXL1	5 (26)
CEBPA	2 (11)
RAS	4 (21)
GATA2	2 (11)
SRSF2	3 (16)
SF3B1	2 (11)
RUNX1	5 (26)

Abbreviations: AML, acute myeloid leukemia; BM, bone marrow; ELN, European LeukemiaNet; HiDAC, high-dose cytarabine based; HMA, hypomethylating agent; IDAC, intermediate-dose cytarabine-based; MDS, myelodysplastic syndrome; SCT, stem cell transplantation.
[a]For patients who had relapsed acute myeloid leukemia after allogeneic SCT, the included regimens were received before allogeneic SCT.
[b]Targeted therapies included: IDH1 inhibitor, anti-CD33 antibody-drug conjugate, BET inhibitor, SYK inhibitor, Grb-2 antisense oligonucleotide, and SMAC mimetic.
[c]The mutations listed were present in ≥2 patients.

summarized in Table 1. The median age at enrollment was 66 years (range, 22-83 years), and 68% of patients had secondary AML. This was a high-risk population: all 19 patients had adverse-risk disease according to the ELN 2017 risk stratification criteria, and 74% of patients had adverse cytogenetics according to ELN 2017 criteria.[40] The median number of prior treatment regimens for AML was 1 (range, 1-3 prior treatments). Twelve (63%) patients had prior HMA exposure with azacitidine, decitabine, or SGI-110 (an investigational prodrug of decitabine) for MDS or AML. Of the 12 patients with prior HMA exposure, 6 had prior azacitidine exposure, and 6 had prior HMA exposure for AML. Three patients had prior allo-SCT, including 2 who had 2 prior allo-SCTs. *TP53* was the most common mutation (37%) identified.

TABLE 2. Treatment-Related Adverse Events Occurring in ≥10% of Patients

Adverse Event	No. of Patients (%)	
	Any Grade	Grade ≥3
Diarrhea	5 (26.3)	1 (5.3)
Fatigue	5 (26.3)	1 (5.3)
Nausea	5 (26.3)	1 (5.3)
Infusion-related reaction	4 (21.1)	
Oral mucositis	4 (21.1)	
Anorexia	3 (15.8)	1 (5.3)
Constipation	3 (15.8)	
Anemia	3 (15.8)	2 (10.5)
Increased ALT	2 (10.5)	
Chills	2 (10.5)	
Hypertension	2 (10.5)	
Maculopapular rash	2 (10.5)	
Muscle weakness	2 (10.5)	
Pleural effusion	2 (10.5)	
Pneumonitis	2 (10.5)	1 (5.3)
Leukopenia	2 (10.5)	
Neutropenia	2 (10.5)	2 (10.5)[a]
Lymphopenia	2 (10.5)	1 (5.3)

Abbreviation: ALT, alanine aminotransferase.
[a]One of these was grade 4 neutropenia and was the only grade 4 treatment-related adverse event. No grade 5 treatment-related adverse events were documented.

All patients who received at least 1 dose of azacitidine and 1 dose of avelumab were evaluable for efficacy and safety per an intention-to-treat approach.

Safety

All treatment-related AEs (TRAEs) occurring in ≥10% of patients (ie, at least 2 patients) are listed in Table 2. The most common TRAEs were diarrhea (n = 5), fatigue (n = 5), nausea (n = 5), infusion reactions (n = 4), and mucositis (n = 4). IrAEs occurred in only 2 patients (10.5%), and both were pneumonitis (1 grade 3 and 1 grade 2). An additional patient developed grade 2 pneumonia/pneumonitis attributed to cytomegalovirus, which was confirmed by viral culture from a bronchoalveolar lavage sample, and she was treated with valganciclovir. Both patients with possible ICI-related pneumonitis were diagnosed clinically based on hypoxemia in the presence of radiographic findings on computed tomography imaging and no evidence of an alternative explanation after an extensive workup (such as cardiac, pulmonary, or infectious). The first patient with an irAE experienced grade 3 pneumonitis during cycle 3, 98 days after study entrance (she received both doses of avelumab during cycle 1 and

no more doses of avelumab after cycle 1 because of an underlying fungal pneumonia, which immediately preceded cycle 1 of azacitidine plus avelumab). During cycle 2, the patient developed a bacterial pneumonia. During cycle 3, the patient developed worsening bilateral lung ground-glass opacities and hypoxemia without a clear infectious or cardiac etiology despite not having received avelumab for 84 days. In the absence of a clear alternative etiology, this event was attributed as a possible irAE from avelumab. She received steroids for 36 days, was hospitalized for 9 days after pneumonitis onset, and was taken off study after this event because of lack of response to azacitidine plus avelumab. The second patient experienced grade 2 pneumonitis on day 9 during cycle 1 (after the first dose of avelumab). He received steroids for 7 days, was hospitalized for 16 days after pneumonitis onset, and remained on study with azacitidine alone without further avelumab exposure. An additional patient developed grade 3 diarrhea of unclear etiology that self-resolved within 3 days without steroid or immunosuppressive therapy and thus was not considered an irAE but was attributed as possibly (Common Terminology Criteria for Adverse Events attribution is a score of 3 for *possible*) related to azacitidine. A separate patient developed grade 3 colitis, which was attributed to *Clostridium difficile* infection based on positive stool *C. diff* DNA testing. There was 1 grade 4 TRAE (neutropenia), and no grade 5 TRAEs were reported. All AEs of any grade and frequency, regardless of attribution, are listed in Supporting Table 1 and all serious AEs are listed in Supporting Table 2. The most common AEs, irrespective of attribution, were constipation (n = 12), fatigue (n = 11), and muscle weakness (n = 11). The most common grade ≥3 AEs, irrespective of attribution, were neutropenic fever (n = 6) and pneumonia (n = 5).

The median number of cycles of therapy received was 3 (range, 1-7 cycles), and the median time on study was 3.3 months. The median duration of cycle 1 and 2 was 28 and 30 days, respectively. Azacitidine was held for at least 1 dose in 5 patients for the following indications: neutropenic fever (n = 3), patient preference to stop therapy and transition to hospice care (n = 1), and travel difficulties (n = 1). Avelumab was held for at least 1 dose in 13 patients for the following indications (some patients had doses held for multiple indications): pneumonia (n = 2), patient preference (n = 2), travel/scheduling difficulties (n = 2), pneumonitis (n = 1), infusion reaction (n = 1), neutropenic fever (n = 1), elevated creatinine (n = 1), hyperbilirubinemia (n = 1), hypercalcemia (n = 1), and deconditioning (n = 1) (see Supporting Table 3). The median number of avelumab doses received per patient was 5 (range, 1-14 doses). Reasons for study discontinuation were lack or loss of response with subsequent therapy change (n = 8), lack or loss of response without subsequent therapy change (n = 3), transition to hospice care (n = 3), therapy change to ease travel needs per patient preference (n = 1), and death while on treatment (n = 4).

Responses and Survival

The ORR according to IWG 2003 criteria was 10.5%, with 2 patients achieving CRp, as indicated in Table 3. Both patients were positive for minimal residual disease by multiparametric flow cytometry through the course of their response. The first patient had secondary AML, diploid cytogenetics, and mutations in *TET2* and *RUNX1* and was initially treated with cladribine plus SGI-110 (a prodrug of decitabine) without sufficient response, and he remained transfusion-dependent on platelets. He received azacitidine plus avelumab (3 mg/kg cohort) with 7% BM blasts pretreatment. He achieved CRp with 2% blasts at the end of cycle 1 and had 0% blasts at the end of cycle 3. He continued on therapy for 6 cycles (7.6 months on treatment), remaining red blood cell transfusion-independent but platelet transfusion-dependent. During cycle 5, the patient was beginning to lose response, with the emergence of 1% to 2% blasts in the PM (BM was deferred to confirm relapse). After cycle 6, he became newly transfusion-dependent on red blood cells in addition to platelets. Treatment was discontinued without subsequent therapy change because of patient preference to transition to supportive care locally (patient was from out of state). The second patient with an objective response had de novo AML, complex cytogenetics, and mutations in *ASXL1*, *SRSF2*, *SETBP1*, and *RUNX1*. He was refractory to 7 + 3 and started azacitidine plus avelumab (10 mg/kg) with 35% BM blasts pretreatment. The patient achieved CRp with 4% blasts at the end of cycle 1 and had 4% blasts at the end of cycle 2. The patient experienced grade 2 pneumonitis after his first dose of avelumab and did not receive further avelumab for the remainder of the study. He did not have further BM biopsies and continued on study protocol with azacitidine alone for a total of 5 cycles (5 months). The patient came off protocol because of difficulty traveling and continued azacitidine monotherapy closer to home for at least 4 more months. He died from disease progression approximately 6 months after coming off protocol.

Three additional patients had BM blast reductions of >50% from pretherapy (51% → 25%, 32% → 12%, and 40% → 13%; median time to >50% blast reduction, 26 days) that did not meet IWG criteria for a partial response

TABLE 3. Best International Working Group Response Attained on Trial, N = 19

Characteristic	No. of Patients(%)
Overall response rate	2 (10.5)
CR	0 (0.0)
CRi/CRp	2 (10.5)[a]
PR/MLFS	0 (0.0)
50% Blast reduction without count recovery[b]	3 (15.8)
Stable disease >6 mo[c]	1 (5.3)
Nonresponders	13 (68.4)
Median no. of cycles to best response	
CRi/CRp	1
Blast reduction: Median [range][b]	1 [1-3]
30-Day mortality	2 (10.5)
60-Day mortality	4 (21.0)

Abbreviations: CR, complete remission; CRi, complete remission with incomplete count recovery; CRp, complete remission with residual thrombocytopenia; MLFS, morphologic leukemia-free state; PR, partial response.
[a]Both patients had CRp and were positive for minimal residual disease by flow cytometry through response.
[b]Blast reduction without count recovery was defined as a reduction in the bone marrow blast percentage by at least one-half without recovery to an absolute neutrophil count ≥1000/μL and a platelet count ≥100,000/μL.
[c]Stable disease was defined as the absence of CR, CRi, PR, MLFS, hematologic improvement without evidence of clinical deterioration or progressive disease, maintained >6 months on study. The stable disease in this patient was maintained for 7.8 months.

or for CR/CRi/CRp, and 1 patient had stable disease for 7.8 months. The remaining 13 patients had no evidence of response or clinical benefit. The 30-day mortality was 11%; 1 patient died on day 4 from rapidly progressive disease, and one patient died on day 21 from sepsis secondary to pneumonia. An additional 2 deaths occurred between treatment days 31 and 60; 1 from rapidly progressive disease after 1 cycle with transition to hospice care and the other during cycle 2 from unknown causes at home. At the time of data analysis, all 19 patients had died. The median EFS was 3.6 months (range, 0.1-10.2 months) (Fig. 1A). The median OS was 4.8 months (range, 0.1-11 months) (Fig. 1B). The median OS in salvage 1 versus salvage >1 patients was 5.8 versus 4.6 months ($P = .84$), respectively. The median OS in *TP53*-mutated patients was 4.8 months. The median OS in patients with prior HMA exposure versus HMA-naive patients was 5.7 versus 4.6 months ($P = .53$), respectively. The 2 patients who achieved CRp had an OS of 10.2 and 11 months.

Immune Profiling by Mass Cytometry

To characterize cellular markers that may predict ICI efficacy, we performed mass cytometry (CyTOF) on BM aspirate and PB samples from 9 patients who were treated on study. We first assessed pretherapy PD-L1 and PD-L2 surface expression by performing CyTOF on nonpermeabilized BM and PB blasts (Fig. 2). For all patients

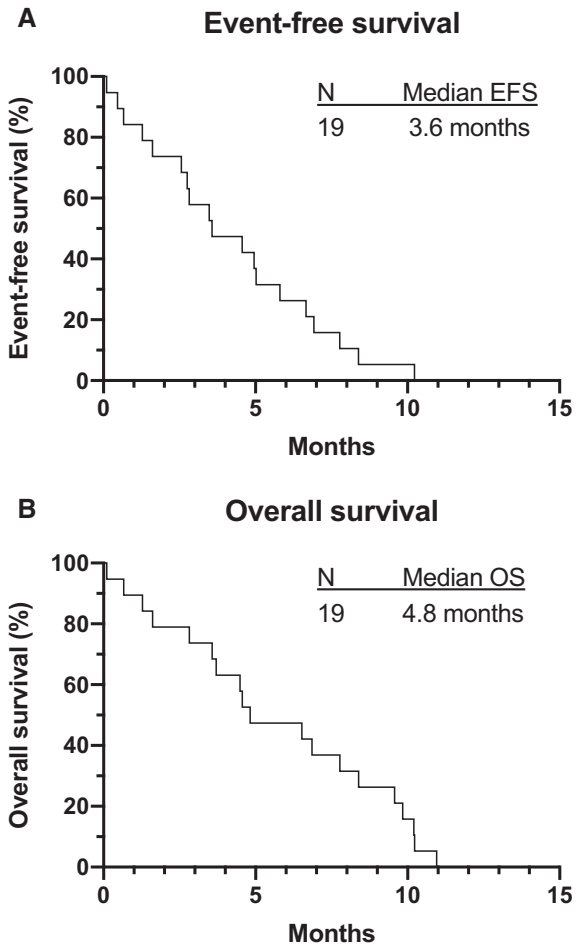

Figure 1. Survival analyses, including (A) event-free survival (EFS) and (B) overall survival (OS), are illustrated for all 19 patients who were treated on the clinical trial of azacitidine plus avelumab.

assessed, there were significantly more BM blasts expressing PD-L2 than PD-L1 (median, 34.9% vs 12%; $P < .005$) (Table 4). Double-positive (PD-L1-positive/PD-L2-positive) blasts accounted for only 4% (median) of BM blasts. Similar to BM blasts, PB blasts displayed higher expression of PD-L2 versus PD-L1 (Figs. 2 and 3).

Next, we assessed whether the percentage of BM blasts expressing PD-L2 and PD-L1 changed during treatment with azacitidine plus avelumab by performing mass cytometry on serially obtained BM aspirate samples from 8 patients. For all 8 patients, PD-L2 expression remained more abundant than PD-L1 expression at each time point (see Supporting Fig. 1). Finally, we evaluated BM blast expression of other immune-related markers, including OX40, LAG3, PD-1, and CTLA-4. Expression of these markers was assessed pretherapy and compared with expression on BM blasts from samples obtained before trial discontinuation

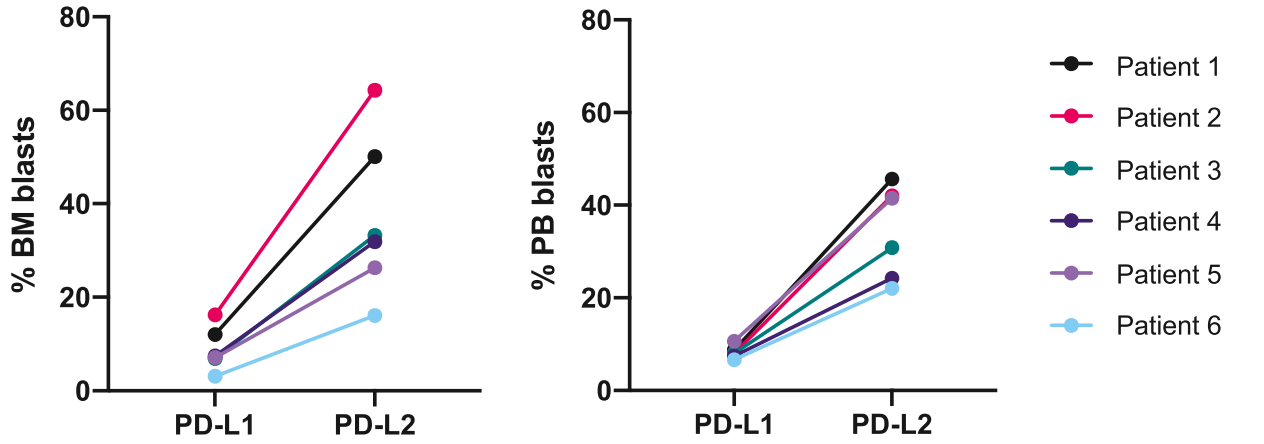

Figure 2. Pretreatment PD-L1 and PD-L2 expression levels are illustrated on peripheral blood (PB) blasts and bone marrow (BM) blasts in 6 patients. Displayed are the percentages of acute myeloid leukemia blasts that were PD-L1–positive versus PD-L2–positive in (*Left*) BM and (*Right*) PB in pretreatment samples from 6 different patients.

TABLE 4. Immunophenotype of Bone Marrow Blasts Pretreatment With Azacitidine Plus Avelumab

Patient	% Bone Marrow Blasts	% PD-L1+	% PD-L2+	% PD-L1+/PD-L2+ (Double Positive)	Best Response on Therapy
1	28	12.0	50.1	6.6	Stable disease
2	53	16.2	64.3	10.7	No response
3	27	9.0	34.9	3.2	No response
4	59	8.2	26.9	2.4	No response
5	7	7.1	26.3	4.0	CRp
6	51	3.1	16.9	0.6	Blast reduction
7	45	12.4	32.9	4.0	No response
8	38	21.9	53.3	11.3	No response
9	57	31.6	62.4	21.3	No response

Abbreviations: +, positive; CRp, complete remission with residual thrombocytopenia.

to assess increase, decrease, or stable expression of the immune marker on BM blasts (see Supporting Fig. 2). We noted that PD-L2 was the most frequent immune marker to be increased by >5% from baseline on BM blasts (in 5 of 8 patients) during treatment. No other correlations were found in the change in blast surface immune-related marker expression during treatment. Most of the immune checkpoints interrogated were present on only a subset of BM blasts in each patient, and PD-L2 (median, 34%), TIGIT (median, 20.5%), and CTLA-4 (median, 18.5%) were the most abundant checkpoints expressed at baseline. Given that only 2 of the patients analyzed had evidence of an antileukemic response to treatment (2 of 8 evaluated [patients 5 and 6]), we did not perform analysis comparing responders with nonresponders.

DISCUSSION

On the basis of historical evidence of a T-cell–mediated antileukemic effect from allo-SCT and donor lymphocyte infusion, as well as more recent data demonstrating early efficacy signals of CTLA-4 and PD-1 ICIs in AML, we conducted a study to assess the combination of azacitidine and the anti–PD-L1 antibody avelumab in patients with R/R AML. The regimen was well tolerated. Four patients died while on active treatment; no deaths were directly attributable to treatment. Only 2 patients had irAEs (both pneumonitis), and 1 patient permanently discontinued avelumab treatment because of the irAE (grade 2 pneumonitis). Notably, this patient was 1 of only 2 patients who experienced an objective response, with a BM blast reduction from 35% to 4%. Although the patient only received 1 dose of avelumab (after which he developed pneumonitis), he maintained a clinical response to azacitidine monotherapy for several more cycles, suggesting the possibility of immune-mediated disease control. In solid tumor malignancies, the occurrence of irAEs may correlate with enhanced response to ICI therapy.[41]

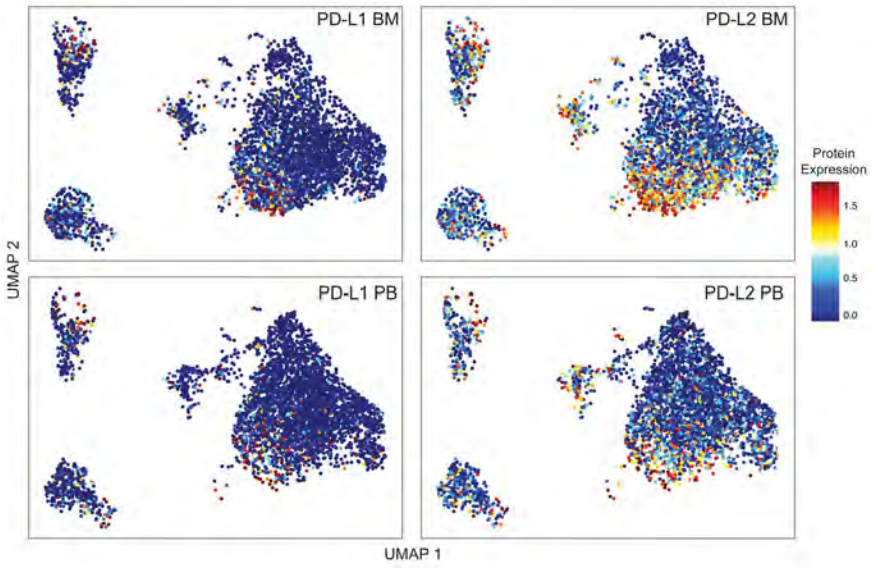

Figure 3. Representative PD-L1/PD-L2 baseline expression in bone marrow (BM) and peripheral blood (PB) are shown. This representative cytometry by time-of-flight plot from a patient's BM and PB illustrates relative PD-L1 and PD-L2 expression on blasts.

The ORR in this study was 11% (both CRp), with a median OS of 4.8 months in all patients and a median OS of 5.7 months in previously HMA-naive patients. This efficacy is comparable to the historical CR/CRi rate of 16% and the median OS of 6.7 months achieved with azacitidine monotherapy in a large cohort of previously HMA-naive patients with R/R AML and suggests that the addition of avelumab did not add clinical benefit.[4] These results stand in contrast to those from a previous phase 2 study of azacitidine plus nivolumab for R/R AML (ClinicalTrials.gov identifier NCT02397720) in which the ORR was 33% (CR/CRi rate, 22%), the median OS in all patients was 6.3 months, and the median OS in salvage 1 patients was 10.6 months.[7] In that study, previously HMA-naive patients had a very encouraging ORR of 52%. Both the current study and the azacitidine plus nivolumab study were conducted in a similar patient population during similar time frames at the same institution: median age, 66 versus 70 years; median 1 versus 2 prior lines of therapy; 63% versus 64% of patients with prior HMA exposure; median pretreatment BM blast percentage, 35% versus 40%; and 16% versus 19% with prior allo-SCT.[7] Thus the main apparent difference between these 2 studies, with the caveats of cross-trial comparisons, appears to be use of the anti–PD-1 nivolumab in the prior trial and use of the anti–PD-L1 avelumab in the current trial.

Interestingly, these results do not appear unique to nivolumab or avelumab. Two additional phase 2 trials of ICI for AML recently performed at other centers also suggest contrasting efficacy between anti–PD-1 and anti–PD-L1 therapy. In a phase 2 study of the anti–PD-1 ICI pembrolizumab with azacitidine (ClinicalTrials.gov identifier NCT02845297), 2 cohorts were enrolled: 1 cohort of patients with R/R AML and 1 cohort of treatment-naive patients who were ineligible for intensive chemotherapy.[9] In the R/R AML cohort, the ORR was 32% (CR/CRi, 14%) with median OS of 10.8 months, similar to results from the azacitidine plus nivolumab study.[9] Notably, the treatment-naive cohort had an ORR of 71% (CR/CRi, 47%) and a median OS of 13.1 months.[9] A separate international, randomized phase 2 study compared azacitidine with or without the anti–PD-L1 durvalumab for frontline treatment-naive patients who had higher risk MDS or AML (ClinicalTrials.gov identifier NCT02775903).[11] That study included 129 patients with AML: 64 patients received azacitidine with durvalumab, and 65 received azacitidine alone.[11] The CR/CRi rates were similar in both arms (31% vs 35%, respectively), as was the median OS (13 vs 14.4 months, respectively), suggesting no benefit from the addition of durvalumab.[11] Thus, based on these 4 publicly presented studies of azacitidine with ICI for patients with AML, 2 conclusions may be suggested. First, azacitidine with an ICI (anti–PD-1 or anti–PD-L1), as with almost all other AML therapies, appears to be

more effective in treatment-naive patients than in patients with R/R disease. Second, regardless of frontline or R/R disease, anti–PD-L1 therapy appears to generate inferior response and OS compared with anti–PD-1 therapy in combination with azacitidine. It is important to note that both of these conclusions must be interpreted within the limitations and constraints of cross-trial comparisons, and with only 1 of the 4 studies including a randomized cohort (azacitidine with or without durvalumab).

Given that ICI therapy with PD-1 versus PD-L1 blockade has not been directly assessed in a randomized trial for any malignancy, it must be acknowledged that comparing these 2 approaches implements an inherently biased method of comparing outcomes between clinical trials. However, there is precedent for anti–PD-1 therapy to lead to improved outcomes compared with anti–PD-L1 therapy. In a recently published meta-analysis of 19 randomized controlled trials of ICI therapy with anti–PD-1 versus anti–PD-L1 for solid tumors, anti–PD-1–based therapy resulted in improved OS and progression-free survival compared with anti–PD-L1.[42] It is possible that a similar phenomenon exists in AML. The basis for such a difference may be caused in part by the inability of anti–PD-L1 ICIs to block PD-L2. In the classic PD-1–mediated immune axis, tumor cells expressing PD-L1 and/or PD-L2 can engage the PD-1 receptor on circulating/infiltrating T cells, thereby promoting peripheral immune tolerance of tumor cells.[5] PD-L1 is expressed on numerous cell types, whereas PD-L2 is expressed primarily on hematopoietic cells, including myeloid leukocytes.[43-46] Emerging data have shown that PD-L2 may play an important role in solid tumor immune evasion and that PD-L2 has a higher affinity for PD-1 than does PD-L1.[47,48] Because anti–PD-1 antibodies block the interaction between PD-1/PD-L1 and PD-1/PD-L2, both ligands are blocked with these ICIs, whereas anti–PD-L1 antibodies leave PD-L2 free to engage PD-1 and potentially allow immune evasion/tolerance.

AML blasts have been shown to express *PD-L1*, *PD-L2*, and *PD-1* at the mRNA level, and coexpression of different immune checkpoint transcripts correlates with inferior outcomes.[25,26] Expression of mRNA does not always correlate with protein expression (including for *PD-L1* and *PD-L2*) and, to our knowledge, PD-L2 surface protein expression has not been extensively characterized on AML blasts.[45] We found that 8 of 9 patients assessed by mass cytometry had >25% PD-L2–positive pretreatment blasts (median PD-L2 protein expression on blasts, 34.9%). By comparison, only 1 of 9 patients had >25% PD-L1–positive pretreatment blasts (median PD-L1 expression, 12%). Given that these patients had not had prior ICI exposure pretreatment, these data suggest that the elevated baseline PD-L2:PD-L1 ratio was not due to selective pressure by treatment with an anti–PD-L1 antibody. Although surface expression patterns varied during treatment, all patients assessed had more blasts expressing PD-L2 compared with PD-L1 at each time point. Furthermore, in nearly all patients at each time point examined, PD-L2 was the most frequently expressed of 10 examined immune markers on BM blasts. PD-L2 was also the most common immune marker for which BM expression increased by >5% on BM blasts from pretreatment to end of treatment. Although our study is limited by a small sample size, and only a subset of patients had BM aspirate samples with sufficient quality/quantity of cells to undergo immune marker profiling by CyTOF, the conserved findings across all examined patients at all time points of higher PD-L2 surface protein expression on BM blasts compared with PD-L1 appears notable. Together, these data suggest that high pretherapy PD-L2 expression and increasing on-therapy PD-L2 expression may have promoted PD-L2–mediated escape from anti–PD-L1 therapy. To our knowledge, this study provides the first characterization of PD-L2 surface expression on AML blasts and provides a baseline observation on which to pursue future studies investigating PD-L2 as a potential means of immune escape in AML.

In conclusion, blockade of the PD-1/PD-L axis with anti–PD-1 antibodies may be a superior method of disrupting peripheral immune tolerance than anti–PD-L1 ICIs for AML because of the high expression of PD-L2 found on AML blasts. Future ICI studies in myeloid malignancies may be best served by focusing on anti PD-1–based therapies.

FUNDING SUPPORT

This work was supported in part by The University of Texas MD Anderson Cancer Center Support Grant (CA016672), The University of Texas MD Anderson Cancer Center Leukemia Specialized Programs of Research Excellence grant (CA100632), the Charif Souki Cancer Research Fund, the Dick Clark Immunotherapy Fund, and generous philanthropic contributions to the MD Anderson Moon Shots Program.

CONFLICT OF INTEREST DISCLOSURES

Tapan M. Kadia reports grants from Amgen, Ascentage, AstraZeneca, Bristol-Myers Squibb, Celgene, and Incyte; grants and personal fees from AbbVie, Genentech, Jazz Pharmaceuticals, and Pfizer; and personal fees from Novartis outside the submitted work. Courtney D. DiNardo reports grants from Calithera; grants and personal fees from AbbVie, Agios, Celgene, Daiichi Sankyo, ImmuneOnc, and Novartis; and personal fees Bayer, Jazz Pharmaceuticals, MedImmune, and Notable Labs outside the submitted work. Elias Jabbour reports research grants and consultancy from AbbVie, Adaptive Biotechnology, Amgen, Bristol-Myers Squibb, Pfizer, and Takeda outside the submitted work. Farhad

Ravandi reports honoraria from Daichii, and honoraria and service on an advisory board from Astellas and Novartis. Marina Konopleva reports grants from Ablynx, Agios, Ascentage, AstraZeneca, Calithera, Cellectis, Eli Lilly, Rafael Pharmaceutical, and Sanofi; grants and other support from AbbVie, F. Hoffman La-Roche, Forty-Seven, Genentech, and Stemline Therapeutics; and other support from Amgen, Kisoji, Reata Pharmaceutical outside the submitted work; and has a patent (US 7,795,305 B2: "CDDO-Compounds and Combination Therapie") with royalties paid to Reata Pharm, a patent ("Combination Therapy With a Mutant IDH1 Inhibitor and a BCL-2") licensed to Eli Lilly, and a patent (62/993,166: Combination of a MCL-1 Inhibitor and Midostaurin, Uses and Pharmaceutical Compositions Thereof") pending to Novartis. Naval Daver reports research funding from AbbVie, Amgen, Astellas, Bristol-Myers Squibb, Daiichi Sankyo, FATE Therapeutics, Genentech, Gilead, Glycomimetics, Hanmi, ImmunoGen, Karyopharm, Newave, Novimmune, Pfizer, Sevier, Trillium, and Trovagene; personal fees from AbbVie, Agios, Astellas, Bristol-Myers Squibb, Celgene, Daiichi Sankyo, Genentech, Gilead, KITE, Novartis, Pfizer, Servier, STAR Therapeutics, Syndax, Trillium, and Trovagene; grants from the SagerStrong Foundation; grants and other support from Affymetrix; personal fees from Blueprint Medicines, Incyte, LFB Biotechnologies, Pacylex Pharmaceuticals, and Roche Diagnostics; other support from Cellectis, Daiichi Sankyo, Plexxikon, and Samus Therapeutics; personal fees and other support from Celgene, DAVA Oncology, MustangBio, and Novartis; and personal fees, nonfinancial support, and other support from AbbVie and Stemline Therapeutics outside the submitted work. The remaining authors made no disclosures.

AUTHOR CONTRIBUTIONS

Kapil Saxena: Designed the study, collected and analyzed the data, and wrote the article. **Shelley Herbrich:** Designed the study, collected and analyzed the data, and wrote the article. **Naveen Pemmaraju:** Enrolled patients. **Tapan M. Kadia:** Enrolled patients. **Courtney D. DiNardo:** Enrolled patients. **Gautam Borthakur:** Enrolled patients. **Sherry Pierce:** Collected and analyzed the data. **Elias Jabbour:** Enrolled patients. **Sa A. Wang:** Performed the molecular and cytogenetic analysis. **Carlos Bueso-Ramos:** Performed the molecular and cytogenetic analysis. **Sanam Loghavi:** Performed the molecular and cytogenetic analysis. **Guillin Tang:** Performed the molecular and cytogenetic analysis. **Cora M. Cheung:** Enrolled patients. **Lynette Alexander:** Enrolled patients. **Steven Kornblau:** Enrolled patients. **Michael Andreeff:** Enrolled patients. **Guillermo Garcia-Manero:** Enrolled patients. **Farhad Ravandi:** Enrolled patients. **Marina Konopleva:** Designed the study, enrolled patients, collected and analyzed the data, and wrote the article. **Naval Daver:** Designed the study, enrolled patients, collected and analyzed the data, and wrote the article. All authors contributed to data collection, reviewed and approved the article, and shared final responsibility for the decision to submit the article for publication.

REFERENCES

1. Short NJ, Konopleva M, Kadia TM, et al. Advances in the treatment of acute myeloid leukemia: new drugs and new challenges. *Cancer Discov*. 2020;10:506-525. doi:10.1158/2159-8290.CD-19-1011
2. Ravandi F, Ritchie EK, Sayar H, et al. Vosaroxin plus cytarabine versus placebo plus cytarabine in patients with first relapsed or refractory acute myeloid leukaemia (VALOR): a randomised, controlled, double-blind, multinational, phase 3 study. *Lancet Oncol*. 2015;16:1025-1036. doi:10.1016/S1470-2045(15)00201-6
3. Roboz GJ, Rosenblat T, Arellano M, et al. International randomized phase III study of elacytarabine versus investigator choice in patients with relapsed/refractory acute myeloid leukemia. *J Clin Oncol*. 2014;32:1919-1926. doi:10.1200/JCO.2013.52.8562
4. Stahl M, DeVeaux M, Montesinos P, et al. Hypomethylating agents in relapsed and refractory AML: outcomes and their predictors in a large international patient cohort. *Blood Adv*. 2018;2:923-932. doi:10.1182/bloodadvances.2018016121
5. Wei SC, Duffy CR, Allison JP. Fundamental mechanisms of immune checkpoint blockade therapy. *Cancer Discov*. 2018;8:1069-1086. doi:10.1158/2159-8290.CD-18-0367
6. Vaddepally RK, Kharel P, Pandey R, Garje R, Chandra AB. Review of indications of FDA-approved immune checkpoint inhibitors per NCCN Guidelines with the level of evidence. *Cancers (Basel)*. 2020;12:738. doi:10.3390/cancers12030738
7. Daver N, Garcia-Manero G, Basu S, et al. Efficacy, safety, and biomarkers of response to azacitidine and nivolumab in relapsed/refractory acute myeloid leukemia: a nonrandomized, open-label, phase II study. *Cancer Discov*. 2019;9:370-383. doi:10.1158/2159-8290.CD-18-0774
8. Davids MS, Kim HT, Bachireddy P, et al. Ipilimumab for patients with relapse after allogeneic transplantation. *N Engl J Med*. 2016;375:143-153. doi:10.1056/NEJMoa1601202
9. Gojo I, Stuart RK, Webster J, Zeidner JF. Multi-center phase 2 study of pembrolizumab (Pembro) and azacitidine (AZA) in patients with relapsed/refractory acute myeloid leukemia (AML) and in newly diagnosed (≥65 Years) AML patients [abstract]. *Blood*. 2019;134(suppl 1):832.
10. Ravandi F, Assi R, Daver N, et al. Idarubicin, cytarabine, and nivolumab in patients with newly diagnosed acute myeloid leukaemia or high-risk myelodysplastic syndrome: a single-arm, phase 2 study. *Lancet Haematol*. 2019;6:e480-e488. doi:10.1016/S2352-3026(19)30114-0
11. Zeidan AM, Cavenagh J, Voso MT, Silverman LR. Efficacy and safety of azacitidine (AZA) in combination with the anti-PD-L1 durvalumab (Durva) for the front-line treatment of older patients (pts) with acute myeloid leukemia (AML) who are unfit for intensive chemotherapy (IC) and pts with higher-risk myelodysplastic syndromes (HR-MDS): results from a large, international, randomized phase 2 study [abstract]. *Blood*. 2019;134(suppl 1):829.
12. Zeidner JF, Vincent BG, Esparza S, Ivanova A. Final clinical results of a phase II study of high dose cytarabine followed by pembrolizumab in relapsed/refractory AML [abstract]. *Blood*. 2019;134(suppl 1):831.
13. Mussai F, De Santo C, Abu-Dayyeh I, et al. Acute myeloid leukemia creates an arginase-dependent immunosuppressive microenvironment. *Blood*. 2013;122:749-758. doi:10.1182/blood-2013-01-480129
14. Mussai F, Egan S, Higginbotham-Jones J, et al. Arginine dependence of acute myeloid leukemia blast proliferation: a novel therapeutic target. *Blood*. 2015;125:2386-2396. doi:10.1182/blood-2014-09-600643
15. Muller-Thomas C, Heider M, Piontek G, et al. Prognostic value of indoleamine 2,3 dioxygenase in patients with higher-risk myelodysplastic syndromes treated with azacytidine. *Br J Haematol*. 2020;190:361-370. doi:10.1111/bjh.16652
16. Lamble AJ, Lind EF. Targeting the immune microenvironment in acute myeloid leukemia: a focus on T cell immunity. *Front Oncol*. 2018;8:213. doi:10.3389/fonc.2018.00213
17. Yarchoan M, Hopkins A, Jaffee EM. Tumor mutational burden and response rate to PD-1 inhibition. *N Engl J Med*. 2017;377:2500-2501. doi:10.1056/NEJMc1713444
18. Chalmers ZR, Connelly CF, Fabrizio D, et al. Analysis of 100,000 human cancer genomes reveals the landscape of tumor mutational burden. *Genome Med*. 2017;9:34. doi:10.1186/s13073-017-0424-2
19. Horowitz MM, Gale RP, Sondel PM, et al. Graft-versus-leukemia reactions after bone marrow transplantation. *Blood*. 1990;75:555-562.
20. Weiden PL, Flournoy N, Thomas ED, et al. Antileukemic effect of graft-versus-host disease in human recipients of allogeneic-marrow grafts. *N Engl J Med*. 1979;300:1068-1073. doi:10.1056/NEJM197905103001902
21. Schmid C, Labopin M, Nagler A, et al. Donor lymphocyte infusion in the treatment of first hematological relapse after allogeneic stem-cell transplantation in adults with acute myeloid leukemia: a retrospective risk factors analysis and comparison with other strategies by the EBMT Acute Leukemia Working Party. *J Clin Oncol*. 2007;25:4938-4945. doi:10.1200/JCO.2007.11.6053
22. Teague RM, Kline J. Immune evasion in acute myeloid leukemia: current concepts and future directions. *J Immunother Cancer*. 2013;1:1. doi:10.1186/2051-1426-1-13
23. Brodska B, Otevrelova P, Kuzelova K. Correlation of PD-L1 surface expression on leukemia cells with the ratio of PD-L1 mRNA variants and with electrophoretic mobility. *Cancer Immunol Res*. 2016;4:815-819. doi:10.1158/2326-6066.CIR-16-0063
24. Brodska B, Otevrelova P, Salek C, Fuchs O, Gasova Z, Kuzelova K. High PD-L1 expression predicts for worse outcome of leukemia patients with concomitant NPM1 and FLT3 mutations. *Int J Mol Sci*. 2019;20:2823. doi:10.3390/ijms20112823
25. Yang H, Bueso-Ramos C, DiNardo C, et al. Expression of PD-L1, PD-L2, PD-1 and CTLA4 in myelodysplastic syndromes is enhanced

by treatment with hypomethylating agents. *Leukemia*. 2014;28:1280-1288. doi:10.1038/leu.2013.355
26. Chen C, Liang C, Wang S, et al. Expression patterns of immune checkpoints in acute myeloid leukemia. *J Hematol Oncol*. 2020;13:28. doi:10.1186/s13045-020-00853-x
27. Zhang L, Gajewski TF, Kline J. PD-1/PD-L1 interactions inhibit antitumor immune responses in a murine acute myeloid leukemia model. *Blood*. 2009;114:1545-1552. doi:10.1182/blood-2009-03-206672
28. Zhou Q, Munger ME, Highfill SL, et al. Program death-1 signaling and regulatory T cells collaborate to resist the function of adoptively transferred cytotoxic T lymphocytes in advanced acute myeloid leukemia. *Blood*. 2010;116:2484-2493. doi:10.1182/blood-2010-03-275446
29. Zhou Q, Munger ME, Veenstra RG, et al. Coexpression of Tim-3 and PD-1 identifies a CD8+ T-cell exhaustion phenotype in mice with disseminated acute myelogenous leukemia. *Blood*. 2011;117:4501-4510. doi:10.1182/blood-2010-10-310425
30. Assi R, Kantarjian H, Ravandi F, Daver N. Immune therapies in acute myeloid leukemia: a focus on monoclonal antibodies and immune checkpoint inhibitors. *Curr Opin Hematol*. 2018;25:136-145. doi:10.1097/MOH.0000000000000401
31. Williams P, Basu S, Garcia-Manero G, et al. The distribution of T-cell subsets and the expression of immune checkpoint receptors and ligands in patients with newly diagnosed and relapsed acute myeloid leukemia. *Cancer*. 2019;125:1470-1481. doi:10.1002/cncr.31896
32. Daver N, Boddu P, Garcia-Manero G, et al. Hypomethylating agents in combination with immune checkpoint inhibitors in acute myeloid leukemia and myelodysplastic syndromes. *Leukemia*. 2018;32:1094-1105. doi:10.1038/s41375-018-0070-8
33. De Sousa Linhares A, Battin C, Jutz S, et al. Therapeutic PD-L1 antibodies are more effective than PD-1 antibodies in blocking PD-1/PD-L1 signaling. *Sci Rep*. 2019;9:11472. doi:10.1038/s41598-019-47910-1
34. Cheson BD, Bennett JM, Kopecky KJ, et al. Revised recommendations of the International Working Group for Diagnosis, Standardization of Response Criteria, Treatment Outcomes, and Reporting Standards for Therapeutic Trials in Acute Myeloid Leukemia. *J Clin Oncol*. 2003;21:4642-4649. doi:10.1200/JCO.2003.04.036
35. Thall PF, Sung HG. Some extensions and applications of a Bayesian strategy for monitoring multiple outcomes in clinical trials. *Stat Med*. 1998;17:1563-1580. doi:10.1002/(sici)1097-0258(19980730)17:14<1563::aid-sim873>3.0.co;2-l
36. Chen H, Lau MC, Wong MT, Newell EW, Poidinger M, Chen J. Cytofkit: a Bioconductor package for an integrated mass cytometry data analysis pipeline. *PLoS Comput Biol*. 2016;12:e1005112. doi:10.1371/journal.pcbi.1005112
37. Hahne F, LeMeur N, Brinkman RR, et al. flowCore: a Bioconductor package for high throughput flow cytometry. *BMC Bioinformatics*. 2009;10:106. doi:10.1186/1471-2105-10-106
38. Levine JH, Simonds EF, Bendall SC, et al. Data-driven phenotypic dissection of AML reveals progenitor-like cells that correlate with prognosis. *Cell*. 2015;162:184-197. doi:10.1016/j.cell.2015.05.047
39. Becht E, McInnes L, Healy J, et al. Dimensionality reduction for visualizing single-cell data using UMAP. *Nat Biotechnol*. 2019;37:38-44. doi:10.1038/nbt.4314
40. Dohner H, Estey E, Grimwade D, et al. Diagnosis and management of AML in adults: 2017 ELN recommendations from an international expert panel. *Blood*. 2017;129:424-447. doi:10.1182/blood-2016-08-733196
41. Zhou X, Yao Z, Yang H, Liang N, Zhang X, Zhang F. Are immune-related adverse events associated with the efficacy of immune checkpoint inhibitors in patients with cancer? A systematic review and meta-analysis. *BMC Med*. 2020;18:87. doi:10.1186/s12916-020-01549-2
42. Duan J, Cui L, Zhao X, et al. Use of immunotherapy with programmed cell death 1 vs programmed cell death ligand 1 inhibitors in patients with cancer: a systematic review and meta-analysis. *JAMA Oncol*. 2020;6:375-384. doi:10.1001/jamaoncol.2019.5367
43. Giannopoulos K. Targeting immune signaling checkpoints in acute myeloid leukemia. *J Clin Med*. 2019;8:236. doi:10.3390/jcm8020236
44. Latchman Y, Wood CR, Chernova T, et al. PD-L2 is a second ligand for PD-1 and inhibits T cell activation. *Nat Immunol*. 2001;2:261-268. doi:10.1038/85330
45. Okazaki T, Honjo T. PD-1 and PD-1 ligands: from discovery to clinical application. *Int Immunol*. 2007;19:813-824. doi:10.1093/intimm/dxm057
46. Freeman GJ, Long AJ, Iwai Y, et al. Engagement of the PD-1 immunoinhibitory receptor by a novel B7 family member leads to negative regulation of lymphocyte activation. *J Exp Med*. 2000;192:1027-1034. doi:10.1084/jem.192.7.1027
47. Philips EA, Garcia-Espana A, Tocheva AS, et al. The structural features that distinguish PD-L2 from PD-L1 emerged in placental mammals. *J Biol Chem*. 2020;295:4372-4380. doi:10.1074/jbc.AC119.011747
48. Yang H, Zhou X, Sun L, Mao Y. Correlation between PD-L2 expression and clinical outcome in solid cancer patients: a meta-analysis. *Front Oncol*. 2019;9:47. doi:10.3389/fonc.2019.00047

CyTOF XT

The Next Generation of Mass Cytometry

Introduction

CyTOF® Technology. Mass cytometry is a powerful technology that utilizes a time-of-flight mass spectrometer to enable the detection of single cells tagged with isotopically pure metal-labeled reagents. CyTOF overcomes the limitations of fluorescence-based detection systems by separating signals according to differences in isotope mass instead of wavelength. The negligible signal overlap between masses allows for simultaneous detection of over 50 targets in a single sample tube, a panel size that has not been achieved by any flow or spectral cytometer to date. The use of a universal internal standard—multi-element calibration beads—makes it possible to normalize data across instruments and experiments. Mass cytometry thus generates the highest-parameter snapshot of phenotype and function for every cell.

CyTOF Value. Mass cytometers provide impressively high resolution of cytometric profiles, empowering both basic research and practical biomarker-driven clinical research to potentially optimize and personalize disease management. CyTOF instruments have proven to be valuable additions to cytometry core facilities and service labs, and have been adopted for use by key clinical research consortia[1,2,3] and in scores of Clinical Research Trials (see Related documents).

The NeXT Generation. Fluidigm now introduces a new generation of mass cytometer, the CyTOF XT™, (Figure 1). The novel design, fully automated sample acquisition, and easier operational workflows of CyTOF XT simplify the planning and execution of high-parameter cell profiling studies.

Objectives

This application note presents information on key CyTOF XT features demonstrating the following advances in instrument benefits and performance:

- Fully automated acquisition with the new Autosampler to increase productivity and sample throughput with negligible carryover
- Unique system design and software logic to sense and remove clogs
- Automated detector voltage (DV) optimization to maintain signal stability during extended acquisitions
- High degree of agreement between data collected on CyTOF XT and Helios™ instruments
- An array of data management improvements, including on-the-fly normalization and processing, the latest industry file format (FCS 3.1), optimized storage requirements, a range of troubleshooting options, and many more

Figure 1. CyTOF XT, featuring a streamlined design and automatic sample acquisition.

CyTOF XT enables walk-away sample acquisition for increased productivity

Improving on previous CyTOF instruments that required manual loading of each sample before acquisition. CyTOF XT revolutionizes sample delivery with the Autosampler Module and a simplified front end assembly. The new Autosampler consists of 4 major components: the sample probe, a syringe-based pump unit, a tray for acquisition and cleaning solutions, and most important, a carousel that holds 13 sample tubes chilled at 4–8 °C. The Autosampler enables automated sample delivery over long acquisitions while maintaining sample integrity.

The CyTOF XT with the Autosampler Module automates the following processes:

- Tuning the instrument
- Cleaning the sample fluidics
- Acquisition of samples already in suspension
- Resuspension, addition of EQ™ Calibration Beads, and acquisition of pelleted samples
- Detection and removal of clogs

This combination of features greatly reduces the need for operator interaction with the instrument during sample acquisition. Hands-on interaction is required only to load calibration beads and set up samples in the carousel (Figure 2). In addition, CyTOF Software v8.0 for CyTOF XT performs data normalization during sample acquisition, which further frees up operator time while the data file is processed automatically.

Routine workday comparison

Although many workflow steps for Helios and CyTOF XT are similar, there are several key differences. Figure 2 highlights the significant time savings and streamlined workflow of a model workday using CyTOF XT as compared to a workday with Helios. In this example (Figure 2A), 10 whole blood samples stained with the Maxpar® Direct™ Immune Profiling Assay™ (Cat. No. 201325) are acquired in a typical 8-hour workday. Highlighting the instrument's advancement in extended acquisition, Figure 2B demonstrates the ability of CyTOF XT to acquire 42 samples within a 23-hour period. The following sections describe these example workdays on Helios and CyTOF XT in greater detail.

Helios is optimized for single-tube data acquisition.

After the plasma is ignited and the Helios system is warmed up, tuning solution must be loaded manually, followed by instrument tuning, a bead sensitivity test, and conditioning of the plasma with Maxpar Cell Acquisition Solution (CAS, Cat. No. 201240). The first sample may then be loaded into the Sample Loader for acquisition according to the sample criteria selected. In the workday example (Figure 2A, Helios), purple time bars between samples indicate the manual handling steps, such as sample preparation (resuspension and filtering), data normalization, and cleaning between samples with CyTOF Washing Solution (Cat. No. 201071) and CAS. In this example, user intervention is required for routine instrument cleaning and shutdown procedures at the end of a workday. The Helios acquisition of these 10 samples with monitoring requires approximately 7 hr 15 min. (Figure 2A, Helios).

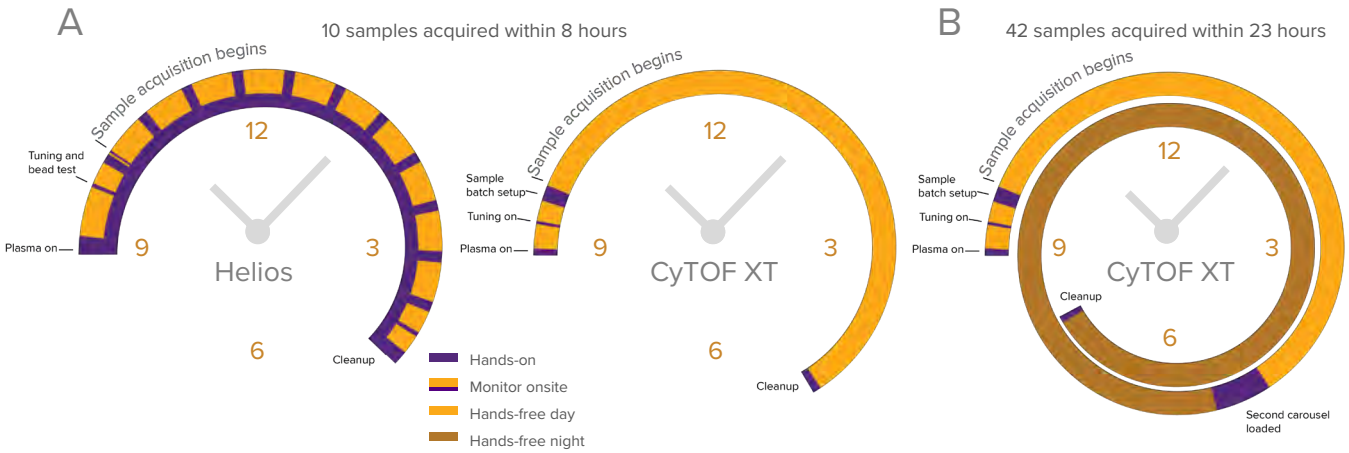

Figure 2. Comparison of a model workday on Helios and CyTOF XT. A) Representation of Helios (left) and CyTOF XT (right) acquisition of 10 tubes of whole blood samples stained with the Maxpar Direct Immune Profiling Assay. Each purple block represents hands-on time when interaction with the instrument is required. Orange blocks represent hands-free automated periods. **B)** Representation of an extended CyTOF XT acquisition when, upon completion of the first 10 samples, the carousel is reloaded with a new batch of 12 samples stained with the Maxpar Direct Immune Profiling Assay and 1 large-volume (12 mL) tube of a 20-plex barcoded sample for unattended acquisition. This model example illustrates how 42 samples could be acquired on the CyTOF XT within a 23-hour period.

CyTOF XT reduces hands-on instrument time and increases sample throughput.

CyTOF XT workflow steps are similar to those for Helios, but most are automated. An operator only needs to load the bottle tray with required solutions (including an improved high-ionic-strength solution, Maxpar Cell Acquisition Solution Plus for CyTOF XT, Cat. No. 201244), ignite and warm up plasma, start the automated tuning protocol, load the carousel with samples, select acquisition criteria, and walk away while the system does the rest (Figure 2A, CyTOF XT).

The CyTOF XT automatically adds EQ beads, resuspends pelleted samples and mixes prior to acquisition, performs washes, notifies the operator upon successful completion of a batch, normalizes and saves files, completes extended cleaning after batch acquisition, and shuts down plasma at the end of a workday. User attention is needed only for nebulizer maintenance cleaning after the instrument shuts itself down. The carousel is accessible during batch acquisition, allowing an operator to add new samples or replace the acquired tubes with a new batch of samples for continuous acquisition. Finally, the Autosampler carousel is cooled and kept at 4–8 °C, maintaining sample integrity for many hours and ensuring high quality data.

In contrast to Helios, the automated sample acquisition on CyTOF XT (Figure 2A, orange time bar) frees up operator time while instrument automation and programming do the work. Acquisition of the 10 assay tubes occurs unattended for 7 hr 50 min on the CyTOF XT, enabling the operator to perform other activities through the day.

CyTOF XT extends the workday with walk-away automation.

CyTOF XT provides an opportunity to go beyond the 8-hour workday with sample acquisition for an overnight run. Figure 2B illustrates how the Autosampler and CyTOF Software v8.0 for CyTOF XT enable increased sample throughput. An additional 12 samples stained with the Maxpar Direct Immune Profiling Assay plus a 20-plex barcoded sample may be run unattended overnight after a standard 8-hour workday on CyTOF XT, bringing the total number of samples run to 42.

Batch sample acquisition is possible because the Autosampler applies stringent washing conditions to ensure consistent data collection and reduce sample carryover, while detecting and resolving clogs during acquisition. Refer to the next sections for more about carryover tests and CyTOF XT unclogging capabilities.

CyTOF XT delivers sample batch acquisitions without sample carryover

The walk-away sample preparation and acquisition enabled by CyTOF XT is achieved through the sample handling advancements of the Autosampler. Sample carryover is a concern for any sample introduction system. This section describes the built-in cleaning of sample probe and Autosampler lines, which minimizes carryover.

CyTOF XT is designed to perform automated washes of the sample line fluidics. Both the inside and outside of the sample probe are washed between samples. Different pre-wash settings can be applied to avoid carryover depending on the sample type: Light, Medium (default setting), and Heavy, which vary in washing time, pulsing, and/or solutions used. For more information, refer to the CyTOF Software v8.0 Help for CyTOF XT (FLDM-00045), also available as the software integrated help guide.

To demonstrate the absence of unwanted sample carryover, the following test was performed.

Sample carryover study design

Two separate sets of human peripheral blood mononuclear cell (PBMC) samples were barcoded using 2 different barcoding workflows: Cell-ID™ 20-Plex Pd Barcoding Kit (Cat. No. 201060) for palladium (Pd) barcoding up to 20 samples, and 7 individual cadmium (Cd)-labeled anti-CD45 antibodies from Fluidigm for 35-plex live-cell barcoding. Barcoding uniquely labels multiple individual samples with a combination of Pd or Cd isotopes, allowing the samples to be pooled together in 1 tube for staining and acquisition. Individual samples can then be identified based on their unique combination of Pd or Cd isotopes. (To learn more about barcoding options, refer to The Benefits of Palladium Barcoding on Data Quality and Workflow (FLDM-00012) and Enabling Live-Cell Barcoding with Anti-CD45 Antibodies in Suspension Mass Cytometry (FLDM-00488) available at fluidigm.com.)

Replicates from each barcoded and pelleted sample were loaded into the CyTOF XT carousel in quadruplicate, in alternating order of Pd- and Cd-barcoded samples. The default pre-wash setting was applied before each sample. The number of all collected events per tube was approximately 2×10^6 for Pd-barcoded samples and 1.5×10^6 for Cd-barcoded samples.

Sample carryover test results and summary

The number of Pd-barcoded events carried over to Cd-barcoded samples was negligible. Fewer than 10 events

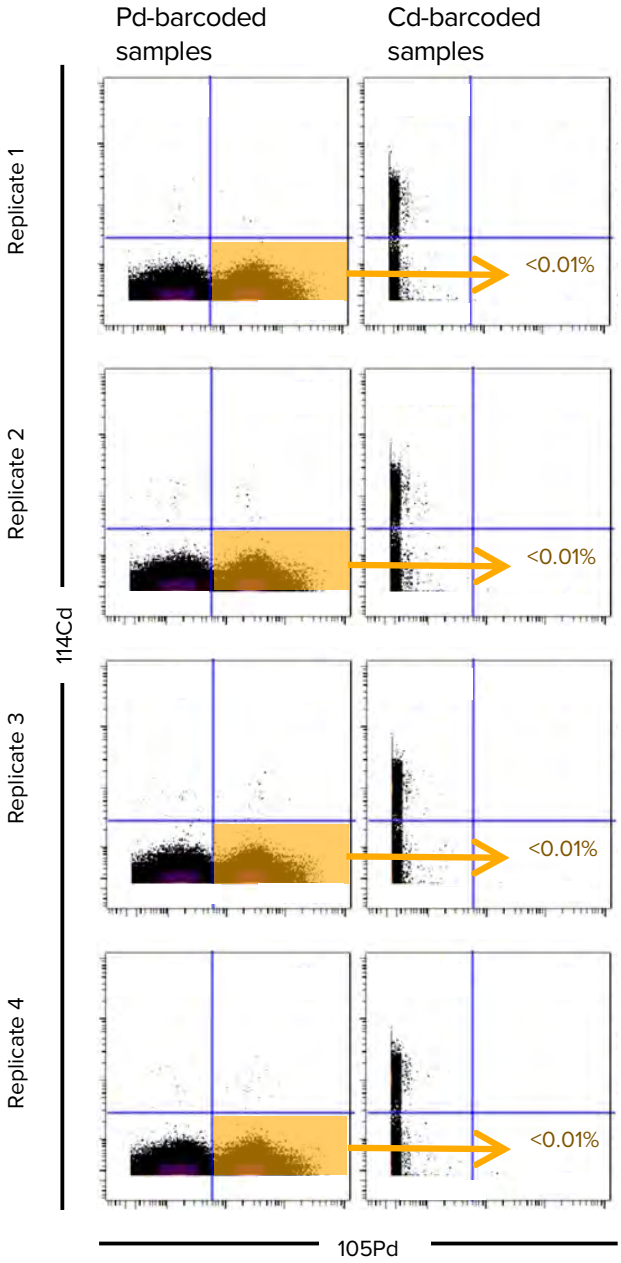

Figure 3. Negligible Pd-barcoded sample carryover observed in subsequent Cd-barcoded samples. A set of 8 Pd- and Cd-barcoded samples was run in quadruplicate in alternating order to assess the carryover of Pd-barcoded cells to the next Cd-barcoded sample. Default pre-wash settings were applied. Biaxial plots of ^{105}Pd vs. ^{114}Cd show Cd-positive and Pd-positive populations. Samples were gated on live singlet cell events identified using the cleanup strategy described in Approach to Bivariate Analysis of Data Acquired Using the Maxpar Direct Immune Profiling Assay (400248). The percentage of Pd-barcoded sample carryover is shown in the adjacent Cd-barcoded sample.

out of all 600,000 Pd+ live events, or <0.01% carryover, were observed (Figure 3). The results demonstrate that the Autosampler has effective washing between samples when default settings are used on the CyTOF XT. The automated pre-wash settings can be customized for more stringent cleaning if required for samples that are anticipated to be challenging to maintain in single-cell suspension. Following the clog prevention recommendations outlined in the next section on challenging sample handling will also minimize carryover.

CyTOF XT is uniquely designed to automatically detect and resolve clogs

Clogging can disrupt and delay cytometry instrument workflow. Helios and CyTOF XT rely on different strategies to manage and unclog the sample fluidics.

Clog management on Helios and CyTOF XT

For challenging samples on the Helios system, a clog becomes apparent when the sample flow rate drops from 30 µL/min to 0 µL/min. The operator must then perform a manual unclogging procedure.

In contrast to Helios, the CyTOF XT Autosampler software detects potential clogs by monitoring whether pressure and flow parameters fluctuate beyond set thresholds. Upon detecting a blockage, the software executes a routine that mimics the manual unclogging procedure typically performed by an operator. To best demonstrate the improvements made to clog management and resolution on CyTOF XT, a dissociated tissue sample test was performed.

Dissociated tissue sample study design for CyTOF XT

Multiple replicates of cells from dissociated mouse intestinal tissue were run for several hours on a CyTOF XT at the optimized concentration of 0.5 x 10^6 cells/mL. Dissociated cells from solid tissue were chosen because this sample type is known to be more difficult to maintain as a single-cell suspension. Dissociated mouse tissue samples were stained according to Maxpar Cell Surface Staining with Fresh Fix Protocol (400276) and prepared using validated workflows, which include filtering through 35 µm cell strainers before sample acquisition. A batch of 12 dissociated mouse intestinal cell samples in pelleted format was loaded into the carousel and a set volume was acquired. The pressure in the sample introduction line was monitored and recorded during sample acquisition. Sample pressure logs and data quality were analyzed upon completion of the run.

Dissociated tissue sample test results and summary

Figure 4A illustrates the pressure changes during the acquisition of the mouse intestinal cell samples using the default unclogging parameters on CyTOF XT. All samples were acquired successfully. As shown in Figure 4A, Sample 1 triggered the automated unclogging routine 4 times while Samples 2 and 3 were acquired without interruptions. Note that despite the occurrence of multiple clogs during the acquisition, marker signal intensity was not affected by the automated unclogging protocol as demonstrated by comparing Sample 1 to Sample 2 and Sample 3 (Figure 4B). Additionally, only approximately 14% of the expected 700,000 events were lost due to the 4 clogs in Sample 1 (Figure 4C). More important, the automated unclogging routine extended the acquisition by only 30 minutes and completed a batch of samples without need for manual intervention.

CyTOF XT is uniquely designed to detect and automatically resolve clogs. The combination of automated features (sample acquisition, unclogging, and instrument shutdown), makes CyTOF the most productive high-parameter cytometer on the market.

A

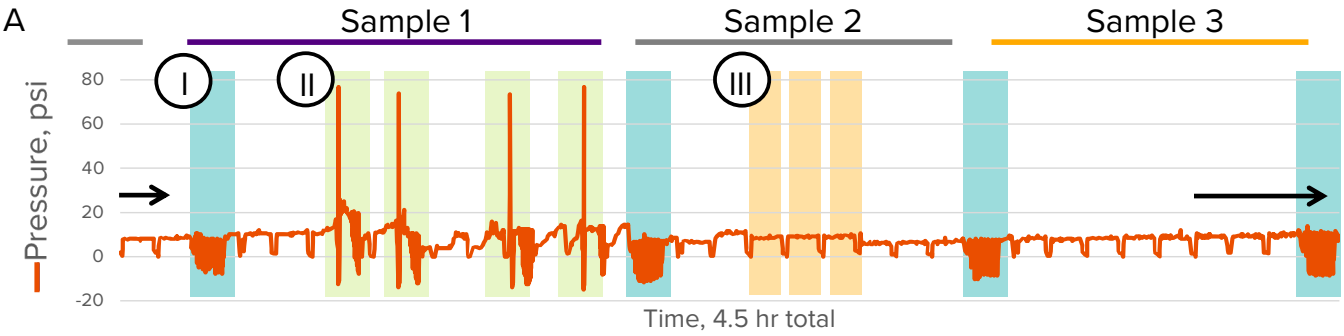

B

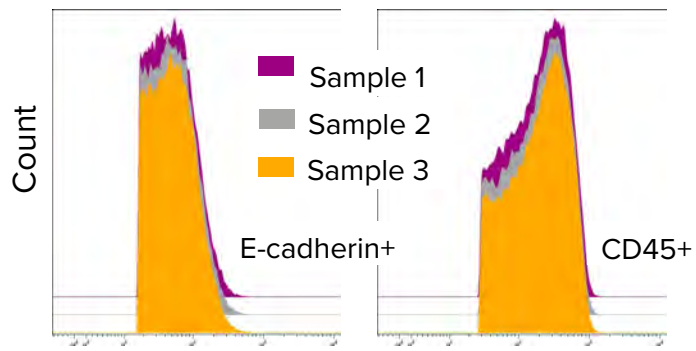

Median signal intensity	E-cadherin+	CD45+
Sample 1	49.068	206.416
Sample 2	49.518	207.846
Sample 3	49.895	210.411

C

	Sample 1	Sample 2	Sample 3
Events found	599,673	693,124	719,634
Bead events found	29,457	31,540	32,538
Time	1 hr 56 min	1 hr 29 min	1 hr 29 min
Clogs found	4	0	0
Clogs resolved	4	n/a	n/a

Figure 4. Automated unclogging by CyTOF XT resolves blockages with no impact on data quality. 12 samples (2.5 mL each) were acquired automatically with several occurrences of high pressure due to multiple clogs in single samples. **A)** Pressure monitoring of the 12 samples identified 3 consecutive samples with varying unclogging routine experiences. Section I (light blue) denotes washing steps between samples. During this time, rapid pressure swings are observed as positive to negative pressure readings, which function to remove the remaining sample in the line. Similarly, pressure during the unclogging routine (Section II, light green) fluctuates to effectively remove the clog and enable the continuation of the acquisition. A rhythmic pattern (Section III, light orange) in the pressure readings is seen in the acquisition of Sample 2 and Sample 3. This pattern is caused by the change in pressure detected between single loops of a sample that are loaded into the Autosampler module. The loop accommodates 250 µL of the sample volume and the entire acquisition happens in intervals, hence the rhythmic pressure pattern. **B)** The automatic unclogging routine did not impact signal intensity, as illustrated by the unchanged signal intensity of 2 major populations between all 3 samples. **C)** Summary of collected events and detected clogs.

Tips for success

Recommendations to reduce clogging:

Sample preparation. Wash samples with Maxpar CAS Plus twice immediately prior to loading the carousel.

Sample filtration. All samples should be filtered through appropriately sized cell strainers to prevent cell aggregates and large particles from entering the fluidics. Best practice is not to force the sample through the mesh with a pipette but instead gently pipette the sample through the mesh cap. Avoid using a pipette to aspirate any remaining sample from the inner side of the straining cap.

Cell concentration. Optimize cell concentration based on sample type. Acquire potentially challenging samples at 0.5 x 10^6 cells/mL or less.

Pre-wash settings. Select a heavy pre-wash cycle for challenging samples.

Acquisition volume. Split large volume samples into smaller volume acquisitions over multiple tubes.

Regular instrument maintenance is key. Clean and maintain parts and fluidics as per Fluidigm recommendation. For more detail, refer to the CyTOF XT User Guide (FLDM-00254) and the CyTOF Software v8.0 Help for CyTOF XT (FLDM-00045), also available as the software integrated help guide.

Detailed recommendations for reducing clogs can also be found in the CyTOF Software v8.0 Help for CyTOF XT (FLDM-00045).

CyTOF XT delivers optimal data quality over extended acquisitions.

In some cases, a typical workday of 8 hours may not be sufficient to fulfill the requirements of the experiment, as when running samples for a large study. Previous sections demonstrated that the CyTOF XT is uniquely designed to accommodate long unattended runs and can successfully resolve clogs and avoid sample carryover. The following section assesses the CyTOF XT detector's potential to maintain a high level of performance during long hours of ion detection.

A new feature of CyTOF XT is the automatic adjustment of the detector voltage. This ensures signal stability regardless of acquisition time.

Extended acquisition study design

The goal of this study was to confirm that all marker signal intensities were maintained at the same level and did not decrease over time due to any loss of sensitivity by the CyTOF XT detector. Twelve tubes containing various samples were loaded into the carousel for long-term unsupervised acquisition. To assess the impact of time on data quality, the first and last tube of the carousel were loaded with the same sample. This sample was prepared by staining PBMC with surface and nuclear markers according to the Maxpar Nuclear Antigen Staining with Fresh Fix Protocol (400277). The time difference between acquisition of the sample in Run 1 and Run 12 was approximately 19 hours. During this time, the chilled carousel maintained the samples in suspension at 4–8 °C. Test results are presented in Figure 5.

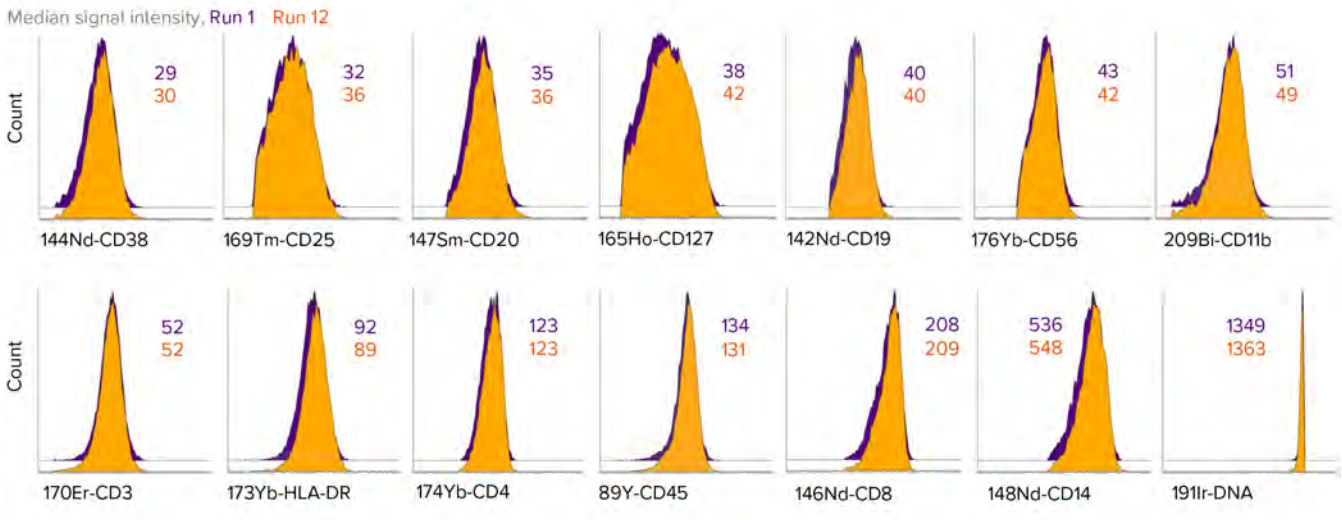

Figure 5. Signal stability over 19 hours of acquisition. 12 tubes of various sample types were continuously collected on CyTOF XT over 19 hours. Run 1 and Run 12 are replicates of the same sample and were acquired first and last, respectively. Run 12 and Run 1 demonstrated the same level of signal. 14 markers are shown as representative data in order of their cell marker signal intensities (low to high). Numbers represent signal intensities (median) over the 19-hour period.

Extended acquisition study results and summary

Fourteen surface markers of low, medium, and high expression range were analyzed. The absolute difference in median signal intensity for each marker was calculated between Run 1 and Run 12. Low expression markers with signal intensity <50 dual counts (CD38, CD25, CD20, CD127, CD19, CD56) showed an average difference of only 4.9%. Medium expression markers (≥50 and 200 dual counts: CD11b, CD3, HLA-DR, CD4, CD45) exhibited an average difference of 1.9%. High expression markers with signal of >200 counts (CD8, CD14, DNA) demonstrated a negligible average difference of 1.2%.

This study demonstrates that the automated detector voltage optimization of CyTOF XT can sustain a constant level of instrument sensitivity during extended runs.

Comparable data performance on Helios and CyTOF XT

Successful completion of extended runs is facilitated by CyTOF Software v8.0 for CyTOF XT, which has been optimized to improve the experience of acquiring samples, data processing, and high-parameter data storage. The enhancements include the following:

- CyTOF XT software automates detector voltage optimization during acquisition, maintaining comparable sensitivity throughout extended acquisitions.
- The software improves upon the built-in sample standardization, using EQ Six Element or EQ Four Element Calibration Beads (Cat. Nos. 201245 and 201078, respectively) to minimize technical variability. The sample normalization algorithm better identifies the EQ calibration beads on the fly, delivering ready-to-analyze data immediately after acquisition.
- CyTOF XT software records a linear mode data (LMD) file, which captures all 135 channels for post-acquisition reprocessing and troubleshooting. Both unprocessed and normalized flow cytometry standard (FCS) files are recorded using FCS 3.1 format. The final output files have been optimized for more efficient use of data storage.

These CyTOF XT software advancements significantly enhance data processing and workflows while maintaining comparable performance between Helios and CyTOF XT. This is illustrated in the section below.

Study design to compare signal intensities and population frequencies on Helios and CyTOF XT

Two independent experiments were performed to demonstrate the comparability of data with regards to signal intensities and cell population frequencies between CyTOF XT and Helios data. Tests were run on CyTOF XT and Helios in parallel using a single donor PBMC sample in Experiment 1 and a single donor whole blood sample in Experiment 2.

Experiment 1: PBMC study design

PBMC from a single donor were stained with the Maxpar Direct Immune Profiling Assay and run in triplicate on both CyTOF XT and Helios in parallel. PBMC sample preparation and acquisition were performed according to recommendations in the Maxpar Direct Immune Profiling Assay Cell Staining and Data Acquisition User Guide (400286), and the Helios User Guide (400250) or the CyTOF Software v8.0 Help for CyTOF XT (FLDM-00045), also available as the software integrated help guide. Data was normalized using the applicable CyTOF Software and analyzed with Maxpar Pathsetter™, a fully automated data analysis solution for samples processed with the Maxpar Direct Immune Profiling Assay. Maxpar Pathsetter generates a report with frequencies of defined populations and their signal intensities. As a comparative analysis, each population was gated manually in Cytobank and compared between the instruments. The manual gating strategies were applied following the technical note: Approach to Bivariate Analysis of Data Acquired Using the Maxpar Direct Immune Profiling Assay (400248).

Experiment 2: Whole blood study design

A test similar to Experiment 1 was performed with whole blood stained with the Maxpar Direct Immune Profiling Assay and run in triplicate on both CyTOF XT and Helios in parallel. Data were normalized and analyzed as described in Experiment 1.

Comparison of signal intensity and population frequency

The automated Maxpar Pathsetter analysis compiled cell classification data from the triplicate PBMC and whole blood datasets acquired on Helios or CyTOF XT. The results of 35 cell populations were graphed in the upper panel of Figures 6 and 7 for PBMC and whole blood samples, respectively. Comparison of population frequencies of data files from Helios and CyTOF XT automatically analyzed in Maxpar Pathsetter demonstrated comparable results for replicate samples between the two instruments (Figures 6 and 7, upper panels). The percent difference was <3.2% and <17.4% for major (>20% of all live events) and minor (<20% of all live events) populations, respectively, in both experiments (Appendix, Tables S1 and S4). The lower panels of Figures 6 and 7 include examples of signal intensities for major populations that were manually gated. The median intensities of positive populations were comparable between Helios and CyTOF XT by manual gating (data not shown).

Using this dataset, an assessment of staining quality for each marker on CyTOF XT and Helios was conducted.

Maxpar Pathsetter performs a staining assessment using a statistical approach called strictly standardized mean difference (SSMD or β). SSMD considers the median and median absolute deviations of both positive and negative populations to assess the resolution of each marker, known as a β value. A higher β value indicates a higher marker resolution that translates to a better separation of positive and negative populations. For the PBMC and whole blood tests, the β value demonstrated a high level of reproducibility across CyTOF XT and Helios data (Appendix, Tables S2 and S6). Furthermore, β values for CyTOF XT data generally exceeded those of Helios.

Deming regression was also used to statistically compare population frequencies, median signal intensities, and β values for both PBMC and whole blood tests performed on Helios and CyTOF XT (Appendix, Figures S1–S4). There was no significant difference between these measurements on each instrument except in the β values of the whole blood tests, which were higher on CyTOF XT. Deming regression analysis found statistically higher B values for samples acquired on CyTOF XT relative to Helios. (Appendix, Figure S4).

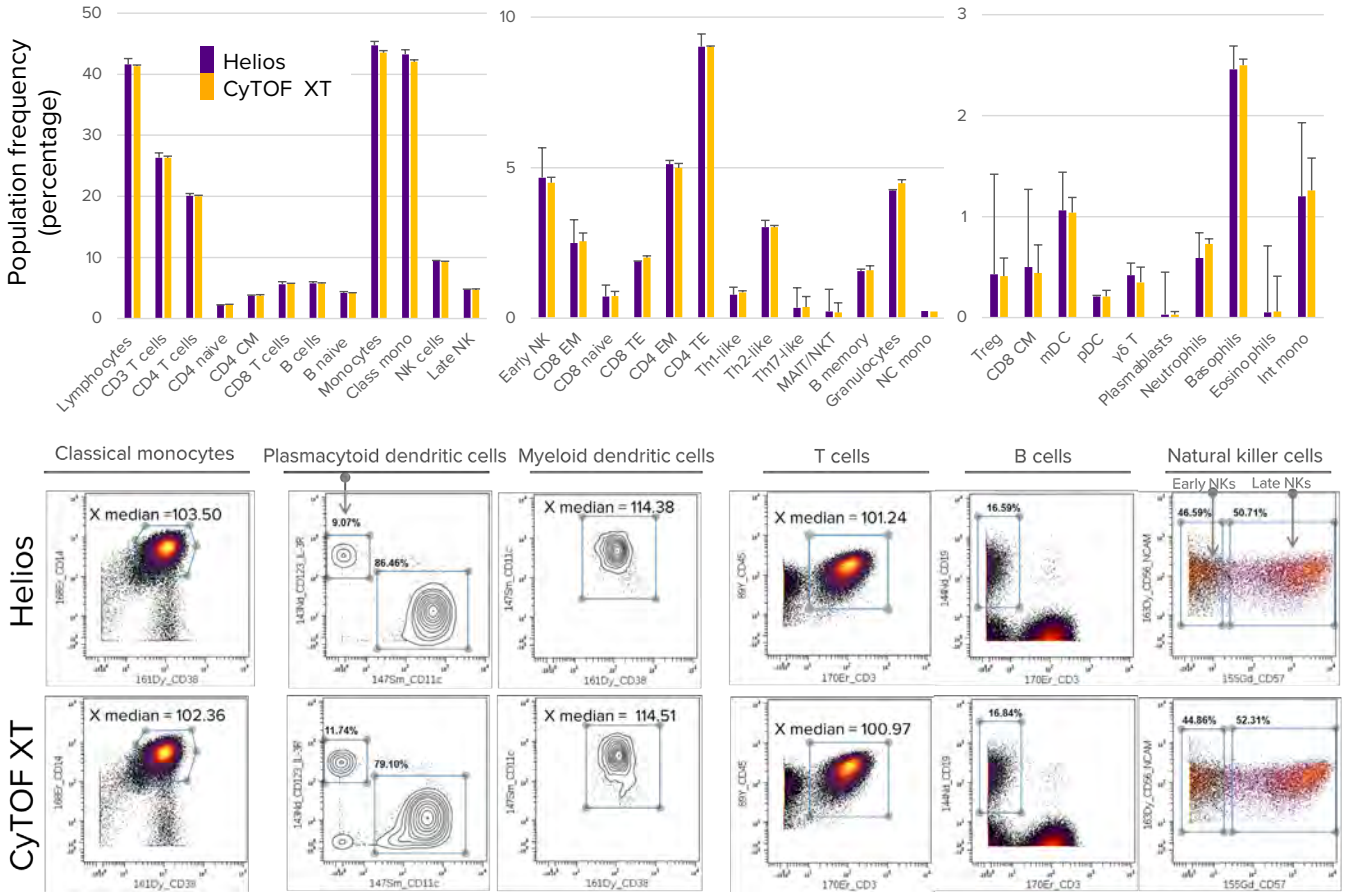

Figure 6. Comparison of PBMC cell population frequencies and signal intensities between Helios and CyTOF XT 6 replicates of PBMC from the same donor were stained with the Maxpar Direct Immune Profiling Assay, pooled together, and split into 6 tubes for acquisition on Helios and CyTOF XT, with 300,000 events acquired per sample. Automated population frequency data obtained from Maxpar Pathsetter analysis is presented in the bar charts (upper panel). Biaxial plots of major populations (lower panel) are used to compare signal intensity (median) or percentage of events as specified in each corresponding plot between Helios and CyTOF XT by manual gating.

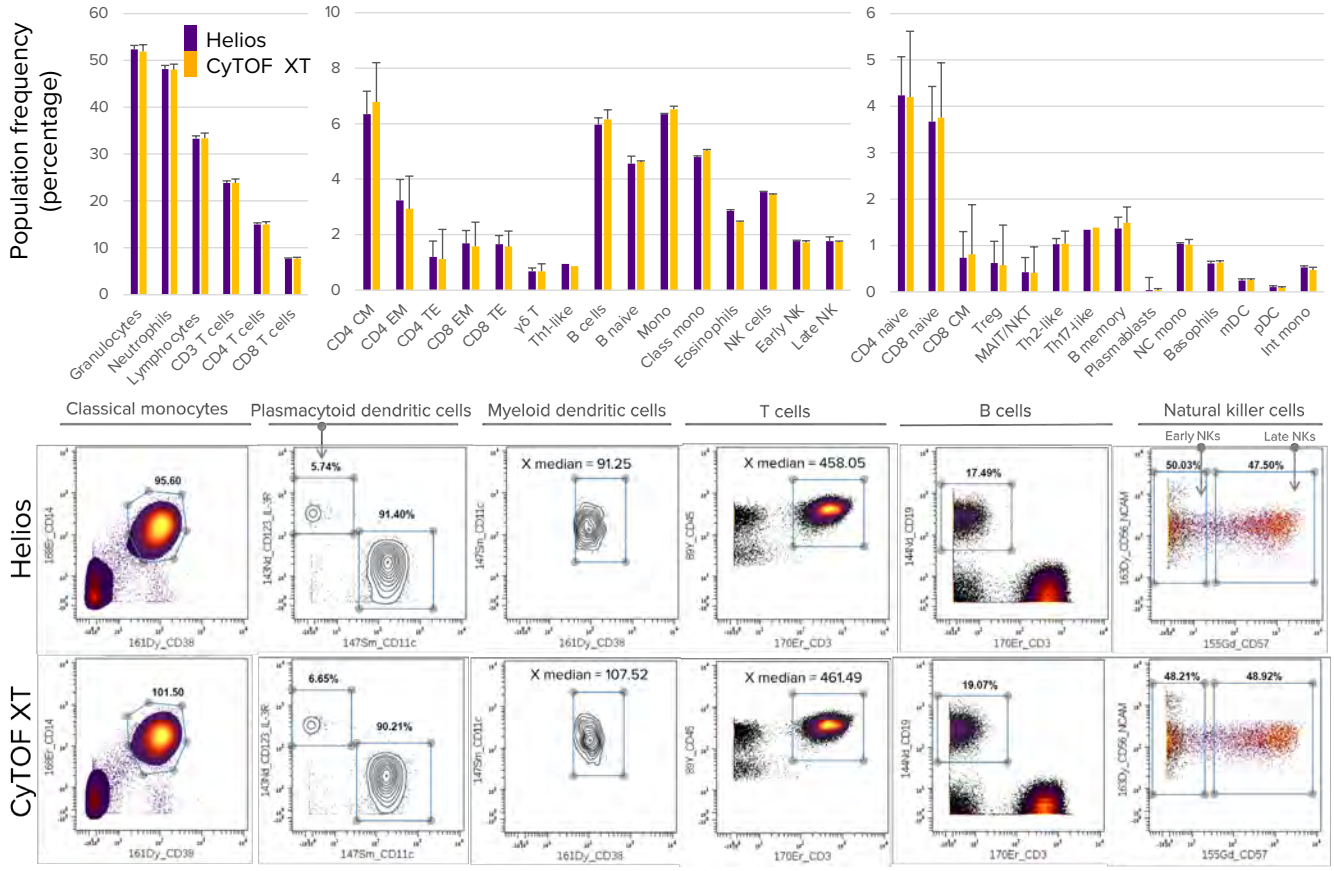

Figure 7. Comparison of stained whole blood cell population frequencies and signal intensities between Helios and CyTOF XT. 6 replicates of whole blood from the same donor were stained with the Maxpar Direct Immune Profiling Assay, pooled together, and split into 6 tubes for acquisition on Helios and CyTOF XT, with 400,000 events acquired per sample. Automated population frequency data obtained from Maxpar Pathsetter analysis is presented in the bar charts (upper panel). Biaxial plots of major populations (lower panel) are used to compare signal intensity (median) and percentage of events as specified in each corresponding plot between Helios and CyTOF XT by manual gating.

CyTOF XT can resolve rare populations.

The high-quality data delivered by CyTOF XT enables the identification of both abundant and rare populations in a sample. An example step-by-step manual gating strategy is shown in Figure 8, demonstrating that 2 replicates of the same sample acquired on both instruments reproducibly resolve markers to identify a desired cell population. The MAIT/NKT CD4– cell population was chosen because it is a rare population that comprises only 0.4% of the total live cell population in whole blood. As shown in the far-right biaxial plot with fixed gates in Figure 8, the same sample acquired on Helios and CyTOF XT yielded a similar number of MAIT/NKT CD4– cells (1,047 and 1,055, respectively) out of 400,000 total events collected.

In this section we showed that comparable performance between Helios and CyTOF XT is demonstrated through the analysis of signal intensities, cell population frequencies, and marker resolution of samples stained with a high parameter-marker panel.

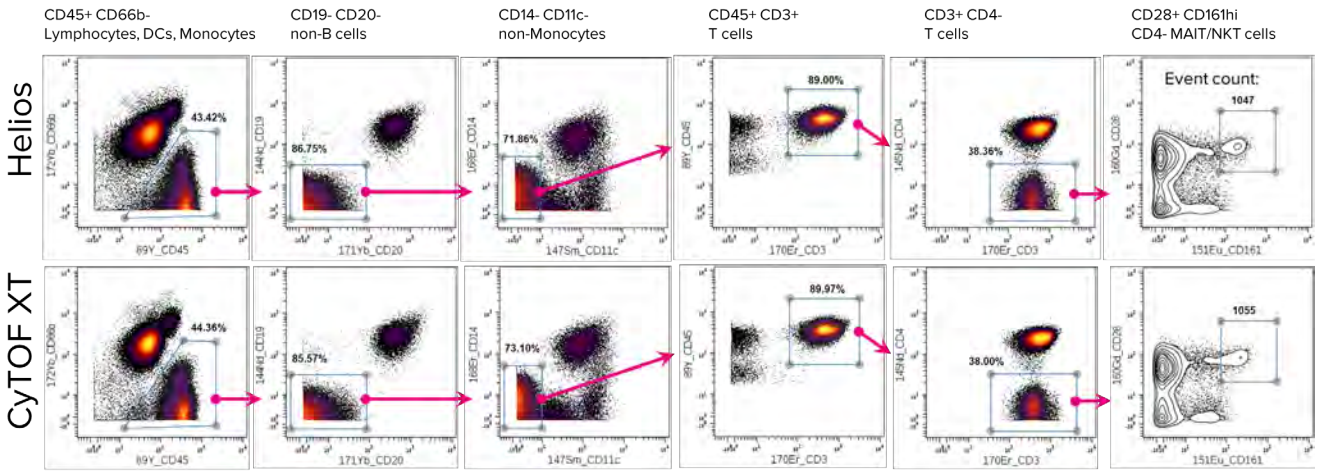

Figure 8. Manual gating strategy of the rare MAIT/NKT CD4– T cell populations, acquired from the same whole blood sample on both Helios and CyTOF XT. An example step-by-step gating strategy for a given rare population after applying the cleanup strategy and gating outlined in Approach to Bivariate Analysis of Data Acquired Using the Maxpar Direct Immune Profiling Assay (400248) is presented. All 35 populations can be identified both manually and automatically using normalized files from both instruments. As shown in the CD28/CD161 gate, the total number of MAIT/NKT CD4– T cells is highly comparable between Helios and CyTOF XT.

Summary

CyTOF XT is a new generation of CyTOF instrument that shares the same reliable level of performance with its predecessor, Helios, but with several key improvements:

- The novel Autosampler design and new CyTOF Software v8.0 for CyTOF XT features automated sample acquisition, EQ bead addition to samples, unclogging, normalization, cleaning, and plasma shutdown. Together, these features improve workflows to reduce hands-on time without impacting data quality.
- Batch acquisition enables up to 13 sample tubes to be loaded into the chilled carousel of the Autosampler module, with the added option to add more samples upon completion of earlier tubes, for added productivity and flexibility.
- An onboard bottle tray and a chilled Autosampler carousel facilitate extended acquisitions.
- Robust automated pre-wash cycles minimize sample carryover.
- Automated detector voltage optimization function helps to maintain consistent signal intensities over the course of extended acquisitions.
- On-the-fly data processing and normalization with the latest FCS format (version FCS 3.1) provides faster time to results with smaller file sizes.

Conclusion

Mass cytometry is widely recognized as a technology that brings a level of multiplexing, precision, and reproducibility to cell analysis not enabled by other single-cell platforms.

CyTOF XT further enhances the capabilities of mass cytometry with workflow automation that refines and simplifies sample processing and data acquisition.

This next generation CyTOF instrument offers a new level of autonomy and reproducibility through streamlined operation, automated system monitoring, and easier system maintenance, making CyTOF XT the superior choice for high-parameter cytometric analysis in clinical and translational research studies.

References

1 Chen, H.X., Song, M., Maecker, H.T. et al. “Network for biomarker immunoprofiling for cancer immunotherapy: Cancer Immune Monitoring and Analysis Centers and Cancer Immunologic Data Commons (CIMAC-CIDC).” *Clinical Cancer Research* (2021): doi:10.1158/1078-0432.CCR-20-3241.

2 Accelerating Partnership Detailed Research Plan: RA, SLE and Related Autoimmune Disorders Steering Committee. National Institute of Arthritis and Musculoskeletal Diseases.

3 Guo, N., van Unen, V., Ijsselsteijn, M.E. et al. “A 34-marker panel for imaging mass cytometric analysis of human snap-frozen tissue.” *Frontiers in Immunology* 11 (2020): 1466. doi:10.3389/fimmu.2020.01466.

Related documents

Go to fluidigm.com and search for the following related documents.

- Use of CyTOF Technology in Clinical Research Trials Data Sheet
- The Benefits of Palladium Barcoding on Data Quality and Workflow Application Note (FLDM-00012)
- Enabling Live-Cell Barcoding with Anti-CD45 Antibodies in Suspension Mass Cytometry Application Note (FLDM-00488)
- CyTOF XT User Guide (FLDM-00254)
- Helios, a CyTOF System User Guide (400250)
- Maxpar Direct Immune Profiling Assay Cell Staining and Data Acquisition User Guide (400286)
- CyTOF Software v8.0 Help for CyTOF XT (FLDM-00045)
- Approach to Bivariate Analysis of Data Acquired Using the Maxpar Direct Immune Profiling Assay Technical Note (400248)
- Maxpar Cell Surface Staining with Fresh Fix Protocol (400276)
- Maxpar Nuclear Antigen Staining with Fresh Fix Protocol (400277)

Appendix: Supplemental material

Data analysis of population frequencies and signal intensities

The following section details additional analysis of files described in the application note. Two sets of tables and figures are provided for live singlet events of PBMC and whole blood. Samples were acquired in triplicate on both Helios and CyTOF XT. Raw FCS data were normalized in CyTOF Software and then analyzed in Maxpar Pathsetter for summary statistics and calculations of β values. Databases from Maxpar Pathsetter were extracted and further analyzed in NCSS Statistical Analysis and Graphics software program for Deming regression.

Mean, standard deviation (SD), and percent coefficient of variation (%CV) of population frequencies of PBMC samples stained using the Maxpar Direct Immune Profiling Assay from the same donor prepared in individual assay tubes, pooled together, and split into 2 sets of triplicates, 1 triplicate set per instrument

Helios

	Population % Live	Mean	SD	% CV
1	Lymphocytes	41.58	0.99	2.38
2	CD3 T cells	26.35	0.77	2.92
3	CD8 T cells	5.61	0.42	7.46
4	CD8 naive	0.72	0.10	13.26
5	CD8 central memory	0.50	0.07	14.25
6	CD8 effector memory	2.50	0.12	4.93
7	CD8 terminal effector	1.89	0.19	10.01
8	CD4 T cells	20.09	0.38	1.89
9	CD4 naive	2.23	0.01	0.47
10	CD4 central memory	3.72	0.12	3.11
11	CD4 effector memory	5.12	0.22	4.29
12	CD4 terminal effector	9.02	0.26	2.84
13	γδ T cells	0.42	0.02	3.86
14	MAIT/NKT	0.23	0.02	7.58
15	B cells	5.77	0.25	4.30
16	B naive	4.18	0.23	5.57
17	B memory	1.57	0.02	1.32
18	Plasmablasts	0.03	0.01	38.11
19	Natural killer cells	9.45	0.06	0.68
20	Early natural killer	4.67	0.03	0.70
21	Late natural killer	4.78	0.03	0.67
22	Monocytes	44.72	0.66	1.48
23	Classical monocytes	43.28	0.73	1.69
24	Intermediate monocytes	1.20	0.07	6.11
25	Non-classical monocytes	0.24	0.02	6.70
26	Plasmacytoid dendritic cells	0.21	0.00	1.58
27	Myeloid dendritic cells	1.06	0.03	2.70
28	Granulocytes	4.24	0.10	2.37
29	Neutrophils	0.59	0.06	10.46
30	Basophils	2.46	0.04	1.65
31	Eosinophils	0.05	0.00	8.69
32	Treg	0.43	0.01	2.78
33	Th1-like	0.78	0.00	0.30
34	Th2-like	3.02	0.09	3.03
35	Th17-like	0.35	0.04	11.94

CyTOF XT

	Population % Live	Mean	SD	% CV
1	Lymphocytes	41.33	0.18	0.44
2	CD3 T cells	26.31	0.28	1.08
3	CD8 T cells	5.74	0.03	0.47
4	CD8 naive	0.74	0.02	2.66
5	CD8 central memory	0.44	0.04	8.62
6	CD8 effector memory	2.55	0.02	0.73
7	CD8 terminal effector	2.01	0.05	2.65
8	CD4 T cells	20.03	0.15	0.74
9	CD4 naive	2.27	0.06	2.54
10	CD4 central memory	3.76	0.15	4.01
11	CD4 effector memory	4.99	0.25	5.03
12	CD4 terminal effector	9.01	0.11	1.20
13	γδ T cells	0.35	0.12	34.37
14	MAIT/NKT	0.19	0.00	0.20
15	B cells	5.79	0.05	0.87
16	B naive	4.17	0.06	1.33
17	B memory	1.59	0.04	2.47
18	Plasmablasts	0.03	0.00	11.57
19	Natural killer cells	9.23	0.15	1.64
20	Early natural killer	4.50	0.04	0.91
21	Late natural killer	4.73	0.12	2.46
22	Monocytes	43.52	0.35	0.80
23	Classical monocytes	42.04	0.32	0.76
24	Intermediate monocytes	1.26	0.04	3.03
25	Non-classical monocytes	0.22	0.01	6.06
26	Plasmacytoid dendritic cells	0.21	0.02	11.34
27	Myeloid dendritic cells	1.04	0.04	3.95
28	Granulocytes	4.48	0.12	2.64
29	Neutrophils	0.73	0.04	5.94
30	Basophils	2.50	0.03	1.36
31	Eosinophils	0.06	0.01	16.86
32	Treg	0.41	0.02	4.39
33	Th1-like	0.86	0.01	1.71
34	Th2-like	3.02	0.03	0.88
35	Th17-like	0.37	0.04	10.39

Table S1. Descriptive statistics of population frequencies as percentage of total live singlet cells for 1 triplicate from Helios and CyTOF XT

Population frequencies for each PBMC replicate stained with the Maxpar Direct Immune Profiling Assay from the same donor prepared in individual assay tubes, pooled together, and split into 2 sets of triplicates, 1 triplicate set per instrument

% of All Live	Helios Replicate 1	Helios Replicate 2	Helios Replicate 3	CyTOF XT Replicate 1	CyTOF XT Replicate 2	CyTOF XT Replicate 3
Lymphocytes	41.97	40.45	42.31	41.41	41.12	41.46
CD3 T cells	26.71	25.47	26.88	26.24	26.06	26.62
CD8 T cells	5.85	5.12	5.85	5.75	5.71	5.75
CD8 naive	0.82	0.63	0.73	0.72	0.76	0.73
CD8 central memory	0.59	0.45	0.48	0.42	0.41	0.48
CD8 effector memory	2.49	2.38	2.62	2.54	2.57	2.55
CD8 terminal effector	1.96	1.67	2.03	2.07	1.97	2.00
CD4 T cells	20.19	19.67	20.41	19.95	19.94	20.20
CD4 naive	2.23	2.22	2.24	2.31	2.20	2.30
CD4 central memory	3.76	3.81	3.59	3.87	3.81	3.59
CD4 effector memory	5.18	4.87	5.30	4.88	4.82	5.28
CD4 terminal effector	9.01	8.76	9.27	8.89	9.10	9.04
γδ T cells	0.43	0.43	0.40	0.35	0.23	0.47
MAIT/NKT	0.24	0.24	0.21	0.19	0.19	0.19
B cells	5.88	5.49	5.95	5.84	5.74	5.78
B naive	4.31	3.91	4.32	4.19	4.10	4.20
B memory	1.55	1.56	1.59	1.61	1.61	1.54
Plasmablasts	0.02	0.02	0.04	0.04	0.03	0.04
Natural killer cells	9.38	9.49	9.48	9.32	9.32	9.06
Early natural killer	4.63	4.69	4.69	4.54	4.51	4.46
Late natural killer	4.74	4.80	4.80	4.78	4.81	4.60
Monocytes	44.23	45.48	44.46	43.47	43.90	43.20
Classical monocytes	42.71	44.11	43.03	42.02	42.37	41.73
Intermediate mono	1.27	1.12	1.21	1.25	1.31	1.24
Non-classical mono	0.25	0.25	0.22	0.21	0.22	0.23
Plasmacytoid dendritic	0.20	0.20	0.21	0.23	0.22	0.18
Myeloid dendritic	1.05	1.05	1.10	1.07	1.06	1.00
Granulocytes	4.33	4.26	4.13	4.49	4.36	4.60
Neutrophils	0.63	0.52	0.62	0.78	0.73	0.69
Basophils	2.49	2.49	2.42	2.51	2.54	2.47
Eosinophils	0.05	0.06	0.05	0.05	0.07	0.05
Treg	0.43	0.41	0.44	0.40	0.44	0.40
Th1-like	0.78	0.78	0.77	0.85	0.88	0.86
Th2-like	3.10	2.92	3.03	3.01	3.01	3.05
Th17-like	0.30	0.37	0.38	0.33	0.39	0.40

Table S2. Raw values of population frequencies as percentage of total live singlet cells for 2 sets of triplicates from Helios and CyTOF XT. The numbers were extracted from Maxpar Pathsetter analysis results.

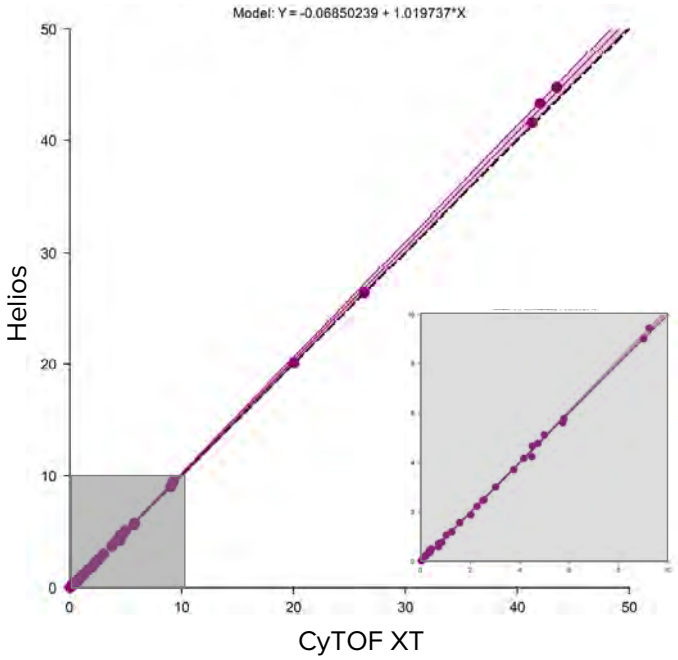

Figure S1. Deming regression of population frequencies between the 2 sets of triplicate data from Table S2. Null hypothesis is accepted at a significance level of 0.05, indicating high similarity between the 2 datasets.

Beta values of marker intensities of each PBMC replicate stained with Maxpar Direct Immune Profiling Assay from the same donor on both instruments

	Helios Replicate 1	Helios Replicate 2	Helios Replicate 3	CyTOF XT Replicate 1	CyTOF XT Replicate 2	CyTOF XT Replicate 3
CD38	4.15	4.45	4.23	3.63	3.52	3.42
CD14	5.39	5.41	5.80	5.29	5.55	5.35
CD19	4.17	4.33	4.27	4.42	4.51	4.39
CD3	4.35	4.43	4.40	4.39	4.49	4.57
CD45RA	2.57	2.43	2.57	2.26	2.68	2.35
CXCR3	0.52	0.53	0.52	0.46	0.49	0.48
CXCR5	1.04	1.02	1.03	1.02	1.03	1.03
CCR4	1.48	1.72	2.04	1.37	1.75	2.40
TCRgd	1.83	1.91	2.21	2.49	2.77	1.76
CD28	3.51	3.52	3.22	3.58	3.38	3.35
CD127	2.97	2.94	2.98	2.89	3.03	2.97
CD56	3.54	3.62	3.56	3.71	3.76	3.68
CD161	3.09	3.09	3.85	3.94	3.70	4.16
CD8	3.27	3.52	3.25	3.13	3.20	3.12
CD4	5.38	5.48	5.36	5.51	5.56	5.55
CCR7	2.41	2.83	2.84	2.72	2.82	2.86
CD25	2.66	2.55	2.57	2.82	2.65	2.68
HLADR	3.15	3.10	3.14	3.33	3.22	3.16
CD20	3.16	3.23	3.14	3.38	3.35	3.17
IgD	2.71	2.80	2.63	2.84	2.83	2.80
CD57	2.84	2.80	2.92	2.81	2.83	2.69
CD66b	3.70	3.61	3.62	3.85	3.78	3.39
CD123	4.01	3.94	4.04	3.97	3.98	4.00
CD11c	6.66	6.98	6.73	7.31	7.00	6.87
CD27	2.61	2.91	2.80	2.91	2.93	2.95
CD45	1.63	1.93	2.08	1.80	1.66	1.92
CCR6	1.65	1.63	1.63	1.63	1.61	1.57
CD294	3.82	3.70	3.78	3.08	2.93	2.75
CD16	1.83	1.79	1.86	1.75	1.85	1.74
CD45RO	1.57	1.54	1.64	1.41	1.58	1.47

Table S3. Beta (β) values of marker intensities of each replicate from Helios and CyTOF XT. The numbers were extracted from Maxpar Pathsetter analysis results.

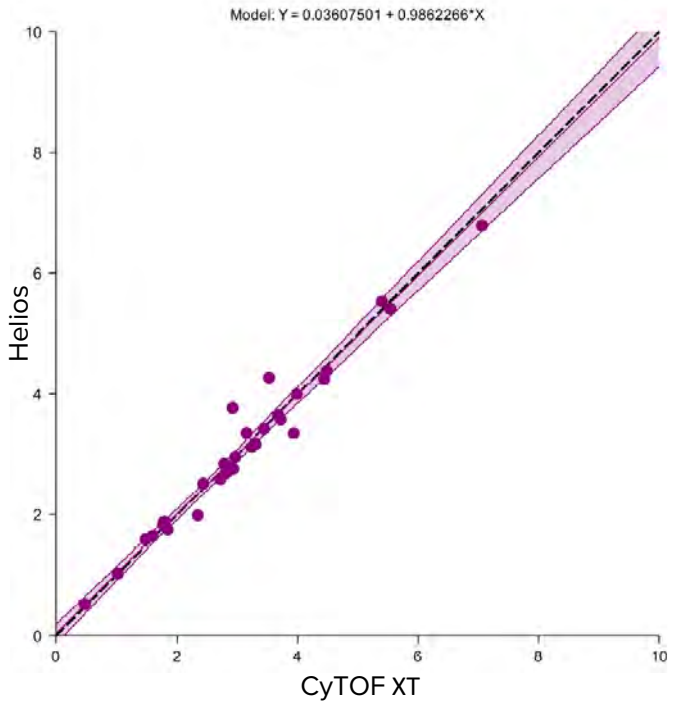

Figure S2. Deming regression of β values of marker intensities from Table S3. Null hypothesis is accepted at a significance level of 0.05, indicating high similarity between the 2 datasets.

Mean, SD, and %CV of population frequencies of whole blood samples stained with the Maxpar Direct Immune Profiling Assay from the same donor prepared in individual assay tubes, pooled together, and split into 2 sets of triplicates, 1 triplicate set per instrument

Helios

	Population % Live	Mean	SD	% CV
1	Lymphocytes	33.34	0.57	1.71
2	CD3 T cells	23.84	0.47	1.96
3	CD8 T cells	7.73	0.12	1.56
4	CD8 naive	3.67	0.07	1.83
5	CD8 central memory	0.73	0.02	3.22
6	CD8 effector memory	1.68	0.05	2.89
7	CD8 terminal effector	1.65	0.04	2.34
8	CD4 T cells	15.02	0.32	2.12
9	CD4 naive	4.24	0.14	3.36
10	CD4 central memory	6.34	0.24	3.72
11	CD4 effector memory	3.23	0.27	8.40
12	CD4 terminal effector	1.20	0.02	1.69
13	γδ T cells	0.68	0.03	3.94
14	MAIT/NKT	0.42	0.01	2.17
15	B cells	5.97	0.16	2.62
16	B naive	4.56	0.13	2.82
17	B memory	1.37	0.04	2.66
18	Plasmablasts	0.04	0.01	15.40
19	Natural killer cells	3.53	0.10	2.97
20	Early natural killer	1.77	0.04	2.49
21	Late natural killer	1.76	0.06	3.47
22	Monocytes	6.35	0.16	2.59
23	Classical monocytes	4.79	0.10	1.99
24	Intermediate monocytes	0.53	0.02	4.55
25	Non-classical monocytes	1.04	0.05	4.72
26	Plasmacytoid dendritic cells	0.10	0.00	2.46
27	Myeloid dendritic cells	0.24	0.01	5.81
28	Granulocytes	52.39	0.83	1.59
29	Neutrophils	48.19	0.76	1.57
30	Basophils	0.61	0.02	3.40
31	Eosinophils	2.86	0.11	3.84
32	Treg	0.62	0.03	5.20
33	Th1-like	0.94	0.03	3.38
34	Th2-like	1.03	0.05	4.90
35	Th17-like	1.34	0.02	1.68

CyTOF XT

	Population % Live	Mean	SD	% CV
1	Lymphocytes	33.44	1.07	3.20
2	CD3 T cells	23.84	0.87	3.65
3	CD8 T cells	7.72	0.27	3.47
4	CD8 naive	3.76	0.14	3.77
5	CD8 central memory	0.81	0.07	8.14
6	CD8 effector memory	1.58	0.04	2.71
7	CD8 terminal effector	1.57	0.03	1.76
8	CD4 T cells	15.03	0.56	3.75
9	CD4 naive	4.20	0.17	4.10
10	CD4 central memory	6.78	0.34	4.98
11	CD4 effector memory	2.93	0.03	0.90
12	CD4 terminal effector	1.12	0.11	9.72
13	γδ T cells	0.68	0.02	2.74
14	MAIT/NKT	0.41	0.03	6.16
15	B cells	6.16	0.04	0.69
16	B naive	4.63	0.02	0.48
17	B memory	1.49	0.04	2.57
18	Plasmablasts	0.04	0.00	9.51
19	Natural killer cells	3.45	0.19	5.48
20	Early natural killer	1.72	0.12	6.80
21	Late natural killer	1.73	0.07	4.28
22	Monocytes	6.52	0.20	3.09
23	Classical monocytes	5.03	0.10	2.04
24	Intermediate monocytes	0.47	0.04	8.89
25	Non-classical monocytes	1.02	0.06	5.80
26	Plasmacytoid dendritic cells	0.09	0.00	5.04
27	Myeloid dendritic cells	0.25	0.02	8.88
28	Granulocytes	51.95	1.42	2.73
29	Neutrophils	48.04	1.18	2.46
30	Basophils	0.63	0.02	3.79
31	Eosinophils	2.46	0.22	8.98
32	Treg	0.57	0.02	4.20
33	Th1-like	0.86	0.06	7.12
34	Th2-like	1.04	0.03	2.98
35	Th17-like	1.39	0.06	4.22

Tables S4. Descriptive statistics of population frequencies as percentage of total live singlet cells for triplicate sample data from Helios and CyTOF XT

Population frequencies of each whole blood sample stained with the Maxpar Direct Immune Profiling Assay from the same donor prepared in individual assay tubes, pooled together, and split into 2 sets of triplicates, 1 triplicate set per instrument

	Helios Replicate 1	Helios Replicate 2	Helios Replicate 3	CyTOF XT Replicate 1	CyTOF XT Replicate 2	CyTOF XT Replicate 3
Lymphocytes	32.90	33.98	33.13	34.66	33.01	32.66
CD3 T cells	23.53	24.37	23.61	24.81	23.57	23.13
CD8 T cells	7.63	7.86	7.69	8.00	7.69	7.47
CD8 naive	3.63	3.74	3.63	3.89	3.78	3.61
CD8 central memory	0.71	0.75	0.74	0.89	0.77	0.78
CD8 effector memory	1.69	1.73	1.63	1.62	1.58	1.53
CD8 TE	1.61	1.64	1.69	1.60	1.56	1.54
CD4 T cells	14.80	15.38	14.86	15.67	14.80	14.61
CD4 naive	4.31	4.34	4.08	4.32	4.27	4.00
CD4 central memory	6.13	6.30	6.59	7.16	6.62	6.55
CD4 effector memory	3.18	3.52	2.99	2.95	2.90	2.95
CD4 terminal effector	1.18	1.23	1.20	1.23	1.01	1.12
γδ T cells	0.68	0.70	0.65	0.70	0.68	0.67
MAIT/NKT	0.41	0.43	0.41	0.44	0.40	0.40
B cells	5.80	6.00	6.11	6.19	6.11	6.18
B naive	4.41	4.59	4.66	4.66	4.63	4.61
B memory	1.35	1.36	1.42	1.49	1.45	1.53
Plasmablasts	0.04	0.05	0.03	0.04	0.03	0.04
Natural killer cells	3.57	3.61	3.41	3.67	3.34	3.34
Early natural killer	1.79	1.80	1.72	1.86	1.64	1.67
Late natural killer	1.78	1.81	1.69	1.81	1.70	1.67
Monocytes	6.41	6.48	6.17	6.74	6.46	6.35
Classical monocytes	4.81	4.88	4.69	5.15	4.99	4.96
Intermediate mono	0.54	0.54	0.50	0.51	0.46	0.43
Non-classical mono	1.07	1.06	0.98	1.08	1.02	0.96
Plasmacytoid dendritic	0.10	0.10	0.10	0.10	0.09	0.09
Myeloid dendritic	0.24	0.25	0.22	0.28	0.23	0.25
Granulocytes	52.88	51.42	52.86	50.32	52.64	52.90
Neutrophils	48.71	47.32	48.54	46.69	48.60	48.84
Basophils	0.59	0.63	0.61	0.65	0.61	0.61
Eosinophils	2.82	2.78	2.99	2.21	2.60	2.58
Treg	0.59	0.65	0.63	0.59	0.56	0.55
Th1-like	0.95	0.96	0.90	0.92	0.86	0.79
Th2-like	1.02	1.09	0.99	1.08	1.04	1.02
Th17-like	1.32	1.37	1.35	1.45	1.33	1.40

Table S5. Raw values of population frequencies as percentage of total live singlet cells of 2 sets of triplicates from Helios and CyTOF XT. The numbers were extracted from Maxpar Pathsetter analysis results.

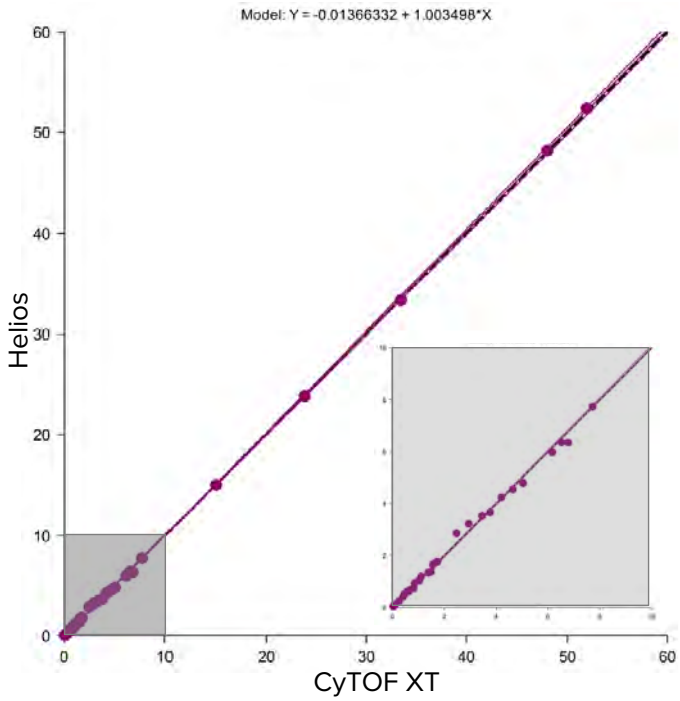

Figure S3. Deming regression of population frequencies between 2 sets of triplicates from Table S5. Null hypothesis is accepted at a significance level of 0.05, indicating high similarity between the 2 datasets.

Beta values of marker intensities of each whole blood sample stained with the Maxpar Direct Immune Profiling Assay from the same donor on both instruments

	Helios Replicate 1	Helios Replicate 2	Helios Replicate 3	CyTOF Replicate 1	CyTOF Replicate 2	CyTOF Replicate 3
CD38	4.28	4.26	4.25	4.55	4.32	4.49
CD14	3.15	3.10	3.14	3.83	3.61	3.80
CD19	6.06	5.96	6.11	6.91	6.80	6.82
CD3	7.38	7.11	7.12	7.00	7.01	7.23
CD45RA	2.57	2.59	2.72	3.08	2.78	3.12
CXCR3	0.71	0.71	0.71	0.72	0.72	0.71
CXCR5	7.14	7.18	7.25	7.43	7.41	7.50
CCR4	2.29	2.26	2.57	2.65	2.51	2.68
TCRgd	5.04	4.88	4.79	4.89	4.95	4.83
CD28	5.07	4.76	4.92	5.20	5.29	5.42
CD127	2.58	2.59	2.51	2.55	2.50	2.60
CD56	5.00	4.92	4.88	5.13	5.16	5.06
CD161	3.68	3.91	3.74	3.71	3.83	3.79
CD8	6.78	6.69	6.64	7.44	7.33	7.40
CD4	6.91	6.69	6.62	7.80	7.30	7.61
CCR7	4.78	4.71	4.61	4.41	4.44	4.70
CD25	2.19	2.15	2.25	2.39	2.36	2.35
HLADR	4.54	4.52	4.46	4.71	4.78	4.81
CD20	7.11	6.89	6.71	7.35	7.32	7.30
IgD	4.85	4.65	4.68	4.61	4.67	4.70
CD57	2.65	2.60	2.77	2.64	2.56	2.66
CD66b	5.57	5.48	5.42	5.73	5.56	5.70
CD123	4.56	4.60	4.77	4.45	5.40	4.50
CD11c	4.20	4.92	5.08	4.23	5.05	4.63
CD27	3.93	3.98	3.70	3.90	3.87	3.94
CD45	3.82	3.81	3.80	4.26	4.15	4.30
CCR6	4.36	4.32	4.41	4.82	4.70	4.85
CD294	4.21	4.14	4.16	4.58	4.44	4.48
CD16	3.20	3.14	3.10	3.31	3.16	3.34
CD45RO	3.19	3.13	3.21	3.59	3.53	3.49

Table S6. Beta (β) values of marker intensities of each replicate from Helios and CyTOF XT. The numbers were extracted from Maxpar Pathsetter analysis results.

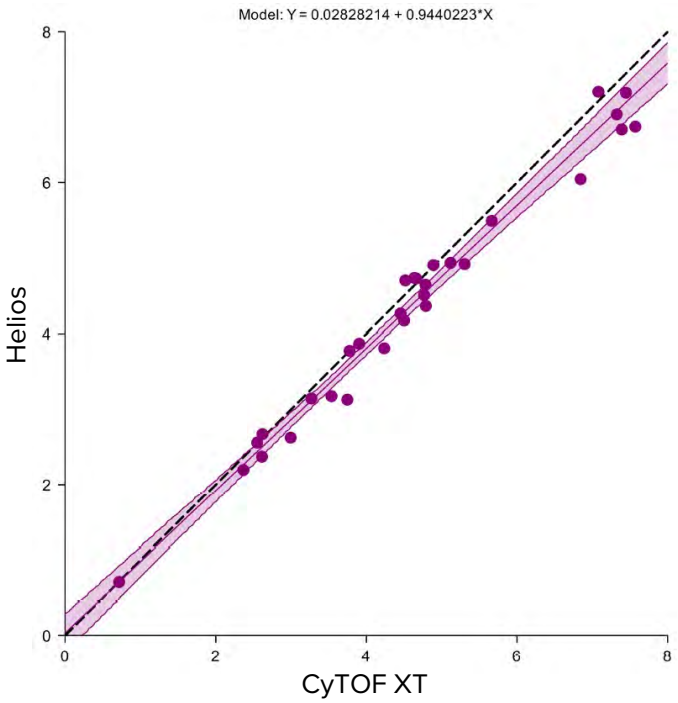

Figure S4. Deming regression of β values of marker intensities from Table S6. Alternative hypothesis is accepted at a significance level of 0.05 because the β values from CyTOF XT are higher than from Helios, indicating better marker resolution. This translates to a better separation of negative and positive populations.

Learn more at **fluidigm.com/cytof.xt**

Or contact: **tech.support@fluidigm.com**

CORPORATE HEADQUARTERS
2 Tower Place, Suite 2000
South San Francisco, CA 94080 USA
Toll-free: 866 359 4354 in the US and Canada
Fax: 650 871 7152
fluidigm.com

SALES
North America | +1 650 266 6170 | info-us@fluidigm.com
Europe/EMEA | +33 1 60 92 42 40 | info-europe@fluidigm.com
Latin America | +1 650 266 6170 | info-latinamerica@fluidigm.com
Japan | +81 3 3662 2150 | info-japan@fluidigm.com
China (excluding Hong Kong) | +86 21 3255 8368 | info-china@fluidigm.com
All other Asian countries | +1 650 266 6170 | info-asia@fluidigm.com

For Research Use Only. Not for use in diagnostic procedures.

FLDM-00462 Rev 01

Received: 25 July 2019 | Revised: 29 October 2019 | Accepted: 5 November 2019

DOI: 10.1002/cyto.b.21858

ORIGINAL ARTICLE

CLINICAL CYTOMETRY WILEY

Multi-site reproducibility of a human immunophenotyping assay in whole blood and peripheral blood mononuclear cells preparations using CyTOF technology coupled with Maxpar Pathsetter, an automated data analysis system

Charles Bruce Bagwell[1] | Benjamin Hunsberger[1] | Beth Hill[1] | Donald Herbert[1] | Christopher Bray[1] | Thirumahal Selvanantham[2] | Stephen Li[2] | Jose C. Villasboas[3] | Kevin Pavelko[3] | Michael Strausbauch[3] | Adeeb Rahman[4] | Gregory Kelly[4] | Shahab Asgharzadeh[5] | Azucena Gomez-Cabrero[5] | Gregory Behbehani[6] | Hsiaochi Chang[6] | Justin Lyberger[6] | Ruth Montgomery[7] | Yujiao Zhao[7] | Margaret Inokuma[1] | Ofir Goldberger[8] | Greg Stelzer[8]

[1]Verity Software House, Topsham, Maine

[2]Fluidigm Canada Inc., Markham, Ontario, Canada

[3]Mayo Clinic, Immune Monitoring Core, Rochester, MN

[4]Icahn School of Medicine at Mount Sinai, New York, New York

[5]Children's Hospital Los Angeles, Los Angeles, California

[6]Ohio State University, Columbus, Ohio

[7]Yale School of Medicine, New Haven, Connecticut

[8]Fluidigm Corporation, San Francisco, California

Correspondence
C. Bruce Bagwell, PO Box 247, Topsham, ME 04086.
Email: cbb@vsh.com

Abstract

High-dimensional mass cytometry data potentially enable a comprehensive characterization of immune cells. In order to positively affect clinical trials and translational clinical research, this advanced technology needs to demonstrate a high reproducibility of results across multiple sites for both peripheral blood mononuclear cells (PBMC) and whole blood preparations. A dry 30-marker broad immunophenotyping panel and customized automated analysis software were recently engineered and are commercially available as the Fluidigm® Maxpar® Direct™ Immune Profiling Assay™. In this study, seven sites received whole blood and six sites received PBMC samples from single donors over a 2-week interval. Each site labeled replicate samples and acquired data on Helios™ instruments using an assay-specific acquisition template. All acquired sample files were then automatically analyzed by Maxpar Pathsetter™ software. A cleanup step eliminated debris, dead cells, aggregates, and normalization beads. The second step automatically enumerated 37 immune cell populations and performed label intensity assessments on all 30 markers. The inter-site reproducibility of the 37 quantified cell populations had consistent population frequencies, with an average %CV of 14.4% for whole blood and 17.7% for PBMC. The dry reagent coupled with automated data analysis is not only convenient but also provides a high degree of reproducibility within and among multiple test sites resulting in a comprehensive yet practical solution for deep immune phenotyping.

KEYWORDS

cytometry automation, cytometry standardization, kits, percentage precision

1 | INTRODUCTION

Multi-site studies have been successfully performed in flow cytometry, but only a few multi-site mass cytometry studies have been reported (Blazkova et al., 2017; Leipold et al., 2018) and no mass cytometry-based study has examined the reproducibility of whole blood preparations or dry antibody panels. In mass cytometry, the use of an inductively coupled plasma mass spectrometer to detect heavy metal-tagged probes on a single-cell basis mitigates the issue of spectral overlap between detection channels, easily allowing for the use of >40 simultaneous measurements.

Peripheral blood mononuclear cell (PBMC) preparations have useful storage characteristics, which is helpful for doing multi-site studies. However, immunophenotyping of whole blood specimens is an industry-standard for clinical trials and other types of clinical studies. The ability to standardize both PBMC and whole blood immunophenotyping worldwide would have far-reaching ramifications. In a typical flow cytometry experiment workflow, several areas of variability have been identified. Controlling such factors as reagents, sample handling, instrument setup, and data analysis can lead to standardization (Maecker, McCoy, & Nussenblatt, 2012).

This study is part of an initiative to produce a commercially available product that addresses many of the factors important in developing a standardized immune monitoring assay for mass cytometry. The system consists of a dry antibody product capable of identifying many important immune populations, an instrument setup template, and automated cleanup and analysis software that enumerates a broad spectrum of immune cell types. The core of the panel is based on the recommendation of the Human ImmunoPhenotyping Consortium of the Human Immunology Project (Finak et al., 2016; Maecker et al., 2012). Eight additional antibodies (CD28, CD45, CD57, CD66b, CD294, CD161, CXCR5, and TCRγδ) were added to the panel to better delineate T-cells, NK cells, and granulocytes, and one marker was dropped (CD24). In addition to the antibodies, the dry antibody cocktail also includes rhodium for the discrimination of live/dead cells (Ornatsky et al., 2008). The details of the 30-marker panel are shown in Table 1, and the workflow is shown in Figure 1.

The analysis of the panel was performed by Maxpar Pathsetter software, which uses probability state modeling (PSM) (Bagwell, 2010; Bagwell et al., 2015; Bagwell et al., 2018, Leipold, Maecker, & Stelzer, 2016) to obtain frequencies for 37 immune populations (see Table 2 for model phenotype definitions) as well as stain assessments for all 30 markers. PSM-derived results have been previously shown to correlate well with manual gating (Herbert, Miller, & Bagwell, 2012; Li et al., 2018, 2019; Miller, Hunsberger, & Bagwell, 2012; Wong et al., 2014; Wong, Hunsberger, Bruce Bagwell, & Davis, 2013). Many different validation tests needed to be performed prior to releasing this product. These tests included liquid versus dry panel, intra-assay repeatability, intermediate precision, manual gating versus modeling correlations, and inter-site reproducibility. Most of these validations are presented in a publicly available white paper. Deep Immune Profiling with the Maxpar Direct Immune Profiling System 400247 A2) and data from other tests have been added to the Supporting Information. The purpose of this study is to report in detail on the last stage of validation where the reproducibility of the kit/analysis system was evaluated by multiple sites for both PBMC and whole blood samples from healthy human subjects.

TABLE 1 Maxpar direct immune profiling assay 30-marker panel with clones and heavy metals

Target	Clone	Metal
Anti-human CD45	HI30	89Y
Live/dead 103Rh-Intercalator (500 μM)	N/A	103Rh
Anti-human CD196/CCR6	G034E3	141Pr
Anti-human CD123	6H6	143Nd
Anti-human CD19	HIB19	144Nd
Anti-human CD4	RPA-T4	145Nd
Anti-human CD8a	RPA-T8	146Nd
Anti-human CD11c	Bu15	147Sm
Anti-human CD16	3G8	148Nd
Anti-human CD45RO	UCHL1	149Sm
Anti-human CD45RA	HI100	150Nd
Anti-human CD161	HP-3G10	151Eu
Anti-human CD194/CCR4	L291H4	152Sm
Anti-human CD25	BC96	153Eu
Anti-human CD27	O323	154Sm
Anti-human CD57	HCD57	155Gd
Anti-human CD183/CXCR3	G025H7	156Gd
Anti-human CD185/CXCR5	J252D4	158Gd
Anti-human CD28	CD28.2	160Gd
Anti-human CD38	HB-7	161Dy
Anti-human CD56/NCAM	NCAM16.2	163Dy
Anti-human TCRgd	B1	164Dy
Anti-human CD294	BM16	166Er
Anti-human CD197/CCR7	G043H7	167Er
Anti-human CD14	63D3	168Er
Anti-human CD3	UCHT1	170Er
Anti-human CD20	2H7	171Yb
Anti-human CD66b	G10F5	172Yb
Anti-human HLA-DR	LN3	173Yb
Anti-human IgD	IA6-2	174Yb
Anti-human CD127	A019D5	176Yb

2 | MATERIALS AND METHODS

2.1 | Study sites

A total of seven sites (six in the United States plus Fluidigm Canada) were selected to participate in these reproducibility studies. These sites are designated as Sites 1, 2, 3, 4, 5, 6, and 7. Site 1 received whole blood products in Week 1 of the study, for which it is designated as Site 1A, and in the second week of the study received whole

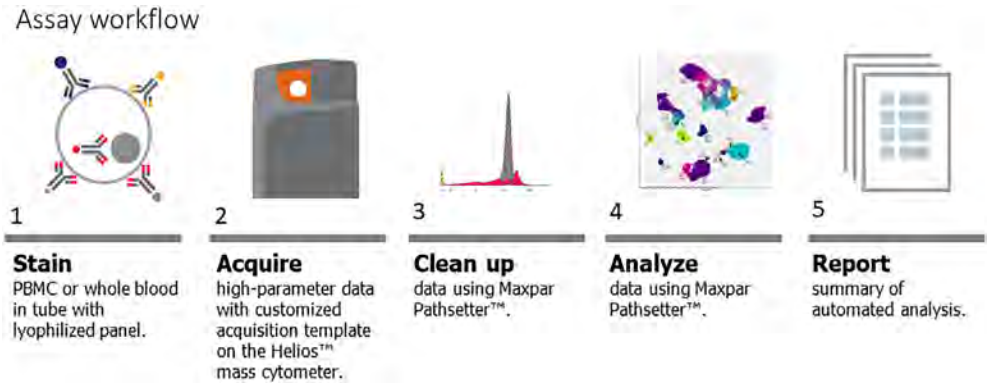

FIGURE 1 Assay workflow. Based on the broad immune cell phenotyping flow panels for the Human Immune Project (Maecker et al., 2012), the Maxpar Direct Immune Profiling Assay was designed as an optimized panel of 30 dry antibodies plus DNA intercalators in a single tube for staining whole blood and PBMC. Data were acquired on a Fluidigm Helios and analyzed using Maxpar Pathsetter, a customized automated analysis system powered by GemStone 2.0. Pathsetter software automatically cleans the data file by eliminating dead cells, debris, aggregates, and normalization beads. Modeling software then identifies and enumerates a broad spectrum of immune populations and presents the results in summary reports [Color figure can be viewed at wileyonlinelibrary.com]

blood products from a second draw from the same donor, for which it is designated as Site 1B. Site 1 did not participate in the PBMC part of the study. Sites 2, 3, and 4 received whole blood and PBMC samples in Week 1, and Sites 5, 6, and 7 received the products in the second week. All sites were given careful instructions on the staining and analysis procedures, and Fluidigm Field Application Specialists were on hand to provide general guidance on all the procedures.

2.2 | Whole blood collection and shipping

Human whole blood was obtained from Discovery Life Sciences (Huntsville, AL). Whole blood from a single healthy donor was collected into eight individual BD Vacutainer® blood collection tubes containing heparin as an anticoagulant. Two tubes of the whole blood were shipped on cold packs to each study site overnight in a temperature-controlled shipping container.

2.3 | Whole blood staining

An additional heparin blocking step was performed (100 U/ml) for 20 min at room temperature to reduce nonspecific binding between metal-tagged antibodies and eosinophils (Rahman, Tordesillas, & Berin, 2016). Afterward, 270 µl of blood was added directly to four dry antibody tubes and allowed to incubate for 30 min at room temperature. Immediately following staining, erythrocytes were lysed by the addition of 250 µl of Cal-Lyse directly to the staining tube. The tubes were gently vortexed and allowed to incubate for 10 min at room temperature followed by the addition of 3 ml of Maxpar water and an additional 10 min of incubation. The tubes were washed three times in Maxpar Cell Staining Buffer (CSB) followed by fixation in 1.6% paraformaldehyde for 10 min. Following fixation, the cells were spun to a pellet, the fixative removed, and the pellet was resuspended in 1 ml of the 125 nm Cell-ID™ Intercalator-Ir (Ornatsky et al., 2008) and incubated overnight at 4° (See Figure 1 for the assay workflow).

2.4 | PBMC specimens

One lot of cryopreserved PBMC from a single healthy donor was obtained from a commercial biological specimen supply source (Discovery Life Sciences) and reserved as the reference lot for the study. Two vials of cryopreserved PBMC were shipped on dry ice to each of six sites. The PBMC samples were thawed based on the manufacturer's (Discovery Life Sciences) recommendations, which was to thaw in serum-free media with no anti-aggregate.

2.5 | PBMC staining

A vial of cryopreserved PBMC was thawed and washed. The viability and cell count were determined and the cells were washed in CSB. After the wash, the cells were resuspended in CSB to a concentration of 6×10^7 cells/ml. FC receptors were blocked by adding 5 µl of Human TruStain FcX to 3×10^6 cells in 50 µl and incubated for 10 min. About 215 µl of CSB was then added to the PBMC. About 270 µl of the PBMC was added directly added to each of the four dry antibody tubes for antibody staining (see Table 1). After a 30-min incubation, the cells were washed twice in CSB, followed by fixation in 1.6% paraformaldehyde for 10 min. Following fixation, the cells were spun to a pellet, the fixative was removed, and the pellet was resuspended in 1 ml of the 125 nM Cell-ID Intercalator-Ir and incubated overnight at 4°.

2.6 | Sample acquisition

Following the overnight incubation, the PBMC fixed cells were washed twice in CSB and twice with Maxpar Cell Acquisition Solution (CAS) with a final resuspension of the cells at 1×10^6 cells/ml in CAS containing 0.1× EQ™ Four Element Calibration Beads. Whole blood sample acquisition was also performed the next day post staining on a Helios system utilizing CyTOF® Software version 6.7.1016 using the Maxpar Direct Immune Profiling Assay template. All instruments were

TABLE 2 Immune cell populations and model definitions

Index	Populations	Model phenotypes
1	Lymphocytes	CD3 T cells + B cells + NK cells + plasmablasts
2	CD3 T cells	CD8 T cells + CD4 T cells + γδ T cells + MAIT/NKT cells
3	CD8 T cells	CD3+ CD66b- CD19- CD8+ CD4- CD14- CD161- TCRgd- CD123- CD11c-
4	CD8 naïve	CD8 T cells + CD45RA+ CCR7+ CD27+
5	CD8 central memory	CD8 T cells + CD45RA- CCR7+ CD27+
6	CD8 effector memory	CD8 T cells + CCR7- CD27+
7	CD8 terminal effector	CD8 T cells + CCR7- CD27-
8	CD4 T cells	CD66b- CD3+ CD8- CD4+ CD14- TCRgd- CD11c-
9	CD4 naïve	CD4 T cells + CD45RA+ CCR7+ CD27+
10	CD4 central memory	CD4 T cells + CD45RA- CCR7+ CD27+
11	CD4 effector memory	CD4 T cells + CD45RA- CCR7- CD27+
12	CD4 terminal effector	CD4 T cells + CD45RA- CCR7- CD27-
13	Tregs	CD4 T cells + CD25+ CD127- CCR4+
14	Th1-like	CD4 T cells + CXCR3+ CCR6- CXCR5- CCR4-
15	Th2-like	CD4 T cells + CXCR3- CCR6- CXCR5- CCR4+
16	Th17-like	CD4 T cells + CXCR3- CCR6+ CXCR5- CCR4+
17	γ T cells	CD66b- CD3+ CD8dim,- CD4- CD14- TCRgd dim,+
18	MAIT/NKT cells	CD66b- CD3+ CD4- CD14- CD161+ TCRgd- CD28+ CD16-
19	B cells	CD3- CD14- CD56- CD16 dim,- CD19+ CD20+ HLA-DR dim,+
20	B naïve	B cells + CD27-
21	B memory	B cells + CD27+
22	Plasmablasts	CD3- CD14- CD16-,dim CD66b- CD20- CD19+ CD56- CD38++ CD27+
23	NK cells	CD14- CD3- CD123- CD66b- CD45RA+ CD56 dim,+
24	NK early	NK cells + CD57-
25	NK late	NK cells + CD57+
26	Monocytes	CD3- CD19- CD56- CD66b- HLA-DR+ CD11c+
27	Monocytes classical	Monocytes + CD14+ CD38+
28	Monocytes transitional	Monocytes + CD14 dim CD38 dim
29	Monocytes non-classical	Monocytes + CD14- CD38-
30	DCs	pDCs + mDCs
31	pDCs	CD3- CD19- CD14- CD20- CD66b- HLA-DR dim,+ CD11c- CD123+
32	mDCs	CD3- CD19- CD14- CD20- HLA-DR dim,+ CD11c dim,+ CD123- CD16 dim,- CD38 dim,+ CD294- HLA-D
33	Granulocytes	Neutrophils + basophils + eosinophils + CD66b- neutrophils
34	Neutrophils	CD66b dim,+ CD16+ HLA-DR-
35	Basophils	HLA-DR- CD66b- CD123 dim,+ CD38+ CD294+
36	Eosinophils	CD14- CD3- CD19- HLA-DR- CD294+ CD66b dim,+
37	CD66b- neutrophils	CD3- CD19- CD66b- CD56- HLA-DR- CD123- CD45-

The above table shows the 37 immune cell populations enumerated and their associated model phenotypes.
The modeling algorithm is designed to fit the measurements in the order listed by the phenotype. Nomenclature such as TCRγδ dim,+ means that dim to positive events were selected. Occasionally the same marker is modeled twice, where the first time is a broader classification and the last time is a more specific classification. See Section 4 for details on the subsetting and staging rationales for monocytes, CD8 T-cells, and CD4 T-cells.

equipped with a WB Injector, and all samples were acquired in CAS containing 0.1× EQ beads. Prior to the start of the study, all instruments were evaluated to ensure performance at above the minimum Helios system specifications for calibration. Following the instrument tuning and bead sensitivity test, the system was preconditioned with CAS. A minimum of 400,000 events for whole blood and 300,000 events for PBMC were acquired per file at a typical acquisition rate of 250–500 events/s.

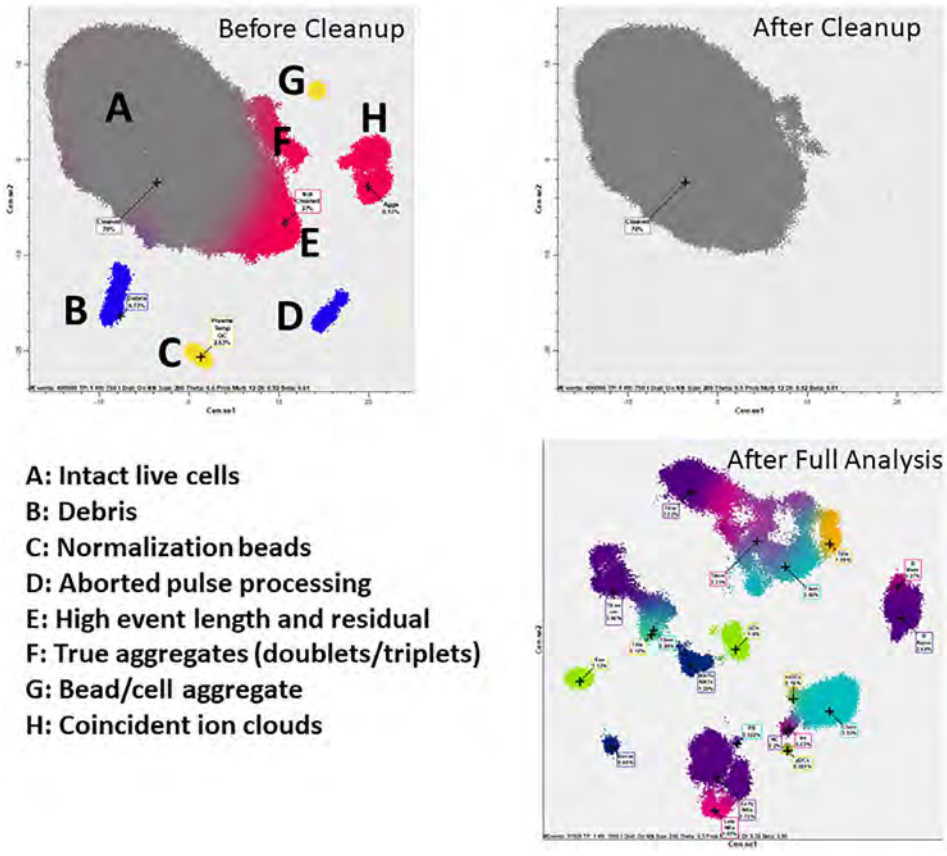

FIGURE 2 Cleanup and analysis Cen-se′ maps: The top two panels are Cen-se′ maps created from the QC measurements: DNA1, DNA2, Live/Dead, Beads, Event Length, Residual, Center, Width, and Offset. The top-left panel represents the raw normalized data from one file and the top-right the associated cleaned exported data. In the top-left panel, A (dark gray) are the live intact events, B (blue) are the low-DNA1 or debris events, C (yellow) are the normalization beads, D (blue) are events with zero pulse-processing parameters (Residual, Center, Width, and Offset), E (red) are "not cleaned events" with high Residual and Event Lengths, F (red) are true aggregates with high DNA1 and DNA2 intensities, G (yellow) are bead/cell aggregates, and H (red) are coincident ion clouds with low and high center values. The top-right panel is the Cen-se′ map of only the "cleaned" events. The bottom panel shows the same data with all markers selected after cleanup and modeling [Color figure can be viewed at wileyonlinelibrary.com]

2.7 | Data normalization

After acquisition, data were normalized using the CyTOF Software v. 6.7.1016. This method normalizes the data to a global standard, called a bead passport, determined for each log of EQ beads. This passport contains a profile of mean Di counts of all the masses for a particular lot of the beads as determined by multiple measurements during the manufacture of the EQ beads. The normalization factor is the ratio of passport median Di values to bead singlet population median Di values of the encoding isotopes. Isotopes in the EQ beads cover the mass range measurable on the CyTOF instrument. The normalization factors for mass channels between the encoding isotopes are linearly interpolated. All mass channel values for all events are then multiplied by these normalization factors to obtain the normalized values, and data are written to the normalized file.

2.8 | Data analysis

FCS files generated by the Helios were analyzed by Maxpar Pathsetter, an automated analysis system powered by GemStone™ 2.0.41 (Verity Software House, Topsham, ME). Initial analyses process raw normalized FCS3.0 files with a specially designed Cleanup PSM model. The Cleanup model leverages Gaussian pulse-processing parameters such as Center, Width, Offset, and Residual as well as DNA intercalators to eliminate unwanted events. Subsequent to cleanup, the program produces new FCS3.0 files consisting of only intact live singlet cells. This new cleaned file is then processed by an automated analysis of a second model, which also uses PSM to identify and label the major immune cell populations in sample files.

This system is integrated with dimensionality-reduction mapping known as Cauchy Enhanced Nearest-neighbor Stochastic Embedding (Cen-se′™), which generates a visual display of high-dimensional data labeled with the major cell populations. Figure 2 shows a Cen-se′ map of only QC measurements from one of the whole blood files in the study before and after the cleanup procedure (see top-left and right panels) as well as a map of all markers after full analysis (see bottom-right panel). All analyses were done on the same mid-level PC (Intel® Core™ i7-6700 CP @3.40 GHz RAM: 24 GB x64-based processor). The average run time for the whole blood Cleanup Stage was 37.3 s with a range of 36.5–37.9. The run time statistics for the other parts of the study were PBMC Cleanup Stage: 33.2 s (32.2–39.7), whole blood Phenotyping and Cen-se' Stage: 207.7 s (137.3–227.9), PBMC Phenotyping and Cen-se' Stage: 233.6 s (212.8–282.1). The complete average analysis time for the whole blood samples was 4.1 min and for PBMCs, 4.4 min.

3 | RESULTS

3.1 | Whole blood

A total of 32 whole blood-derived files from seven different sites were analyzed by the cleanup phase of the analysis (see Table 3 for a summary of the results). On average, 70.9% of the events were considered desirable "live intact cells"; 26.9% were excluded because they were classified as dead cells, debris, true aggregates, aborted pulses,

TABLE 3 Whole blood cleanup summary statistics

Multi-site whole blood reproducibility study: Cleanup statistics[a]														
Site	**Replicate**	**%Clean[b]**	**%Excluded**	**%Beads**	**%Unclass[c]**	**%Debris**	**%Dead**	**%Aggs**	**CeO_2 ratio**	**Acq rate**	**%CD19+ CD3+ [d]**	**%CD14+ CD3+ [e]**	**Total cells**	**Run time [f]**
Site 1A	1	65.1	32.7	1.9	0.4	9.9	0.1	13.8	1.6	406.1	0.3	0.5	400,000	37.1
	2	61.4	36.1	1.6	1.0	14.6	0.2	12.3	1.7	410.7	0.3	1.0	400,000	37.7
	3	65.8	32.4	1.4	0.5	11.9	0.1	11.7	1.3	353.0	0.2	0.4	400,000	37.9
	4*	51.9	45.0	1.2	1.8	27.3	0.8	9.3	1.5	444.9	0.2	21.5	400,000	37.5
Site 2	1	72.4	24.9	2.5	0.2	7.4	0.1	8.4	1.8	244.1	0.2	0.5	400,000	37.5
	2	72.5	24.8	2.5	0.2	6.4	0.1	9.1	1.8	269.4	0.2	0.5	398,479	37.2
	3	71.0	26.8	2.1	0.2	9.5	0.1	8.2	1.8	272.9	0.2	0.5	400,000	37.7
	4	75.0	22.5	2.4	0.1	4.9	0.1	9.0	1.8	246.3	0.2	0.6	400,000	37.0
Site 3	1	69.2	26.9	3.6	0.3	12.8	0.0	7.5	0.8	264.7	0.2	0.3	400,000	37.2
	2	61.4	34.8	3.3	0.5	20.6	0.0	7.7	1.9	260.4	0.2	0.5	400,000	37.2
	3	67.9	29.3	2.3	0.5	16.9	0.1	5.8	1.4	184.4	0.2	0.7	398,553	37.4
	4	72.3	23.0	4.5	0.2	6.7	0.0	9.8	2.0	349.0	0.2	0.4	400,000	37.1
Site 4	1	74.7	23.4	1.7	0.1	4.0	0.1	11.6	2.9	330.1	0.3	0.3	398,439	37.0
	2	72.3	26.2	1.0	0.5	5.2	0.1	13.6	2.8	389.9	0.3	0.4	400,000	37.4
	3	74.1	24.8	0.7	0.4	3.4	0.1	14.5	2.8	384.2	0.3	0.3	400,000	37.1
	4	70.2	29.0	0.6	0.2	4.4	0.1	16.5	2.9	402.4	0.4	0.5	400,000	37.4
Site 1B	1	69.3	28.5	1.9	0.2	9.2	0.1	11.5	1.6	327.3	0.2	0.5	400,000	37.3
	2	68.6	29.7	1.4	0.3	10.2	0.1	11.3	1.6	333.6	0.2	0.5	400,000	37.3
	3*	43.4	53.8	1.2	1.6	38.8	1.3	8.1	2.0	496.9	0.2	21.2	400,000	37.7
	4	74.5	24.3	0.9	0.3	7.0	0.1	11.1	1.8	305.6	0.2	0.8	400,000	37.2
Site 5	1*	67.1	29.0	3.3	0.5	15.5	0.3	8.0	1.1	293.5	0.2	18.7	400,000	37.7
	2	71.5	26.0	2.3	0.2	4.2	0.1	13.7	1.2	386.5	0.2	3.3	400,000	37.3
	3	72.5	24.8	2.5	0.2	3.3	0.1	14.5	1.1	373.8	0.2	1.6	400,000	37.3
	4	71.0	27.0	1.8	0.1	4.7	0.1	14.0	1.2	391.4	0.2	0.8	400,000	37.4
Site 6	1	79.0	20.1	0.8	0.2	3.0	0.0	11.8	1.4	278.4	0.2	1.0	400,000	37.0
	2	76.7	22.6	0.5	0.2	5.8	0.0	10.8	1.4	286.0	0.1	1.0	392,922	36.5
	3	78.5	20.7	0.7	0.1	4.3	0.0	9.8	1.4	264.9	0.1	1.2	400,000	37.2
	4	77.7	21.6	0.5	0.1	4.3	0.1	11.6	1.4	290.4	0.1	1.0	395,841	37.2
Site 7	1	78.1	19.4	2.4	0.1	3.7	0.2	11.3	1.6	317.7	0.2	0.3	400,000	37.3
	2	81.5	16.1	2.3	0.1	3.0	0.2	9.4	1.6	260.1	0.1	0.3	400,000	37.2
	3	80.7	17.6	1.6	0.1	2.4	0.2	12.2	1.7	333.6	0.2	0.5	400,000	37.2

(Continues)

TABLE 3 (Continued)

Multi-site whole blood reproducibility study: Cleanup statistics[a]														
Site	Replicate	%Clean[b]	%Excluded	%Beads	%Unclass[c]	%Debris	%Dead	%Aggs	CeO_2 ratio	Acq rate	%CD19+ CD3+[d]	%CD14+ CD3+[e]	Total cells	Run time[f]
	4	83.0	15.7	1.2	0.1	2.5	0.2	10.7	1.7	304.6	0.1	0.4	400,000	37.2
Averages		70.9	26.9	1.8	0.4	9.0	0.2	10.9	1.7	326.8	0.2	2.6	399,507	37.3

All FCS files were automatically analyzed by the Cleanup model.
The %Clean column quantifies the percentage of total events that were exported without debris, dead cells, aggregates, and normalization beads. %Excluded are the non-bead excluded events and %Beads are the normalization bead percentage. %Unclass are the percentage of unclassified events. The %Clean+%Excluded+%Bead+%Unclass fields add to 100%. %Debris are the sub DNA1 events that are not beads, % Aggs are the high DNA1 events, and %Dead are the events that are Live/Dead+. CeO+ ratio is an indicator of plasma temperature and should be less than 3.0. The acquisition rate is the number of acquired events/s, which is recommended to be approximately 350 events/s. The %CD19 + CD3+ and %CD14 + CD3+ columns are indicators of cell aggregation and coincident ion clouds. Total Cells are the total number of events acquired for analysis, and Run Time is the length of time in seconds for cleanup analysis. Three files were excluded due to background signal in the Er168 channel.

or coincident ion clouds; 1.8% were normalization beads; and 0.4% were unclassified. Approximately 13.2% of the excluded events were debris, 10.9% were high DNA1 aggregates, and the %dead cell count was low at 0.2%. All files had CeO+ ratios, a measure of plasma temperature, of less than 3. The average acquisition rate was approximately 326.8 events/s, and the average % of aggregates was reasonably low (%CD19 + CD3+ and %CD14 + CD3+ less than 0.2 and 2.6%, respectively). A total of 400,000 events were considered by the cleanup routine, and the average time spent in this step was approximately 37 s.

The deep immunophenotyping frequency results for whole blood are summarized in Table 4. The left side of the table shows the enumerated populations, and the numbers indicate the percentages of live intact cells in each of the replicates from all seven sites. Three replicates (Site 1A Rep 4, Site 1B Rep 3, and Site 5 Rep 1) were excluded due to background signal in the Er168 channel (see Section 4 for details). Figure 3 summarizes the inter-site reproducibility of all populations with both *SD*s and %CV of each population. Means, *SD*s, and %CVs from Sites 1A, 2, 3, and 4 were calculated separately from Sites 1B, 5, 6, and 7 because they were from a different sample. Statistics from both sets of sites were averaged. The percentages of live intact cells for each population and *SD*s are summarized in the top panel, and the %CVs are presented as a bar graph in the bottom panel. The inter-site average %CV was 14.4%, ranging from 2.3 to 96.6%, with higher %CVs generally associated with very low-frequency populations. The intra-site reproducibility is summarized in Table 5 and had an average %CV of 7.9%.

3.2 | PBMC

A total of 24 FCS3.0 PBMC-derived files from six different sites were analyzed by the cleanup phase of the analysis (See Table 6 for a summary of the results). On average, 76.7% of the events were considered desirable "live intact cells"; 21.4% were excluded because they were classified as dead cells, debris, true aggregates, aborted pulses, or coincident ion clouds; 1.8% were normalization beads, and 0.08% were unclassified. Approximately 4.2% of the excluded events were debris, 0.9% were dead, and 11.4% were high DNA1 aggregates. All files had CeO+ ratios of less than 3.5. The average acquisition rate was approximately 300 events/s, and the average % of double-positive aggregates was reasonably low (%CD19 + CD3+ and % CD14 + CD3+ less than 0.3 and 2.3%, respectively). Approximately 300,000 events were considered by the cleanup routine, and the average time spent in this step was approximately 33 s.

The deep immunophenotyping results are summarized in Table 7. The left side of the table shows the enumerated populations, and the numbers indicate the percentages of live intact cells from the four replicates from all six sites. Figure 4 summarizes the inter-site reproducibility of the percentages with both *SD*s as well as %CV. The percentiles and *SD*s are summarized in the top panel, and the %CVs presented as a bar graph in the bottom panel. The percentages, *SD*s, and %CVs were an average of Cohort 1 (Week 1) and 2 statistics. The average and median %CV were 17.7 and 13.7%, respectively. The

TABLE 4 Multi-site whole blood reproducibility study

Whole blood reproducibility study: Population percentages[a]																												
Blood source	Donor week 1[b]																Same donor week 2[c]											
Site	Site 1A[d]			Site 2				Site 3				Site 4				Site 1B			Site 2			Site 6				Site 7			
Replicate	1[e]	2	3	1	2	3	4	1	2	3	4	1	2	3	4	1	2	4	2	3	4	1	2	3	4	1	2	3	4
Lymphocytes	28.2	27.8	29.4	25.7	27.3	26.2	28.2	24.9	26.7	24.7	25.5	27.1	26.9	25.6	27.0	22.1	22.1	21.2	18.3	19.4	18.0	21.5	20.3	20.3	19.3	22.4	22.4	20.8	22.3
CD3 T cells	19.9	19.4	20.5	18.0	19.0	18.3	19.6	17.7	18.6	17.4	18.4	19.2	18.9	17.6	19.1	15.7	15.5	14.8	12.8	13.9	12.7	15.2	14.3	14.4	13.7	15.9	15.9	15.1	15.8
CD8 T cells	4.4	4.3	4.6	4.1	4.3	4.1	4.5	4.1	4.3	4.0	4.2	4.5	4.4	4.2	4.4	3.3	3.3	3.1	2.8	3.0	2.8	3.3	3.0	3.1	2.9	3.5	3.5	3.3	3.5
CD8 naïve	2.7	2.6	2.8	2.6	2.6	2.6	2.8	1.9	2.3	2.0	2.4	2.7	2.6	2.5	2.6	2.0	2.0	1.9	1.7	1.8	1.7	2.0	1.8	1.8	1.7	2.0	2.1	2.0	2.1
CD8 central memory	0.6	0.5	0.6	0.4	0.4	0.4	0.4	0.9	0.8	0.7	0.5	0.6	0.5	0.5	0.5	0.4	0.3	0.3	0.3	0.3	0.3	0.3	0.3	0.3	0.3	0.4	0.3	0.3	0.3
CD8 effector memory	1.0	1.0	1.1	1.0	1.1	1.0	1.1	1.1	1.1	1.1	1.1	1.0	1.1	1.1	1.1	0.8	0.8	0.8	0.7	0.7	0.8	0.9	0.8	0.9	0.8	1.0	0.9	0.9	1.0
CD8 terminal effector	0.2	0.2	0.2	0.2	0.2	0.2	0.2	0.2	0.2	0.2	0.2	0.2	0.2	0.2	0.2	0.1	0.2	0.2	0.1	0.1	0.1	0.1	0.1	0.1	0.1	0.2	0.2	0.1	0.1
CD4 T cells	12.8	12.5	13.1	11.4	12.1	11.7	12.5	11.3	11.7	10.9	11.6	12.3	12.1	11.7	12.3	10.1	9.8	9.5	8.0	8.8	7.9	9.7	9.1	9.2	8.9	9.9	10.0	9.5	10.0
CD4 naïve	2.8	2.7	2.9	3.0	3.3	3.0	3.4	1.5	1.9	1.8	2.2	2.7	2.8	2.8	2.8	2.3	2.2	2.2	2.2	2.4	2.1	2.4	2.2	2.2	2.2	2.3	2.4	2.2	2.4
CD4 central memory	4.3	4.3	4.2	3.3	3.5	3.4	3.6	4.4	4.4	3.9	3.9	3.9	3.5	2.8	4.0	3.2	3.2	3.0	1.8	2.1	2.0	2.9	2.7	2.7	2.5	2.7	2.7	2.5	2.9
CD4 effector memory	4.5	4.4	4.8	4.0	4.2	4.1	4.4	4.3	4.2	4.2	4.4	4.5	4.7	5.1	4.3	3.6	3.5	3.4	3.2	3.4	2.9	3.4	3.2	3.4	3.2	3.8	3.9	3.8	3.7
CD4 terminal effector	1.1	1.1	1.2	1.1	1.2	1.1	1.1	1.0	1.2	1.1	1.1	1.2	1.1	1.0	1.2	1.0	0.9	1.0	0.8	0.9	0.9	1.0	0.9	0.9	0.9	1.1	1.0	1.0	1.0
γδ T cells	1.5	1.4	1.5	1.4	1.4	1.4	1.5	1.3	1.4	1.4	1.5	1.4	1.4	1.5	1.5	1.2	1.2	1.2	1.1	1.1	1.1	1.2	1.2	1.1	1.1	1.3	1.3	1.2	1.2
MAIT/NKT cells	1.2	1.2	1.2	1.1	1.1	1.1	1.1	1.0	1.1	1.1	1.1	1.0	1.0	0.2	0.9	1.2	1.1	1.0	1.0	1.0	1.0	1.0	0.9	1.0	0.9	1.1	1.2	1.1	1.1
B cells	3.6	3.5	3.8	2.9	3.2	3.0	3.4	2.2	3.0	2.2	1.6	3.0	2.9	3.0	2.8	2.4	2.5	2.3	1.7	2.0	1.7	2.0	1.9	1.8	1.7	2.3	2.2	2.0	2.2
B Naïve	3.2	3.1	3.4	2.6	2.8	2.7	3.1	1.9	2.6	1.9	1.4	2.7	2.5	2.6	2.5	2.1	2.2	2.1	1.5	1.8	1.5	1.7	1.7	1.5	1.5	2.0	2.0	1.8	2.0
B memory	0.3	0.4	0.4	0.3	0.3	0.3	0.3	0.3	0.3	0.3	0.2	0.3	0.3	0.3	0.3	0.2	0.3	0.2	0.2	0.3	0.2	0.2	0.2	0.2	0.2	0.2	0.2	0.2	0.2
Plasmablasts	0.0	0.0	0.0	0.0	0.0	0.0	0.0	0.0	0.0	0.0	0.0	0.0	0.0	0.0	0.0	0.0	0.0	0.0	0.0	0.0	0.0	0.0	0.0	0.0	0.0	0.0	0.0	0.0	0.0
NK cells	4.7	4.9	5.1	4.8	5.1	4.9	5.2	5.0	5.2	5.0	5.4	4.9	5.1	5.0	5.1	4.1	4.1	4.0	3.7	3.5	3.6	4.3	4.1	4.1	3.9	4.3	4.2	3.7	4.2
NK early	3.9	4.0	4.3	3.7	4.0	3.8	4.1	4.4	4.5	4.4	4.7	3.9	4.0	4.0	4.0	3.4	3.4	3.3	2.8	2.7	2.7	3.5	3.4	3.3	3.1	3.3	3.2	2.8	3.2
NK late	0.8	0.8	0.9	1.0	1.1	1.1	1.1	0.6	0.6	0.7	0.7	1.1	1.1	1.0	1.1	0.7	0.7	0.7	0.9	0.8	0.9	0.8	0.8	0.8	0.8	1.0	1.0	0.9	1.0
Monocytes	3.6	3.7	3.8	4.0	4.0	3.8	3.9	2.7	3.0	2.8	2.6	3.2	2.6	1.9	2.5	3.0	3.1	3.3	2.6	4.4	4.0	4.2	4.4	4.6	4.4	4.6	4.8	4.8	4.7
Monocytes classical	3.2	3.3	3.4	3.5	3.6	3.4	3.5	2.0	2.4	2.1	2.2	2.8	2.1	1.5	2.1	2.7	2.9	3.0	2.3	4.1	3.7	3.8	4.0	4.2	4.1	4.3	4.4	4.5	4.4
Monocytes Intermediate	0.2	0.2	0.3	0.2	0.2	0.2	0.2	0.4	0.4	0.4	0.2	0.2	0.2	0.2	0.2	0.1	0.2	0.2	0.1	0.1	0.2	0.2	0.2	0.2	0.2	0.2	0.2	0.2	0.2
Monocytes nonclassical	0.2	0.2	0.2	0.2	0.2	0.2	0.2	0.3	0.3	0.3	0.2	0.2	0.2	0.2	0.2	0.1	0.1	0.1	0.1	0.2	0.1	0.2	0.2	0.2	0.2	0.2	0.2	0.1	0.1
DCs	0.3	0.5	0.3	0.2	0.2	0.2	0.3	0.3	0.4	0.5	0.3	0.2	0.3	0.2	0.3	0.2	0.2	0.2	0.3	0.3	0.3	0.2	0.2	0.2	0.2	0.2	0.2	0.2	0.2
pDCs	0.1	0.1	0.1	0.1	0.1	0.1	0.1	0.1	0.1	0.1	0.1	0.1	0.1	0.1	0.1	0.1	0.1	0.1	0.1	0.1	0.1	0.1	0.1	0.1	0.1	0.1	0.1	0.1	0.1
mDCs	0.2	0.4	0.2	0.2	0.2	0.1	0.2	0.2	0.1	0.4	0.2	0.1	0.2	0.2	0.2	0.2	0.2	0.2	0.2	0.2	0.2	0.2	0.2	0.2	0.1	0.1	0.2	0.2	0.2
Granulocytes	64.1	64.3	63.1	65.3	63.6	65.8	63.4	65.4	64.4	66.9	66.3	65.3	66.4	66.4	66.6	71.2	70.8	70.9	74.2	72.7	74.6	70.8	71.0	71.5	73.0	69.0	68.7	70.2	69.1
Neutrophils	61.7	62.1	61.0	63.3	61.8	63.8	61.6	62.7	60.9	63.8	63.9	61.2	63.1	59.3	61.9	69.4	68.9	68.7	72.3	70.5	72.8	69.0	69.2	69.9	71.0	67.4	67.1	68.6	67.5

(Continues)

TABLE 4 (Continued)

Whole blood reproducibility study: Population percentages[a]																											
Blood source	Donor week 1[b]																Same donor week 2[c]										
Site	Site 1A[d]			Site 2				Site 3				Site 4				Site 1B				Site 2				Site 6				Site 7			
Replicate	1[e]	2	3	1	2	3	4	1	2	3	4	1	2	3	4	1	2	3	4	2	3	4	1	2	3	4	1	2	3	4
Basophils	0.7	0.7	0.8	0.7	0.7	0.7	0.7	0.7	0.7	0.7	0.7	0.6	0.7	0.6	0.6	0.6	0.7	0.6	0.6	0.5	0.6	0.6	0.5	0.6	0.6	0.6	0.7	0.7	0.6	0.6
Eosinophils	1.1	1.0	0.8	1.1	1.0	1.1	1.0	0.9	0.9	0.9	1.0	1.0	1.0	1.0	1.0	0.9	0.9	0.9	0.9	0.9	0.9	1.0	1.0	1.0	1.0	1.0	0.9	0.9	1.0	1.0
CD66b- Neuts	0.6	0.5	0.6	0.4	0.1	0.2	0.1	1.1	1.9	1.5	0.7	2.6	1.6	5.7	3.2	0.4	0.4	0.7	0.7	0.5	0.7	0.6	0.3	0.2	0.1	0.1	0.0	0.0	0.0	0.0
Tregs	0.4	0.4	0.4	0.4	0.4	0.4	0.4	0.2	0.2	0.2	0.3	0.3	0.3	0.3	0.3	0.4	0.3	0.3	0.3	0.3	0.3	0.3	0.3	0.3	0.3	0.3	0.3	0.3	0.3	0.3
Th1-like	0.9	1.0	1.0	0.7	0.9	0.8	0.9	1.3	1.3	1.2	1.1	1.0	1.1	1.0	1.1	0.7	0.7	0.6	0.7	0.7	0.7	0.7	0.7	1.2	0.7	0.6	0.7	0.7	0.7	0.7
Th2-like	0.9	0.8	0.9	0.7	0.7	0.7	0.8	1.0	1.1	1.0	0.9	0.8	0.8	0.8	0.8	0.7	0.7	0.6	0.6	0.5	0.6	0.5	0.6	0.9	0.6	0.5	0.7	0.7	0.6	0.7
Th17-like	0.6	0.6	0.7	0.6	0.6	0.6	0.6	0.3	0.4	0.3	0.5	0.6	0.6	0.6	0.6	0.6	0.5	0.5	0.5	0.4	0.4	0.4	0.5	0.2	0.5	0.5	0.5	0.6	0.6	0.5

The above table summarizes all the frequency results for all sites and populations in terms of percent live intact cells.
[a]All samples were stained with Maxpar Direct Immune Profiling Assay.
[b]Same donor of whole blood sent to left four test sites.
[c]Same donor was drawn in week two and sent to right four test sites.
[d]Four replicates per site were processed except for three files with high background in 163Er channel (see Section 4).
[e]Population percentages are of intact live cells.

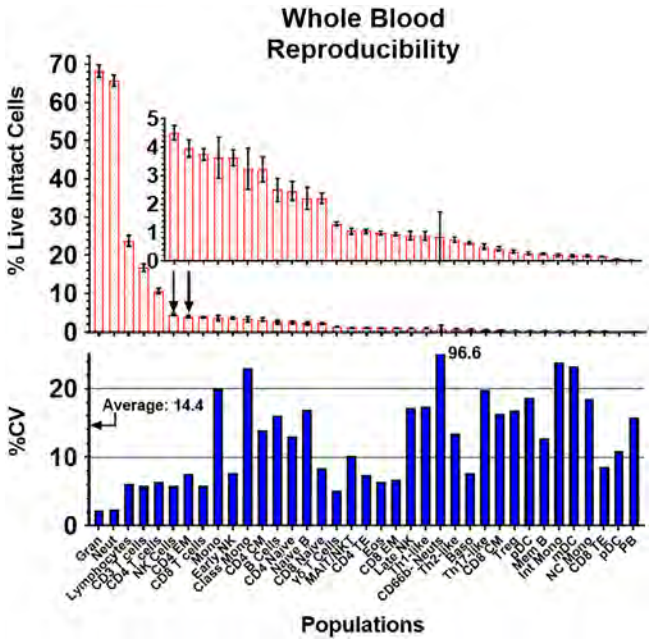

FIGURE 3 Whole blood reproducibility. The top panel shows the mean and ± *SD* percentage of live intact cells for all 37 evaluated populations across all seven sites. The bottom panel shows the associated %CVs for each population where the average was 14.4% [Color figure can be viewed at wileyonlinelibrary.com]

intra-site reproducibility is summarized in Table 8 and had an average and median %CV of 8.4 and 4.5%, respectively, for all sites and populations.

4 | DISCUSSION

The average event inclusion percentage for this study was approximately 70% for whole blood (see Table 3) and 76.7% for PBMC (see Table 6), which are generally comparable to gate-based inclusion percentages (data not shown). The site-to-site variability is probably either due to different environmental factors during the shipping of the samples or to slightly different site specimen handling techniques. The increase in %CD14+ CD3+ in Table 3 is due to the inclusion of the three files with a high CD14 Er168 background.

The average acquisition rate for both the whole blood and PBMC studies was approximately 300 events/s. Although the acquisition system can be set for faster rates, the Poisson nature of ion cloud formation creates more coincident clouds at faster rates. Most of these coincident events are removed in the cleanup stage, but the routine is not 100% effective in eliminating these events. A rate between 250 and 350 events/s is currently recommended by Fluidigm (Fluidigm, 2018).

The Cleanup model exports FCS3.0 data that are not only available for PSM automated analysis but also for other types of cytometry analysis as well. For investigators interested in oncological samples, the DNA selection parts of the Cleanup model can easily be deactivated in order that DNA hyperdiploid populations are not

TABLE 5 Whole blood intra-site reproducibility

Whole blood intra-site reproducibility %CV										
Population	**Site 1A**	**Site 2**	**Site 3**	**Site 4**	**Average Wk 1**	**Site 1B**	**Site 5**	**Site 6**	**Site 7**	**Average Wk 2**
Lymphocytes	2.8	4.1	4.0	1.5	3.1	2.4	8.3	5.2	4.2	4.0
CD3 T cells	2.6	3.7	3.1	2.2	2.9	2.9	8.4	6.0	2.8	3.9
CD8 T cells	3.3	3.5	3.7	3.1	3.4	3.6	6.5	7.9	2.6	4.2
CD8 naïve	3.5	4.0	7.8	3.8	4.8	4.3	8.4	7.0	2.6	5.1
CDS central memory	4.9	5.0	18.5	8.4	9.2	6.0	5.3	12.4	2.8	8.0
CDS effector memory	2.5	4.5	1.9	3.7	3.1	2.7	4.0	9.9	4.4	4.1
CDS terminal effector	3.7	4.1	6.8	9.7	6.1	12.0	9.7	6.4	8.7	7.5
CD4 T cells	2.6	4.0	3.0	1.9	2.9	2.9	10.3	4.7	2.9	3.9
CD4 naïve	4.1	5.7	17.7	2.1	7.4	2.0	7.1	2.9	3.8	5.9
CD4 central memory	3.3	4.5	7.4	15.3	7.6	8.0	23.3	3.9	7.5	9.0
CD4 effector memory	4.2	4.8	0.6	8.6	4.6	2.2	6.0	6.3	1.7	4.3
CD4 terminal effector	9.4	6.1	4.2	7.3	6.7	3.6	8.1	10.6	1.4	6.4
γδ T cells	3.9	3.8	4.7	3.1	3.9	1.5	5.9	7.3	4.3	4.3
MAIT/NKT cells	3.4	1.9	2.4	10.9	4.6	4.0	2.6	12.0	4.1	5.1
B cells	4.0	6.5	23.5	1.9	9.0	3.1	11.8	12.5	5.7	8.7
B naïve	4.4	6.6	25.4	2.0	9.6	2.6	10.7	13.6	5.9	9.0
B memory	2.8	6.9	12.8	3.9	6.6	7.0	20.6	8.5	5.0	8.2
Plasmablasts	11.3	9.7	15.5	21.7	14.5	10.3	16.3	15.8	11.7	14.1
NK cells	4.3	4.1	8.5	1.7	4.6	1.6	9.0	3.2	9.4	5.2
NK early	4.3	5.0	7.0	1.9	4.6	2.1	12.6	5.8	10.1	5.9
NK late	4.5	1.5	19.6	4.0	7.4	0.9	6.9	8.8	7.5	6.8
Monocytes	2.7	1.9	4.2	10.7	4.9	5.4	21.2	2.0	1.1	6.0
Monocytes classical	2.7	2.0	3.6	13.5	5.5	5.6	22.2	2.8	1.2	6.6
Monocytes transitional	4.4	9.3	29.5	7.9	12.8	6.8	10.6	16.5	2.7	11.2
Monocytes non-classical	5.2	5.8	13.1	6.6	7.7	2.4	19.5	7.5	8.7	8.5
DCs	35.0	7.9	21.4	16.7	20.3	5.4	8.5	4.7	4.7	13.8
pDCs	5.8	3.0	9.7	1.6	5.0	11.0	15.0	9.6	7.0	7.5
mDCs	43.4	11.9	26.3	24.1	26.4	3.2	6.1	6.1	3.7	16.8
Granulocytes	1.2	1.9	1.6	0.8	1.4	0.2	2.6	2.1	1.2	1.4
Neutrophils	1.0	l.8	2.1	2.6	1.9	0.5	2.5	2.1	1.2	1.7
Basophils	5.6	2.6	1.5	7.9	4.4	4.3	6.5	7.0	1.9	4.6
Eosinophils	14.4	3.8	3.5	4.1	6.5	2.0	5.5	3.1	2.6	5.1
CD66b- Neuts	8.6	73.7	38.9	53.2	43.6	36.6	35.9	66.1	37.4	43.8
Tregs	5.0	2.6	25.1	3.7	9.1	5.6	7.0	4.5	4.6	7.5
Th1-like	2.9	7.0	6.4	4.9	5.3	5.9	8.6	30.0	6.2	8.6
Th2-like	3.9	4.0	5.2	5.2	4.6	7.0	11.0	19.3	7.6	7.5
Th17-like	4.9	5.6	14.5	1.9	6.7	3.8	13.2	29.9	3.9	9.4
Mean	6.4	6.6	10.9	7.7	7.9	5.2	10.7	10.4	5.5	7.9

removed. However, if these measurements are deactivated, the number of true aggregates in the exported "cleaned" file is likely to increase. The data obtained in the multi-site study were generated using a prototype panel lot. Three out of 24 runs were excluded from the data presented due to background signals in the Er168 channel, which has been eliminated in subsequent manufacturing lots.

The staging approach for CD8 T-cells (see Table 2) was to first model the downregulation of CCR7 and CD27 to stratify events into three compartments: naïve + central memory, effector memory, and terminal effector. CD45RA was found not to be a good modeling marker for staging because of its relatively wide line-spread (data not shown) and branched nature (Inokuma, Maino, & Bagwell, 2013). The

TABLE 6 PBMC cleanup summary statistics

Multi-site PBMC reproducibility study: Cleanup statistics[a]														
Sites	Replicates	% Clean [b]	% Excluded	% Beads	% Unclass [c]	% Debris	% Dead	% Aggs	CeO_2 ratio	Acq rate	%CD19+ CD3+ [d]	%CD14+ CD3+ [e]	Total Cells	Run time[f]
Site 2	1	76.9	21.7	1.4	0.1	4.0	0.3	11.4	1.8	316.5	0.3	1.2	300,000	32.2
	2	75.9	22.8	1.3	0.1	5.2	0.3	11.1	1.9	298.8	0.3	1.4	300,000	33.2
	3	77.3	21.5	1.1	0.1	4.1	0.2	11.1	1.9	313.2	0.3	1.1	300,000	33.0
	4	78.2	20.5	1.3	0.1	4.3	0.2	10.1	1.2	214.2	0.2	1.1	288,975	32.4
Site 3	1	73.7	24.0	2.2	0.1	6.8	0.1	11.4	2.1	266.1	0.4	1.3	298,335	33.1
	2	68.8	28.4	2.6	0.1	8.7	0.1	13.2	2.1	303.5	0.5	1.6	400,000	39.9
	3	76.6	16.7	6.6	0.1	3.0	0.1	7.8	2.0	248.3	0.2	1.2	300,000	33.6
	4	75.2	19.4	5.3	0.1	4.0	0.1	9.0	2.0	279.3	0.3	1.9	300,000	32.9
Site 4	1	72.1	27.0	0.8	0.1	6.2	0.6	15.0	2.8	413.2	0.6	1.5	300,000	33.7
	2	66.4	32.6	0.7	0.2	6.2	0.4	18.2	3.3	414.9	0.5	1.6	300,000	33.3
	3	79.2	19.5	1.2	0.1	4.0	0.3	10.6	3.0	300.0	0.4	1.4	300,000	32.5
	4	76.7	21.7	1.5	0.1	5.1	0.2	11.3	2.9	295.6	0.5	1.5	300,000	32.8
Site 5	1	75.7	22.8	1.4	0.1	2.2	0.2	15.5	1.1	403.8	0.5	1.4	300,000	32.9
	2	78.2	20.0	1.7	0.1	2.0	0.0	13.5	1.1	361.0	0.4	1.3	300,000	32.6
	3	75.9	22.5	1.5	0.1	2.8	0.2	15.2	1.2	394.7	0.4	7.9	300,000	32.7
	4	77.4	20.2	2.2	0.2	8.2	0.4	7.6	1.2	241.5	0.2	14.2	300,000	32.5
Site 6[g]	1	75.6	23.3	1.0	0.1	4.6	3.1	11.0	1.4	254.2	0.2	1.2	300,000	33.0
	2	74.4	24.9	0.6	0.1	6.1	3.6	10.2	1.4	244.7	0.3	1.9	297,593	32.6
	3	83.6	15.3	1.1	0.0	2.5	2.8	5.4	1.4	127.6	0.1	2.0	300,000	32.8
	4	75.7	19.5	4.7	0.1	4.9	4.0	6.5	1.4	164.5	0.2	2.3	300,000	32.4
Site 7	1	81.7	17.4	0.8	0.0	1.9	1.3	11.7	1.7	317.1	0.3	1.3	300,000	32.9
	2	80.7	18.6	0.7	0.0	1.7	1.6	12.9	1.6	356.7	0.3	2.0	300,000	33.0
	3	82.0	17.4	0.6	0.0	1.4	1.0	12.4	1.7	339.4	0.4	1.8	295,265	33.0
	4	83.5	15.9	0.6	0.0	1.4	0.9	11.1	1.9	308.3	0.3	1.7	300,000	32.7
Mean		76.7	21.4	1.8	0.08	4.2	0.9	11.4	1.8	299.1	0.3	2.3	303,340	33.2

[a]All samples were stained with Maxpar Direct Immune Profiling Assay.
[b]Percent of total events. %Cleaned+%Excluded+%Beads+%Unclassified = 100.
[c]Percent of events that were not classified into the cell types Cleaned, Excluded, or Beads.
[d]Percent of CD19+ CD3+ double positives of CD19+ singlets + CD3+ singlets.
[e]Percent of CD14+ CD3+ double positives of CD14+ singlets + CD3+ singlets.
[f]Units of seconds.
[g]The first acquisition of Site 6 samples had insufficient EQ Beads for normalization. Samples were spun down and resuspended again in fresh CAS/0.1 EQ Beads to acquire data for analysis.

system then used a combinatory analysis system called TriCOM to divide the first stage into its naïve and central memory components. The staging approach for CD4 T-cells (see Table 2) was to model the downregulation of CD45RA, CCR7, and CD27 to create the four stages: naïve, central memory, effector memory, and terminal effector. The CD4 T-cell terminal effector was assumed to be CD45RA– because CD45RA+ events were generally not observed in any sample in this study (see Figure 5) and it has been recognized that there are a few if any CCR7– CD45RA+ events in the CD4 T-cell compartment for healthy individuals (Seder & Almed, 2003).

Subclassification of monocytes into Classical, Transitional, and Non-classical used CD14 and CD38 (see Table 2) instead of the more traditional CD14 and CD16 (Picozza, Battistini, & Borsellino, 2013). The patterns produced by CD14 and CD38 were found to classify analogous subpopulations while improving the overall reproducibility of the results (data not shown).

The data presented in Tables 4 and 7 summarize all the cell population frequency results obtained from the whole blood and PBMC studies. An inspection of these tables shows the high degree of reproducibility of the system for almost all immune populations. Figures 3 and 4 summarize the inter-site variability of the whole blood and PBMC studies. The populations are ordered from the highest percentage (left) to the lowest (right) in order to better appreciate the general effect of counting error increasing the magnitude of CVs for

TABLE 7 Multi-site PBMC reproducibility study

Multi-site PBMC reproducibility study: Population percentages[a]																								
Site	Site 2 [b]				Site 3				Site 4				Site 5				Site 6				Site 7			
Replicate	1 [c]	2	3	4	1	2	3	4	1	2	3	4	1	2	3	4	1	2	3	4	1	2	3	4
Lymphocytes	67.1	65.9	66.4	65.7	67.0	67.5	67.4	67.2	65.6	65.7	66.0	66.0	75.6	73.6	65.5	62.4	64.3	64.3	70.1	62.7	68.1	68.3	69.4	69.8
CD3 T cells	50.5	49.8	50.1	50.1	48.6	49.6	48.0	48.4	48.0	47.7	46.1	44.9	50.8	51.6	46.2	40.1	48.6	48.5	46.4	43.5	48.2	48.6	50.6	50.3
CD8 T cells	10.3	10.1	10.2	10.1	10.3	10.4	10.2	10.2	10.3	10.2	10.4	10.3	11.4	11.2	9.8	9.8	10.6	10.6	12.6	10.4	10.6	10.2	10.5	10.5
CD8 naïve	6.2	6.1	6.2	6.1	6.0	6.0	5.9	5.9	6.2	6.4	6.3	6.2	6.2	6.4	5.9	5.3	6.4	6.4	7.4	6.0	6.2	5.8	6.1	5.9
CD8 central memory	0.4	0.4	0.5	0.5	0.5	0.6	0.6	0.6	0.6	0.4	0.5	0.5	0.5	0.4	0.4	0.2	0.5	0.5	0.4	0.4	0.3	0.4	0.4	0.4
CD8 effector memory	2.0	2.1	2.0	2.0	2.2	2.2	2.0	2.1	1.7	1.5	1.7	1.6	2.6	2.5	2.0	2.3	1.9	1.8	2.1	1.9	2.3	2.3	2.2	2.4
CD8 terminal effector	1.6	1.4	1.5	1.6	1.7	1.6	1.7	1.6	1.7	1.8	1.9	2.0	2.2	1.9	1.5	2.0	1.9	1.9	2.7	2.0	1.9	1.8	1.8	1.9
CD4 T cells	32.4	32.0	32.1	32.3	29.9	30.8	29.5	30.0	31.5	31.1	29.2	28.4	29.8	30.7	28.6	23.9	29.7	29.8	24.5	25.4	30.4	30.3	31.6	31.2
CD4 naïve	12.7	12.5	12.4	12.6	11.1	11.4	11.0	11.3	13.5	13.8	12.3	12.6	12.8	13.3	12.7	10.2	11.4	12.2	11.3	9.9	12.4	12.6	13.0	12.6
CD4 central memory	6.4	6.3	7.0	6.5	6.6	6.7	6.7	6.9	6.7	6.1	5.9	5.5	4.4	4.9	4.7	3.3	6.8	6.4	4.1	5.6	5.6	5.1	5.5	5.3
CD4 effector memory	9.8	9.8	9.2	9.7	8.4	8.4	7.9	7.8	6.5	6.6	6.6	6.0	9.0	8.7	8.1	7.2	7.3	7.1	5.3	6.0	8.3	8.6	9.1	9.1
CD4 terminal effector	3.5	3.5	3.6	3.5	3.8	4.3	3.9	4.1	4.8	4.6	4.4	4.2	3.7	3.8	3.1	3.3	4.1	4.2	3.8	3.9	4.1	3.9	4.0	4.1
γδ T cells	4.3	4.4	4.3	4.2	4.6	4.7	4.5	4.6	4.4	4.4	4.5	4.5	6.0	5.3	4.4	4.5	4.4	4.5	5.4	4.6	4.8	4.5	4.6	4.7
MAIT/NKT cells	3.5	3.3	3.5	3.5	3.7	3.7	3.8	3.6	1.8	1.9	1.9	1.8	3.6	4.4	3.3	1.8	4.0	3.6	4.0	3.1	2.4	3.6	3.9	4.0
B cells	7.1	6.6	6.9	6.4	7.6	7.6	8.0	8.0	7.9	8.1	8.6	9.1	8.5	8.0	7.4	6.2	5.3	5.2	5.1	5.8	7.4	7.3	7.3	7.3
B naïve	5.9	5.4	5.6	5.3	6.4	6.4	6.8	6.7	6.7	6.7	7.3	7.8	7.3	6.9	6.3	5.3	4.3	4.3	4.3	4.8	6.3	6.2	6.1	6.2
B memory	1.1	1.1	1.1	1.0	1.1	1.1	1.1	1.2	1.2	1.3	1.3	1.3	1.1	1.0	1.0	0.7	0.9	0.8	0.7	0.9	1.0	1.0	1.0	1.0
Plasmablasts	0.1	0.1	0.1	0.1	0.1	0.1	0.1	0.1	0.1	0.1	0.1	0.1	0.1	0.1	0.1	0.1	0.1	0.1	0.1	0.1	0.1	0.1	0.1	0.1
NK cells	9.6	9.5	9.4	9.1	10.8	10.3	11.4	10.9	9.6	10.0	11.3	11.9	16.4	14.1	11.9	16.2	10.3	10.6	18.6	13.4	12.5	12.3	11.6	12.2
NK early	2.7	2.7	2.7	2.7	3.5	3.4	3.8	3.5	2.9	3.0	3.3	3.6	4.5	3.9	3.1	4.2	3.2	3.3	6.0	4.3	3.6	3.6	3.3	3.5
NK late	6.8	6.8	6.7	6.4	7.3	6.9	7.6	7.3	6.7	7.0	8.0	8.4	11.9	10.2	8.8	12.0	7.1	7.3	12.6	9.1	8.9	8.7	8.3	8.7
Monocytes	24.2	24.6	24.9	24.0	24.3	22.8	25.2	24.9	25.3	25.9	26.0	25.9	15.7	17.3	18.0	14.0	25.5	25.0	21.4	26.0	22.1	22.1	21.1	21.1
Monocytes classical	19.4	19.4	19.9	19.0	19.6	18.2	20.5	20.1	19.0	19.4	19.4	19.2	11.5	13.4	14.6	11.1	19.4	18.9	14.8	19.7	17.8	17.8	17.0	16.9
Monocytes transitional	2.9	3.1	2.9	2.9	2.7	2.6	2.8	2.9	3.3	3.0	3.3	3.3	2.1	2.3	2.8	2.5	3.5	3.4	3.0	3.4	2.6	2.6	2.5	2.5
Monocytes non-classical	1.9	2.1	2.0	2.1	1.9	1.9	1.9	1.9	3.1	3.4	3.3	3.3	2.1	1.7	0.7	0.4	2.6	2.6	3.6	2.9	1.7	1.7	1.6	1.7
DCs	0.9	0.9	0.9	0.8	1.0	1.0	0.9	0.8	1.0	1.2	1.0	1.0	0.7	0.7	0.3	0.2	1.3	1.3	1.5	1.2	1.1	1.0	0.9	1.0
pDCs	0.2	0.2	0.2	0.2	0.2	0.2	0.2	0.2	0.2	0.2	0.2	0.2	0.2	0.2	0.1	0.0	0.2	0.2	0.3	0.2	0.2	0.2	0.2	0.2
mDCs	0.7	0.7	0.7	0.7	0.9	0.9	0.7	0.6	0.8	1.0	0.8	0.7	0.6	0.6	0.2	0.1	1.1	1.1	1.3	1.0	0.9	0.8	0.8	0.8
Tregs	0.8	0.8	0.8	0.8	0.7	0.8	0.7	0.8	0.5	0.5	0.5	0.5	0.6	0.6	0.6	0.4	0.4	0.1	0.4	0.5	0.7	0.7	0.7	0.7
Th1-like	2.0	1.8	2.0	1.9	1.4	1.3	1.4	1.4	1.1	1.1	1.2	1.4	1.9	1.8	1.6	1.0	0.4	0.0	0.3	0.3	0.3	0.3	0.3	0.2

(Continues)

TABLE 7 (Continued)

Multi-site PBMC reproducibility study: Population percentages[a]																							
Site	Site 2[b]				Site 3				Site 4				Site 5				Site 6				Site 7			
Replicate	1[c]	2	3	4	1	2	3	4	1	2	3	4	1	2	3	4	1	2	3	4	1	2	3	4
Th2-like	2.1	2.2	2.1	2.2	2.9	3.2	2.8	3.0	3.1	2.9	2.8	3.0	3.8	4.0	3.7	3.3	5.6	0.0	3.0	4.5	5.2	5.1	5.0	4.1
Th17-like	2.6	2.7	2.6	2.7	2.9	3.0	2.8	2.9	2.5	2.4	2.1	1.5	1.7	1.8	1.6	1.5	0.3	5.7	0.7	0.4	1.6	1.6	2.1	3.1

The above table summarizes all the frequency results for all sites and populations in terms of percent live intact cells.

[a]All samples were stained with Maxpar Direct Immune Profiling Assay.

[b]Four replicates per site were processed.

[c]Population percentages are of live intact cells.

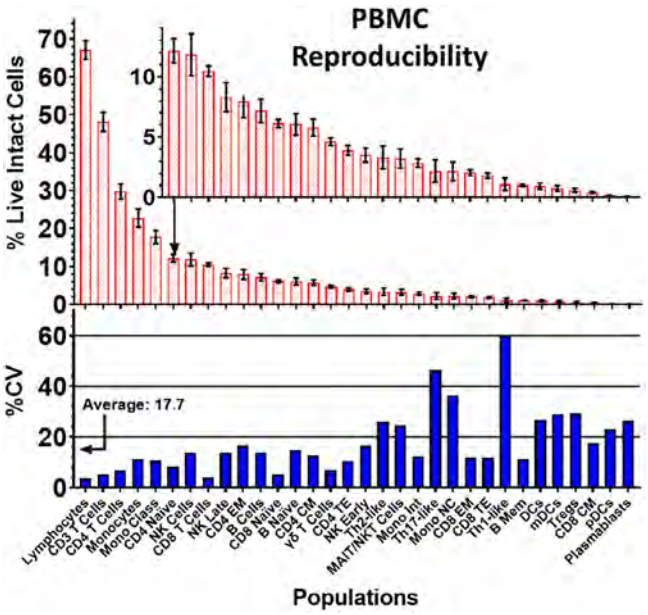

FIGURE 4 Peripheral blood mononuclear cells (PBMC) reproducibility. The top panel shows the mean and ±*SD* percentage of live intact cells for all 37 evaluated populations. Absent from this plot are the granulocyte, neutrophils, basophils, eosinophils, and CD66b− granulocytes. The bottom panel shows the associated %CVs for each population, where the average was 17.7%. The percentages, *SD*s, and %CVs were an average of Cohort 1 (Week 1) and 2 statistics [Color figure can be viewed at wileyonlinelibrary.com]

low-frequency populations. The average %CV for all 37 populations was 14.4% for whole blood and 17.7% for PBMC. The slight increase in variability for the PBMC may be due in part to the extra cell manipulations for this type of preparation. A high %CV was observed for the population labeled as CD66b− neutrophils in whole blood mainly due to its low frequency.

The upper panel insets with the ±*SD* ranges show a high degree of reproducibility even among many of the very low-frequency populations. Some populations are better defined by the panel than others, which explain some of the variability in the %CVs for populations with similar frequencies, and additional markers may be included to enhance identification in studies focused on low-frequency cell populations. The PBMC portion of this study is reasonably comparable to the multi-site study published by Leipold et al. (2018).

Tables 5 and 8 summarize the intra-site reproducibility of the whole blood and PBMC studies. As expected, the average and median intra-site %CV's are lower than the inter-site %CV's due to slight site-to-site biases. Some of the high intra-site %CV's for both whole blood and PBMC were due to outliers in the relatively small number of replicates. There was some disparity in intra-site %CV's across all populations among the sites in the study, which was more pronounced for low-frequency cell types.

The dry nature of the reagent in this assay eliminates most pipetting errors and reduces overall preparation time. An important feature of this system is that additional reagents can be added to

TABLE 8 PBMC intra-site reproducibility

Intra-site PBMC reproducibility %CV								
Population	**Site 2**	**Site 3**	**Site 4**	**Site 5**	**Site 6**	**Site 7**	**Average**	**Median**
Lymphocytes	1.0	0.3	0.3	9.1	5.0	1.2	2.8	1.1
CD3 T cells	0.5	1.4	3.1	11.2	5.1	2.4	4.0	2.7
CD8 T cells	0.9	1.3	0.9	8.2	9.2	1.6	3.7	1.4
CD8 naïve	1.0	0.7	1.6	8.0	9.0	2.6	3.8	2.1
CD8 central memory	10.0	4.6	13.5	25.8	13.4	18.3	14.3	13.4
CD8 effector memory	3.2	4.8	5.0	11.4	5.0	2.8	5.4	4.9
CD8 terminal effector	5.4	1.7	5.6	13.7	19.2	2.4	8.0	5.5
CD4 T cells	0.5	1.9	5.0	10.6	10.3	2.0	5.1	3.5
CD4 naïve	1.0	1.5	5.4	11.2	8.6	2.0	5.0	3.7
CD4 central memory	4.7	1.6	8.0	16.8	20.6	3.9	9.3	6.4
CD4 effector memory	3.2	3.9	4.4	9.6	14.8	4.1	6.7	4.3
CD4 terminal effector	1.2	5.7	5.3	9.6	5.1	2.1	4.8	5.2
γδ T cells	2.0	1.2	0.9	14.6	9.9	2.5	5.2	2.3
MAIT/NKT cells	2.1	2.3	3.1	32.8	11.3	20.9	12.1	7.2
B cells	4.3	2.9	6.4	13.2	5.7	0.6	5.5	5.0
B naïve	4.7	3.1	7.4	13.3	5.6	1.2	5.9	5.1
B memory	2.8	3.9	4.2	18.0	13.6	3.0	7.6	4.1
Plasmablasts	3.7	12.4	13.2	27.0	13.2	5.7	12.5	12.8
NK cells	2.3	4.0	10.1	14.4	29.0	3.3	10.5	7.0
NK early	0.9	4.6	9.4	14.8	30.4	3.8	10.7	7.0
NK late	3.0	3.8	10.4	14.3	28.4	3.1	10.5	7.1
Monocytes	1.6	4.4	1.2	11.0	8.5	2.5	4.9	3.5
Monocytes classical	1.8	5.0	1.1	12.9	12.6	2.6	6.0	3.8
Monocytes transitional	2.6	4.5	4.1	12.0	6.8	1.8	5.3	4.3
Monocytes non-classical	3.8	1.2	4.3	65.3	15.6	2.6	15.5	4.0
DCs	4.3	10.9	10.3	61.5	9.5	7.2	17.3	9.9
pDCs	0.2	5.2	5.6	60.7	13.1	4.7	14.9	5.4
mDCs	5.4	14.3	13.1	61.9	9.4	8.7	18.8	11.3
Tregs	2.7	3.3	8.0	13.5	58.6	4.9	15.2	6.5
Th1-like	5.3	5.6	12.1	24.8	66.7	18.6	22.2	15.3
Th2-like	2.4	4.5	3.9	8.2	73.8	10.6	17.2	6.4
Th17-like	1.9	2.8	20.4	8.1	146.3	33.8	35.6	14.3
Mean	2.8	4.0	6.5	20.2	21.7	5.9	10.2	6.2
Median	2.5	3.8	5.4	13.4	11.9	2.9	6.7	4.6

The 37 tested populations appear in the first column, and the %CVs of the four replicate PBMC samples are summarized for each site. The means and medians of the %CVs for all populations and sites appear on the outside rows and columns.

evaluate new populations because there are numerous open heavy metal channels. The Maxpar Pathsetter software is also designed for users to easily amend the models to take advantage of new markers and cell types.

The performance of the analysis system was designed to do a full and automated analysis in less than 5 min. The Cen-se′ mapping system is a high-resolution and highly parallelized variant of the t-SNE algorithm (van der Maaten, 2009, 2014; van der Maaten & Hinton, 2008) that can create maps of hundreds of thousands of events in 1 min or less.

The dry nature of the reagent coupled with automated data analysis is not only convenient but also provides a high degree of reproducibility within and among multiple test sites, whether they are analyzing whole blood or PBMC samples. This new mass cytometry assay provides a comprehensive yet practical solution for deep immune phenotyping.

ACKNOWLEDGMENTS

The authors wish to acknowledge the helpful editing from Dmitry Bandura, Tony Shuga, and Dorothy McDuffie. This work could not have been done without the resources of both Verity Software and Fluidigm.

CONFLICT OF INTEREST

Authors Bagwell, Hunsberger, Hill, Herbert, Bray, Selvanantham, Li, Inokuma, Goldberger, and Stelzer are currently employed or were employed by either Verity Software House or Fluidigm Corporation. Author Inokuma is a consultant for both Verity Software House and Fluidigm Corporation. This manuscript describes a component of the product, Fluidigm Maxpar Pathsetter, which was a collaborative effort between these two companies.

DISCLOSURES

Fluidigm, Cell-ID, CyTOF, EQ, Helios, Maxpar, and Pathsetter are trademarks and/or registered trademarks of Fluidigm Corporation in the United States and/or other countries. All other trademarks are the sole property of their respective owners. For research use only, not for use in diagnostic procedures.

REFERENCES

Bagwell, C. (2010). Probability state modeling: A new paradigm for cytometric analysis. In V. Litwin & P. Marder (Eds.), *Flow cytometry in drug discovery and development* (p. 281). Hoboken, NJ: John Wiley and Sons Inc.

Bagwell, C. B. (2018). Chapter 2: High-dimensional modeling for cytometry: Building rock solid models using GemStonetm™ and Verity Cen-se'™ high-dimensional t-SNE mapping. In T. S. Hawley & R. G. Hawley (Eds.), *Methods in molecular biology* (Vol. 1678, p. 2018). New York: Springer Science+Business Media LLC.

Bagwell, C. B., Hunsberger, B. C., Herbert, D. J., Munson, M. E., Hill, B. L., Bray, C. M., & Preffer, F. I. (2015). Probability state modeling theory. *Cytometry Part A*, *87*, 646–660.

Bagwell, C. B., Leipold, M., Maecker, H., & Stelzer, G. (2016). *High-dimensional modeling of peripheral blood mononuclear cells from a Helios Instrument*. Seattle, Washington: Washington State Convention Center.

Blazkova, J., Gupta, S., Liu, Y., Gaudilliere, B., Ganio, E. A., Bolen, C. R., … Furman, D. (2017). Multicenter systems analysis of human blood reveals immature neutrophils in males and during pregnancy. *Journal of Immunology*, *198*, 2479–2488.

Finak, G., Langweiler, M., Jaimes, M., Malek, M., Taghiyar, J., Korin, Y., … JP, M. C. (2016). Standardizing flow cytometry immunophenotyping analysis from the human ImmunoPhenotyping consortium. *Scientific Reports*, *6*, 20686.

Fluidigm (2018). Maxpar Human Immune Monitoring Panel Kit Cell Staining and Data Acquisition. In: Fluidigm, editor. PN PRD027 C1 Protocol.

Herbert, D., Miller, D., & Bagwell, C. (2012). Automated analysis of flow cytometric data for CD34+ stem cell enumeration using a probability state model. *Cytometry Part B, Clinical Cytometry*, *82B*, 313–318.

Inokuma, M. S., Maino, V. C., & Bagwell, C. B. (2013). Probability state modeling of memory CD8(+) T-cell differentiation. *Journal of Immunological Methods*, *397*, 8–17.

Leipold, M. D., Obermoser, G., Fenwick, C., Kleinstuber, K., Rashidi, N., McNevin, J. P., … Maecker, H. T. (2018). Comparison of CyTOF assays across sites: Results of a six-center pilot study. *Journal of Immunological Methods*, *453*, 37–43.

Li, S., Majonis, D., Bagwell, C. B., Hunsberger, B. C., Baranov, V. I., & Ornatsky, O. (2018). An efficient human whole blood workflow using CyTOF technology: A lyophilized 30-plex antibody panel coupled with automated data analysis. *Journal of Immunology*, *200*, 120.2.

Li, S., Majonis, D., Bagwell, C. B., Hunsberger, B. C., Baranov, V. I., & Ornatsky, O. (2019). A robust human immunophenotyping workflow using CyTOF technology coupled with Maxpar Pathsetter, an automated data analysis software. *Journal of Immunology*, *202*.

Maecker, H. T., McCoy, J. P., & Nussenblatt, R. (2012). Standardizing immunophenotyping for the human immunology project. *Nature Reviews Immunology*, *12*, 191–200.

Miller, D. T., Hunsberger, B. C., & Bagwell, C. B. (2012). Automated analysis of GPI-deficient leukocyte flow cytometric data using GemStone. *Cytometry Part B, Clinical Cytometry*, *82*, 319–324.

Ornatsky, O. I., Lou, X., Nitz, M., Schafer, S., Sheldrick, W. S., Baranov, V. I., … Tanner, S. D. (2008). Study of cell antigens and intracellular DNA by identification of element-containing labels and metallointercalators using inductively coupled plasma mass spectrometry. *Analytical Chemistry*, *80*, 2539–2547.

Picozza, M., Battistini, L., & Borsellino, G. (2013). Mononuclear phagocytes and marker modulation: When CD16 disappears, CD38 takes the stage. *Blood*, *122*, 456–457.

Rahman, A. H., Tordesillas, L., & Berin, M. C. (2016). Heparin reduces non-specific eosinophil staining artifacts in mass cytometry experiments. *Cytometry Part A*, *89*, 601–607.

Seder, R. A., & Almed, R. (2003). Similarities and differences in CD4+ and CD8 + effector and memory T cell generation. *Nature Immunology*, *4*, 835–842.

van der Maaten, L. (2009). Learning a Parametric Embedding by Preserving Local Structure. In AISTATS. TiCC. Tilburg, The Netherlands: Tilburg University.

van der Maaten, L. (2014). Accelerating t-SNE using tree-based algorithms. *Journal of Machine Learning Research*, *15*, 1–21.

van der Maaten, L., & Hinton, G. (2008). Visualizing data using t-SNE. *Journal of Machine Learning Research*, *9*, 2579–2605.

Wong, L., Hill, B. L., Hunsberger, B. C., Bagwell, C. B., Curtis, A. D., & Davis, B. H. (2014). Automated analysis of flow cytometric data for measuring neutrophil CD64 expression using a multi-instrument compatible probability state model. *Cytometry Part B, Clinical Cytometry*, *88*(4), 227–235.

Wong, L., Hunsberger, B. C., Bruce Bagwell, C., & Davis, B. H. (2013). Automated quantitation of fetomaternal hemorrhage by flow cytometry for HbF-containing fetal red blood cells using probability state modeling. *International Journal of Laboratory Hematology*, *35*, 548–554.

SUPPORTING INFORMATION

Additional supporting information may be found online in the Supporting Information section at the end of this article.

Mass Cytometry: a robust platform for the comprehensive immunomonitoring of CAR-T-cell therapies

By reprograming T-cell specificity, chimaeric antigen receptors' (CARs) function and persistence have changed the landscape of cancer immunotherapy with remarkable efficacy against a range of B-cell malignancies and have many prospective applications.[1,2] Investigating the immune mechanisms that underlie the success of CAR-T-cell therapy is a crucial challenge.[3,4,5] The advent of time-of-flight mass cytometry (CyTOF) has enabled high-dimensional and unbiased examination of complex systems.[6,7] We present here the first contribution of mass cytometry to the comprehensive immunomonitoring of CAR-T-cell therapies.

We constructed an original platform to determine whether identification of CAR-T cells and immune cells lacking CAR (non-CAR) and their functional states in peripheral blood would be possible in a single-pass mass cytometry assay. We therefore customized a commercially available immune panel (Maxpar Direct Immune Profiling System, Fluidigm, San Francisco, CA, USA) for mass cytometry with a CAR-T-cell detection reagent along with complementary markers.[8]

The mass cytometry assay was developed in patients with refractory diffuse large B-cell lymphoma (DLBCL) and acute lymphoblastic leukemia (ALL) treated in our CAR-T-cell programme by tisagenlecleucel (Kymriah, Novartis, Bale, Suisse; Table S1). Patients received a lymphodepletive regimen, CAR-T-cell infusion and post CAR-T-cell care according to standard practices and all gave written informed consent.[9]

Development and robustness of a mass cytometry customized panel for CAR and non-CAR immune cell determination

The Maxpar Direct Immune Profiling System, bringing together mass cytometry technology, a 30-antibody panel and fully automated reporting, is a high-dimensional immune profiling assay designed to broadly look at the phenotypes and functions of immune cell subsets through a single-tube view. So far, no metal-tagged antibodies for mass cytometry that identify CAR-T cells have been described. Therefore, we customized the Maxpar panel by developing a cadmium ($^{106/116}$Cd)–anti-biotin CD19Fc (106/116 cadmium metal isotopes, Fluidigm, Canada; pure anti-biotin antibody and CD19Fc Detection Reagent, biotin, Milteny Biotec, Bergisch Gladbach, Germany) that identify CAR-T cells and validated its robustness by comparison with routine assays. CAR-T cells were usually assessed by flow cytometry, using the CAR Detection Reagents (Miltenyi), and by quantitative polymerase chain reaction (qPCR) using an assay commercialized to quantify HIV-1 (Generic HIV DNA Cell® test for research use, Biocentric, Bandol, France).[10,11] These two assays performed similarly ($r = 0{\cdot}6782$, $P < 0{\cdot}0001$ by Spearman correlation; $n = 44$; Fig 1A and Figure S1). Over a broad range of frequencies from 0·12 to 22% $CD3^+$ CAR-T cells, we showed that, for the detection of CAR-T cells, results obtained with our $^{106/116}$Cd–anti-biotin CD19Fc used for mass cytometry

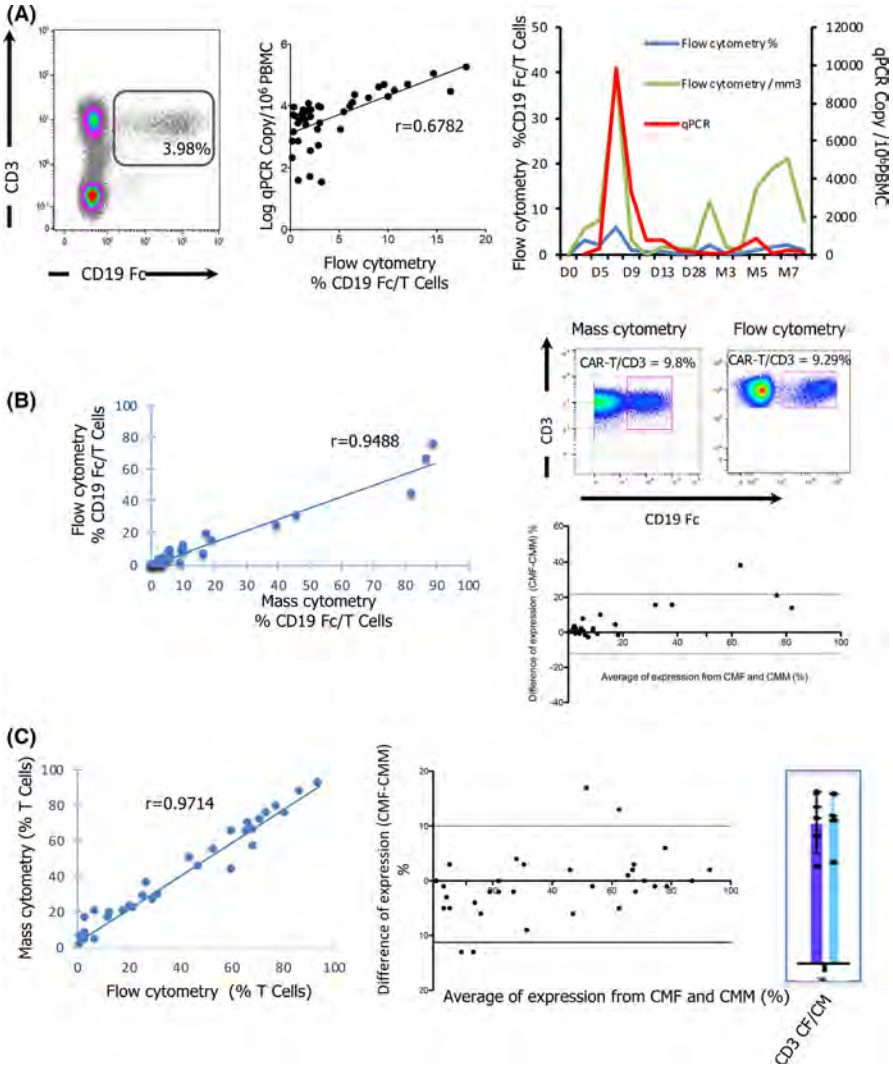

Fig 1. Robustness of mass cytometry for the monitoring of blood chimaeric antigen receptor (CAR)-T cells and immune cells. Peripheral blood mononuclear cells from 10 patients having received CAR-T cells were stained and analyzed to determine the populations of CAR-T and immune cells using mass cytometry, flow cytometry and quantitative polymerase chain reaction (qPCR). For flow cytometry, data acquisition and analyses were performed on a Navios flow cytometer (Beckman Coulter, Villepinte, France); for qPCR, data were acquired on a Light Cycler® 480 (Roche Diagnostics, Meylan, France); for mass cytometry, data were acquired on a Helios machine and analyzed using Maxpar Pathsetter software (Gemstone, Verity Software House, Topsham, ME, San Francisco, CA, USA with Fluidigm) with integrated dimensionality reduction mapping (Cen-se™). (A) Routine assays for peripheral CAR-T-cell determination using flow cytometry and qPCR. Representative biaxial plot of $CD3^+$ and $CD19Fc^+$ CAR-T cells (left panel). Flow cytometry for measurement of the percentage of $CD19Fc^+$ CAR-T cells (Miltenyi Biotec) and qPCR for quantification of long-terminal repeat (LTR) sequences (Generic HIV DNA Cell®test for research use, Biocentric, Bandol, France) performed similarly ($n = 44$; $P < 0{\cdot}001$ using a Spearman correlation [GraphPad software, Prism, San Diego, CA, USA]; middle panel). Representative quantification of CAR-T cells over time using the two assays. qPCR copies of HIV; percentage of $CD3^+/CD19Fc^+$ CAR-T cells using flow cytometry; absolute value (/mm^3) of $CD3^+/CD19Fc^+$ CAR-T cells (right panel). (B) Strong agreement between the percentages of $CD19Fc^+$ CAR-T cells as determined by mass and flow cytometry ($n = 72$). Pearson correlation between the quantification of CAR-T cells using our cadmium ($^{106/119}$Cd)–anti-biotin, CD19Fc and the CD19 CAR Detection reagent (Miltenyi) for respectively mass and flow cytometry; the linear regression line is shown on the left panel. Representative biaxial plot of percentage of $CD3^+/CD19Fc^+$ CAR-T cells using mass and flow cytometry and Bland–Altman validation method (right panel). (C) Validation of the customized mass cytometry panel for T-cell composition ($n = 52$). Mann–Whitney U test (GraphPad; left panel) together with the Bland–Altman validation method (middle panel) confirmed that mass cytometry correlated strongly with routine flow cytometry assays for measurement of the main subsets of T cells (CD3, −4, −8, -HLA-DR, −69, −25, −45RA, −45RO). These data also allowed to convert CAR–T cells detected by mass or flow cytometry into the absolute value of viable $CD3^+$ cells, as measured by single-platform flow cytometry (right panel). CMF, flow cytometry; CMM, mass cytometry. [Colour figure can be viewed at wileyonlinelibrary.com]

strongly correlated with those obtained by flow cytometry (Pearson correlation; $r = 0{\cdot}95$, $P < 0{\cdot}05$; $n = 72$; confirmed by the validation method of Bland–Altman; Fig 1B).

We also completed the panel with four other anti-human markers (NKP30, PD1, CD163 and CD69, tagged with ^{159}Tb, ^{175}Lu, ^{165}Ho and ^{162}Dy, respectively; Fluidigm) and checked that

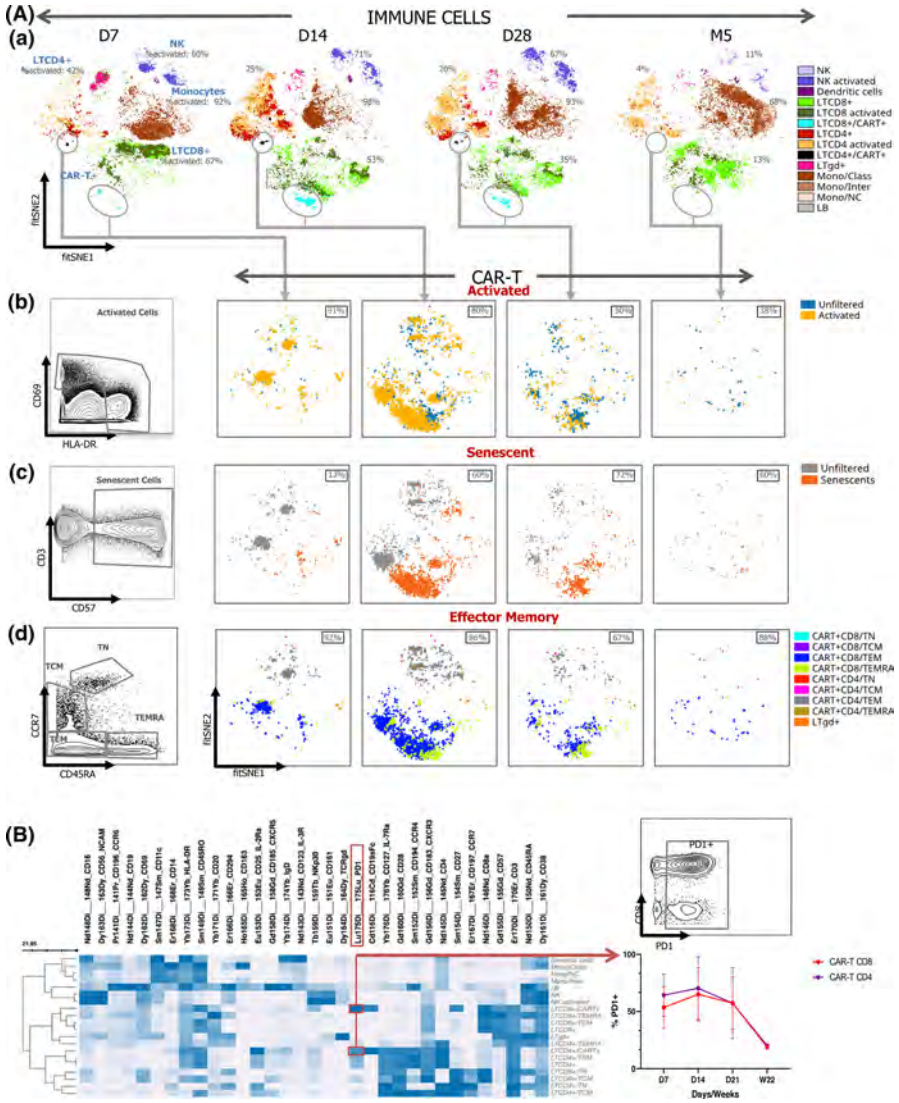

Fig 2. Automated identification of cell populations and their functional states by mass cytometry. (A) *t*-Distributed stochastic neighbour embedding (t-SNE) overview of identity and activity of chimaeric antigen receptor (CAR) and non-CAR immune cells over time after CAR-T-cell administration, analyzed with the OMIQ software in order to obtain the t-SNE maps. Shown is one representative patient. (a) Overview of non-CAR immune cells and subsets and their activated and non-activated states. Activated $CD4^+$ and $CD8^+$ cells, cytolytic natural killer (NK) cells and classical monocytes are revealed through combinatorial expression of respectively HLA-DR and CD69, CD16/CD56/NKp30 and CD14/CD16 over time after administration; the mean percentage of activated cells in the different populations is indicated. Activation reached a maximum on Day 7 or 14 and then decreased with time. Cells are manually coloured according to their immune cell lineage. (b, c, d) Overview of CAR-T-cell activation and antigen-experience state (b) Activation profiles of CAR-T cells: the expression of HLA-DR and CD69 shows that almost all CAR- T cells were activated during the 14 days following administration (percentages over time indicate CAR-T cells expressing HLA-DR and CD69). Black identifies unsigned (non-activated) CAR-T cells isolated by manual gating (c) As a result of their activation, most of the CAR T cells were senescent, as shown by their CD57 expression; percentage of senescent cells over time is indicated (d) The differential expression patterns of CCR7 and CD45 RA identify the maturation and antigen-experience states of CAR-T cells, such as naïve, effector, effector memory and central memory (left panel). Most CAR-T cells are effector memory T cells; the percentage of both TEM and TEMRA cells is indicated. (B) Clustering of CAR and non-CAR immune cells. (Left) Clustering. Data from blood samples collected on day 14 after CAR-T-cell administration were pooled, clustered and automatically annotated with the OMIQ software offering an overview of highly expressed markers on specific populations (n = 5). (Right) PD1 expression on CAR-T cells over time. Note the high expression of PD1 until day 28 on $CD8^+$ CAR-T cells. [Colour figure can be viewed at wileyonlinelibrary.com]

the identification of the main immune cell populations and subsets together with automatic data analyses remained valid using this customized panel. As shown in Fig 1C, the customized Maxpar panel and flow cytometry strongly correlated for the detection and quantification of immune cell subsets (r = 0·97, P < 0·05; confirmed by the Bland–Altman method).[12]

Customized mass panel-supported comprehensive immunomonitoring after CAR-T cell administration

The combination of antibodies in our customized Maxpar panel allowed characterization of CAR and non-CAR immune cells and their functional states, in a single pass and over time (Fig 2A). Data were analyzed via the Maxpar Pathsetter software (Gemstone) which generates a visual display of high-dimensional data.

We present here preliminary observations on peripheral blood of five patients followed over time after CAR-T-cell administration. Kinetics of CAR and non-CAR immune cell activation is poorly known and Fig 2A, panels a and b give a simple and comprehensive picture of their massive activation. Almost all (92 ± 4%) CAR-T cells, mainly $CD8^+$, were activated on day 7 as demonstrated by HLA-DR and CD69 expression (Fig 2A, panel b). Activation decreased from day 14 but activated CAR-T could be detected up to five months post administration. Exhaustion and senescence are critical dysfunctional states impacted by persistent stimulation and a high level of senescence was observed in CAR-T cells (mean, 65 ± 5% from day 14 to 28; Fig 2A, panel c). Among non-CAR immune cells (Fig 2A, panel a), macrophages/monocytes have been reported as key mediators in CAR-T-related toxicities; here almost all monocytes demonstrated an inflammatory profile of M1 monocytes $CD14^{++}C16^-$ (mean, 93 ± 4%) on days 7 and 14. The combinatorial expression of HLA-DR and CD69, and CD16/CD56/NKp30, demonstrated the activated states of $TCD8^+$ lymphocytes (mean, 82 ± 7%) and cytolytic NK cells (mean, 65 ± 4%) respectively on days 7 and 14.

It is now clear that less differentiated lymphocytes are more effective in the transfer of immunity for adoptive cell therapy and our approach also provided information regarding maturation and antigen-experience states (naïve, effector, central memory) of CAR and non-CAR cells by evaluating the differential expression patterns of CCR7 and CD45RA.[13] In our small group of patients, the effector memory state of CAR-T cells varied from 64% to 95% (Fig 2A, panel d). Finally, this platform allowed the clustering of CAR and non-CAR immune cells and offered an overview of highly expressed markers on specific subpopulations (Fig 2B). We could note a high expression of PD1 until day 28 on $CD8^+$ CAR-T cells (mean, 53 ± 4%) suggesting that CAR-T cells could in part circumvent the PD-L1/PD1 brake.[14] The expression of PD1 and some chemokine receptors on CAR-T cells could be a sensitive biomarker as suggested by the three patients who achieved complete or partial responses and this could support further investigations.

This integrated method could also track signatures for personalized therapeutic strategies. In Figure S2, we also report the real-time characterization of an activated population of Th17 lymphocytes in blood and bone marrow samples of a patient that experienced a profound aplasia after CAR-T-cell administration. This suggested that haematologic toxicity following CAR-T-cell infusions could be due to immune-mediated bone marrow failure as described in sporadic aplastic anaemia and provide orientations for adapted therapeutic strategies.

Together, we found that mass cytometry-based platform offers a powerful and reliable tool for comprehensive description of CAR-T and environmental immune cell subsets and opens new opportunities to identify immune signatures and support personalization of therapeutic strategy to enhance CAR-T-cell efficacy.

Acknowledgements

We thank Bénédicte Hoareau-Coudert et Angélique Vinit for technical support and Clément Dumas for help in mass cytometric analysis.

Funding

This work was supported by grants from the Société Française de Greffe de Moelle and Association Capucine.

Author contributions

AC and CP performed mass cytometric analyses and wrote the paper. MC developed the mass-tagged CAR-T-cell antibody. ET analyzed qPCR data. CB discussed results. DR-W and SNG took patients in care and discussed results. EL and AG supervised the cytometric analyses and discussed results. FN conceived of and designed the experiments, supervised the research and wrote the paper.

Conflict of interest

The authors declare to have no potential conflicts of interest regarding the present work.

Aurélien Corneau[1,*]
Christophe Parizot[2,3,*]
Mustapha Cherai[2,3]
Eve Todesco[4]
Catherine Blanc[1]
Elena Litvinova[2]
Stéphanie Nguyen[5]
Damien Roos-Weil[5]
Amélie Guihot[2,3]
Francoise Norol[5]

[1]Sorbonne Université (Univ. Paris 06), UMS37-PASS, Plateforme de cytométrie, Hôpital Pitié-Salpêtrière, [2]Assistance Publique-Hôpitaux de Paris (AP-HP), Hôpital Pitié-Salpêtrière, Département d'Immunologie F-75013, [3]Sorbonne Université (Univ. Paris 06), INSERM U1135, Centre d'Immunologie et des Ma-ladies Infectieuses (CIMI-Paris), Hôpital Pitié-Salpêtrière, [4]Assistance Publique-Hôpitaux de Paris (AP-HP), Hôpital Pitié-Salpêtrière, Laboratoire de Virologie, F-75013 and

[5]*Assistance Publique-Hôpitaux de Paris (AP-HP), Service d'Hématologie, Hôpital Pitié Salpêtrière, Paris, F-75013, France.*
E-mail: f.norol@aphp.fr
*AC and CP contributed equally to this work.

Keywords: chimaeric antigen receptor-T cells, immunomonitoring, mass cytometry

First published online 26 May 2021
doi: 10.1111/bjh.17551

Supporting Information

Additional supporting information may be found online in the Supporting Information section at the end of the article.

Table SI. Characteristics of the patients.

Fig S1. The CAR-T-cell detection reagent from Miltenyi Biotec (Bergisch Gladbach, Germany) provides better discrimination in comparison with the Acrobiosystems (Newark, DE, USA) reagent for $CD19^{+}$ CAR-T-cell determination.

Fig S2. Signature associated with post CAR-T cells aplasia in a given patient. Real-time characterization of activated populations of Th17 and CD69 lymphocytes and regulatory T lymphocytes (TReg) in the blood and bone marrow of a patient displaying profound aplasia on day 60 after CAR-T-cell administration (left and middle panels). Note that in blood, the Th17 cell population is present at a high level compared to that in a panel of patients who rapidly recovered following CAR-T-cell infusion (right panel). Black indicates unsigned cell populations.

References

1. June CH, Sadelain M. Chimeric antigen receptor therapy. *N Engl J Med*. 2018;**379**:64–73.
2. Mueller KT, Maude SL, Porter DL, Frey N, Wood P, Han X, et al. Cellular kinetics of CTL019 in relapsed/refractory B-cell acute lymphoblastic leukemia and chronic lymphocytic leukemia. *Blood*. 2017;**130**:2317–25.
3. Shah NN, Fry T. Mechanisms of resistance to CAR T cell therapy. *Nat Rev Clin Oncol*. 2019;**16**:372–85.
4. Fraietta JA, Lacey SF, Orlando EJ, Pruteanu-Malinici I, Gohil M, Lundh S, et al. Determinants of response and resistance to CD19 chimeric antigen receptor (CAR) T cell therapy of chronic lymphocytic leukemia. *Nat Med*. 2018;**24**:563–71.
5. Du M, Hari P, Hu Y, Mei H. Biomarkers in individualized management of chimeric antigen receptor T cell therapy. *Biomarker*. 2020;**8**:1–13.
6. Gadalla R, Noamani B, MacLeod BL, Dickson RJ, Guo M, Xu W, et al. Validation of CyTOF against flow cytometry for immunological studies and monitoring of human cancer clinical trials. *Front Oncol*. 2019;**9**:415.
7. Hartmann FJ, Babdor J, Gherardini PF, Amir E-A, Jones K, Sahaf B, et al. Comprehensive immune monitoring of clinical trials to advance human immunotherapy. *Cell Rep*. 2019;**28**:819–31.
8. Bagwell CB, Hunsberger B, Hill B, Herbert D, Bray C, Selvanantham T, et al. Multi-site reproducibility of a human immunophenotyping assay in whole blood and peripheral blood mononuclear cells preparations using CyTOF technology coupled with Maxpar Pathsetter, an automated data analysis system. *Cytometry B Clin Cytom*. 2020;**98**:146–60.
9. Lee DW, Santomasso BD, Locke FL, Ghobadi A, Turtle CJ, Brudno JN, et al. ASBMT consensus grading for cytokine release syndrome and neurologic toxicity associated with immune effector cells. *Biol Blood Marrow Transplant*. 2019;**25**:625–38.
10. De Oliveira SN, Wang J, Ryan C, Morrison SL, Kohn DB, Hollis RP. A CD19/Fc fusion protein for detection of anti-CD19 chimeric antigen receptors. *J Transl Med*. 2013;**11**:23.
11. Hauser JR, Hong H, Babady NE, Papanicolaou GA, Tang Y-W. False-positive results for human immunodeficiency virus type 1 nucleic acid amplification testing in chimeric antigen receptor T cell therapy. *J Clin Microbiol*. 2019;**58**:e01420–e1519.
12. Appay V, Dunbar PR, Callan M, Klenerman P, Gillespie GMA, Papagno L, et al. Memory CD8+ T cells vary in differentiation phenotype in different persistent virus infections. *Nat Med*. 2002;**8**:379–85.
13. McLellan AD, Ali Hosseini Rad SM. Chimeric antigen receptor T cell persistence and memory cell formation. *Immunol Cell Biol*. 2019;**97**:664–74.
14. Dong E, Yue X-Z, Shui L, Liu B-R, Li Q-Q, Yang Y, et al. IFN-γ surmounts PD-L1/PD1 inhibition to CAR-T cell therapy by upregulating ICAM-1 on tumor cells signal transduction and targeted. *Therapy*. 2021;**6**:20.

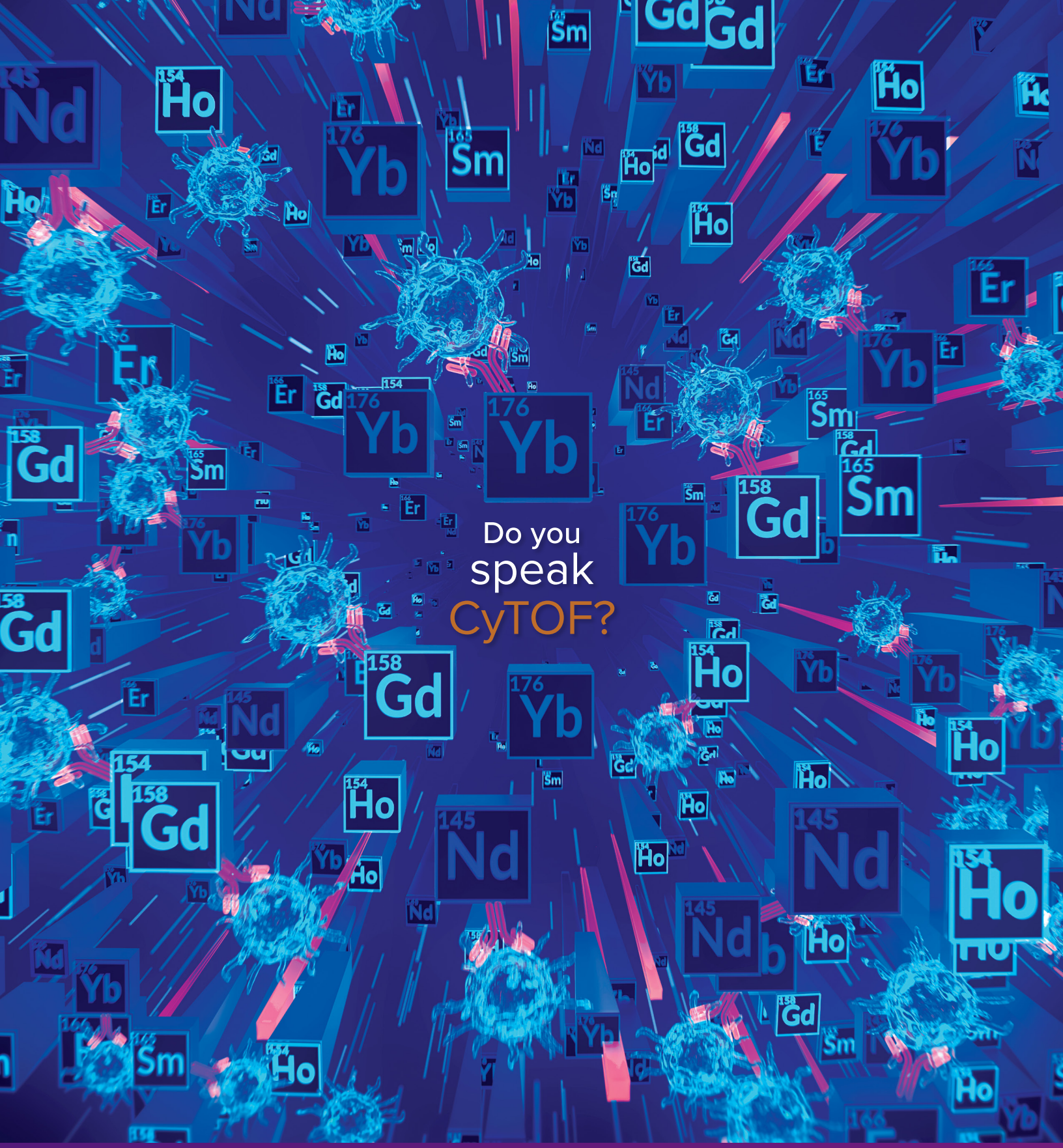

FLUIDIGM®

CyTOF®

Learn more: fluidigm.com